DEVELOPMENT OF A POTENTIAL FLOW PROGRAM FOR THE HYDRODYNAMIC PROBLEMS OF MULTIPLE BODIES AT ZERO OR NONZERO FORWARD SPEED AND ITS APPLICATIONS

A Dissertation

by

YUJIE LIU

Submitted to the Office of Graduate and Professional Studies of
Texas A&M University
in partial fulfillment of the requirements for the degree of

DOCTOR OF PHILOSOPHY

Chair of Committee,	Jeffrey M. Falzarano
Committee Members,	Moo-Hyun Kim
	Richard S. Mercier
	Hamn-Ching Chen
Head of Department,	Sharath Girimaji

August 2018

Major Subject: Ocean Engineering

ABSTRACT

The configuration of multiple floaters is of growing interest in offshore operations. An in-house program, MDLMultiDYN, is developed to evaluate the hydrodynamics of the multiple bodies.

The fully nonlinear problem in potential theory is decomposed into 1st order and 2nd order problems. Applying the Green function method, the source formula is adopted to solve for the 1st order problem for multiple bodies with zero or nonzero speed. The added mass and damping for an asymmetric case are derived. The theory to simplify the boundary condition is discussed.

To capture the physical resonance, the irregular frequencies must be removed. The theory to ensure the uniqueness of the solution is reviewed and improved. Four methods are proposed to evaluate the log singularity at the internal free surface, which is a necessary step in the extended boundary condition method. The jump conditions are discussed and the effective formula to remove the irregular frequencies is presented.

The 2nd order problem is also discussed. The formula of the 2nd order force and moment for a general case are presented. The importance of removing the irregular frequency effect is discussed. Additionally, improvement is made to accurately calculate the wave elevation around the waterline of the floater. The wave elevation can be calculated in an approximately analytical way.

The problem of two box barges side-by-side is investigated in both the CFD approach and the potential method. The results are validated against the experimental data. Excellent agreement between the CFD results and the experimental data is achieved. The discrepancy between the results from the potential method and the CFD approach is contributed by the friction effect of the ship hull at the selected wave frequency. Finally, the current artificial damping methods are discussed and an alternative wall damping method is proposed. The effectiveness of the method is discussed by comparison against the experimental data.

The study provides a complete and comprehensive study in the potential theory to evaluate the hydrodynamic loads and responses of multiple floaters. By comparisons against CFD results and experimental data, we gain a deeper understanding of the interaction phenomenon.

DEDICATION

To my wife and my parents.

ACKNOWLEDGMENTS

I would like to express my deepest gratitude to my advisor and the committee chair, Dr Falzarano, for his patience, encouragement and scholarly advices throughout my graduate study.

I am very grateful to my committee members Dr Richard Mercier, Dr Moo-Hyun Kim, Dr Hamn-Ching Chen and previous committee member Dr Othon Rediniotis for their guidance, teachings and encouragement. Their courses have helped me build a solid foundation in developing the thesis work. I am also thankful to Dr Francis Noblesse for his valuable advice on the Green function and helpful comments on the papers about the irregular frequency removal methods.

I am thankful to Dr. Paul Hess from ONR EMSF Program, Andy Silver from NSWC-CD and Alex Landsburg from the SNAME T&R Program for providing partial support of the research work.

I am grateful to the staffs of the library. They helped me find all kinds of articles and books around the world. Also, thanks to Lisa Wilson, Laura Byrd, Caleb Mullins and Chris Grunkemeyer who are always very helpful and kind hearted.

Last but not least, I would like to give a heartfelt thanks to my parents, my beloved wife Wenwen for their firm support and constant encouragement throughout my PhD study. I also would like to thank all my friends who have helped me during this period of time.

CONTRIBUTORS AND FUNDING SOURCES

Contributors

This work was supported by a dissertation committee consisting of Professors Jeffrey Falzarano, Moo-Hyun Kim and Hamn-Ching Chen of the Department of Ocean Engineering and Professor Richard Mercier of the Department of Civil Engineering.

The data analyzed for Chapter 7 was provided by Dr Wenhua Zhao, University of Western Australia.

All other work conducted for the dissertation was completed by the student independently.

Funding Sources

Graduate study was supported by a fellowship from Texas A&M University. Also partial support was provided by Office of Naval Research under ONR Grant N000-14-16-1-2281 and Society of Naval Architects and Marine Engineers.

NOMENCLATURE

Φ	time dependent wave potential
ζ	wave elevation at the free surface
k	wave number
P	time dependent pressure
$\overline{\Phi}$	potential defined in translating coordinate
$\overline{\Phi}_{rel}$	wave potential for the relative velocity in vessel translating coordinate
S	instantaneous wetted surface
S_m	mean wetted surface
$\vec{X}$	position vector in the static global coordinate
$\vec{X}_0$	position of the origin of the translating global coordinate
$\vec{X}'$	position vector in vessel coordinate
$\Phi^{(1)}$	potential of the first order
$\Phi^{(2)}$	potential of the second order
g	gravity acceleration
ω_I	radian frequency of incident wave
ω_e	encounter radian frequency
U	forward speed of the vessel
β	the angle of wave direction with respect to the positive x axis
$\vec{n}$	normal vector on the ship hull surface at instantaneous position
$\vec{n}'$	normal vector on the ship hull surface in equilibrium position

$\vec{\eta}$	translation of the vessel
$\eta_i^{(1)}(i=1,2,3)$	1st order translation of the vessel
$\eta_i^{(1)}(i=4,5,6)$	1st order rotation of the vessel
$\eta_i^{A(1)}(i=1,2,3)$	time independent part of 1st order translation of the vessel
$\eta_i^{A(1)}(i=4,5,6)$	time independent part of 1st order translation of the vessel
$\vec{\alpha}$	rotation of the vessel
J_0	Bessel function of the first kind
$\phi^{(1)}$	time independent potential of the first order
$\phi_i^{(1)}$	time independent internal potential of the first order
$\phi_I^{(1)}$	time independent part of the 1st order incident potential
$\phi_I^{*(1)}$	time independent part of the 1st order incident potential for unit amplitude of the wave
$\phi_D^{(1)}$	time independent part of the 1st order diffraction potential
$\phi_D^{*(1)}$	time independent part of the 1st order diffraction potential for unit amplitude of the wave
$\phi_i^{*(1)}$	time independent part of the 1st order diffraction potential for unit amplitude of the motion
V_n	time dependent normal velocity on the ship hull surface
v_n	time independent normal velocity on the ship hull surface
G	Green function
P	pressure on the instantaneous wetted surface
$P^{(1)}$	1st order pressure on the equilibrium wetted surface
$P^{(2)}$	2nd order pressure on the equilibrium wetted surface
σ	source strength
$p^{d(1)}$	time independent part of the first order dynamic pressure
$p^{d(1)}$	time independent part of the first order dynamic pressure

M	the mass matrix
M^a	the added mass matrix
B	the damping matrix
C	the restoring matrix
$A_{ij}^{\langle l \rangle}$	element of the added mass matrix for the lth body
$A_{ij}^{\langle n,l \rangle}$	radiation effect on body n from body l
$\zeta_r^{(1)}$	relative wave elevation
C_{wl}	the contour of the waterline

TABLE OF CONTENTS

Page

LIST OF FIGURES

FIGURE Page

LIST OF TABLES

TABLE Page

1. INTRODUCTION [1]

1.1 Background and Motivations

Multi-body operations are routinely performed in offshore activities. Multiple floaters can complement each other in functionality and fully utilize the equipment on board. This scenario can reduce development and operation cost and improve profit margin. Thus, it may help the industry to be less vulnerable to fluctuating oil and gas prices.

Currently, there are several configurations regarding multi-body operations. One classical example is the side-by-side case of the FLNG (Floating Liquefied Natural Gas) and LNGC (Liquefied Natural Gas Carrier). The integrated concept has moved the land-based factory offshore. The FLNG will produce and process the natural gas and off-load it to the close-by LNGC. The LNGC will carry the gas to the export terminal near shore or on shore. This scenario will reduce the cost and the negative environmental impact to the local area. It has a great potential in future offshore gas explorations. The gap resonance is the key to evaluate the interaction effects of this plan. We need to quantify the interaction effects to ensure the safety of such operation. This configuration can be shown in Figure 1.1.

[1]Part of the chapter is reprinted with permission from "Frequency Domain Analysis of the Interactions Between Multiple Ships with Nonzero Speed in Waves or Current-Wave Interactions" by Yujie Liu, Jeffrey Falzarano, 2017. *Proceedings of the ASME 2017 36th International Conference on Ocean, Offshore and Arctic Engineering*, pp. 1-17 Copyright 2017 by ASME.

[1]Part of the chapter is reprinted with permission from "Irregular Frequency Removal Methods: Theory and Applications in Hydrodynamics" by Yujie Liu, Jeffrey Falzarano, 2017. *Journal of Marine System and Ocean Technology*, Vol 12, Issue 2, pages 49-64. Copyright 2017 by Sociedade Brasileira de Engenharia Naval.

[1]Part of the chapter is reprinted with permission from "A method to remove irregular frequencies and log singularity evaluation in wave-body interaction problems" by Yujie Liu, Jeffrey Falzarano, 2017. *Journal of Ocean Engineering and Marine Energy*, Vol 3, Issue 2, pages 161-189. Copyright 2017 by Springer International Publishing Switzerland.

[1]Part of the chapter is reprinted with permission from "Suppression of irregular frequency in multi-body problem and free-surface singularity treatment" by Yujie Liu, Jeffrey Falzarano, 2017. *Proceedings of the ASME 2016 35th International Conference on Ocean, Offshore and Arctic Engineering*, pages 1-11. Copyright 2017 by ASME.

[1]Part of the chapter is reprinted with permission from "Suppression of Irregular Frequency Effect in Hydrodynamic Problems and Free-Surface Singularity Treatment" by Yujie Liu, Jeffrey Falzarano, 2017. *Journal of Offshore Mechanics and Arctic Engineering*, Vol.139 051101 pages 1-16. Copyright 2017 by ASME.

[1]Part of the chapter is reprinted with permission from "Improvement on the Accuracy of Mean Drift Force Calculation" by Yujie Liu, Jeffrey Falzarano, 2017. *Proceedings of the ASME 2017 36th International Conference on Ocean, Offshore and Arctic Engineering* pages 1-13. Copyright 2017 by ASME.

Figure 1.1: The Configuration of Side-by-side Offloading (Reprinted from The Energy Collective [1])

Another example is the multi-body floatover installation. For the offshore installation, usually a heavy lift crane is adopted to lift up the topside and mated with the facility jacket. Later, the concept of the floatover installation gains more popularity because of the efficiency in time and cost. The installation vessel is required to be able to submerge under the water and reemerge. The vessel will transport the equipment to the location and install it there. The requirement for the vessel is relatively high. Recently, an innovative concept is proposed. The installation will be finished by two vessels. Each of them has several lifting arms on one side. The arms will grasp the equipment on two sides, lift it up and then install it at the designated location. In this case, the interaction of the vessels cannot be neglected. The allowable operational window and the safety is the key for this scenario. Such a concept can be illustrated in Figure 1.2.

Figure 1.2: The Innovative Concept of Floatover Installation (Reprinted from Rigzone [2])

Besides, in navy operations, the ship-to-ship replenishment is also an example of multi-body operations. The cargo from one ship will be transferred to the other ship when they are both moving forward in the presence of waves. This kind of operation is called the "most dangerous operation in a peaceful time", which has emphasized the complexity of the phenomenon and the importance of the safety. It can be shown in Figure 1.3.

Figure 1.3: Replenishment between Moving Ships (Reprinted from Armed with Science [3])

In all of these problems, it is crucial to understand the hydrodynamic interaction effects between the floaters, in order to be cost-efficient and also satisfy safety requirements. Motivated by these, we have started the research in multi-body interactions.

1.2 Literature Review

1.2.1 Multibody Problems

In the development of potential theory, researchers first proposed the strip theory for the seakeeping problems of ships. This method has converted a 3D problem into 2D, which can be analyzed by a small amount of computation efforts. Later, the 3D panel method was developed. It has overcome the limitation of the strip theory and has provided more accurate hydrodynamic estimations on the forces and responses of the floaters. There are generally two approaches to solve the 3D problem: Rankine sources and the 3D Green function. Besides, the CFD techniques are also adopted to get the insightful understanding of the problem.

The 3D problem contains a Laplace equation and multiple boundary conditions. A single Rankine source does not satisfy all of the boundary conditions. Thus, the source was distributed over the corresponding boundary, for example, the free surface boundary condition. The theoretical basis was studied by Hess and Smith[4]. They proposed the analytical method to calculate the influence of the source at an arbitrary spatial point and performed the analysis about an arbitrary-shaped, non-lifting, 3D bodies. Hess and Wilcox[5] modeled the free surface by introducing the image sources. The Rankine methods were used to solve hydrodynamic problems in both the frequency domain by Nakos[6] and the time domain by Nakos[7], Kring[8].

The 3D Green function is a tool to decompose the problem into two subproblems: finding the Green function and finding the source strength. The researchers, therefore, have their allocation of work in this problems. Extensive research has been done in the evaluation of the Green function, including Noblesse[9], Telste and Noblesse[10], Newman[11], Newman[12], Newman[13] etc. Once the Green function is ready, we can use the potential formula or the source formula to resolve the hydrodynamic problems.

In the multi-body problem, similar patterns can be found. The researchers first tried to apply the strip method to solve a two-body problem. The assumption of slender body is naturally inherited in the multi-body problems. The researchers include Kim[14], Ohkusu[15] and Yeung[16]. Later, Oortmerssen[17] used the 3D linear diffraction theory to study the interactions between two floaters. Løken[18] explicitly formulated the whole problem and extended the method to a N-body problem.

Afterwards, researchers are still trying to explore the limit of the slender theory and search for alternative methods. Kodan[19] extended Ohkusu[15]'s method and studied the hydrodynamic interaction between two parallel floaters in oblique sea with zero forward speed. The results were validated against the experimental data and a good agreement was achieved. As an improvement, Fang and Kim[20] considered the nonzero forward speed effect when applying the strip method. On the other hand, Kagemoto[21] applied an exact algebraic method to investigate the hydrodynamics of multiple 3D bodies in waves. Based on the idea of multiple scattering and eigenfunction expansions, Mavrakos and Koumoutsakos[22] found the velocity potential analytically.

Gradually, researchers continued the investigation of 3D panel method in multi-body interaction problems. Korsmeyer[23] assumed a rigid free surface and applied 3D panel method to discuss the interaction effects between the two ships in the restricted water. This method can be applied for arbitrarily shaped bodies bounded by irregular surfaces. Teigen[24] discussed the barge and mini-TLP system. They pointed out that the coupled analysis are necessary for the multi-body system. The differences from the single-body problem result from the local wave enhancement and shielding effects. However, the added mass is not much affected.

In the zero-speed cases, Buchner[25] developed a simulation model for the side-by-side configuration. The lid method is proposed in the article to improve the drift force prediction. Huijsmans[26] also applied the lid method in a similar case, using CPM (Constant Panel Method). Later, Choi and Hong[27] began to use HOBEM (Higher Order Boundary Element Method) to investigate the problem because the results of HOBEM are more accurate and fast convergent than those of CPM. Kashiwagi, Endo and Yamaguchi[28] also applied HOBEM to study the LNG-FPSO system. In

the validation part, they have compared the results from the near-field, the far-field methods and the experimental data for a modified Wigley model and a rectangular barge model. The comparison shows a good match in general. But what is happening inside the gap? How will the strong interaction affect the prediction of the forces? The questions are still unsolved. Kristiansen and Faltinsen[29] provided a speculation that the flow separation is the main cause of the discrepancy between the measured response and the results from linear theory.

In the nonzero-speed cases, Chen and Fang[30] formulated the problem using the Green function approach. They adopted the algorithm by Telste and Noblesse[10]. They compared their results against that in Kodan[19] for the zero-speed case. When the speed is nonzero, they compared their results against that from the strip theory. There are some discrepancies between the 2D and 3D results. They believe that the results from the 3D method are more reasonable. Fonfach[31] did a comparative CFD study of the interaction between a smaller tug boat and a large tanker at low speed. They used four models to study the problem, including inviscid flow, turbulent viscous flow, inviscid free-surface flow, viscous free-surface flow models. The conclusion is that the influence of the viscosity is weak while the free-surface effects greatly affect the interaction even at very low values of the Froude number. Besides the Green function approach, Xiang and Faltinsen[32] adopted rankine methods to study the problem of multi-body hydrodynamics with nonzero forward speed and proved the feasibility.

Besides the research in the pure body-wave hydrodynamic interactions, researchers also introduced the mooring lines and risers into the systems of multiple bodies. Kim[33] did a thorough study on the coupled analysis on multiple floating platforms with mooring lines and risers. Koo and Kim [34] studied the coupled motion of FPSO and LNG carrier with mooring lines in time domain. They compared two methods to evaluate the interaction effects. The input of the time-domain simulation is from the frequency domain analysis. Xie[35] adopted the Reverse Multi-Input/Single-Output (R-MISO) method to perform a thorough study on a coupled barge and ship system. She discussed the pitch motion of the barge in the two-body configuration and compared against that in the one-body case. The roll and heave motion of the ship were also studied to demonstrate the

effect of interactions in different wave directions.

1.2.2 Irregular Frequency

We will use the first order potential theory to study the hydrodynamics of the multi-body problems. When two huge floaters are in close proximity, the hydrodynamic interactions will become complex and significant.

In such problems, the potential-theory-based method will result in "resonance" when there is a gap. This "resonance" was overpredicted in numerical simulations and thus considered as unphysical. Besides, the resonance resulting from the potential-theory-based method can be divided into two categories: one is the resonance from the irregular frequencies, the other perhaps from the limitation of potential theory. Sometimes, the resonance caused by the irregular frequencies will be confused with the true resonance. Thus, it needs to be removed.

Irregular frequencies result from the ill condition of the linear system in boundary integral problems. In other words, the matrix to be solved is almost singular at some frequencies. The solver can still provide some results because of the limited accuracy of numerical techniques and computer round-off errors. The irregular frequency effect in wave-body interaction was first found by John[36]. The harmful effects in hydrodynamic analysis were identified by Frank[37]. The characteristic "sharp spikes" resulted from the irregular frequency effect were observed in added mass and damping, which affected the accuracy of final results. The undesirable "spikes" will be confused with the physical resonance especially in the multi-body interaction problems. Therefore, this effect must be removed in order to expand the applications of boundary integral methods in the hydrodynamic analysis.

Researchers first sought for the feasible approaches to remove this effect for one or two frequencies. Afterwards, several applicable methods for more frequencies and more general shapes were proposed. The modified-integral method and the extended-boundary-condition method are the two approaches to resolve this problem.

In the study of the modified-integral method, Ursell[38] investigated this problem analytically. He put a wave source at the center of the circle and did not observe the irregular frequency ef-

fects for shorter wavelengths. This analytical study indicates such a technique can be adopted in the numerical evaluation of such problems. Schenck[39] applied the combined integral equations at selected internal points, leading to an overdetermined system. Burton and Miller[40] also adopted a modified Green function in the acoustic wave scattering problem. Jones[41] added a source at the origin to remove the interior eigenmode effects in acoustics. Inspired by Ursell[38], Ogilvie and Shin[42] modified the Green function integral by adding a source or dipole at the center of the internal free surface for the wave-body interaction problem. Sayer[43] also examined the suggestions from Ursell[38] on a symmetric body in finite water depth. Later on, Ursell[44] demonstrated that a sequence of singularities can remove all the irregular frequencies, resulting in a method applicable to the general case. Wu and Price[45] extended this method to a twin-hull problem. Lau and Hearn[46] adopted the combined integral equation to study this problem. Lee and Sclavounos[47] further developed the modified integral method. Lee[48] pointed out that the final effect was determined by the choices of the linear combination coefficients. He converted this problem into an optimization one and used the condition number at the first irregular frequency as the objective function. Besides, Kress[49] did a similar problem conversion in acoustic and electromagnetic scattering. Zhu[50] also discussed this method and proved its effectiveness.

On the other hand, Martin[51] applied null equations in setting up the equation system. Liapis[52] combined null equations to the original equation set, making it valid for all frequencies. Qiu[53] discussed the irregular frequency removal in the panel-free method.

The extended-boundary-condition method was proposed by Wood[54], mentioned in Angell[55]. They enforced a fixed lid condition on the internal free surface. Ohmatsu[56] validated the method for the 2D case. Kleinman[57] revisited this method by applying a strict mathematical derivation. He proved the uniqueness in the potential formulation. Rezayat[58] improved the method from Schenck[39] and applied the "lid" method in elastodynamics. Zhu[50] followed Kleinman[57], validating the effectiveness of his method. Lee[59] further discussed this approach in a more general way, including the second order effect.

In numerical evaluation, special care is needed for the integral of the Green function across the

free surface panels. It is because there will exist a log singularity if the panel is located on $z = 0$ based on Noblesse[9] and Newman[11]. Newman[60] proposed one method to evaluate the log singularity, however, important information is missing about the final expression and assumptions. Based on the idea of converting the integral across the pyramid bottom surface to that on the surrounding four surfaces, we have developed our own method for evaluation, ending up with different expressions but with accuracy up to 10^{-7} when comparing against Newman's[60] results in the free surface panels only.

From the timeline of the development, the extended-boundary-condition method gradually showed its advantages. It is convenient to use, especially for users without abundant experience with such problems.

1.2.3 Second Order Wave Forces

Based on the perturbation method, we can break down the nonlinear problem into zeroth, first, second and higher orders. We can compute the corresponding potentials in order to find the forces and moments on the floaters. The second order wave forces contain the contribution from the first and second order potentials. However, at this step, we are not able to compute the second order potential. Still, we can try to dig out more information based on the first order potentials. We can take the time average of the expressions of the second order forces and moments. Then the terms containing the second order potential will vanish. The time average is named as the mean drift forces and moments when the forward speed is zero and added wave resistance when nonzero. We will briefly review the development of the mean drift forces and moments and move onto the added resistance. The two parts have shown somewhat parallel development although it seems that drift forces would come first.

To study the drift forces, there are generally two methods: far-field and near-field. Maruo[61] proposed the far-field method for the first time and computed the forces on the floater. On top of that, Newman[62] derived the analytical equations for the drift forces and moments on an arbitrary body. Comparisons are made against the experiment results. Later on, Faltinsen and Michelsen[63] used the far-field method on a 3D body. The near-field method was developed by Pinkster and

Oortmerssen[64]. They directly integrated the pressure on the floater body and kept the terms up to the second order. Ogilvie[65] summarized the research in the second order hydrodynamic effects. He discussed the concept and analysis methods and generalized the formula for the drift forces and moments. Also, he has clarified some uncertain parts in the coordinate transformation.

The research in added resistance dates back to Maruo[66], who has introduced the first far-field approach. Later on, Maruo[67] and Joosen[68] further elaborated the far-field approach. Based on the approach of Maruo[67], Gerritsma and Beukelman[69] proposed the radiated energy approach. Strom-Tejsen[70] compared the results from the above researchers' approaches and identified the discrepancy between the methods and experimental data. Salvesen[71] followed the idea of Gerritsma and Beukelman[69] and used the STF strip theory to calculate the added resistance. Later, Salvesen[72] compared the results against the experimental data from Strom-Tejsen[70]. Afterwards, the near-field method was introduced by Faltinsen[73]. He achieved good validation results and observed the deficiency of the current method in short waves. He also proposed a estimation formula to improve it. Hsiung and Huang[74] implemented the near-field method for a 3D body. The measured results are compared against the computations. Satisfactory results were achieved. More recently, Kashiwagi[75] applied the enhanced unified theory (EUT) to study the added resistance and identified the discrepancy in short wave length. Liu[76] improved the 3D far-field method of Maruo to make it applicable to the short wave lengths. They got a good match when validating the results against the experimental data. Kashiwagi[77] conducted the experiments on a blunt and a slender Wigley hull. They measured the motion and force in surge, heave and pitch directions. Also the added wave resistance is measured too. The measured results are compared against the computed results by EUT and they are consistent in general except the area near the peak.

1.2.4 Improvement of Mean Drift Forces

In the theory to study the floater motions in waves, there are unsteady and steady excitations from the waves. The unsteady part leads to the periodic oscillations of the floater. The steady part is contributed by the higher order components, which are usually too small to significantly affect

the first order oscillations of the floater but will generate a steady force on the floater.

Mathematically speaking, if we use the perturbation method to study the hydrodynamic problem of the floater in waves. We will divide the fully nonlinear problem into first order, second order and higher order problems. For simplicity, we will focus on the first order and second order problems. The first order terms are of the same frequency of the incident waves while the frequency of the second order terms double the wave frequency. However, when we take the time average of the second order forces and moments, some terms remain in the expression. Those terms are steady second order terms, which will generate a constant excitation on the floater. The time independent components are named "mean drift" forces and moments.

There are two approaches to study the first order and second order problems: far-field and near-field. Herein, we will mainly discuss the contribution from the relative wave elevation in the near field methods. The near field method was developed by Pinkster and Oortmerssen[64]. The basic idea of the near field method is to integrate the pressure on the wetted area of the floater and keep the terms up to the second order. Later, Pinkster[78] summarized the computations of the second order mean drift forces. Lee[79] re-derived the formula for the second order forces and moments. He did the study of the mean drift forces on the submerged spheroid. The more complete expressions of the drift forces were given in Lee[80].

In the expressions of the mean drift forces, there is one important component resulted from the relative wave elevation. More exactly, the term comes from the integral on the wetted area above the mean water level. To calculate the component accurately, we need to evaluate the absolute wave elevation at the waterline. In other cases, the wave elevation is named the wave run-up. Newman[81] mentioned the extrapolation method for the potential value and the average technique of the values based on the control points and on the vertical extrapolation. The specific details of the methods were not provided. However, in the commercial software WAMIT, the potential value at the waterline panel centroid is used to represent the potential value at the waterline. This is an approximation, requiring the waterline panel must be small enough.

We noticed the seemingly inconsistency between the previous research and the technique in

WAMIT and decided to study the methods to accurately calculate the wave elevation at the water-line around the floater. The detailed discussion and the explanation of the theory are presented in Chapter 6.

1.2.5 Side-by-side Offloading Problem

The side-by-side offloading is one type of configurations when the FLNG offloads the liquefied natural gas to the LNGC nearby. It is very challenging because the two ships stay closely to each other, forming a narrow gap between the two giant floaters. Inaccurate estimation of the interaction effects may lead to unexpected damage or collision of the ships. In the theoretical research and experimental study, it is observed that the wave resonance will happen inside the gap at some incident wave frequencies. It is unclear how much effect the wave resonance will cause to the two-body system. That is the reason why it is of growing interest to understand the phenomenon happening inside the gap and how to estimate the effects from the wave resonance on the two-body system.

This problem arises when the researchers were studying the interactions of multiple floaters using the panel method based on the potential theory. An unphysical resonance was observed inside the gap between the two large floaters. As a result, the wave elevation and the interaction force predicted by the panel method are too high based on one's physical intuitive. Thus, researchers began the investigation of the unreasonable phenomenon.

The research about this problem includes the study in 2D and 3D cases, using experimental study, CFD approaches and potential methods.

In the study of the 2D problem, Miao et al. [82] investigated the problem using the linear potential theory. They identified the strong interactions between the two floaters close-by and recommended more study for 3D cases. Saitoh[83] investigated the problem in 2D through the series of experiments. They studied the effects from gap width, draft on the wave height inside the gap.

Faltinsen[84] proposed the domain decomposition method, breaking down the problem into several domains. Meanwhile, more unknowns and more equations about the boundaries of the

different domains are introduced. Singular characters of the traces are considered in formulating the local solutions of the complex velocities at edges. Finally, the analytically oriented solution is obtained to predict the piston-like sloshing in a moonpool. Kristiansen[29] tried the vortex tracking method and concluded that the vortex shedding inside the gap may lead to part of the energy loss.

Later, as the twin paper with Faltinsen[84], Faltinsen[85] introduced a dynamic boundary condition inside the gap and resolve the potential problem. The dynamic boundary condition is based on the pressure drop estimation and empirical formulas on some coefficients. By modeling the dynamic free surface, it becomes unnecessary to model the complex phenomenon happening inside the fluid domain. The results of such methods show a good agreement with the experimental data.

Liu[86] added a damping free surface near the floater and also decomposed the domain into several parts with damped boundary condition on the vertical surfaces. Damping happens on the gap free surface and the interface of the boundaries. By matching the experimental data, the author proposed a linear model to fit the damping coefficient against characteristics of the box and fluid domain.

Later, CFD techniques were adopted to study the 2D side-by-side problem. Lu[87] began to study the problem by both panel method and CFD techniques. They enforced the damping lid method inside the gap in the panel method and achieved a good match with the experimental results by Saitoh[83] and Iwata[88]. Moradi[89] discussed the effects from the gap configuration, body breadth, gap width and draft on the gap resonance characteristics. Moradi[90] also discussed the water depth effect on the gap resonance. However, all the discussions are on the 2D cases. The 3D case still needs more investigation to shed light on the mechanism of the gap resonance.

In the study of 3D problems, Buchner[91] proposed the lid method inside the gap. They enforced the no-penetration condition on the lid and found this method can suppress the resonance. Later, Chen[92] proposed the damping lid method. They added a dissipative term in the free surface boundary condition inside the gap. Chen[93] discussed the damping method applied in the multi-body problem. The authors introduced damping coefficients for the free surface boundary condition and the body boundary conditions. The method basically reduced the source strength by

adjusting the terms associated with the damping effects. However, one needs to tune the damping coefficients on the free surface and body boundary by comparison against the experimental data. Meanwhile, by modifying the equations of the system, it is likely that the resonance frequency will have a tiny shift with a nonzero damping coefficient. This method was used by Pauw[94], Bunnik[95] and Lu[96]. They all reported satisfactory results can be obtained by this method.

Zhu[97] treated the 3D side-by-side problem by the linear potential method in frequency domain and investigated the effect of the gap width on the resonant frequency and amplitude. Teigen[98] applied the panel method up to second order to investigate the problem. They concluded that the wave amplification inside the gap is sensitive to the wave frequency and wave heading. The surprising second order effect is observed around the two barges. Zhu[99] studied the effect of gap in the multiple box barge problems. Only the radiation potential is considered herein. They concluded that the sway motion showed a strong interaction effect at certain wave number. Sun[100] applied 1st and 2nd order panel method to investigate the dependency of the wave elevation on box motion, spacing, wave direction, draft. They observed a similar behavior in 1st order and 2nd order potential along the gap. Markeng[101] investigated pressure damping method and Newtonian cooling damping model in 2D cases and implemented the latter one in the 3D potential flow solver. The authors concluded the Newtonian cooling damping model is relatively more effective to model the resonance. The damping coefficient still needs to be tuned against the experimental data.

Zhao[102] conducted the experiment to study two identical box barges side-by-side. The two box barges are fixed. In the experiments, different modes of gap resonance have been observed. This is a very good resource to study the side-by-side problems because the experiment has eliminated the effects of the ship motion and focused on the diffraction effects. It will be helpful to understand the physical mechanism. Wang[103] discussed the process to build the 3D model in CFD package OpenFOAM and applied convergence study to find the suitable mesh topology and size, domain size and boundary conditions. Finally, the generated waves are consistent with the observations in the experiment.

1.3 Summary of the Dissertation

In this dissertation, the numerical tool, MDLMultiDYN, based on the potential theory is developed for the hydrodynamic problem of multiple bodies with zero and non-zero forward speed. During the development, we have solved the 1st order problem for an arbitrary number of floaters, the irregular frequency problem and the time averaged 2nd order problem. Additionally, we make some improvements to the 2nd order problem to increase the accuracy of the prediction. After the development is finished, it is adopted to study the hydrodynamic problem of the two box barges side-by-side. To understand the physical phenomenon, the CFD approach is also applied to investigate the fluid domain around the gap. Based on the results from the CFD approach, an artificial damping method is proposed to obtain the reasonable wave elevation inside the gap.

Chapter 1 is a general introduction and background to all the other chapters. Chapter 2 introduces the perturbation technique to decompose the nonlinear problem into 1st and 2nd order problems. Chapter 3 discusses the extension of the 1st order to consider multiple bodies. Chapter 4 resolves the irregular frequency problems. Chapter 5 focuses on the 2nd order problem. Chapter 6 is an extension of Chapter 5 and discusses about the improvement of the calculation of mean drift forces. Chapter 7 starts to address the side-by-side problem. Chapter 8 continues the discussion of the same problem with Chapter 7 and discusses about the artificial damping method.

In Chapter 2, we start from the most general nonlinear expression of the body-wave interaction problem. We demonstrate the process to convert the sea keeping problem to that with a small forward speed and how the perturbation technique simplifies the problem to make it solvable. The assumptions and motivations of each step are presented and discussed.

In Chapter 3, we present the steps to further simplify the problem, which include the steps to convert it into a frequency domain problem, the introduction of the linear Green function, the potential formula and the source formula. The key idea in solving for the potential is the principle of superposition. It is the basis to solve for the problem with forward speed effect. The general formula without the assumptions of symmetry to solve for the added mass and damping are derived accordingly in Appendix A. The formula for zero-speed and nonzero-speed problems

are derived. Finally, the results for the zero-speed problem from MDLMultiDYN are compared against WAMIT. A close comparison is achieved. The results for the nonzero-speed case are presented as well. The intermediate steps to obtain the result are relevant to a well known theorem. However, we prove that there are some inconsistencies with that theorem [104], which are discussed in Appendix E, F and G. However, the theorem is beyond the main focus of the paper. Thus, we just present why it has some inconsistencies but have not implemented the correct form to obtain results.

In Chapter 4, we discuss the irregular frequency removal problem. We prove its uniqueness using Sommerfeld radiation condition, harmonize several theories about the topic and implement an extended boundary condition method[105]. The key step to apply the method is to evaluate the log singularity in an accurate way. We propose 4 different methods to handle various possible situations[106][107]. Method 2 is adopted in most applications because of its high accuracy and efficiency. Method 3 and 4 are alternative approaches to deal with less common cases. The motivation behind the methods is to find a fast converge series to represent the integral. Therefore, the transformation of the integral and the search for the basis functions are both important and necessary. Herein, we adopt Green's 2nd identity to transform the integral and luckily find a series to represent the terms. Finally, the efficiency and accuracy of the studied methods for the log singularity are discussed. The method is implemented in our in-house program MDLMultiDYN and achieves consistent results with WAMIT[108].

In Chapter 5, we address the 2nd order problem. We derived the formula for the 2nd order forces and moments. To avoid solving for the 2nd order potential, we take the time average to eliminate the 2nd order potential and motion, thus becoming the mean drift force (zero speed) and added resistance (with forward speed). Consistent results with WAMIT are again obtained for the zero speed cases.

Chapter 6 is a complement to Chapter 5. This chapter specially discusses the assumptions used to calculate the wave elevation along the waterline, which is an important component in the expressions of the mean drift force or added resistance. We explain the possible reason why the

analytical approach is not adopted in the commercial software WAMIT. Alternatively, we propose an extrapolation method to circumvent the singularity of points located on the edge of the waterline panels, we validate the method by studying the contour plots and prove the effectiveness when compared against WAMIT[109].

Chapter 7 discusses about the experiment of two box barges side-by-side and the information we can obtain by the CFD simulation and the potential method. We apply the commercial software STAR-CCM+ and our in-house software MDLMultiDYN to simulate the model test. From the results, we conclude that the viscous effect is dominant for the wave frequency we select and for this specific model.

Chapter 8 focuses on the modified potential method. We first review the general ideas of the damping methods: domain decomposition method and lid method. The mathematical concepts and the limitations are discussed. In both types of methods, the unphysical effect are introduced to the model to ensure a reasonable result. Inspired by this idea, we propose an alternative approach to resolve the problem. The wall damping method proposed herein is an improvement upon XB Chen[93]. In this method, a lid is no longer needed. However, the damping coefficient needs to be frequency dependent. Gaussian kernel functions are applied to describe the relationship. Finally, consistent results with the experimental data are obtained for the wave gauge in the middle of the gap. This method is the first step to develop the categories of methods without lid. The motivation is to use the small amount of measured data and a simplified model to generate engineering acceptable results. More improvements can be made upon this method, given more data and a more general and powerful model can be developed in the future.

To sum up, the in-house program, MDLMultiDYN, is developed during the study of all the topics. The program adopts the object oriented approach and is highly flexible to incorporate more modules. It can resolve the problems of multiple bodies, irregular frequency removal and mean drift forces or added resistance. It serves as the basis for the study more problems, for example, the finite depth Green function[110], the QTF (Quadratic Transfer Function) and the 2nd order potential etc. The investigation of the phenomenon occurring inside the gap of a side-by-side

configuration explains the reason for the discrepancy between the results from potential method and experimental data. The wall damping approach provides an alternative to view the artificial damping problem. It is effective and can be improved into a more powerful model.

2. NONLINEAR BODY-WAVE INTERACTION PROBLEM [1]

In this chapter, we will first review the classical body-wave interaction problem, then study the changes of the equations when the floater has a nonzero forward speed, finally adopt the perturbation method to break down the problem into first and second order parts.

2.1 Governing Equation and Boundary Conditions

The solution domain of the body-wave interaction problem can be illustrated in Figure 2.1. This is the domain for the fully nonlinear problem.

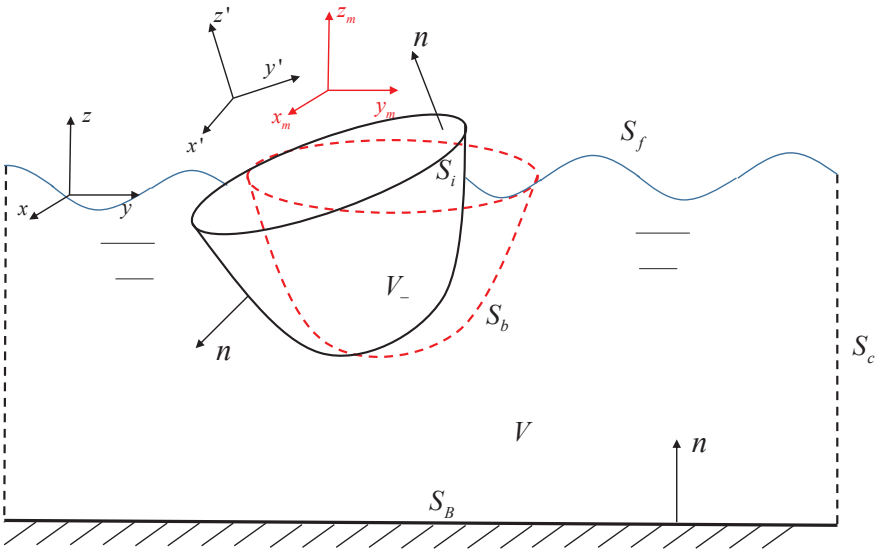

Figure 2.1: Solution Domain of the Body-Wave Interaction Problem (zero speed)

where, n is the normal vector on a certain surface, positive when pointing outward into the fluid domain. S_B is the bottom surface, which is described by $z = -h$. S_b is the body surface. S_f is the

[1] Part of the chapter is reprinted with permission from "Frequency Domain Analysis of the Interactions Between Multiple Ships with Nonzero Speed in Waves or Current-Wave Interactions" by Yujie Liu, Jeffrey Falzarano, 2017. *Proceedings of the ASME 2017 36th International Conference on Ocean, Offshore and Arctic Engineering*, pp. 1-17 Copyright 2017 by ASME.

free surface, which can be described by $z = \zeta(x, y, t)$. S_c is the control surface in the far field. S_i is the internal free surface. V is the fluid domain. V_- is the internal domain of the floater.

The equations for the body-wave interaction problem can be listed as follows:

$$\nabla^2\Phi = 0 \qquad in\ fluid\ domain \tag{2.1}$$

$$\frac{\partial\zeta}{\partial t} + \frac{\partial\Phi}{\partial x}\frac{\partial\zeta}{\partial x} + \frac{\partial\Phi}{\partial y}\frac{\partial\zeta}{\partial y} = \frac{\partial\Phi}{\partial z} \qquad at\ z = \zeta(x, y, t) \tag{2.2}$$

$$\frac{\partial\Phi}{\partial t} + \frac{1}{2}\vec{\nabla}\Phi\cdot\vec{\nabla}\Phi + g\zeta = C - \frac{p_a}{\rho} \qquad at\ z = \zeta(x, y, t) \tag{2.3}$$

$$\vec{n}\cdot\nabla\Phi = \vec{n}\cdot\vec{V}^{body} \qquad at\ body\ surface \tag{2.4}$$

$$\frac{\partial\Phi}{\partial z} = 0 \qquad on\ z = -h \tag{2.5}$$

$$\lim_{r\to\infty} r(\frac{\partial\Phi}{\partial r} - ik\Phi) = 0 \qquad at\ control\ surface \tag{2.6}$$

$$\frac{\partial\Phi}{\partial t} + \frac{1}{2}\vec{\nabla}\Phi\cdot\vec{\nabla}\Phi + \frac{P}{\rho} + gz = C \qquad in\ fluid\ domain \tag{2.7}$$

The equation is defined in the global coordinate. Usually, the pressure p_a at the boundary between the wave and the air is set to be zero.

When a vessel is moving forward in the presence of waves, it will be more convenient to study the motion in a translating coordinate. Therefore, we will define 5 types of coordinate systems to describe the problem of zero speed and nonzero speed.

- $Oxyz$: The global coordinate.
- $\overline{O}\bar{x}\bar{y}\bar{z}$: The global translating coordinate, translating at the velocity of the vessel without rotations.
- $O'x'y'z'$: The vessel fixed coordinate, moving with the vessel with rotations. The geometric model is built in this coordinate.
- $Ox_my_mz_m$: The vessel equilibrium coordinate, duplicate with the vessel fixed coordinate when in equilibrium state. This coordinate is used for the cases of zero speed.

- $\overline{O'}\bar{x}'\bar{y}'\bar{z}'$: The vessel translating coordinate. This coordinate translates with the vessel, duplicate with the vessel fixed coordinate when zero speed.

The solution domain for this case can be showed in Figure

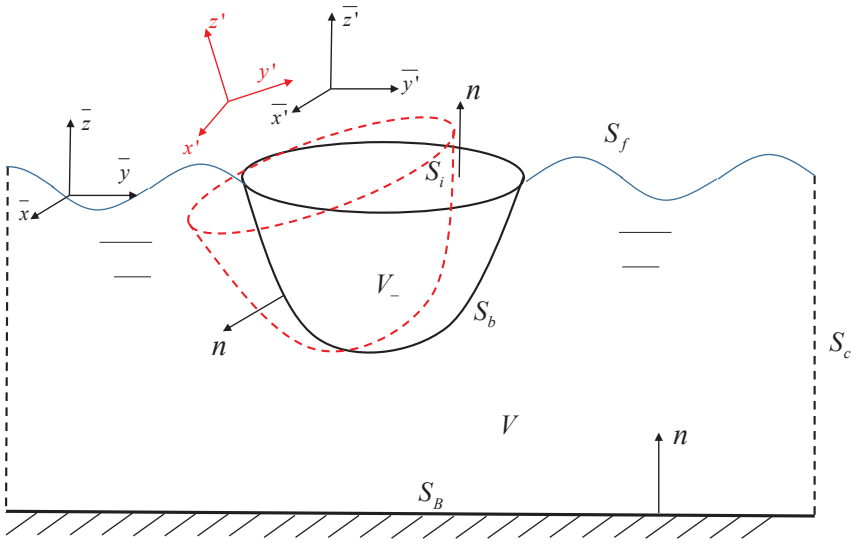

Figure 2.2: Solution Domain of the Body-Wave Interaction Problem (nonzero speed)

The vessel motion can be superimposed by two types of motion: the translating speed U and the 6 DOF (Degree of Freedom) perturbation motion caused by the waves. Based on this fact, an inertia translating coordinate $\overline{O}\bar{x}\bar{y}\bar{z}$ is introduced. The coordinate will be translating together with the vessel at speed U, but may not necessarily duplicate with the vessel translating coordinate $\overline{O'}\bar{x}'\bar{y}'\bar{z}'$. If the vessel does not have any perturbation motion (i.e. moving forward steadily), the vessel translating coordinate $\overline{O'}\bar{x}'\bar{y}'\bar{z}'$ will be duplicated with the vessel fixed coordinate $O'x'y'z'$.

The basic idea is that we want to solve the PDE problem in the global translating coordinate.

Based on Lorentz transformation, we will have the following relationships:

$$\begin{aligned}\bar{x} &= x - Ut \\ \bar{y} &= y \\ \bar{z} &= z \\ \bar{t} &= t\end{aligned} \tag{2.8}$$

Thus, the potential and its derivatives can be defined as follows:

$$\begin{gathered}\Phi(x,y,z,t) = \Phi(\bar{x}+Ut,\bar{y},\bar{z},\bar{t}) = \overline{\Phi}(\bar{x},\bar{y},\bar{z},\bar{t}) = \overline{\Phi}(x-Ut,y,z,t) \\ \frac{\partial \Phi}{\partial t} = (\frac{\partial}{\partial \bar{t}} - U\frac{\partial}{\partial \bar{x}})\overline{\Phi} \\ \frac{\partial \Phi}{\partial x} = \frac{\partial \overline{\Phi}}{\partial \bar{x}} \\ \frac{\partial \Phi}{\partial y} = \frac{\partial \overline{\Phi}}{\partial \bar{y}} \\ \frac{\partial \Phi}{\partial z} = \frac{\partial \overline{\Phi}}{\partial \bar{z}}\end{gathered}$$

where, $\overline{\Phi}$ is the potential defined in the vessel translating coordinate $\overline{O}\bar{x}\bar{y}\bar{z}$ to get the absolute velocity in global coordinate $Oxyz$. Based on the relationships, the PDE set can be converted into:

$$\nabla^2\overline{\Phi} = 0 \qquad in\ fluid\ domain$$
$$\frac{\partial\bar{\zeta}}{\partial\bar{t}} + (\frac{\partial\overline{\Phi}}{\partial\bar{x}} - U)\frac{\partial\bar{\zeta}}{\partial\bar{x}} + \frac{\partial\overline{\Phi}}{\partial\bar{y}}\frac{\partial\bar{\zeta}}{\partial\bar{y}} = \frac{\partial\overline{\Phi}}{\partial\bar{z}} \qquad at\ \bar{z} = \bar{\zeta}(\bar{x},\bar{y},\bar{t})$$
$$\frac{\partial\overline{\Phi}}{\partial\bar{t}} - U\frac{\partial\overline{\Phi}}{\partial\bar{x}} + \frac{1}{2}[(\frac{\partial\overline{\Phi}}{\partial\bar{x}})^2 + (\frac{\partial\overline{\Phi}}{\partial\bar{y}})^2 + (\frac{\partial\overline{\Phi}}{\partial\bar{z}})^2] + g\bar{\zeta} = C \qquad on\ \bar{z} = \bar{\zeta}(\bar{x},\bar{y},\bar{t})$$
$$\vec{n}\cdot\nabla\overline{\Phi} = \vec{n}\cdot\vec{V}^{body} \qquad at\ body\ surface$$
$$\frac{\partial\overline{\Phi}}{\partial\bar{z}} = 0 \qquad on\ \bar{z} = -h$$
$$\lim_{r\to\infty} r(\frac{\partial\overline{\Phi}}{\partial r} - ik\overline{\Phi}) = 0 \qquad at\ control\ surface$$
$$\frac{\partial\overline{\Phi}}{\partial\bar{t}} - U\frac{\partial\overline{\Phi}}{\partial\bar{x}} + \frac{1}{2}[(\frac{\partial\overline{\Phi}}{\partial\bar{x}})^2 + (\frac{\partial\overline{\Phi}}{\partial\bar{y}})^2 + (\frac{\partial\overline{\Phi}}{\partial\bar{z}})^2] + \frac{\overline{P}}{\rho} + g\bar{z} = C \qquad in\ fluid\ domain$$

The set of PDE is different from the one defined in the global coordinate. We can no longer use the same Green function to solve for this problem. However, the Green function requires much efforts to find or to evaluate numerically. The question will be: Can we modify this PDE set such that we can still use the same Green function?

Based on this motivation, we began to introduce another type of potential $\overline{\Phi}_{rel}$. $\overline{\Phi}_{rel}$ satisfies the following equations:

$$\overline{\Phi}_{rel} = \overline{\Phi} - U\bar{x} \tag{2.9}$$

Then the PDE set will become:

$$\nabla^2\overline{\Phi}_{rel} = 0 \qquad in\ fluid\ domain \tag{2.10}$$

$$\frac{\partial\bar{\zeta}}{\partial\bar{t}} + \frac{\partial\overline{\Phi}_{rel}}{\partial\bar{x}}\frac{\partial\bar{\zeta}}{\partial\bar{x}} + \frac{\partial\overline{\Phi}_{rel}}{\partial\bar{y}}\frac{\partial\bar{\zeta}}{\partial\bar{y}} = \frac{\partial\overline{\Phi}_{rel}}{\partial\bar{z}} \qquad at\ \bar{z} = \bar{\zeta}(\bar{x},\bar{y},\bar{t}) \tag{2.11}$$

$$\frac{\partial\overline{\Phi}_{rel}}{\partial\bar{t}} + \frac{1}{2}[(\frac{\partial\overline{\Phi}_{rel}}{\partial\bar{x}})^2 + (\frac{\partial\overline{\Phi}_{rel}}{\partial\bar{y}})^2 + (\frac{\partial\overline{\Phi}_{rel}}{\partial\bar{z}})^2] + g\bar{\zeta} = C + \frac{1}{2}U^2 \qquad on\ \bar{z} = \bar{\zeta}(\bar{x},\bar{y},\bar{t})$$

$$\vec{n}\cdot\nabla\overline{\Phi}_{rel} = \vec{n}\cdot\vec{V}_{rel}^{body} \qquad at\ body\ surface \tag{2.12}$$

$$\frac{\partial\overline{\Phi}_{rel}}{\partial\bar{z}} = 0 \qquad on\ \bar{z} = -h \tag{2.13}$$

$$proper\ radiation\ condition \qquad at\ control\ surface \tag{2.14}$$

$$\frac{\partial\overline{\Phi}_{rel}}{\partial\bar{t}} + \frac{1}{2}[(\frac{\partial\overline{\Phi}_{rel}}{\partial\bar{x}})^2 + (\frac{\partial\overline{\Phi}_{rel}}{\partial\bar{y}})^2 + (\frac{\partial\overline{\Phi}_{rel}}{\partial\bar{z}})^2] + \frac{\bar{P}}{\rho} + g\bar{z} = C + \frac{1}{2}U^2 \qquad in\ fluid\ domain$$

where, the subscript rel stands for the relative velocity with respect to the vessel translating coordinate. Through this transformation, we could not find a explicitly written radiation condition for the $\overline{\Phi}_{rel}$. Therefore, we write "proper radiation condition" in the corresponding place. The PDE set about the potential $\overline{\Phi}_{rel}$ is almost identical to that defined in the global coordinate. Thus, we can use the same Green function to solve such problems. The difference lies in the dynamic boundary condition and Bernoulli equation: there is an extra $\frac{1}{2}U^2$ on the right hand side.

Until this step, we have finished formulating the PDE set for the problem when a floater has a non-zero forward speed. Nevertheless, the solution domain still has a time-dependent wavy boundary on the free surface, which makes the problem still difficult to solve. To resolve the problem, we will assume the wave slope ka is small and wave amplitude a is also small, where k is the wave number. Consequently, a perturbation technique is adopted.

2.2 Perturbation Techniques

To make the problem easier to solve, we want to convert the wavy boundary $\bar{z} = \bar{\zeta}(\bar{x},\bar{y},\bar{t})$ at the free surface to a flat boundary $\bar{z} = 0$. This is achieved by applying Taylor expansion to each term in the free surface boundary condition. The solution domain can be illustrated as Figure 2.3.

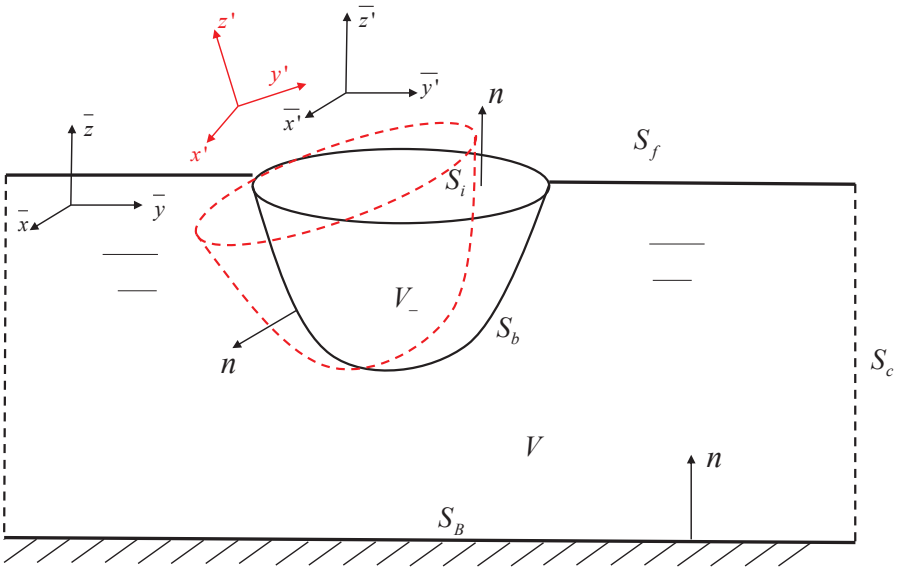

Figure 2.3: Linearized Domain of the Body-Wave Interaction Problem (nonzero speed)

Additionally, we want to find a way to describe the relative body motion of the floater. Since the wave amplitude is small, the body motion can be assumed to be of the same order. Thus, the moving body boundary can be computed by the equilibrium position and the 6 DOF motion.

We will use the perturbation technique to decompose the problem into the 1st order and 2nd order problems. Before moving to that step, we will first discuss the vector transformation between vessel translating coordinate and the vessel fixed coordinate. This is necessary to describe the geometric properties in the vessel translating coordinate based on the information in the vessel fixed coordinate.

For the coordinate transformation, we will follow Ogilvie[65], assume the vessel is undergoing the rotations following the order of roll-pitch-yaw. If we know some vector in the vessel fixed coordinate, we need to map it to the vector in the vessel translating coordinate. If we assume the vessel motion is of order $o(\epsilon)$, we can use the perturbation technique to break down the motion into the first order, second order and higher orders. If we only keep to the second order, the vector

transformation can be written as:

$$\vec{X} = \vec{X}_0 + \vec{X}' + [\vec{\eta} + \vec{\alpha} \times \vec{X}'] + \epsilon^2 H\vec{X}' + o(\epsilon^3)$$
$$\vec{n} = \vec{n}' + \vec{\alpha} \times \vec{n}' + \epsilon^2 H\vec{n}' + o(\epsilon^3)$$

where, $\vec{\eta}, \vec{\alpha}$ are of order $o(\epsilon)$. H is of $o(1)$ and defined as: where, H is defined as:

$$H = \begin{bmatrix} -\frac{1}{2}(\eta_5^{(1)^2} + \eta_6^{(1)^2}) & 0 & 0 \\ \eta_4^{(1)}\eta_5^{(1)} & -\frac{1}{2}(\eta_4^{(1)^2} + \eta_6^{(1)^2}) & 0 \\ \eta_4^{(1)}\eta_6^{(1)} & \eta_5^{(1)}\eta_6^{(1)} & -\frac{1}{2}(\eta_4^{(1)^2} + \eta_5^{(1)^2}) \end{bmatrix}$$

$\vec{X}$ is the vector defined in the global translating coordinate, denoting the instantaneous position of some point P on the floater body. $\vec{X}_0$ is the vector connecting the origin of the translating global coordinate to that of the vessel translating coordinate, $\vec{X}'$ is the vector defined with respect to the vessel translating coordinate, denoting the position of the corresponding point P when vessel is in equilibrium state. Then the vector $(\vec{X} - \vec{X}_0)$ stands for the instantaneous position of the point P in the global translating coordinate.

To conclude, we will Taylor expand the free surface boundary condition with respect to the plane $z = 0$, the moving body boundary condition based on the vessel equilibrium position.

The Taylor expansions on the potential $\overline{\Phi}_{rel}$ and the pressure P can be written as below:

$$\overline{\Phi}_{rel}\big|_S = \overline{\Phi}_{rel}\big|_{S_m} + [(\vec{X} - \vec{X}_0 - \vec{X}') \cdot \vec{\nabla}]\overline{\Phi}_{rel}\big|_{S_m} + o(\epsilon^3)$$
$$P\big|_S = P\big|_{S_m} + [(\vec{X} - \vec{X}_0 - \vec{X}') \cdot \vec{\nabla}]P|_{S_m} + o(\epsilon^3)$$

Meanwhile, we will also perturb the potential $\overline{\Phi}_{rel}$, the relative motion $\vec{\eta}$ and $\vec{\alpha}$ using wave

slope $\epsilon = ka$ in the following way:

$$\begin{aligned}
\overline{\Phi}_{rel}\big|_{S_m} &= \overline{\Phi}^{(0)}_{rel}\big|_{S_m} + \epsilon\overline{\Phi}^{(1)}_{rel}\big|_{S_m} + \epsilon^2\overline{\Phi}^{(2)}_{rel}\big|_{S_m} + o(\epsilon^3) \\
\vec{\eta} &= \epsilon\vec{\eta}^{(1)} + \epsilon^2\vec{\eta}^{(2)} + o(\epsilon^3) \\
\vec{\alpha} &= \epsilon\vec{\alpha}^{(1)} + \epsilon^2\vec{\alpha}^{(2)} + o(\epsilon^3) \\
\vec{X} - \vec{X}_0 &= \epsilon\vec{\eta}^{(1)} + \epsilon^2\vec{\eta}^{(2)} + \vec{X'} + \epsilon\vec{\alpha}^{(1)} \times \vec{X'} + \epsilon^2\vec{\alpha}^{(2)} \times \vec{X'} + \epsilon^2 H\vec{X'} + o(\epsilon^3) \\
\vec{n} &= \vec{n'} + \epsilon\alpha^{(1)} \times \vec{n'} + \epsilon^2\vec{\alpha}^{(2)} \times \vec{n'} + \epsilon^2 H\vec{n'} + o(\epsilon^3) \\
P\big|_S &= P^{(0)}\big|_{S_m} + \epsilon P^{(1)}\big|_{S_m} + \epsilon^2 P^{(2)}\big|_{S_m} + o(\epsilon^3)
\end{aligned}$$

where, the superscript "(0)" stands for the zeroth order. In some references, the order can be relevant to the Froude number.

After applying the techniques of the Taylor expansion and perturbation, we will decompose the PDE into different orders and keep it up to the second order. So far, we have only used the first order terms in the PDE set to solve for it and used the second order terms in the expressions of the forces. Considering the complexity and the length in the expressions of the 2nd order terms in the PDE set, we will only keep up to $o(\epsilon)$.

The $o(1)$, $o(\epsilon)$ PDE set can be summarized as below:

$o(1)$:

$$\begin{aligned}
&\nabla^2\overline{\Phi}^{(0)}_{rel} = 0 \qquad in\ fluid\ domain \\
&\frac{\partial\overline{\Phi}^{(0)}_{rel}}{\partial\bar{z}} = 0 \qquad on\ \bar{z} = 0 \\
&\frac{\partial\overline{\Phi}^{(0)}_{rel}}{\partial\bar{t}} + \frac{1}{2}[(\frac{\partial\overline{\Phi}^{(0)}_{rel}}{\partial\bar{x}})^2 + (\frac{\partial\overline{\Phi}^{(0)}_{rel}}{\partial\bar{y}})^2 + (\frac{\partial\overline{\Phi}^{(0)}_{rel}}{\partial\bar{z}})^2] = \frac{1}{2}U^2 \qquad on\ \bar{z} = 0 \\
&\vec{n'} \cdot \vec{\nabla}\overline{\Phi}^{(0)}_{rel} = 0 \qquad at\ body\ surface \\
&\frac{\partial\overline{\Phi}^{(0)}_{rel}}{\partial\bar{z}} = 0 \qquad on\ \bar{z} = -h \\
&P^{(0)}\big|_S = -\rho g\bar{z}\big|_{S_m}
\end{aligned} \tag{2.15}$$

$o(\epsilon)$:

$$
\begin{aligned}
&\nabla^2\overline{\Phi}^{(1)}_{rel} = 0 \qquad in\ fluid\ domain \\
&\frac{\partial\bar{\zeta}^{(1)}}{\partial\bar{t}} + \vec{\nabla}\overline{\Phi}^{(0)}_{rel}\cdot\vec{\nabla}\bar{\zeta}^{(1)} = \frac{\partial\overline{\Phi}^{(1)}_{rel}}{\partial\bar{z}} + \bar{\zeta}^{(1)}\frac{\partial^2\overline{\Phi}^{(0)}_{rel}}{\partial\bar{z}^2} \qquad on\ \bar{z}=0 \\
&\frac{\partial\overline{\Phi}^{(1)}_{rel}}{\partial\bar{t}} + \vec{\nabla}\overline{\Phi}^{(0)}_{rel}\cdot\vec{\nabla}\overline{\Phi}^{(1)}_{rel} + g\bar{\zeta}^{(1)} + \bar{\zeta}^{(1)}\frac{\partial^2\overline{\Phi}^{(0)}_{rel}}{\partial\bar{z}\partial\bar{t}} + \bar{\zeta}^{(1)}\frac{\partial}{\partial\bar{z}}(\frac{1}{2}\vec{\nabla}\overline{\Phi}^{(0)}_{rel}\cdot\vec{\nabla}\overline{\Phi}^{(0)}_{rel}) = 0 \qquad on\ \bar{z}=0 \\
&(\vec{\bar{\alpha}}^{(1)}\times\vec{n'})\cdot\vec{\nabla}\overline{\Phi}^{(0)}_{rel} + \vec{n'}\cdot\vec{\nabla}\overline{\Phi}^{(1)}_{rel} = \vec{n'}\cdot\dot{\vec{\bar{\eta}}}^{(1)} + \vec{n'}\cdot(\dot{\vec{\bar{\alpha}}}^{(1)}\times\vec{X'}) \qquad at\ body\ surface \\
&\frac{\partial\overline{\Phi}^{(1)}_{rel}}{\partial\bar{z}} = 0 \qquad on\ \bar{z}=-h \\
&P^{(1)}\big|_S = \big[-\rho(\frac{\partial}{\partial\bar{t}} - U\frac{\partial}{\partial\bar{x}})\overline{\Phi}^{(1)}_{rel} - \rho g\vec{k}\cdot(\vec{\bar{\eta}}^{(1)} + \vec{\bar{\alpha}}^{(1)}\times\vec{X'})\big]\big|_{S_m}
\end{aligned}
\tag{2.16}
$$

If there are no wave in the fluid domain, we will have a steady potential Φ_s to reflect the effect caused by the ship moving in calm water. It is a different type of problem. Herein, we are discussing more about the seakeeping ability of the floater. Thus, we will neglect the steady potential Φ_s. Based on this assumption, we can assume $\overline{\Phi}^{(0)}_{rel} = -Ux$. This is an approximation method to consider the forward speed effect in the seakeeping problems because based on this assumption the body boundary condition in the $o(1)$ problem will not be satisfied. However, we are still interested in whether such method will provide some reasonable results. We will move forward and derive the corresponding equations.

If $\overline{\Phi}^{(0)}_{rel} = -Ux$, the PDE set of $o(\epsilon)$ will be:

$$\nabla^2\overline{\Phi}^{(1)}_{rel} = 0 \qquad in\ fluid\ domain$$

$$\frac{\partial\bar{\zeta}^{(1)}}{\partial\bar{t}} - U\frac{\partial\bar{\zeta}^{(1)}}{\partial\bar{x}} = \frac{\partial\overline{\Phi}^{(1)}_{rel}}{\partial\bar{z}} \qquad on\ \bar{z} = 0$$

$$\frac{\partial\overline{\Phi}^{(1)}_{rel}}{\partial\bar{t}} - U\frac{\partial\overline{\Phi}^{(1)}_{rel}}{\partial\bar{x}} + g\bar{\zeta} = 0 \qquad on\ \bar{z} = 0$$

$$\vec{n'}\cdot\vec{\nabla}\overline{\Phi}^{(1)}_{rel} = \vec{n'}\cdot[\dot{\vec{\bar{\eta}}}^{(1)} + \dot{\vec{\bar{\alpha}}}^{(1)}\times\vec{X'} - U(\vec{\bar{\alpha}}^{(1)}\times\vec{i})] \qquad at\ body\ surface$$

$$\frac{\partial\overline{\Phi}^{(1)}_{rel}}{\partial\bar{z}} = 0 \qquad on\ \bar{z} = -h$$

$$proper\ radiation\ condition \qquad at\ control\ surface$$

If we combine the free surface kinematic boundary condition and the dynamic condition, we can get the following PDE set:

$$\nabla^2\overline{\Phi}^{(1)}_{rel} = 0 \qquad in\ fluid\ domain$$

$$-\frac{1}{g}(\frac{\partial}{\partial\bar{t}} - U\frac{\partial}{\partial\bar{x}})^2\overline{\Phi}^{(1)}_{rel} = \frac{\partial\overline{\Phi}^{(1)}_{rel}}{\partial\bar{z}}$$

$$\vec{n'}\cdot\vec{\nabla}\overline{\Phi}^{(1)}_{rel} = \vec{n'}\cdot[\dot{\vec{\bar{\eta}}}^{(1)} + \dot{\vec{\bar{\alpha}}}^{(1)}\times\vec{X'} - U(\vec{\bar{\alpha}}^{(1)}\times\vec{i})] \qquad at\ body\ surface$$

$$\frac{\partial\overline{\Phi}^{(1)}_{rel}}{\partial\bar{z}} = 0 \qquad on\ \bar{z} = -h$$

$$proper\ radiation\ condition \qquad at\ control\ surface$$

The second order equations for the forces will be discussed in Chapter 5.

3. 1ST ORDER PROBLEM[1]

In this chapter, we will discuss the 1st order equations for a single floater with zero forward speed, with nonzero forward speed and then expand it to multi-body cases.

3.1 Governing Equation and Boundary Conditions

The PDE set for the 1st order equations is as below:

$$\nabla^2\Phi^{(1)} = 0 \qquad in\ fluid\ domain \tag{3.1}$$

$$-\frac{1}{g}\frac{\partial^2\Phi^{(1)}}{\partial t^2} = \frac{\partial\Phi^{(1)}}{\partial z} \qquad on\ z = 0 \tag{3.2}$$

$$\vec{n'}\cdot\vec{\nabla}\Phi^{(1)} = \vec{n'}\cdot[\dot{\vec{\eta}}^{(1)} + (\dot{\vec{\alpha}}^{(1)}\times\vec{X'})] \qquad at\ body\ surface \tag{3.3}$$

$$\lim_{r\to\infty} r(\frac{\partial\Phi^{(1)}}{\partial r} - ik\Phi^{(1)}) = 0 \qquad at\ control\ surface \tag{3.4}$$

$$\frac{\partial\Phi^{(1)}}{\partial z} = 0 \qquad on\ z = -h \tag{3.5}$$

As derived in the previous chapter, the PDE set for the nonzero forward speed case is:

$$\nabla^2\overline{\Phi}^{(1)}_{rel} = 0 \qquad in\ fluid\ domain$$

$$-\frac{1}{g}(\frac{\partial}{\partial\bar{t}} - U\frac{\partial}{\partial\bar{x}})^2\overline{\Phi}^{(1)}_{rel} = \frac{\partial\overline{\Phi}^{(1)}_{rel}}{\partial\bar{z}} \qquad on\ \bar{z} = 0$$

$$\vec{n'}\cdot\vec{\nabla}\overline{\Phi}^{(1)}_{rel} = \vec{n'}\cdot[\dot{\vec{\eta}}^{(1)} + \dot{\vec{\alpha}}^{(1)}\times\vec{X'} - U(\vec{\alpha}^{(1)}\times\vec{i})] \qquad at\ body\ surface$$

$$\frac{\partial\overline{\Phi}^{(1)}_{rel}}{\partial\bar{z}} = 0 \qquad on\ \bar{z} = -h$$

$$proper\ radiation\ condition \qquad at\ control\ surface$$

By comparison, we may notice the difference between the two PDE sets. If $U\frac{\partial}{\partial\bar{x}}$ is one order

[1]Part of the chapter is reprinted with permission from "Frequency Domain Analysis of the Interactions Between Multiple Ships with Nonzero Speed in Waves or Current-Wave Interactions" by Yujie Liu, Jeffrey Falzarano, 2017. *Proceedings of the ASME 2017 36th International Conference on Ocean, Offshore and Arctic Engineering*, pp. 1-17 Copyright 2017 by ASME.

smaller than $\frac{\partial}{\partial \bar{t}}$. The free surface boundary condition of the nonzero forward speed case will be:

$$-\frac{1}{g}\frac{\partial^2 \overline{\Phi}_{rel}^{(1)}}{\partial \bar{t}^2} = \frac{\partial \overline{\Phi}_{rel}^{(1)}}{\partial \bar{z}} \qquad on\ z = 0$$

This can be achieved by assuming a relatively smaller forward speed or slender body. However, for the multi-body case, due to the interactions among the bodies, the slender-body assumption may not be valid. In that case, the forward speed U should be smaller compared to the single body case such that $U\frac{\partial}{\partial \bar{x}}$ is one order smaller. Still it is an approximation to introduce the forward speed into the seakeeping problems. We are interested in seeing what changes may appear compared to the zero-speed cases and what may be the limit of such assumptions.

After enforcing this assumption, the two PDE sets are almost identical except for the body boundary conditions. We will first discuss the multi-body problem assuming zero forward speed and then extend it to the problem with nonzero forward speed.

We will study the wave excitation of one frequency at one time. The incident potential for the zero-speed problem in the deep water can be written as below:

$$\Phi_I = \frac{igA}{\omega_I}\exp[-ik_I(x\cos\beta + y\sin\beta)]\exp(k_I z)\exp(i\omega_I t)$$

where, the wave heading angle β is defined in Figure 3.1. The phase of the incident wave is defined with respect to the origin of the global coordinate. It will be zero at the origin when $t = 0$. The vessel equilibrium coordinate can be rotated by the angle $XBODY(4)$. The z-axis of the vessel equilibrium coordinate will be parallel to that of the global coordinate.

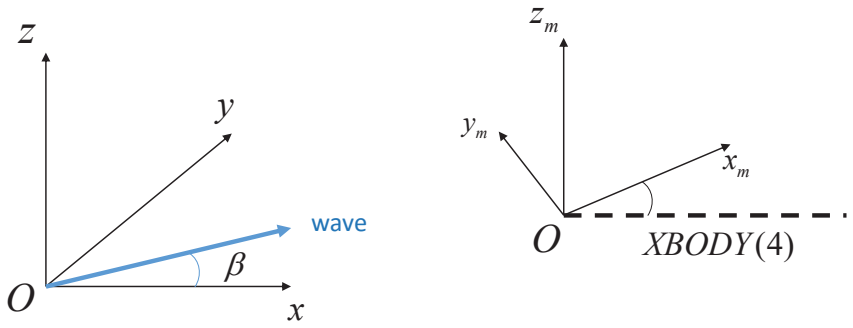

Figure 3.1: Definition of Wave Heading Angle in Global Coordinate

Based on the coordinate transformation, the potential in the vessel translating coordinate can be defined as:

$$\begin{aligned}\Phi_I(x,y,z,t) &= \Phi_I(\bar{x}+Ut,\bar{y},\bar{z},\bar{t}) \\ &= \frac{igA}{\omega_I}\exp[-ik_I(\bar{x}\cos\beta+\bar{y}\sin\beta)]\exp(k_I\bar{z})\exp[i(\omega_I-k_IU\cos\beta)\bar{t}] \\ &= \overline{\Phi_I}(\bar{x},\bar{y},\bar{z},\bar{t})\end{aligned}$$

where,k_I is the wave number of the incident wave in the global coordinate. The encounter radian frequency ω_e can be defined as $\omega_e = \omega_I - k_IU\cos\beta$.

This is a sinusoidal excitation. If we are interested in the steady state, we may similarly assume the potentials resulting from the existence of the floater and the motion also have a factor $e^{i\omega t}$. So are the 6 DOF motions of the floater. Herein, we will first discuss about the Green function and then how the different potentials are proposed. In the discussion of the Green function part, we assume $V_{\boldsymbol{n}} = \vec{n'}\cdot[\dot{\vec{\eta}}^{(1)} + (\dot{\vec{\alpha}}^{(1)} \times \vec{X'})]$ to simplify the notations.

Based on the above assumptions, the first order potential and the motion terms can be written

as:

$$\Phi^{(1)} = Re\{\phi^{(1)} e^{i\omega t}\}$$

$$V_{\boldsymbol{n}} = Re\{v_{\boldsymbol{n}} e^{i\omega t}\}$$

where, $\phi^{(1)}$, $v_{\boldsymbol{n}}$ are complex variables and independent of time t. In such a way, we converted the PDE set from the real domain to the complex domain. We will only focus on how to solve for the complex time-independent terms. In the latter derivation, we will omit the symbol Re but please note that we are still interested in the real part of the final results, which has the physical meaning.

The PDE set can be written as below:

$$\nabla^2 \phi^{(1)} = 0 \qquad in\ fluid\ domain\ V \tag{3.6}$$

$$-\omega^2 \phi^{(1)} + g\frac{\partial \phi^{(1)}}{\partial z} = 0 \qquad on\ z = 0 \tag{3.7}$$

$$\frac{\partial \phi^{(1)}}{\partial n} = v_n \qquad at\ body\ surface \tag{3.8}$$

$$\lim_{r\to\infty} r(\frac{\partial \phi^{(1)}}{\partial r} - ik\phi^{(1)}) = 0 \qquad at\ control\ surface \tag{3.9}$$

$$\frac{\partial \phi^{(1)}}{\partial z} = 0 \qquad on\ z = -h \tag{3.10}$$

Only the body boundary condition will vary depending on the specific body shape. The Green function method can be a good choice to this problem. If the Green function can satisfy the boundary conditions except the body boundary conditions. The problem will be greatly simplified. Because the introduction of the Green function method has decomposed one problem into two separate problems: finding the Green function and finding the potential value on the floater surface.

Based on the Green 2nd identity, the corresponding Green function will satisfy the following

equations:

$$\nabla^2 G = 4\pi\delta(\boldsymbol{x}-\boldsymbol{\xi}) \qquad \boldsymbol{x},\boldsymbol{\xi} \in V \tag{3.11}$$

$$\frac{\omega^2}{g}G - \frac{\partial G}{\partial z} = 0, \qquad on\ z=0 \tag{3.12}$$

$$ikG - \frac{\partial G}{\partial n} = 0, \qquad at\ control\ surface \tag{3.13}$$

$$\frac{\partial G}{\partial z} = 0, \qquad on\ z=-h \tag{3.14}$$

In here, we will adopt the Noblesse Green function as below:

$$G = \frac{1}{r} + \frac{1}{r'} + 2f^*[R_0(h,v) - i\pi J_0(h)exp(v)] \tag{3.15}$$

where, $f^* = \omega^2 L/g$, $\rho = [(x-\xi)^2+(y-\eta)^2]^{\frac{1}{2}}$, $r = [\rho^2+(z-\zeta)^2]^{\frac{1}{2}}$, $r' = [\rho^2+(z+\zeta)^2]^{\frac{1}{2}}$, $h = f^*\rho$, $v = f^*(z+\zeta)$, J_0 is Bessel function of the first kind at order 0, R_0 is the function defined in Telste and Noblesse[10]. In the limiting case when $d \to 0$, $R_0 = -ln(d-v) + ln(2) - \gamma$ with error $O(d\,ln(d))$.

3.2 Potential Formulation

If the Green function satisfies the governing equation and three boundary conditions, we substitute these relations back to the Green 2nd identity formula, then:

$$-4\pi\phi^{(1)}(\boldsymbol{x}) = \iint_{S_b} \frac{\partial\phi^{(1)}(\boldsymbol{\xi})}{\partial n_{\boldsymbol{\xi}}} G(\boldsymbol{x};\boldsymbol{\xi})dS_{\boldsymbol{\xi}} - \iint_{S_b} \phi^{(1)}(\boldsymbol{\xi})\frac{\partial G(\boldsymbol{x};\boldsymbol{\xi})}{\partial n_{\boldsymbol{\xi}}}dS_{\boldsymbol{\xi}}, \qquad \boldsymbol{x} \in V$$

The above equation is also named as *Potential Formulation*. As long as $\phi^{(1)}$ on boundaries are known, the potential at arbitrary position inside the domain will be found. To solve for the boundary values of $\phi^{(1)}$, this equation will be solved:

$$-2\pi\phi^{(1)}(\boldsymbol{x}) + \iint_{S_b} \phi^{(1)}(\boldsymbol{\xi})\frac{\partial G(\boldsymbol{x};\boldsymbol{\xi})}{\partial n_{\boldsymbol{\xi}}}dS_{\boldsymbol{\xi}} = \iint_{S_b} \frac{\partial\phi^{(1)}(\boldsymbol{\xi})}{\partial n_{\boldsymbol{\xi}}} G(\boldsymbol{x};\boldsymbol{\xi})dS_{\boldsymbol{\xi}}, \qquad \boldsymbol{x} \in S_b$$

The equation is also named as *Fredholm 2nd-Kind Integral Equation*. $\frac{\partial \phi^{(1)}(\boldsymbol{\xi})}{\partial n_{\boldsymbol{\xi}}} = v_n$ on body surface S_b.

3.3 Source Formulation

The source formulation has more advantages in calculating the induced velocity at the body surface. To define it, we need to apply Green's 2nd identity to the fluid domain and the domain enclosed by the floater.

For the potential which satisfies the PDE set 3.1, if applying Green's 2nd identity, we will get:

$$\int_{S_b} \big[\, \phi^{(1)}(\boldsymbol{\xi}) \frac{\partial G(\boldsymbol{x}, \boldsymbol{\xi})}{\partial n_{\boldsymbol{\xi}}} - G(\boldsymbol{x}, \boldsymbol{\xi}) \frac{\partial \phi^{(1)}(\boldsymbol{\xi})}{\partial n_{\boldsymbol{\xi}}} \big] dS_{\boldsymbol{\xi}} = \alpha(\boldsymbol{x}) \phi^{(1)}(\boldsymbol{x}) \tag{3.16}$$

herein, $\alpha(\boldsymbol{x})$ satisfies:

$$\alpha(\boldsymbol{x}) = \begin{cases} 4\pi & \text{if } \boldsymbol{x} \in V \\ 2\pi & \text{if } \boldsymbol{x} \in S_b \\ 0 & \text{if } \boldsymbol{x} \in V_- \end{cases}$$

When the flow of interest happens in the domain V_-, we probably need to define the internal potential function $\phi_i^{(1)}$ inside the domain V_-. The internal potential function $\phi_i^{(1)}$ is introduced to help us derive both the source and doublet formulations. Here let $\phi_i^{(1)}$ satisfy:

$$\nabla^2 \phi_i^{(1)} = 0 \qquad in\ V_- \tag{3.17}$$

$$-\omega^2 \phi_i^{(1)} + g \frac{\partial \phi_i^{(1)}}{\partial z} = 0 \qquad on\ S_f \tag{3.18}$$

Similarly, we can get:

$$\int_{S_b} \big[\, \phi_i^{(1)}(\boldsymbol{\xi}) \frac{\partial G(\boldsymbol{x}, \boldsymbol{\xi})}{\partial n_{\boldsymbol{\xi}}} - G(\boldsymbol{x}, \boldsymbol{\xi}) \frac{\partial \phi_i^{(1)}(\boldsymbol{\xi})}{\partial n_{\boldsymbol{\xi}}} \big] dS_{\boldsymbol{\xi}} = [\alpha(\boldsymbol{x}) - 4\pi] \phi_i^{(1)}(\boldsymbol{x}) \tag{3.19}$$

Herein, $\alpha(\boldsymbol{x})$ follows the same definition as above.

If we subtract equation 3.16 from equation 3.19, we will get:

$$\begin{aligned}
&\alpha(\boldsymbol{x})\phi^{(1)}(\boldsymbol{x}) - [\alpha(\boldsymbol{x}) - 4\pi]\phi_i^{(1)}(\boldsymbol{x}) \\
&= \iint_{S_b} [\phi^{(1)}(\boldsymbol{\xi}) - \phi_i^{(1)}(\boldsymbol{\xi})] \frac{\partial G(\boldsymbol{x};\boldsymbol{\xi})}{\partial n_{\boldsymbol{\xi}}} dS_{\boldsymbol{\xi}} - \iint_{S_b} [\frac{\partial \phi^{(1)}(\boldsymbol{\xi})}{\partial n_{\boldsymbol{\xi}}} - \frac{\partial \phi_i^{(1)}(\boldsymbol{\xi})}{\partial n_{\boldsymbol{\xi}}}] G(\boldsymbol{x};\boldsymbol{\xi}) dS_{\boldsymbol{\xi}}, \\
&\boldsymbol{x} \in V \; or \; V_or \; S_b
\end{aligned}$$

The following case is the basic formulations for boundary integral problems when the field point is located on the body boundary. If the point of interest $\boldsymbol{x}$ approaches the body boundary from V and $x \to S_b$, for the external potential $\phi^{(1)}$, we have:

$$2\pi\phi^{(1)}(\boldsymbol{x}) = \iint_{S_b} \phi^{(1)}(\boldsymbol{\xi}) \frac{\partial G(\boldsymbol{x};\boldsymbol{\xi})}{\partial n_{\boldsymbol{\xi}}} dS_{\boldsymbol{\xi}} - \iint_{S_b} \frac{\partial \phi^{(1)}(\boldsymbol{\xi})}{\partial n_{\boldsymbol{\xi}}} G(\boldsymbol{x};\boldsymbol{\xi}) dS_{\boldsymbol{\xi}}, \; \boldsymbol{x} \in S_b \tag{3.20}$$

For the internal potential $\phi_i^{(1)}$,

$$-2\pi\phi_i^{(1)}(\boldsymbol{x}) = \iint_{S_b} \phi_i^{(1)}(\boldsymbol{\xi}) \frac{\partial G(\boldsymbol{x};\boldsymbol{\xi})}{\partial n_{\boldsymbol{\xi}}} dS_{\boldsymbol{\xi}} - \iint_{S_b} \frac{\partial \phi_i^{(1)}(\boldsymbol{\xi})}{\partial n_{\boldsymbol{\xi}}} G(\boldsymbol{x};\boldsymbol{\xi}) dS_{\boldsymbol{\xi}}, \; \boldsymbol{x} \in S_b \tag{3.21}$$

The -2π is a result of a consistent normal direction with that defined by the external domain. Taking the substraction, then:

$$\begin{aligned}
2\pi[\phi^{(1)}(\boldsymbol{x}) + \phi_i^{(1)}(\boldsymbol{x})] = &\iint_{S_b} [\phi^{(1)}(\boldsymbol{\xi}) - \phi_i^{(1)}(\boldsymbol{\xi})] \frac{\partial G(\boldsymbol{x};\boldsymbol{\xi})}{\partial n_{\boldsymbol{\xi}}} dS_{\boldsymbol{\xi}} \\
&- \iint_{S_b} [\frac{\partial \phi^{(1)}(\boldsymbol{\xi})}{\partial n_{\boldsymbol{\xi}}} - \frac{\partial \phi_i^{(1)}(\boldsymbol{\xi})}{\partial n_{\boldsymbol{\xi}}}] G(\boldsymbol{x};\boldsymbol{\xi}) dS_{\boldsymbol{\xi}}, \; \boldsymbol{x} \in S_b
\end{aligned} \tag{3.22}$$

In this case of enforcing $\phi^{(1)}(\boldsymbol{\xi}) = \phi_i^{(1)}(\boldsymbol{\xi})$ on S_b, we will get the source distribution equation; if $\partial\phi^{(1)}(\boldsymbol{\xi})/\partial n_{\boldsymbol{\xi}} = \partial\phi_i^{(1)}(\boldsymbol{\xi})/\partial n_{\boldsymbol{\xi}}$, then the doublet distribution equation.

For the source formulation, the expression is as below:

$$4\pi\phi^{(1)}(\boldsymbol{x}) = -\iint_{S_b}[\frac{\partial\phi^{(1)}(\boldsymbol{\xi})}{\partial n_{\boldsymbol{\xi}}} - \frac{\partial\phi_i^{(1)}(\boldsymbol{\xi})}{\partial n_{\boldsymbol{\xi}}}]G(\boldsymbol{x};\boldsymbol{\xi})dS_{\boldsymbol{\xi}}$$
$$= \iint_{S_b}\sigma(\boldsymbol{\xi})G(\boldsymbol{x};\boldsymbol{\xi})dS_{\boldsymbol{\xi}},\ \boldsymbol{x} \in S_b \cup V \tag{3.23}$$

On the body boundary, the induced velocity from all the sources on the floater body can be:

$$\frac{\partial\phi^{(1)}}{\partial n_{\boldsymbol{x}}} = -\frac{1}{2}\sigma(\boldsymbol{x}) + \frac{1}{4\pi}\iint_{S_b}\sigma(\boldsymbol{\xi})\frac{\partial G(\boldsymbol{x};\boldsymbol{\xi})}{\partial n_{\boldsymbol{x}}}dS_{\boldsymbol{\xi}} = v_n \tag{3.24}$$

After solving for this equation, we will get the value for the source strength. Substituting the source strength into equation (3.23), the potential on the body surface and inside the fluid domain can be computed.

The numerical techniques to solve for the source strength are discussed in Guha[111].

3.4 Linear Superposition

3.4.1 Zero Speed

In the previous discussion, we are focusing on the Green function. Thus the simplification $V_{\boldsymbol{n}} = \vec{n'} \cdot [\dot{\vec{\eta}}^{(1)} + (\dot{\vec{\alpha}}^{(1)} \times \vec{X'})]$ is adopted for the velocity on the body boundary conditions. Herein, we will discuss how the linear superposition works in the classification of the potentials. Although the three types of potential (incident, diffraction, radiation potentials) are proposed long time ago, we investigate the motivations mainly to shed light on the motivation to resolve the multi-body problem, with zero or nonzero speed.

When observing the PDE set (3.6) - (3.10), we will notice that all the operators are linear. This indicates that linear superposition can be used to find the results. More specific, the solution can be written as:

$$\phi^{(1)} = \phi_1^{(1)} + \phi_2^{(1)} + \phi_3^{(1)} + ...$$

The question will be: how many elements we need to make the solution set is complete? This is hard to prove mathematically. We usually consider the physical effect in the specific problem. The hint may be located in the body boundary condition.

It will be helpful if we expand all the terms in $V_{\boldsymbol{n}}$.

$$\frac{\partial \phi^{(1)}}{\partial n_{\boldsymbol{x}}} = V_{\boldsymbol{n}} = i\omega(n_1' \eta_1^{A(1)} + n_2' \eta_2^{A(1)} + n_3' \eta_3^{A(1)} + n_4' \eta_4^{A(1)} + n_5' \eta_5^{A(1)} + n_6' \eta_6^{A(1)}) \tag{3.25}$$

where, $\vec{\eta}^{(1)} = (\eta_1^{(1)}, \eta_2^{(1)}, \eta_3^{(1)}) = (\eta_1^{A(1)}, \eta_2^{A(1)}, \eta_3^{A(1)}) e^{i\omega t}$, $\vec{\alpha}^{(1)} = (\eta_4^{(1)}, \eta_5^{(1)}, \eta_6^{(1)})$
$= (\eta_4^{A(1)}, \eta_5^{A(1)}, \eta_6^{A(1)}) e^{i\omega t}$, $\vec{n'} = (n_1', n_2', n_3')$, $\vec{X'} \times \vec{n'} = (n_4', n_5', n_6')$. The vector identify $\vec{n'} \cdot (\dot{\vec{\alpha}}^{(1)} \times \vec{X'}) = \dot{\vec{\alpha}}^{(1)} \cdot (\vec{X'} \times \vec{n'})$ is used in here.

In the right hand side of the equation (3.25), there are 7 terms including the hidden zero. It is natural to propose 7 types of element solutions to take care of each term in the body boundary condition. The 7 elements are $\phi_I^{(1)} + \phi_D^{(1)}$, $\sum_{i=1}^{6} \phi_i^{(1)}$, where $\phi_I^{(1)}$ is the incident potential, $\phi_D^{(1)}$ is the diffraction potential due to the existence of the floater , $\sum_{i=1}^{6} \phi_i^{(1)}$ are the radiation potential due to the 6 DOF motion of the floater. The equation is as below:

$$\phi^{(1)} = \phi_I^{(1)} + \phi_D^{(1)} + \sum_{i=1}^{6} \phi_i^{(1)} \tag{3.26}$$

As a result, it is natural to find the equations for each potential respectively.

$$\frac{\partial \phi_D^{(1)}}{\partial n_{\boldsymbol{x}}} = -\frac{\partial \phi_I^{(1)}}{\partial n_{\boldsymbol{x}}}$$
$$\frac{\partial \phi_i^{(1)}}{\partial n_{\boldsymbol{x}}} = i\omega n_i' \eta_i^{A(1)}, \qquad i = 1...6$$

If we introduce the unit-amplitude potential as below:

$$\phi_I^{(1)} = A\phi_I^{*(1)}$$
$$\phi_D^{(1)} = A\phi_D^{*(1)}$$
$$\phi_i^{(1)} = \eta_i^{A(1)}\phi_i^{*(1)}, \qquad i = 1...6$$

The unit-amplitude potentials will satisfy:

$$\frac{\partial \phi_D^{*(1)}}{\partial n_{\boldsymbol{x}}} = -\frac{\partial \phi_I^{*(1)}}{\partial n_{\boldsymbol{x}}}$$
$$\frac{\partial \phi_i^{*(1)}}{\partial n_{\boldsymbol{x}}} = i\omega n_i', \qquad i = 1...6$$

To sum up, we will solve for 7 types of sources σ_D and σ_j $(j = 1 \sim 6)$, which are used to calculate the 7 potentials. The incident potential $\phi_I^{(1)}$ and $\phi_I^{*(1)}$ are solved by:

$$\nabla^2\phi_I^{(1)} = 0 \qquad in\ fluid\ domain\ V$$
$$\frac{\partial \phi_I^{(1)}}{\partial z} = 0 \qquad on\ z = -h$$
$$-\omega^2\phi_I^{(1)} + g\frac{\partial \phi_I^{(1)}}{\partial z} = 0 \qquad on\ z = 0$$

$\phi_D^{(1)}$ and $\phi_D^{*(1)}$ satisfy the equations:

$$\nabla^2\phi_D^{(1)} = 0 \qquad in\ fluid\ domain\ V$$
$$\frac{\partial \phi_D^{(1)}}{\partial z} = 0 \qquad on\ z = -h$$
$$-\omega^2\phi_D^{(1)} + g\frac{\partial \phi_D^{(1)}}{\partial z} = 0 \qquad on\ z = 0$$
$$\frac{\partial \phi_D^{(1)}}{\partial n} = -\frac{\partial \phi_I^{(1)}}{\partial n} \qquad on\ S_b$$
$$\lim_{r\to\infty} r[\frac{\partial \phi_D^{(1)}}{\partial r} - ik\phi_D^{(1)}] = 0 \qquad on\ S_c$$

$\phi_j^{(1)}$ and $\phi_j^{*(1)}(j = 1 \sim 6)$ satisfy the equations:

$$\begin{aligned}
&\nabla^2\phi_j^{(1)} = 0 \qquad in\ fluid\ domain\ V\\
&\frac{\partial\phi_j^{(1)}}{\partial z} = 0 \qquad on\ z = -h\\
&-\omega^2\phi_j^{(1)} + g\frac{\partial\phi_j^{(1)}}{\partial z} = 0 \qquad on\ z = 0\\
&\frac{\partial\phi_j^{(1)}}{\partial n} = i\omega n_j' \qquad on\ S_b\\
&\lim_{r\to\infty} r[\frac{\partial\phi_j^{(1)}}{\partial r} - ik\phi_j^{(1)}] = 0 \qquad on\ S_c
\end{aligned}$$

3.4.2 Nonzero Speed

Similar to the zero speed case, we will investigate the body boundary condition to get some hints to find the solution elements. The difference is that the excitation frequency has become the encounter frequency ω_e, resulted from the Doppler effects.

The body boundary condition is as below:

$$\vec{n'}\cdot\vec{\nabla}\overline{\Phi}_{rel}^{(1)} = \vec{n'}\cdot[\dot{\vec{\bar{\eta}}}^{(1)} + \dot{\vec{\bar{\alpha}}}^{(1)}\times\vec{X'} - U(\vec{\bar{\alpha}}^{(1)}\times\vec{i})] \qquad at\ body\ surface$$

If separating the time dependent term $e^{i\omega t}$, the equation can be written as:

$$\vec{n'}\cdot\vec{\nabla}\overline{\phi}_{rel}^{(1)} = i\omega_e(n_1'\bar{\eta}_1^{A(1)} + n_2'\bar{\eta}_2^{A(1)} + n_3'\bar{\eta}_3^{A(1)} + n_4'\bar{\eta}_4^{A(1)} + n_5'\bar{\eta}_5^{A(1)} + n_6'\bar{\eta}_6^{A(1)}) + U(n_3'\bar{\eta}_5^{A(1)} - n_2'\bar{\eta}_6^{A(1)})$$

Please note that $\vec{\bar{\eta}}^{(1)} = (\bar{\eta}_1^{(1)}, \bar{\eta}_2^{(1)}, \bar{\eta}_3^{(1)}) = (\bar{\eta}_1^{A(1)}, \bar{\eta}_2^{A(1)}, \bar{\eta}_3^{A(1)})e^{i\omega_e t}$.

The 1st order dynamic pressure will be:

$$\frac{\overline{P}^{d(1)}}{\rho} = -(\frac{\partial\overline{\Phi}_{rel}^{(1)}}{\partial\bar{t}} - U\frac{\partial\overline{\Phi}_{rel}^{(1)}}{\partial\bar{x}}) \tag{3.27}$$

Based on the similar considerations, the solution for total potential $\overline{\Phi}_{rel}^{(1)}$ can be:

$$\overline{\Phi}_{rel}^{(1)} = \overline{\Phi}_{rel-I}^{(1)} + \overline{\Phi}_{rel-D}^{(1)} + \sum_{i=1}^{6} \overline{\Phi}_{rel-i}^{(1)} \tag{3.28}$$

where, $\bar{\eta}_i$ is the floater RAO defined relative to the vessel fixed coordinate.

Based on the principal of linear superposition, we will get the following relationships:

$$\begin{aligned}
\vec{n'} \cdot \vec{\nabla} \overline{\phi}_{rel-1}^{*(1)} &= i\omega_e n'_1 \\
\vec{n'} \cdot \vec{\nabla} \overline{\phi}_{rel-2}^{*(1)} &= i\omega_e n'_2 \\
\vec{n'} \cdot \vec{\nabla} \overline{\phi}_{rel-3}^{*(1)} &= i\omega_e n'_3 \\
\vec{n'} \cdot \vec{\nabla} \overline{\phi}_{rel-4}^{*(1)} &= i\omega_e n'_4 \\
\vec{n'} \cdot \vec{\nabla} \overline{\phi}_{rel-5}^{*(1)} &= i\omega_e n'_5 + U n'_3 \\
\vec{n'} \cdot \vec{\nabla} \overline{\phi}_{rel-6}^{*(1)} &= i\omega_e n'_6 - U n'_2
\end{aligned}$$

where, $\overline{\phi}_{rel-i}^{(1)} = \bar{\eta}_i^{A(1)} \overline{\phi}_{rel-i}^{*(1)}$, $\overline{\phi}_{rel-i}^{*(1)}$ is the radiation potential caused by the unit amplitude motion in one of the 6 DOF motion.

The boundary condition is different from that in the zero-speed case. If we would like to use a similar form, we can define the following potentials, which will satisfy:

$$\begin{aligned}
\vec{n'} \cdot \vec{\nabla} \overline{\phi}_{rel-1}^{*0(1)} &= i\omega_e n'_1 \\
\vec{n'} \cdot \vec{\nabla} \overline{\phi}_{rel-2}^{*0(1)} &= i\omega_e n'_2 \\
\vec{n'} \cdot \vec{\nabla} \overline{\phi}_{rel-3}^{*0(1)} &= i\omega_e n'_3 \\
\vec{n'} \cdot \vec{\nabla} \overline{\phi}_{rel-4}^{*0(1)} &= i\omega_e n'_4 \\
\vec{n'} \cdot \vec{\nabla} \overline{\phi}_{rel-5}^{*0(1)} &= i\omega_e n'_5 \\
\vec{n'} \cdot \vec{\nabla} \overline{\phi}_{rel-6}^{*0(1)} &= i\omega_e n'_6
\end{aligned}$$

where, the superscript 0 denotes this formula is similar to that in the zero-speed case. Then we will

have:

$$\begin{aligned}
\overline{\phi}^{*(1)}_{rel-1} &= \overline{\phi}^{*0(1)}_{rel-1} \\
\overline{\phi}^{*(1)}_{rel-2} &= \overline{\phi}^{*0(1)}_{rel-2} \\
\overline{\phi}^{*(1)}_{rel-3} &= \overline{\phi}^{*0(1)}_{rel-3} \\
\overline{\phi}^{*(1)}_{rel-4} &= \overline{\phi}^{*0(1)}_{rel-4} \\
\overline{\phi}^{*(1)}_{rel-5} &= \overline{\phi}^{*0(1)}_{rel-5} + \frac{U}{i\omega_e}\overline{\phi}^{*0(1)}_{rel-3} \\
\overline{\phi}^{*(1)}_{rel-6} &= \overline{\phi}^{*0(1)}_{rel-6} - \frac{U}{i\omega_e}\overline{\phi}^{*0(1)}_{rel-2}
\end{aligned}$$

If using the above relationships, we can use the similar procedures to solve for $\vec{\nabla}\overline{\phi}^{*0(1)}_{rel-i}(i = 1 \sim 6)$ with the zero-speed cases in the program for the nonzero-speed potentials.

3.5 Solution for Source Strength and Numerical Implementation

Thanks to the methods based on Green function, researchers can have work allocation on such problems. Here we only need to let the potential satisfy different body boundary conditions since the Green function is already evaluated thoroughly. If assuming constant source strength on each panel, the equation (3.24) can be discretized as:

$$\begin{aligned}
-\frac{1}{2}\sigma(\boldsymbol{x}) + \sum \frac{1}{4\pi}\sigma(\boldsymbol{\xi}) \iint_{\Delta S_j} \frac{\partial}{\partial n} g(\boldsymbol{x};\boldsymbol{\xi}) dS_{\boldsymbol{\xi}} \\
+ \sum \frac{1}{4\pi}\sigma(\boldsymbol{\xi}) \iint_{\Delta S_j^*} \frac{\partial}{\partial n}(\frac{1}{r(\boldsymbol{x};\boldsymbol{\xi})}) dS_{\boldsymbol{\xi}} = v_n
\end{aligned}$$

$$-\frac{1}{2}\sigma_i + \sum_{j=1}^{N} \frac{1}{2}\alpha^1_{ij}\sigma_j + \sum_{\substack{j=1 \\ j\neq i}}^{N} \frac{1}{2}\alpha^2_{ij}\sigma_j = v_{ni}$$

where,

$$\alpha_{ij}^1 = \frac{1}{2\pi} \iint_{\Delta S_j} \frac{\partial}{\partial n} g(\boldsymbol{x}; \boldsymbol{\xi}) dS_{\boldsymbol{\xi}}$$
$$\alpha_{ij}^2 = \frac{1}{2\pi} \iint_{\Delta S_j^*} \frac{\partial}{\partial n} (\frac{1}{r(\boldsymbol{x}; \boldsymbol{\xi})}) dS_{\boldsymbol{\xi}}$$

Since the analytical expression of Green function is known, it is preferred to evaluate the normal derivative in analytical form. $\frac{\partial}{\partial n} = \boldsymbol{n} \cdot \nabla = n_1 \frac{\partial}{\partial x} + n_2 \frac{\partial}{\partial y} + n_3 \frac{\partial}{\partial z}$, wherein $\boldsymbol{n}$ is normal vector outward fluid domain. Therefore, α_{ij}^1 and α_{ij}^2 can be expressed by:

$$\alpha_{ij}^1 = n_1 \alpha_{ij-x}^1 + n_2 \alpha_{ij-y}^1 + n_3 \alpha_{ij-z}^1$$
$$\alpha_{ij}^2 = n_1 \alpha_{ij-x}^2 + n_2 \alpha_{ij-y}^2 + n_3 \alpha_{ij-z}^2$$

wherein, α_{ij-x}, α_{ij-y}, α_{ij-z} are defined as:

$$\begin{bmatrix} \alpha_{ij-x}^1 \\ \alpha_{ij-y}^1 \\ \alpha_{ij-z}^1 \end{bmatrix} = \frac{1}{4\pi} \iint_{\Delta S_j} \begin{bmatrix} \frac{\partial}{\partial x} g(\boldsymbol{x}; \boldsymbol{\xi}) dS_{\boldsymbol{\xi}} \\ \frac{\partial}{\partial y} g(\boldsymbol{x}; \boldsymbol{\xi}) dS_{\boldsymbol{\xi}} \\ \frac{\partial}{\partial z} g(\boldsymbol{x}; \boldsymbol{\xi}) dS_{\boldsymbol{\xi}} \end{bmatrix} = \frac{1}{4\pi} \iint_{\Delta S_j} \begin{bmatrix} \frac{\partial}{\partial x} (\frac{1}{r'} + \widetilde{G}) dS_{\boldsymbol{\xi}} \\ \frac{\partial}{\partial y} (\frac{1}{r'} + \widetilde{G}) dS_{\boldsymbol{\xi}} \\ \frac{\partial}{\partial z} (\frac{1}{r'} + \widetilde{G}) dS_{\boldsymbol{\xi}} \end{bmatrix}$$

where, r' stands for the position of image source. $\widetilde{G}$ the wavy Green function.

$$\begin{bmatrix} \alpha_{ij-x}^2 \\ \alpha_{ij-y}^2 \\ \alpha_{ij-z}^2 \end{bmatrix} = \frac{1}{4\pi} \iint_{\Delta S_j} \begin{bmatrix} \frac{\partial}{\partial x} (\frac{1}{r(\boldsymbol{x}; \boldsymbol{\xi})}) dS_{\boldsymbol{\xi}} \\ \frac{\partial}{\partial y} (\frac{1}{r(\boldsymbol{x}; \boldsymbol{\xi})}) dS_{\boldsymbol{\xi}} \\ \frac{\partial}{\partial z} (\frac{1}{r(\boldsymbol{x}; \boldsymbol{\xi})}) dS_{\boldsymbol{\xi}} \end{bmatrix}$$

In matrix form,

$$[-I+\alpha][\sigma]=[2v_n]$$

where,

$$\alpha_{ij}=\begin{cases}\alpha_{ij}^1 & i=j\\ \alpha_{ij}^1+\alpha_{ij}^2 & i\neq j\end{cases}$$

Thus $[\sigma]$ is solved by $[\sigma]=[-I+\alpha]^{-1}[2v_n]$. After that, the potential ϕ at arbitrary position in domain V can be computed via the source formula:

$$\phi(\boldsymbol{x})=\frac{1}{4\pi}\iint_{S_b}\sigma(\boldsymbol{\xi})G(\boldsymbol{x};\boldsymbol{\xi})dS_{\boldsymbol{\xi}} \qquad \boldsymbol{x}\in S_b\&\boldsymbol{x}\in V \tag{3.29}$$

In discretized form:

$$\phi(\boldsymbol{x})=\frac{1}{4\pi}\sum_{j=1}^{N}\sigma_j\iint_{\Delta S}G(\boldsymbol{x};\boldsymbol{\xi})dS_{\boldsymbol{\xi}} \qquad \boldsymbol{x}\in S_b\&\boldsymbol{x}\in V$$

$$\phi_i=\sum_{j=1}^{N}\beta_{ij}\sigma_j \qquad \boldsymbol{x}\in S_b\&\boldsymbol{x}\in V$$

where, $\beta_{ij}=\frac{1}{4\pi}\iint_{\Delta S}G(\boldsymbol{x};\boldsymbol{\xi})dS_{\boldsymbol{\xi}}$.

As a supplement, to construct the matrix for above equations, we need to evaluate the following integrals $\iint_{\Delta S}\frac{\partial}{\partial n}(\frac{1}{r})dS$, $\iint_{\Delta S}\frac{1}{r}dS$, $\iint_{\Delta S}\frac{\partial\widetilde{G}}{\partial n}dS$ and $\iint_{\Delta S}\widetilde{G}dS$. The numerical method are summarized by Amitava(2012).

The method to find $\iint_{\Delta S}\frac{\partial}{\partial n}(\frac{1}{r})dS$ is given by Hess and Smith(1964) and $\iint_{\Delta S}\frac{1}{r}dS$ by Katz and Plotkin (2001). The integral $\widetilde{G}$ and $\frac{\partial\widetilde{G}}{\partial n}$ over a panel can be computed by numerical integration methods(e.g. Gauss Quatrature etc).

3.6 Forces and RAO

3.6.1 Zero Speed

Until this step, the potential can be computed throughout the domain V including the body surface. Therefore the relationship between potential and pressure needs to be investigated. In the first order problem, the dynamic pressure can be written as below:

$$P^{d(1)} = -\rho \frac{\partial \Phi^{(1)}}{\partial t} \tag{3.30}$$

where, $\Phi^{(1)} = \phi^{(1)} e^{i\omega t} = \xi \phi^{*(1)} e^{i\omega t}$, wherein ξ stands for the amplitude, $\xi = A$ for the incident and diffracted wave while $\xi = \eta_i^{A(1)}$ for the radiated wave caused by the body motion.

Resulted from the periodicity of the potential $\Phi^{(1)}$, we may assume $P^{d(1)} = p^{d(1)} e^{i\omega t}$, $p^{d(1)} = -\rho i\omega \phi^{(1)} = -\rho i\omega \xi \phi^{*(1)}$. Based on the superposition principal in the potential components, the dynamic pressure from the forced motion is:

$$p_j^{d(1)} = -i\rho\omega \ \phi_j^{(1)} \qquad j = 1 \sim 6$$

Dynamic pressure from diffraction and incident wave potential:

$$p_D^{d(1)} = -i\rho\omega \ (\phi_I^{(1)} + \phi_D^{(1)})$$

Therefore, total dynamic pressure $p^{d(1)}$ will be:

$$\begin{aligned} p^{d(1)} &= -i\rho\omega(\phi_I^{(1)} + \phi_D^{(1)} + \sum_{j=1}^{6} \phi_j^{(1)}) \\ &= -i\rho\omega(A\phi_I^{*(1)} + A\phi_D^{*(1)} + \sum_{j=1}^{6} \eta_j^{A(1)} \phi_j^{*(1)}) \end{aligned}$$

Once the pressure is known, the force exerting on the floater body can be computed:

Wave excitation force (incident and diffracted waves) along one degree of motion:

$$\begin{aligned} F_{Di}^{(1)} &= -\iint_S P_D^{d(1)}\, n_i'\, dS \\ &= \iint_S i\rho\omega\, (\phi_I^{(1)} + \phi_D^{(1)}) e^{i\omega t}\, n_i'\, dS \\ &= \iint_S i\rho\omega (A\phi_I^{*(1)} + A\phi_D^{*(1)}) e^{i\omega t}\, n_i'\, dS \qquad i = 1 \sim 6 \end{aligned}$$

Please note that normal vector $\vec{n}$ is defined inward of fluid domain. Here we have taken a $(-\vec{n})$ to make sure the force is applied on the floater surface.

Force caused by body motion (ith component of force due to jth mode of body motion):

$$\begin{aligned} F_{Ri}^{(1)} &= -\iint_S P_j^{d(1)}\, n_i'\, dS \\ &= \iint_S i\rho\omega (\sum_{j=1}^{6} \eta_j^{A(1)} \phi_j^{*(1)}) e^{i\omega t}\, n_i'\, dS \qquad i = 1 \sim 6 \end{aligned}$$

where, $\vec{n'} = (n_1', n_2', n_3')$ and $\vec{r} \times \vec{n} = (n_4', n_5', n_6') = (y\, n_3' - z\, n_2', z\, n_1' - x\, n_3', x\, n_2' - y\, n_1')$.

We assume the radiation force is associated with the velocity and the motion as below:

$$F_{Ri}^{(1)} = \sum_{j=1}^{6} (-M_{ij}^a \ddot{\eta}_j - B_{ij}\dot{\eta}_j)$$

where, the added mass matrix M_{ij}^a and the damping matrix B_{ij} can be defined as:

$$\begin{aligned} M_{ij}^a &= -\frac{\rho}{\omega} Im[\iint_S \phi_j^{*(1)} n_i' dS] \\ B_{ij} &= -\rho \iint_S Re(\phi_j^{*(1)}) n_i dS \end{aligned}$$

The equation of motion for a single body will be:

$$[M][\ddot{\eta}_i] + [C][\eta_i] = F_{Ri} + F_{Di}$$

Substitute all the terms into this equation, we will get:

$$\sum_{j=1}^{6}[-\omega^2(M_{ij}+M_{ij}^a)+i\omega B_{ij}+C_{ij}]\frac{\eta_j^{A(1)}}{A}=\iint_S i\rho\omega(\phi_I^{*(1)}+\phi_D^{*(1)})\,n_i\,dS$$

The RAO will be solved from it.

3.6.2 Nonzero Speed

When the floater has nonzero forward speed, the process to find the pressure resulted from the incident and diffraction potential is similar to that with zero speed case. Therefore, we will only discuss the radiation potentials herein.

We can define the force resulted from the radiation pressure as below:

$$\begin{aligned}\overline{F}_{Rj}^{(1)}&=-\iint_S n_j'\overline{P}_R^{d(1)}dS=\rho\iint_S n_j'(\frac{\partial}{\partial\bar{t}}-U\frac{\partial}{\partial\bar{x}})(\sum_{k=1}^{6}\bar{\eta}_k^{A(1)}\overline{\phi}_{rel-k}^{*(1)}e^{i\omega_e\bar{t}})dS\\&=\sum_{k=1}^{6}T_{jk}\bar{\eta}_k^{A(1)}e^{i\omega_e\bar{t}}\end{aligned}\tag{3.31}$$

where, $T_{jk}=\rho\iint_S n_j'(i\omega_e-U\frac{\partial}{\partial\bar{x}})\overline{\phi}_{rel-k}^{*(1)}dS$.

In Salvesen[112], the integral regarding the derivative of the potential is converted to an integral only about the potential value. This simplification is based on the generalized Stokes Theorem. Then the expression of T_{jk} can be converted into:

$$T_{jk}=\rho i\omega_e\iint_S n_j'\overline{\phi}_{rel-k}^{*(1)}dS-U\rho\iint_S m_j\overline{\phi}_{rel-k}^{*(1)}dS\tag{3.32}$$

where, $n_j=(n_1',n_2',n_3',n_4',n_5',n_6')$, $m_j=(0,0,0,0,n_3',-n_2')$.

The added mass and damping matrix can be derived based on $\overline{F}_{Rj}^{(1)}$. The specific expressions for each T_{jk}, M_{ij}^a, B_{ij} can be found in Appendix A.

3.7 Extension to Multi-body

3.7.1 Zero Speed

In multi-body case, the analysis will be similar to single-body one. When studying the diffraction forces, all the floaters are assumed to be fixed. When studying the radiation forces, we will assume one floater under forced motion while the rest remain fixed. The process will be repeated for all floaters. This is a more vivid way of describing the linear superposition method. In such a way, we will get the added mass and damping matrix. The details will be discussed in the following sections.

For M bodies, we store panel following this way:

Body 1	Panel N_1
Body 2	Panel N_2
$\vdots$	$\vdots$
Body M	Panel N_M

If writing the equation in matrix form, we will get:

$$\left[A\right]\begin{bmatrix}\sigma_1\\ \vdots\\ \sigma_{N_1}\\ \sigma_{N_1+1}\\ \vdots\\ \sigma_{N_2+N_1}\\ \vdots\\ \sigma_{N_M+N_{M-1}+\ldots+N_1}\end{bmatrix}=\begin{bmatrix}v_1^1\\ \vdots\\ v_{N_1}^1\\ v_1^2\\ \vdots\\ v_{N_2}^2\\ \vdots\\ v_{N_M}^M\end{bmatrix}$$

where, subscript j in v_j^i stands for the panel number while i is the body number. After solving for the source strength for each panel, we can use the equation 3.29 to get potential value, then the pressure and finally the motion of the floater.

In diffraction problem, all $v_k^l = 0$. In radiation problem, when body l is under forced motion, we will have $v_k^l = i\omega n_j$, where i is the imaginary number, $j = 1, 2, ..., 6$, $k = 1, 2, ..., N_l$, otherwise, $v_k^l = 0$.

Finally, we can get added mass as:

$$A_{ij}^{\langle l \rangle} = -\frac{\rho}{\omega} Im[\int_S \phi_j^{\langle l \rangle} n_i^{\langle l \rangle} dS] \qquad for\ lth\ body$$
$$A_{ij}^{\langle n,l \rangle} = -\frac{\rho}{\omega} Im[\int_S \phi_j^{\langle l \rangle} n_i^{\langle n \rangle} dS] \qquad for\ nth\ body (n \neq l)$$

where, $A_{ij}^{\langle n,l \rangle}$ represents the radiation effect on body n from body l. The potential ϕ in above equation is solved from the radiation problem of body l.

The equations of motion for N bodies can be written as:

Body 1:

$$\sum_{j=1}^{6} \Bigg\{ \Big[-\omega^2 (M_{kj}^{\langle 1 \rangle} + A_{kj}^{\langle 1 \rangle}) + i\omega B_{kj}^{\langle 1 \rangle} + C_{kj}^{\langle 1 \rangle} \Big] \bar{\eta}_j^{\langle 1 \rangle} + \Big[-\omega^2 A_{kj}^{\langle 1,2 \rangle} + i\omega B_{kj}^{\langle 1,2 \rangle} \Big] \bar{\eta}_j^{\langle 2 \rangle} \vdots + \Big[-\omega^2 A_{kj}^{\langle 1,N \rangle} + i\omega B_{kj}^{\langle 1,N \rangle} \Big] \bar{\eta}_j^{\langle N \rangle} \Bigg\} = \bar{F}_k^{\langle 1 \rangle} e^{i\omega t}$$

Body 2:

$$\sum_{j=1}^{6} \Bigg\{ \Big[-\omega^2 (M_{kj}^{\langle 2 \rangle} + A_{kj}^{\langle 2 \rangle}) + i\omega B_{kj}^{\langle 2 \rangle} + C_{kj}^{\langle 2 \rangle} \Big] \bar{\eta}_j^{\langle 2 \rangle} + \Big[-\omega^2 A_{kj}^{\langle 2,1 \rangle} + i\omega B_{kj}^{\langle 2,1 \rangle} \Big] \bar{\eta}_j^{\langle 1 \rangle} \vdots + \Big[-\omega^2 A_{kj}^{\langle 2,N \rangle} + i\omega B_{kj}^{\langle 2,N \rangle} \Big] \bar{\eta}_j^{\langle N \rangle} \Bigg\} = \bar{F}_k^{\langle 2 \rangle} e^{i\omega t}$$

Body P:

$$\sum_{j=1}^{6}\Bigg\{\Big[-\omega^2(M_{kj}^{\langle P\rangle}+A_{kj}^{\langle P\rangle})+i\omega B_{kj}^{\langle P\rangle}+C_{kj}^{\langle P\rangle}\Big]\bar{\eta}_j^{\langle P\rangle} + \Big[-\omega^2 A_{kj}^{\langle P,1\rangle}+i\omega B_{kj}^{\langle P,1\rangle}\Big]\bar{\eta}_j^{\langle 1\rangle} \vdots + \Big[-\omega^2 A_{kj}^{\langle P,P-1\rangle}+i\omega B_{kj}^{\langle P,P-1\rangle}\Big]\bar{\eta}_j^{\langle P-1\rangle} + \Big[-\omega^2 A_{kj}^{\langle P,P+1\rangle}+i\omega B_{kj}^{\langle P,P+1\rangle}\Big]\bar{\eta}_j^{\langle P+1\rangle} \vdots + \Big[-\omega^2 A_{kj}^{\langle P,N\rangle}+i\omega B_{kj}^{\langle P,N\rangle}\Big]\bar{\eta}_j^{\langle N\rangle}\Bigg\} = \bar{F}_k^{\langle P\rangle}e^{i\omega t}$$

If writing the above equations into matrix format, we will have:

$$\underset{A}{\Big[(6\times N)\dot{(}6\times N)\Big]}\ \underset{x}{\Big[6\times N\Big]} = \underset{b}{\Big[6\times N\Big]}$$

where, $A = A_{mass} + A_{addedmass} + A_{damping} + A_{stiffness}$.

More details are listed below:

$$x = \begin{bmatrix} 6\times 1 \rightarrow body\ 1 \\ 6\times 1 \rightarrow body\ 2 \\ \vdots \\ 6\times 1 \rightarrow body\ N \end{bmatrix}$$

$$b = FKD\ force \begin{bmatrix} 6 \times 1 \rightarrow body\ 1 \\ 6 \times 1 \rightarrow body\ 2 \\ \vdots \\ 6 \times 1 \rightarrow body\ N \end{bmatrix}$$

$$A_{mass}\ or\ A_{restore} = \begin{bmatrix} body1 & & & \\ [6 \times 6] & & & \\ & body2 & & \\ & [6 \times 6] & & \\ & & \ddots & \\ & & & bodyN \\ & & & [6 \times 6] \end{bmatrix}$$

$$A_{addedmass} + A_{damping} = \begin{bmatrix} 1 \leftarrow 1 & 1 \leftarrow 2 & & 1 \leftarrow N \\ [6 \times 6] & [6 \times 6] & \cdots & [6 \times 6] \\ 2 \leftarrow 1 & 2 \leftarrow 2 & & 2 \leftarrow N \\ [6 \times 6] & [6 \times 6] & \cdots & [6 \times 6] \\ \vdots & \vdots & & \vdots \\ N \leftarrow 1 & N \leftarrow 2 & & N \leftarrow N \\ [6 \times 6] & [6 \times 6] & \cdots & [6 \times 6] \end{bmatrix}$$

In the above equation, $i \leftarrow j$ stands for the effects on degree of freedom (DOF) i from DOF j. After resolving it, the RAO of all floaters will be found.

3.7.2 Nonzero Speed

When the speed of the multiple floaters are not the same, we still want to solve the problem in the frequency domain. Noticing that $e^{i\omega_e t}$ is the time dependent factor for the single body with nonzero speed, the encounter frequency should be the same for all the bodies in the fluid domain. This is implying we need to assume the floaters are moving at the same speed along the same direction so that the problems can still be solved by a similar procedure.

The calculation of the added mass and damping for nonzero speed is similar to that for a single body case. The equation structure is similar to that for zero speed when we are solving for the RAO. Thus, we will not repeat writing out the equations for the case with nonzero speed.

3.8 Results and Discussions

This section contains the validations of our in-house program for multi-body cases. We will use a large box barge and the KVLCC as the basic cases. Single-body analysis has been performed over the two vessels. We get high consistency compared against WAMITv5. Then we have validated the side-by-side case at oblique sea condition. Below are the resulting figures.

The dimensions of the box barge and KVLCC are listed as below:

Table 3.1: Floater Particulars

(m)	Box Barge	KVLCC
L	400	320
B	60	58
T	40	30
k_{xx}	24	23.2
k_{yy}	100	80
k_{zz}	100	80

The case set-up is demonstrated as below:

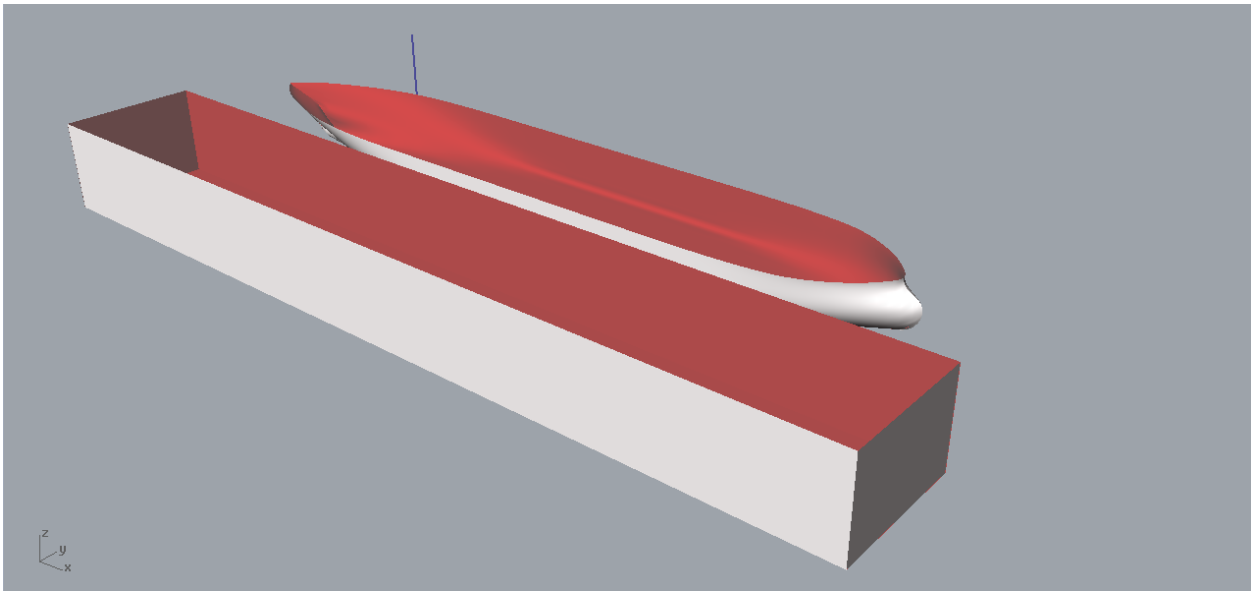

Figure 3.2: Box Barge and KVLCC Side-by-side

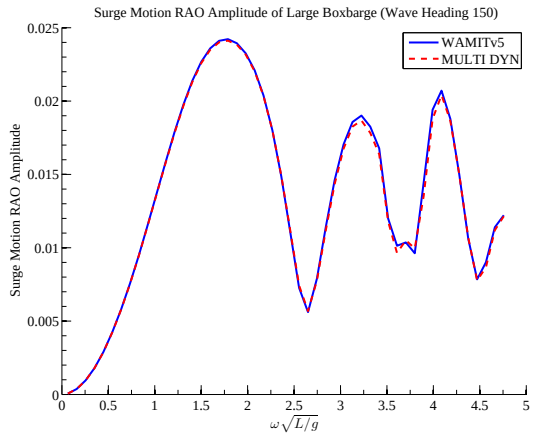

(a) Surge RAO Amplitude vs $\omega\sqrt{L/g}$

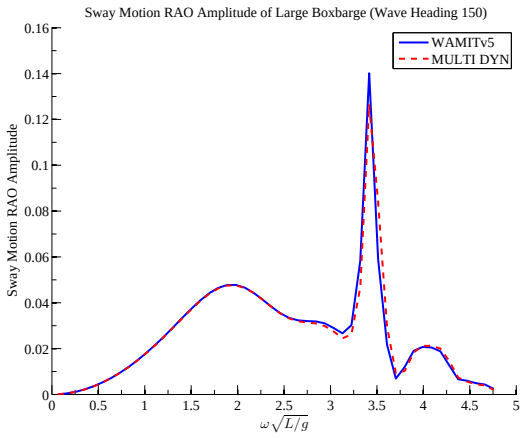

(b) Sway RAO Amplitude vs $\omega\sqrt{L/g}$

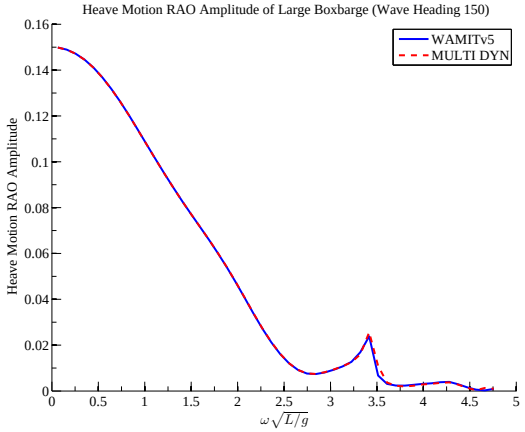

(c) Heave RAO Amplitude vs $\omega\sqrt{L/g}$

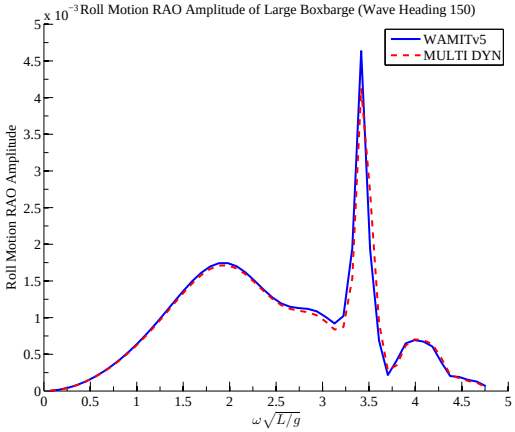

(d) Roll RAO Amplitude vs $\omega\sqrt{L/g}$

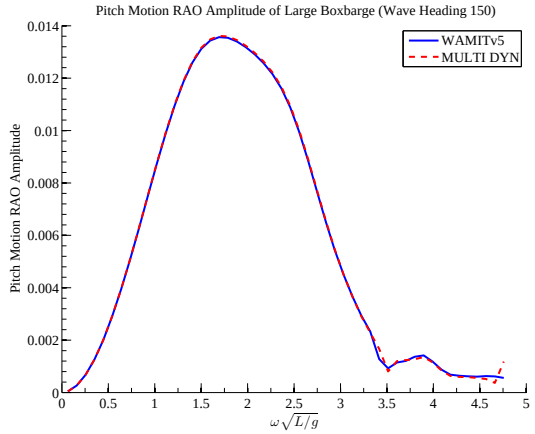

(e) Pitch RAO Amplitude vs $\omega\sqrt{L/g}$

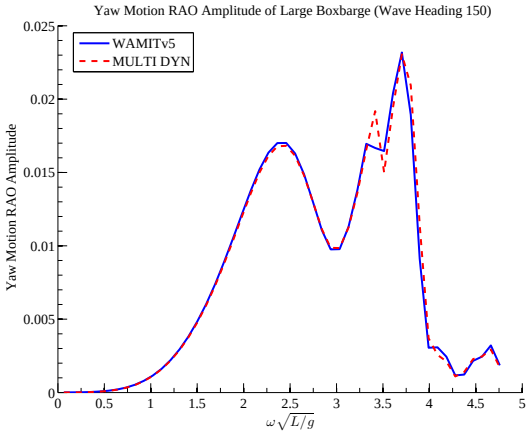

(f) Yaw RAO Amplitude vs $\omega\sqrt{L/g}$

Figure 3.3: A comparison of KVLCC-Box Barge Side-by-side Case in WAMITv5 and MDL Multi DYN: RAO amplitude of Box Barge when Wave Heading Angle = 150

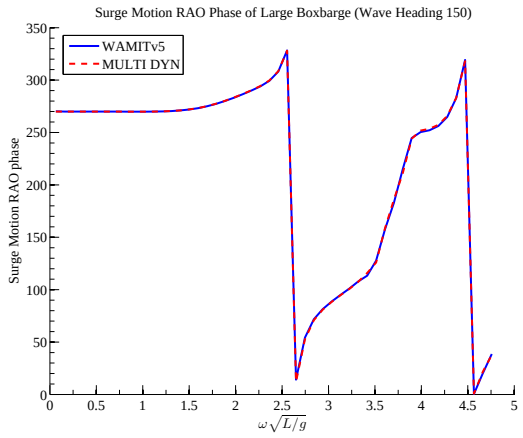

(a) Surge RAO Phase vs $\omega\sqrt{L/g}$

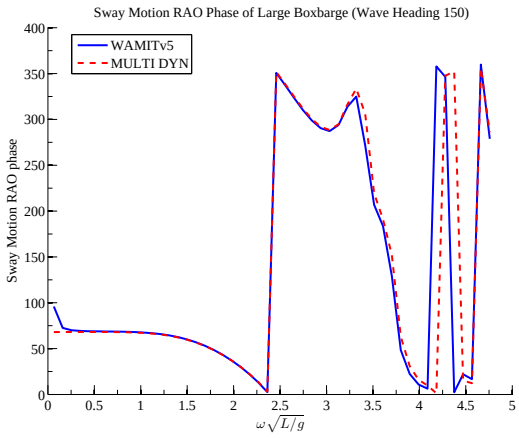

(b) Sway RAO Phase vs $\omega\sqrt{L/g}$

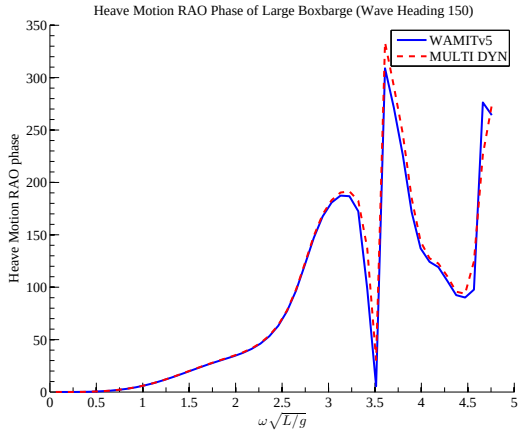

(c) Heave RAO Phase vs $\omega\sqrt{L/g}$

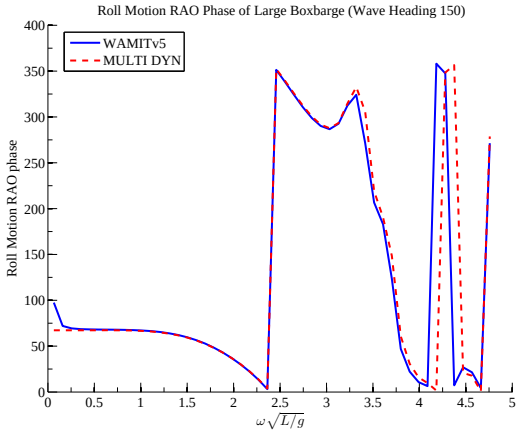

(d) Roll RAO Phase vs $\omega\sqrt{L/g}$

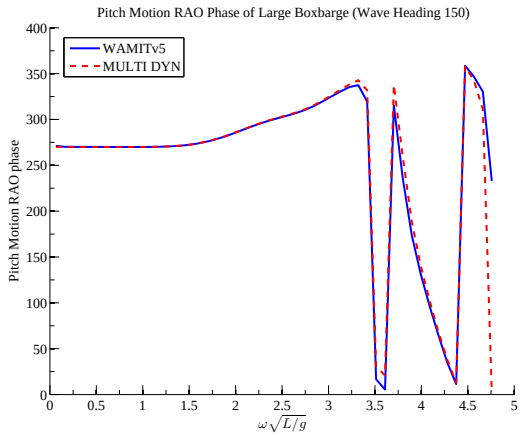

(e) Pitch RAO Phase vs $\omega\sqrt{L/g}$

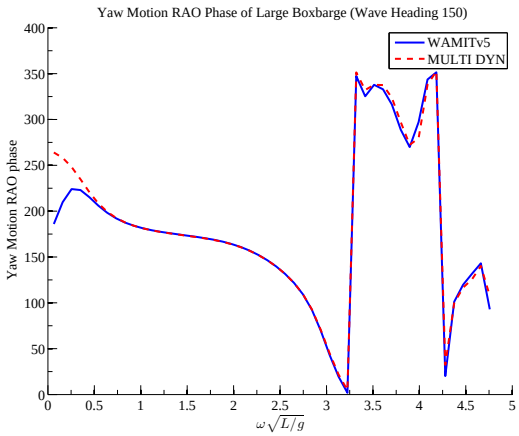

(f) Yaw RAO Phase vs $\omega\sqrt{L/g}$

Figure 3.4: A comparison of KVLCC-Box Barge Side-by-side Case in WAMITv5 and MDL Multi DYN: RAO phase of Box Barge when Wave Heading Angle = 150

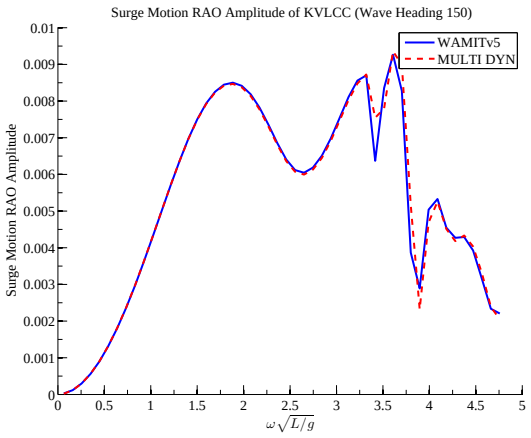

(a) Surge RAO Amplitude vs $\omega\sqrt{L/g}$

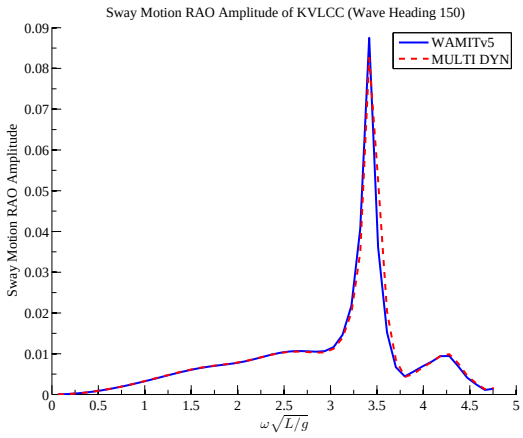

(b) Sway RAO Amplitude vs $\omega\sqrt{L/g}$

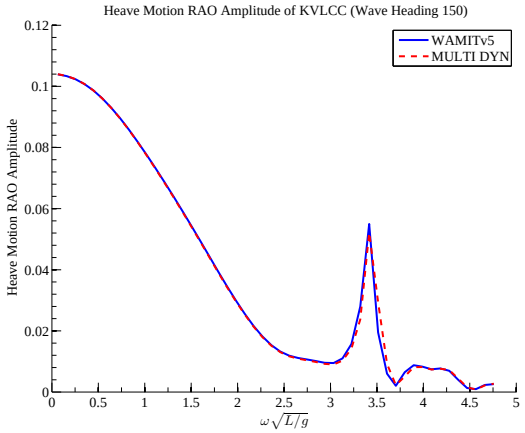

(c) Heave RAO Amplitude vs $\omega\sqrt{L/g}$

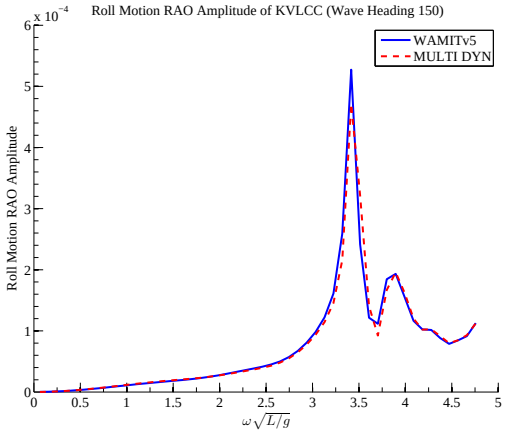

(d) Roll RAO Amplitude vs $\omega\sqrt{L/g}$

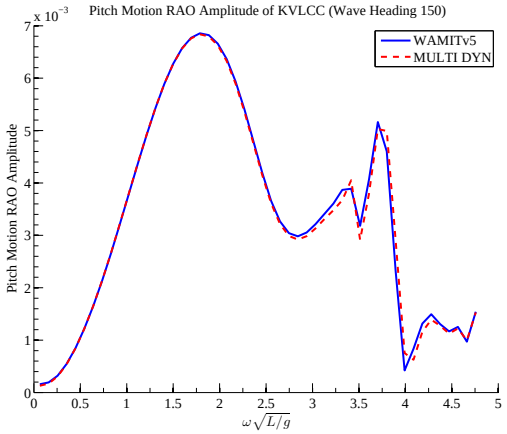

(e) Pitch RAO Amplitude vs $\omega\sqrt{L/g}$

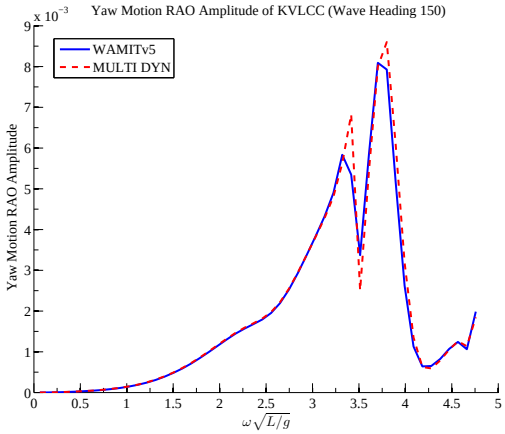

(f) Yaw RAO Amplitude vs $\omega\sqrt{L/g}$

Figure 3.5: A comparison of KVLCC-Box Barge Side-by-side Case in WAMITv5 and MDL Multi DYN: RAO amplitude of KVLCC when Wave Heading Angle = 150

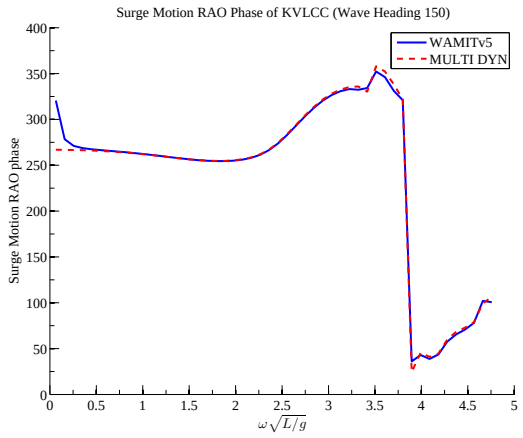

(a) Surge RAO Phase vs $\omega\sqrt{L/g}$

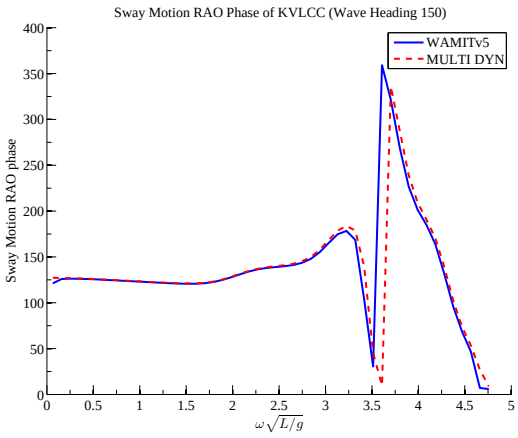

(b) Sway RAO Phase vs $\omega\sqrt{L/g}$

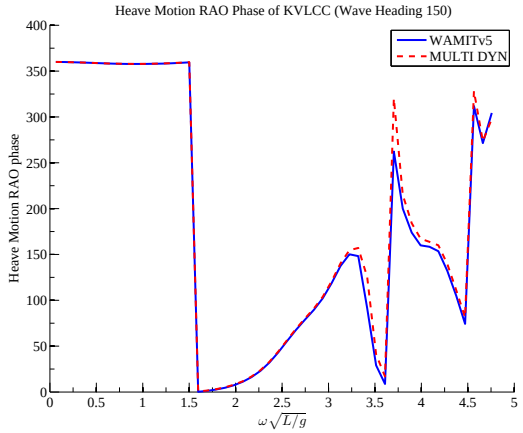

(c) Heave RAO Phase vs $\omega\sqrt{L/g}$

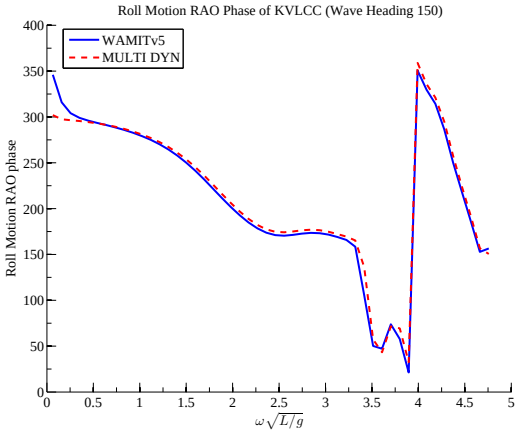

(d) Roll RAO Phase vs $\omega\sqrt{L/g}$

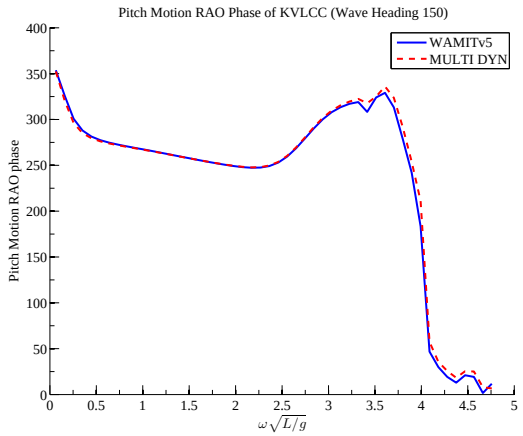

(e) Pitch RAO Phase vs $\omega\sqrt{L/g}$

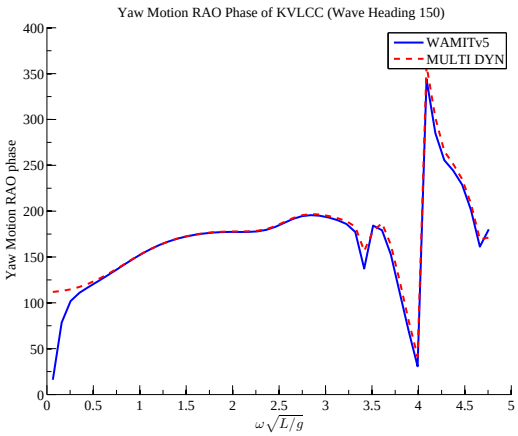

(f) Yaw RAO Phase vs $\omega\sqrt{L/g}$

Figure 3.6: A comparison of KVLCC-Box Barge Side-by-side Case in WAMITv5 and MDL Multi DYN: RAO phase of KVLCC when Wave Heading Angle = 150

As can be seen from the above figures, we have achieved very good consistency with WAMITv5. Our program has the capability to analyze multi-body cases.

If considering the forward speed effects, we also performed the simulations for one Wigley Hull and two Wigley Hulls. The one-body case is validated against MDL HydroD[113], developed by Tava[111].

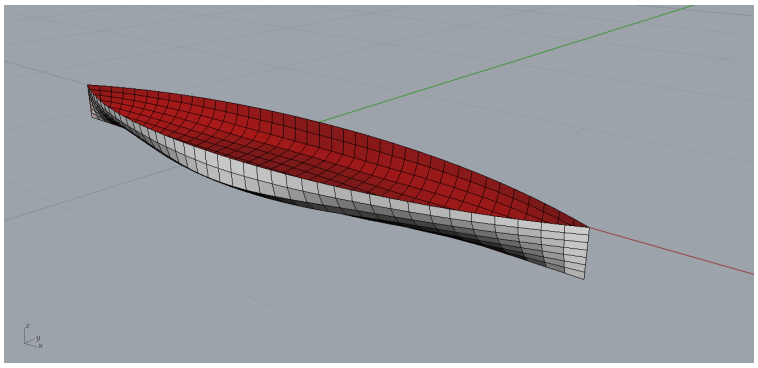

Figure 3.7: Perspective view of Wigley hull

Currently, we do not have benchmark software to compute the multi-body cases with nonzero forward speed. Herein, we will only provide the results for different forward speeds.

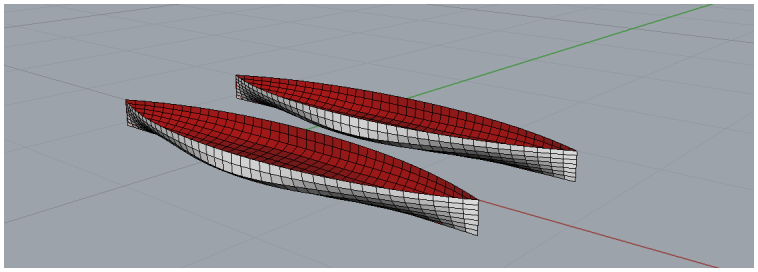

Figure 3.8: Perspective view of two Wigley hulls

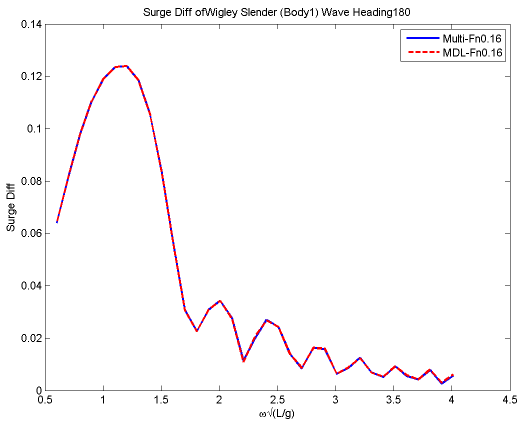

(a) Surge FKD Force vs $\omega\sqrt{L/g}$

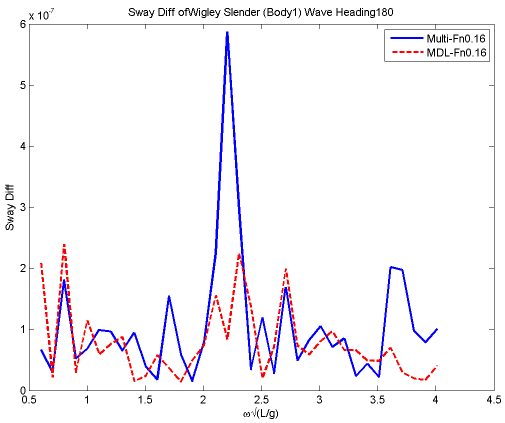

(b) Sway FKD Force vs $\omega\sqrt{L/g}$

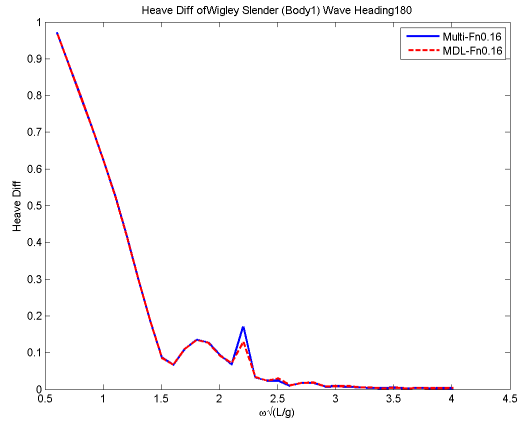

(c) Heave FKD Force vs $\omega\sqrt{L/g}$

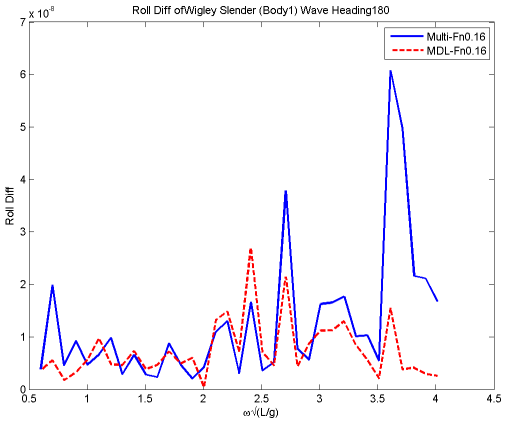

(d) Roll FKD Force vs $\omega\sqrt{L/g}$

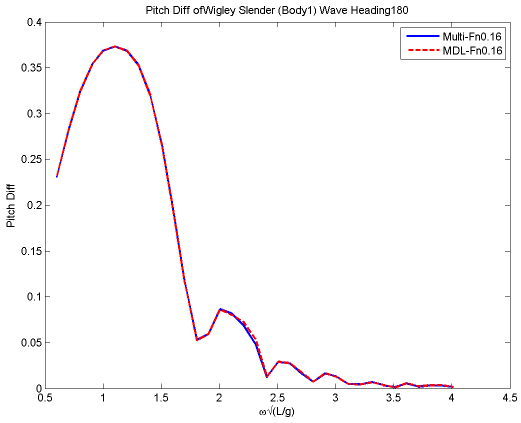

(e) Pitch FKD Force vs $\omega\sqrt{L/g}$

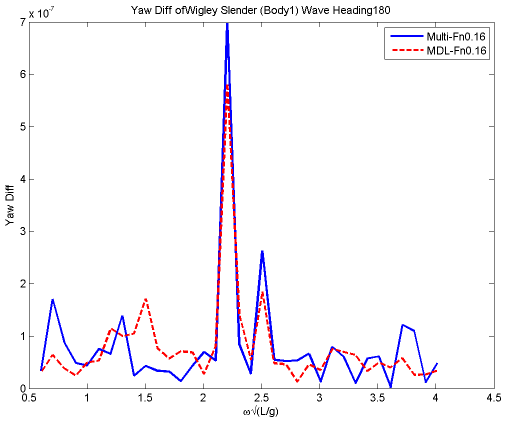

(f) Yaw FKD Force vs $\omega\sqrt{L/g}$

Figure 3.9: A comparison of a Single Wigley Hull in MDL HydroD and Multi Multi DYN: FKD Force when Wave Heading Angle = 180

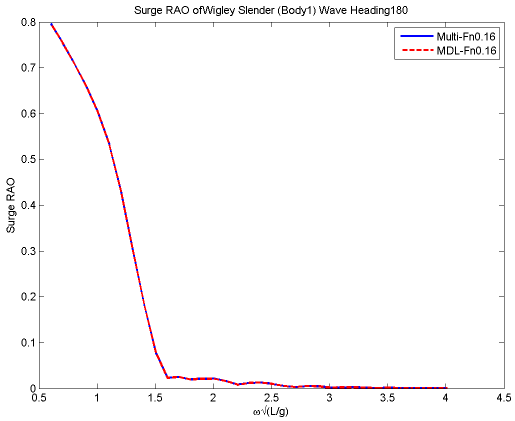

(a) Surge FKD RAO vs $\omega\sqrt{L/g}$

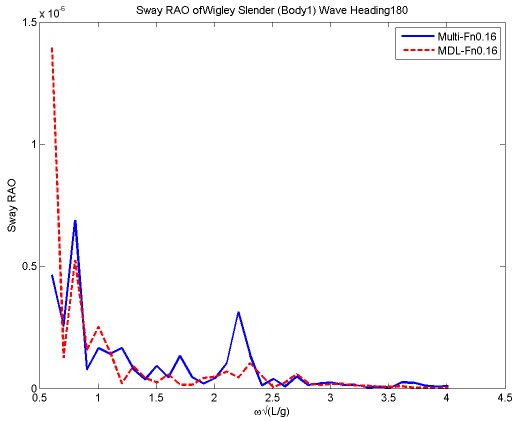

(b) Sway FKD RAO vs $\omega\sqrt{L/g}$

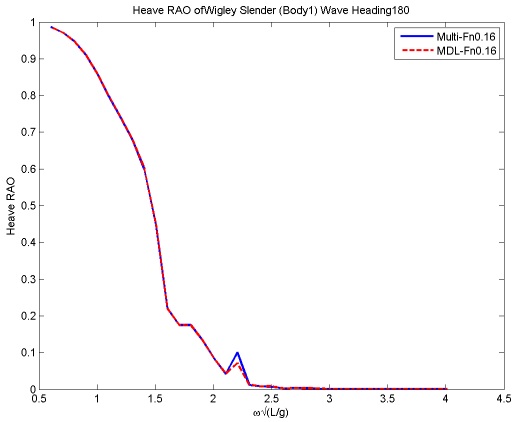

(c) Heave FKD RAO vs $\omega\sqrt{L/g}$

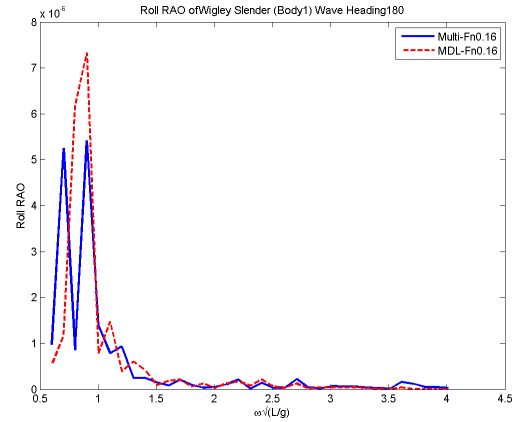

(d) Roll FKD RAO vs $\omega\sqrt{L/g}$

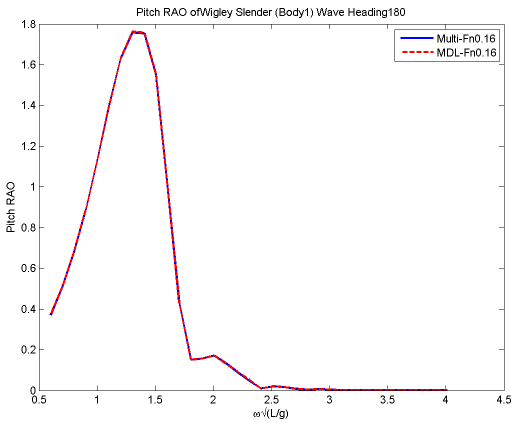

(e) Pitch FKD RAO vs $\omega\sqrt{L/g}$

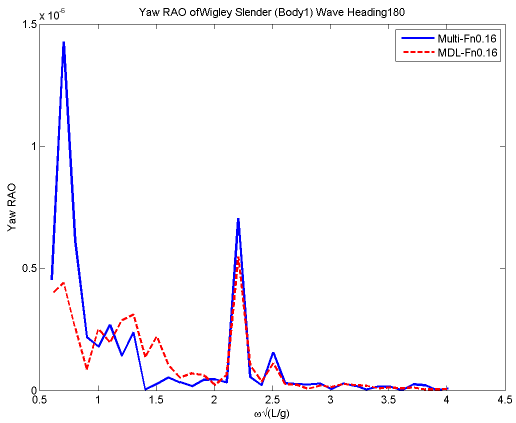

(f) Yaw FKD RAO vs $\omega\sqrt{L/g}$

Figure 3.10: A comparison of a Single Wigley Hull in MDL HydroD and Multi Multi DYN: RAO when Wave Heading Angle = 180

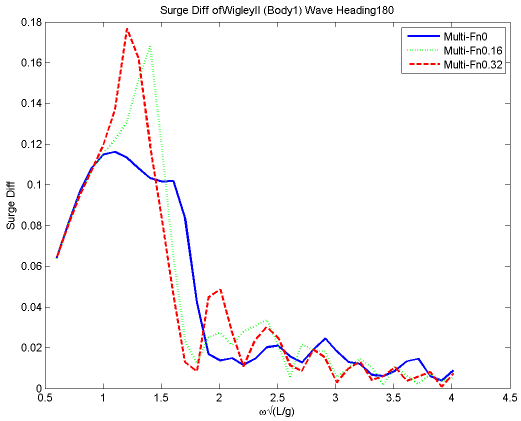

(a) Surge FKD Force vs $\omega\sqrt{L/g}$

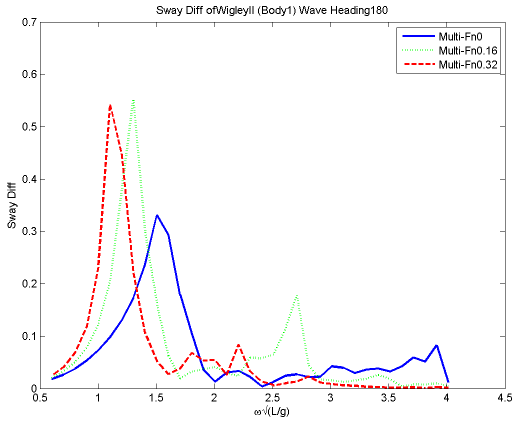

(b) Sway FKD Force vs $\omega\sqrt{L/g}$

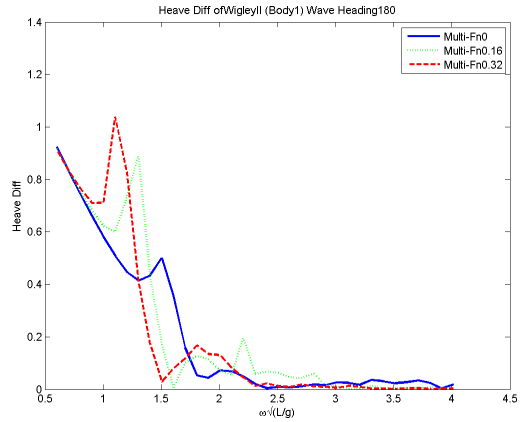

(c) Heave FKD Force vs $\omega\sqrt{L/g}$

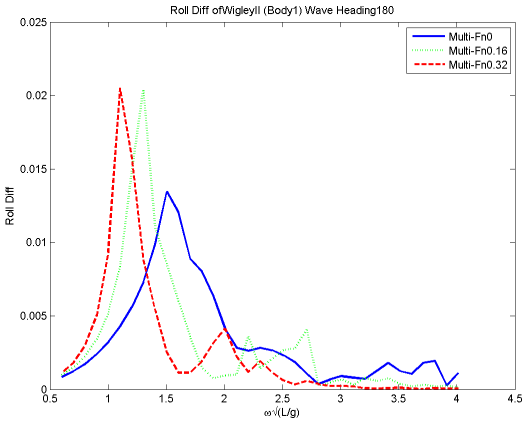

(d) Roll FKD Force vs $\omega\sqrt{L/g}$

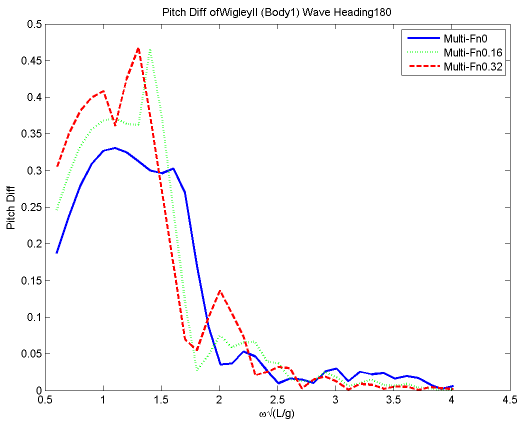

(e) Pitch FKD Force vs $\omega\sqrt{L/g}$

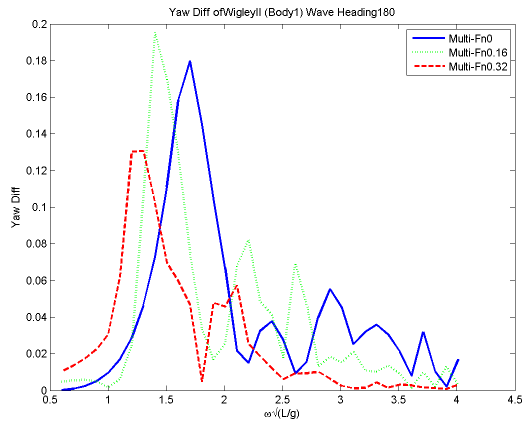

(f) Yaw FKD Force vs $\omega\sqrt{L/g}$

Figure 3.11: A comparison of Two Wigley Hulls at Different Forward Speeds: FKD Force when Wave Heading Angle = 180

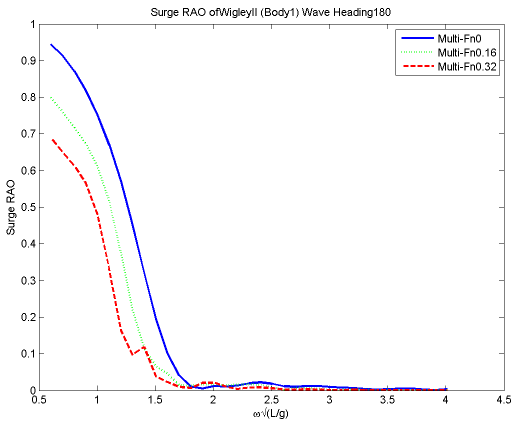

(a) Surge RAO vs $\omega\sqrt{L/g}$

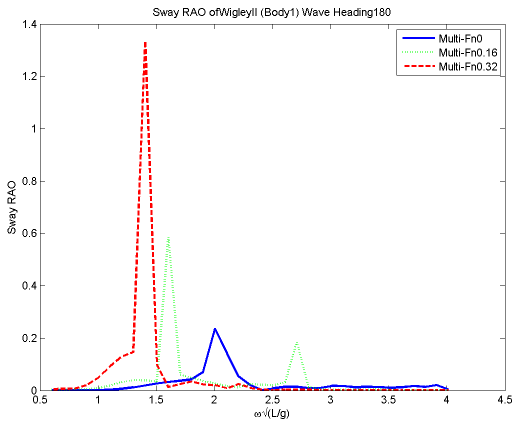

(b) Sway RAO vs $\omega\sqrt{L/g}$

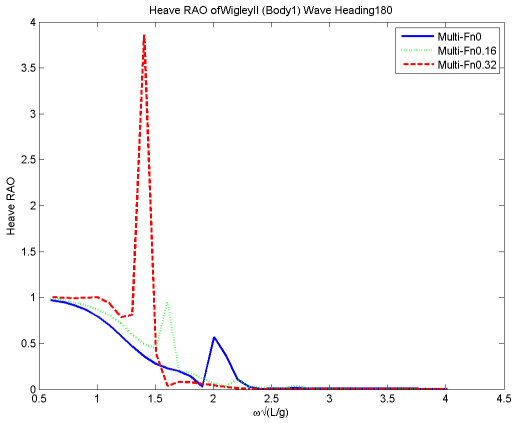

(c) Heave RAO vs $\omega\sqrt{L/g}$

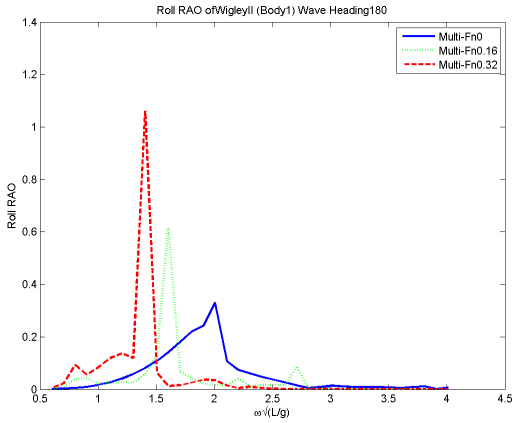

(d) Roll RAO vs $\omega\sqrt{L/g}$

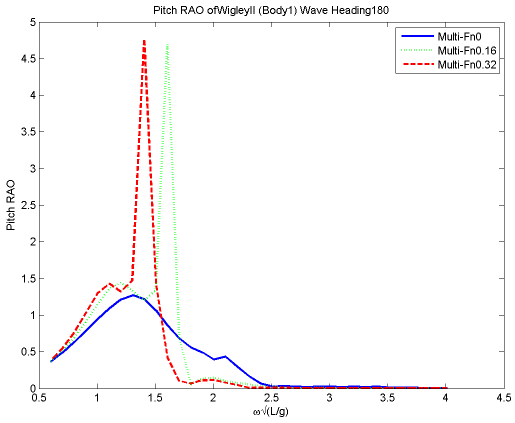

(e) Pitch RAO vs $\omega\sqrt{L/g}$

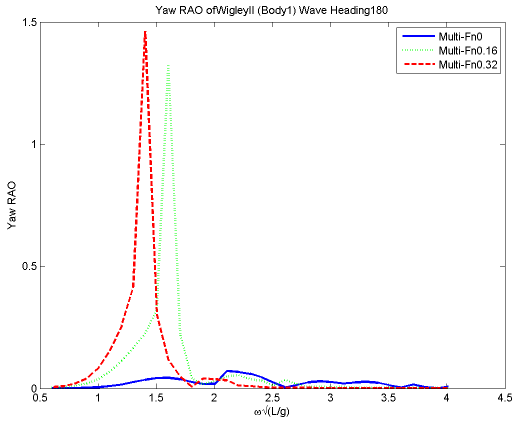

(f) Yaw RAO vs $\omega\sqrt{L/g}$

Figure 3.12: A comparison of Two Wigley Hulls at Different Forward Speeds: RAO when Wave Heading Angle = 180

4. IRREGULAR FREQUENCY REMOVAL [1]

In this chapter, we will briefly discuss the concept of the modified-integral method and discuss the extended-boundary-condition method in detail. The incomplete parts in previous literature are clarified. Based upon our study, we will adopt the extended boundary condition method in the implementation section. Since we were using a different definition of the Green function and the normal vector in our in-house program (Guha[111]). Hence, we will revisit the uniqueness proof in Kleiman[57] to demonstrate the resulting changes in the intermediate steps and the final conclusions. The discussion will enable the reader to easily view the reasons for the difference in the final expressions and implement this extended-boundary-condition method.

4.1 Mathematical Background

In studying the hydrodynamics of floating bodies, we sequentially calculate the source strength σ, the potential ϕ, the pressure p and the force F. The final output is based on the solution for the potential or source strength. To get the value of the potential from body boundary conditions, we need to solve the following equation.

$$2\pi\phi(\boldsymbol{x}) + \iint_{S_b} \phi(\boldsymbol{\xi}) \frac{\partial G(\boldsymbol{x}, \boldsymbol{\xi})}{\partial n_{\boldsymbol{\xi}}} dS_{\boldsymbol{\xi}} = \iint_{S_b} \frac{\partial \phi(\boldsymbol{\xi})}{\partial n_{\boldsymbol{\xi}}} G(\boldsymbol{x}; \boldsymbol{\xi}) dS_{\boldsymbol{\xi}}, \ \boldsymbol{x} \in S_b$$

[1]Part of the chapter is reprinted with permission from "Irregular Frequency Removal Methods: Theory and Applications in Hydrodynamics" by Yujie Liu, Jeffrey Falzarano, 2017. *Journal of Marine System and Ocean Technology*, Vol 12, Issue 2, pages 49-64. Copyright 2017 by Sociedade Brasileira de Engenharia Naval.

[1]Part of the chapter is reprinted with permission from "A method to remove irregular frequencies and log singularity evaluation in wave-body interaction problems" by Yujie Liu, Jeffrey Falzarano, 2017. *Journal of Ocean Engineering and Marine Energy*, Vol 3, Issue 2, pages 161-189. Copyright 2017 by Springer International Publishing Switzerland.

[1]Part of the chapter is reprinted with permission from "Suppression of irregular frequency in multi-body problem and free-surface singularity treatment" by Yujie Liu, Jeffrey Falzarano, 2017. *Proceedings of the ASME 2016 35th International Conference on Ocean, Offshore and Arctic Engineering*, pages 1-11. Copyright 2017 by ASME.

[1]Part of the chapter is reprinted with permission from "Suppression of Irregular Frequency Effect in Hydrodynamic Problems and Free-Surface Singularity Treatment" by Yujie Liu, Jeffrey Falzarano, 2017. *Journal of Offshore Mechanics and Arctic Engineering*, Vol.139 051101 pages 1-16. Copyright 2017 by ASME.

If converting it into a matrix form, we get:

$$[A][\phi] = [b]$$

From the theory of ordinary differential equations, we assume the matrix equation has its homogeneous form. Thus, there will be a homogeneous solution and a particular one: $\phi = \phi_h + \phi_p$. Based on the property of matrices, the following conclusion can be drawn:

a) If $det[A(\omega)] \neq 0$, $\phi_h = 0$, ϕ_p has only one solution.

b) If $det[A(\omega)] = 0$, ϕ_h has infinite solutions, ϕ_p has infinite solutions or none, depending on the value of $[b]$.

Therefore, the second case needs to be avoided and it is necessary to modify the structure of the matrix $[A]$ to become $[A^*]$. The objective is to make the $rank(A^*) = rank(\phi) = rank(A^*, b) = n$ to ensure the uniqueness of the solution. In other words, the homogeneous solution must be zero and only zero.

There are two general approaches to achieve this: One is to construct $[A^*](m \times n)$, where $m > n$, $rank(A^*) = n$, n is the number of unknowns. This method will result in a overdetermined matrix. In some cases, $[A^*]$ has the same rank with $[A]$, but a different structure.

The other is to construct a square matrix $[A^{**}](m \times m)$, where $rank(A^{**}) = m$, the number of unknowns equal to m. This method needs more unknowns and requires to extend the boundary conditions, ensuring it is still a square matrix.

4.1.1 Method I: Modified Green Function Method

The essence of this method is to find more equations which the unknowns satisfy, leading to an overdetermined system but guaranteeing a unique solution. More exactly, it is to choose some points inside the domain V_- where the unknowns still satisfy some boundary conditions. For the external potential ϕ, we have:

$$2\pi\phi(\boldsymbol{x}) = \iint_{S_b} \frac{\partial\phi(\boldsymbol{\xi})}{\partial n_{\boldsymbol{\xi}}} G(\boldsymbol{x};\boldsymbol{\xi}) dS_{\boldsymbol{\xi}} - \iint_{S_b} \phi(\boldsymbol{\xi}) \frac{\partial G(\boldsymbol{x};\boldsymbol{\xi})}{\partial n_{\boldsymbol{\xi}}} dS_{\boldsymbol{\xi}},\ \boldsymbol{x} \in S_b \tag{4.1}$$

$$0 = \iint_{S_b} \frac{\partial \phi(\boldsymbol{\xi})}{\partial n_{\boldsymbol{\xi}}} G(\boldsymbol{x};\boldsymbol{\xi}) dS_{\boldsymbol{\xi}} - \iint_{S_b} \phi(\boldsymbol{\xi}) \frac{\partial G(\boldsymbol{x};\boldsymbol{\xi})}{\partial n_{\boldsymbol{\xi}}} dS_{\boldsymbol{\xi}},\ \boldsymbol{x} \in V_- \tag{4.2}$$

If the uniqueness of the solution can be proven, then the irregular frequencies effects can be removed. The proof is similar to the procedure in Schenck[39]. Under the assumption that ϕ_x satisfies (4.1) and (4.2) and $\phi_y = \phi_x + A\phi_z$ The key equation is:

$$A \iint_{S_b} \phi_z \frac{\partial G}{\partial n_{\boldsymbol{\xi}}} = 0 \qquad \boldsymbol{x} \in V_- \tag{4.3}$$

The conclusion is that $\iint_{S_b} \phi_z \frac{\partial G}{\partial n_{\boldsymbol{\xi}}}$ is not necessarily zero for every $\boldsymbol{x} \in V_-$. Then $A = 0$, ensuring that the solution is unique. So if the chosen points are not the node points of the homogeneous solution for the Dirichlet internal potential problem. The solution will be unique. To ensure the uniqueness, a sufficiently large number of interior points must be selected.

This method will result in an overdetermined problem, which can be solved using a least square approach. However, special treatment will be needed in selecting the interior points and setting up the parameters to remove the irregular frequency effect for an arbitrary shape. To make it convenient to users, the fixed lid method is discussed by Kleinman[57], Zhu[50], Lee[59].

4.1.2 Method II: Extended Boundary Condition Method

The motivation of this method is to convert the overdetermined linear system into a square matrix. Then a direct matrix solver can be utilized. Meanwhile, the irregular frequency corresponds to the sloshing mode of the interior space. Therefore, it would be natural to place a lid on the interior free surface to suppress it. Behind this intuitive reasoning, there is a profound mathematical proof to support it. In this section we will investigate the proof to this method and discuss the difference in the resulting equations based on our choices of Green function and normal vector direction.

4.1.2.1 Jump Conditions

The expressions for the jump conditions will depend on the choice of the expressions of the Green function and the normal vector orientation. In this case, we choose the normal vector to

point outside the body into the fluid domain and the Green function is written as:

$$G = \frac{1}{r} + \frac{1}{r'} + 2f[R_0(h,v) - i\pi J_0(h)exp(v)] \tag{4.4}$$

Thus, the jump conditions equations will be:

$$\lim_{\boldsymbol{x}\to S_b^{\pm}} \int_{S_b} u(\boldsymbol{\xi}) \frac{\partial G(\boldsymbol{x};\boldsymbol{\xi})}{\partial n_{\boldsymbol{\xi}}} dS_{\boldsymbol{\xi}} = \pm u(\boldsymbol{x}) + \int_{S_b} u(\boldsymbol{\xi}) \frac{\partial G(\boldsymbol{x};\boldsymbol{\xi})}{\partial n_{\boldsymbol{\xi}}} \tag{4.5}$$

$$\lim_{\boldsymbol{x}\to S_b^{\pm}} \frac{\partial}{\partial n_{\boldsymbol{x}}} \int_{S_b} u(\boldsymbol{\xi}) G(\boldsymbol{x};\boldsymbol{\xi}) dS_{\boldsymbol{\xi}} = \mp u(\boldsymbol{x}) + \int_{S_b} u(\boldsymbol{\xi}) \frac{\partial G(\boldsymbol{x};\boldsymbol{\xi})}{\partial n_{\boldsymbol{x}}} \tag{4.6}$$

The expressions here will have a sign difference compared with those in Kleinman[57], due to the normal vector definition. Jump conditions are the key to complete the proof. The expression of the jump condition will affect the rest of the equations in all the theorems in Kleinman[57].

4.1.2.2 Kleinman's Logic Flow

The notation rules in this paper are different from that in Kleinman[57]. It will be necessary to let the readers know the corresponding changes in the equations. In this section, we will briefly review the logic flow of Kleinman's proof and discuss about the theorems in our choices of settings.

Kleinman[57] first defined the two operators used in the integral on body boundary S_b.

$$Kv = \int_{S_b} v(\boldsymbol{\xi}) \frac{\partial G(\boldsymbol{x};\boldsymbol{\xi})}{\partial n_{\boldsymbol{x}}} dS_{\boldsymbol{\xi}} \qquad for \qquad \boldsymbol{x} \in S_b \tag{4.7}$$

$$\bar{K}^* v = \int_{S_b} v(\boldsymbol{\xi}) \frac{\partial G(\boldsymbol{x};\boldsymbol{\xi})}{\partial n_{\boldsymbol{\xi}}} dS_{\boldsymbol{\xi}} \qquad for \qquad \boldsymbol{x} \in S_b \tag{4.8}$$

The adjoint problem is defined based on the interior potential ϕ_i. The governing equations are

as below:

$$\nabla^2\phi_i = 0 \qquad in\ V_- \tag{4.9}$$

$$-\omega^2\phi_i + g\frac{\partial\phi_i}{\partial z} = 0 \qquad on\ S_f \tag{4.10}$$

$$\phi_i = f \qquad on\ S_b \tag{4.11}$$

When $f = 0$ and if there exists a nontrivial solution of ϕ_i, the corresponding wave number k will be called the eigenvalues of the adjoint floating body problem.

To this step, we will start the discussion on the functionality of Kleinman's theorems. The first four theorems establish the property of eigenvalues of the adjoint problem and relate the characteristic values of operator K and $\bar{K}^*$. The rest of the theorems investigate the conditions to ensure unique solutions and prove the uniqueness is still ensured after the equations are assembled to form a square matrix.

Theorem 1: The eigenvalues of the adjoint floating body problem are real.

Theorem 2: k is the eigenvalue of adjoint problem $\Rightarrow$ k is the characteristic value of $-K$

Theorem 3: k is the characteristic value of $-K \Rightarrow$ k is the eigenvalue of adjoint problem.

Theorem 4: k is the characteristic value of $-\bar{K}^* \Rightarrow$ k is the eigenvalue of adjoint problem $\Rightarrow$ k is the characteristic value of $-K$.

Theorem 5: If ϕ is continuous and bounded on S_b and

$$\int_{S_b} \phi\frac{\partial G(\boldsymbol{x};\boldsymbol{\xi})}{\partial n_{\boldsymbol{\xi}}} dS_{\boldsymbol{\xi}} = 0 \qquad for\ \boldsymbol{x} \in V_- \cup S_i$$

then $\phi = 0$ on S_b.

Theorem 6: If ϕ is continuous and bounded on S_b and

$$-2\pi\phi(\boldsymbol{x}) + \int_{S_b} \phi(\boldsymbol{\xi}) \frac{\partial G(\boldsymbol{x};\boldsymbol{\xi})}{\partial n_{\boldsymbol{\xi}}} dS_{\boldsymbol{\xi}} = 0 \qquad for\ \boldsymbol{x} \in S_b \tag{4.12}$$

$$\int_{S_b} \phi(\boldsymbol{\xi}) \frac{\partial G(\boldsymbol{x};\boldsymbol{\xi})}{\partial n_{\boldsymbol{\xi}}} dS_{\boldsymbol{\xi}} = 0 \qquad for\ \boldsymbol{x} \in S_i \tag{4.13}$$

then $\phi = 0$ for $\boldsymbol{x} \in S_b \cup S_i$.

Theorem 7: If ϕ_i is continuous and bounded on S_i and

$$-4\pi\phi_i(\boldsymbol{x}) + \int_{S_i} \phi_i(\boldsymbol{\xi}) \frac{\partial G(\boldsymbol{x};\boldsymbol{\xi})}{\partial n_{\boldsymbol{\xi}}} dS_{\boldsymbol{\xi}} = 0 \qquad for\ \boldsymbol{x} \in S_i \tag{4.14}$$

then $\phi_i = 0$ for $\boldsymbol{x} \in S_i$.

If Theorem 7 holds, when we move the field point onto the body surface S_b, we will naturally have:

$$\int_{S_i} \phi_i(\boldsymbol{\xi}) \frac{\partial G(\boldsymbol{x};\boldsymbol{\xi})}{\partial n_{\xi}} dS_{\boldsymbol{\xi}} = 0 \qquad for\ \boldsymbol{x} \in S_b \tag{4.15}$$

To this step, if we add (4.12) with (4.15) and (4.13) with (4.14), the above four equations can assemble a equation set with unknowns to be ϕ, ϕ_i. The equation set is indeed a square matrix. However, one question will come up: after the summation, can we still ensure the original four equations are still satisfied?

In general, when we have $a + b = 0$ and $c + d = 0$, it is natural to get $a + b + c + d = 0$. However, if we only have $a + b + c + d = 0$, we usually cannot get $a + b = 0$ and $c + d = 0$. The uniqueness still remains to be proved. That is the reason why Kleinman[57] proposed the Theorem 8, which is stated below:

Theorem 8: If ϕ and ϕ_i is piecewise continuous on $S_b \cup S_i$ and

$$-2\pi\phi(\boldsymbol{x}) + PV\int_{S_b}\phi(\boldsymbol{\xi})\frac{\partial G(\boldsymbol{x};\boldsymbol{\xi})}{\partial n_{\boldsymbol{\xi}}}dS_{\boldsymbol{\xi}} + \int_{S_i}\phi_i(\boldsymbol{\xi})\frac{\partial G(\boldsymbol{x};\boldsymbol{\xi})}{\partial n_{\xi}}dS_{\boldsymbol{\xi}} = 0 \qquad for\ \boldsymbol{x} \in S_b \quad (4.16)$$

$$-4\pi\phi_i(\boldsymbol{x}) + PV\int_{S_i}\phi_i(\boldsymbol{\xi})\frac{\partial G(\boldsymbol{x};\boldsymbol{\xi})}{\partial n_{\boldsymbol{\xi}}}dS_{\boldsymbol{\xi}} + \int_{S_b}\phi(\boldsymbol{\xi})\frac{\partial G(\boldsymbol{x};\boldsymbol{\xi})}{\partial n_{\boldsymbol{\xi}}}dS_{\boldsymbol{\xi}} = 0 \qquad for\ \boldsymbol{x} \in S_i \quad (4.17)$$

The sign difference herein compared with Kleinman[57] results from the definition of the normal vector. When Kleinman[57] added the four equations together, there seems a typo in the cited equation number but the correct equation was added.

To conclude, we introduce a colorful figure for Theorem 8.

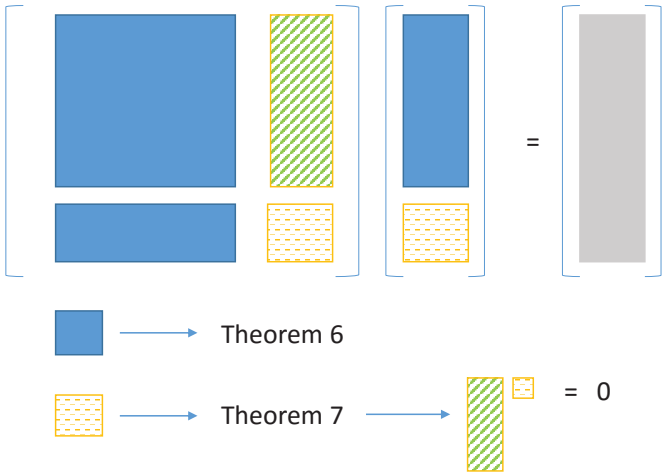

Figure 4.1: The Matrix in Theorem 8

Theorem 6 establishes the overdetermined system indicated by the blue part. The solution for the homogeneous problem is trivial. Theorem 7 established the yellow part, again with trivial solution. When Theorem 7 holds, the product of the green part with the yellow part should equal 0. Thus the four equations make up the whole matrix, which still ensure the uniqueness.

The previous equation is based on the potential formulation. When considering the source formula, we need to solve this equation:

$$4\pi\frac{\partial\phi(\boldsymbol{x})}{\partial n_{\boldsymbol{x}}} = -2\pi\sigma(\boldsymbol{x}) + \int_{S_b}\sigma(\boldsymbol{\xi})\frac{\partial G(\boldsymbol{x};\boldsymbol{\xi})}{\partial n_{\boldsymbol{x}}}dS_{\boldsymbol{\xi}} \qquad for\ \boldsymbol{x}\ \in S_b^+ \tag{4.18}$$

The kernel of the above equation is the transpose of that in equation (4.12). Therefore, to ensure the uniqueness of the source formula, we can construct similar equations as:

$$\begin{aligned}
4\pi\frac{\partial\phi(\boldsymbol{x})}{\partial n_{\boldsymbol{x}}} =& -2\pi\sigma(\boldsymbol{x}) + PV\iint_{S_b}\sigma(\boldsymbol{\xi})\frac{\partial G(\boldsymbol{x};\boldsymbol{\xi})}{\partial n_{\boldsymbol{x}}}dS_{\boldsymbol{\xi}} + \iint_{S_i}\sigma'(\boldsymbol{\xi})\frac{\partial G(\boldsymbol{x};\boldsymbol{\xi})}{\partial n_{\boldsymbol{x}}}dS_{\boldsymbol{\xi}}, \qquad \boldsymbol{x}\in S_b \\
4\pi\frac{\partial\phi_-(\boldsymbol{x})}{\partial n_{\boldsymbol{x}}} =& -4\pi\sigma'(\boldsymbol{x}) + \iint_{S_b}\sigma(\boldsymbol{\xi})\frac{\partial G(\boldsymbol{x};\boldsymbol{\xi})}{\partial n_{\boldsymbol{x}}}dS_{\boldsymbol{\xi}} + PV\iint_{S_i}\sigma'(\boldsymbol{\xi})\frac{\partial G(\boldsymbol{x};\boldsymbol{\xi})}{\partial n_{\boldsymbol{x}}}dS_{\boldsymbol{\xi}}, \qquad \boldsymbol{x}\in S_i
\end{aligned} \tag{4.19}$$

4.1.2.3 Implementation of the Extended Boundary Method

In the previous section, we have discussed the logic flow in Kleinman[57]. This section is specially to discuss the steps required to implement this method.

First, the readers might want to decide upon the definition of the normal vector of the domain and choose one form of the Green function. Afterwards, the jump conditions need to be calculated.

Second, the readers need to formulate the integral equations in Theorems 5, 6, 7, 8 discussed in the previous sections. Theorem 8 provides the final equation required to remove the irregular frequencies.

Third, if using source formula, the user may need to choose equation (4.19) or the following equations, which are discussed in the appendix.

$$
\begin{aligned}
4\pi\frac{\partial\phi(\boldsymbol{x})}{\partial n_{\boldsymbol{x}}} =& -2\pi\sigma(\boldsymbol{x}) + PV\iint_{S_b}\sigma(\boldsymbol{\xi})\frac{\partial G(\boldsymbol{x};\boldsymbol{\xi})}{\partial n_{\boldsymbol{x}}}dS_{\boldsymbol{\xi}} + \iint_{S_i}\sigma'(\boldsymbol{\xi})\frac{\partial G(\boldsymbol{x};\boldsymbol{\xi})}{\partial n_{\boldsymbol{x}}}dS_{\boldsymbol{\xi}} \\
=& 4\pi V_n, \qquad \boldsymbol{x}\in S_b \\
4\pi\frac{\partial\phi_-(\boldsymbol{x})}{\partial n_{\boldsymbol{x}}} =& -4\pi\sigma'(\boldsymbol{x}) + \iint_{S_b}\sigma(\boldsymbol{\xi})\frac{\partial G(\boldsymbol{x};\boldsymbol{\xi})}{\partial n_{\boldsymbol{x}}}dS_{\boldsymbol{\xi}} - PV\iint_{S_i}\sigma'(\boldsymbol{\xi})\frac{\partial G(\boldsymbol{x};\boldsymbol{\xi})}{\partial n_{\boldsymbol{x}}}dS_{\boldsymbol{\xi}} \\
=& 0, \qquad \boldsymbol{x}\in S_i
\end{aligned}
$$

4.1.2.4 Supplement for the Uniqueness Proof

This section will discuss the choice of radiation condition in the uniqueness proof. In Kleinman[57], the author proposed a uniqueness theorem and proved it. This theorem serves as the key part in Theorem 3, 4, 5, 7. However, the reasoning process for one step in Kleinman[57] is not sufficiently understandable, due to the radiation condition he adopted.

The logic flow is described herein. When arriving at this step, Kleinman[57] got the equation:

$$
\begin{aligned}
Im\ k\int_{S_f}|\phi|^2dS + \frac{1}{Re\ k_o}\int_{S_c}\big[(Rek_o)^2|\phi|^2 + (Im\ k_oRe\ \phi + Re\ \frac{\partial\phi}{\partial\rho})^2 + (Im\ k_o\ Im\ \phi \\
+Im\ \frac{\partial\phi}{\partial\rho})^2\big]dS = o(1) \qquad (4.20)
\end{aligned}
$$

Afterwards, he assumed each term should be of order o(1). For the integral on the free surface:

$$
Im\ k\int_{S_f}|\phi|^2dS = o(1) \qquad (4.21)
$$

He assumed the free surface S_f is independent of the radius R of the control surface S_c. Thus he gets:

$$
Im\ k\int_{S_f}|\phi|^2dS = 0 \qquad (4.22)
$$

However, for example, when $a^2+b^2+c^2 = o(1)$, we can only deduce that at least one term is of

o(1). Meanwhile, the free surface S_f is actually bounded by the control surface S_c to form a closed domain for the partial differential equations. This is the insufficiently detailed reasoning part in Kleinman[57].

The problem can be solved if we implement the Sommerfeld radiation condition in deriving equation (4.20):

$$\lim_{R\to\infty} R(\frac{\partial\phi}{\partial R} - ik\phi) = 0 \tag{4.23}$$

In this case, the RHS of (4.20) will be 0. If following similar derivation process, we can obtain the same conclusion as Kleinman[57].

4.2 Evaluation of Green Function for Free Surface Panels

For both the potential formula and the source formula, the derivative of the Green function needs to be evaluated at the free surface. Based on Newman[11] and Noblesse[9], the expressions for the Green function both contain a log term, which will result in a singular value when the field point is infinitesimally close to the source point and both are near the free surface.

Newman:

$$\begin{aligned} G(\boldsymbol{x};\boldsymbol{\xi}) =& \frac{1}{r} + \frac{1}{r'} - 2ke^k(z+\zeta)[log(r' + |z+\zeta|) + (\gamma - log2) + r'] \\ &+ O(r'^2 log r') \end{aligned} \tag{4.24}$$

where, $\boldsymbol{x}$ is the position of field point and $\boldsymbol{\xi}$ the source point. $r^2 = (x-\xi)^2 + (y-\eta)^2 + (z-\zeta)^2$, $r'^2 = (x-\xi)^2 + (y-\eta)^2 + (z+\zeta)^2$, $\gamma = 0.577...$ is the Euler constant.

Noblesse:

$$4\pi G = -(\frac{1}{r} + \frac{1}{r'}) - 2f^*[R_0(h,v) + i\pi J_0(h)exp(v)] \tag{4.25}$$

where, $f^* = \omega^2 L/g$, $\rho = [(x-\xi)^2 + (y-\eta)^2]^{\frac{1}{2}}$, $r = [\rho^2 + (z-\zeta)^2]^{\frac{1}{2}}$, $r' = [\rho^2 + (z+\zeta)^2]^{\frac{1}{2}}$,

$h = f^*\rho,\ v = f^*(z+\zeta),\ J_0$ is Bessel function of the first kind at order 0, R_0 is the function defined in Telste and Noblesse[10]. In the limiting case when $d \to 0$, $R_0 = -ln(d-v) + ln(2) - \gamma$ with error $O(d\, ln(d))$.

In our calculation, this form is used:

$$G = \frac{1}{r} + \frac{1}{r'} + 2f^*[R_0(h,v) - i\pi J_0(h)exp(v)] \tag{4.26}$$

When the field point and the image source point become infinitesimally close, the log term inside both Green functions will become singular. However, the integral value of the log term across the panel is still finite, and depends on the panel size. Based on the numerical evaluation in the next section, it is necessary to consider the log singular effect.

The Green function will have different behaviors when the field point is infinitesimally close to the source point and both are located at the internal free surface. The relations are as below:

$$\frac{\partial G}{\partial z} = kG, \qquad when\ z = 0, \zeta = 0, \boldsymbol{x} \not\to \boldsymbol{\xi}\ or\ \boldsymbol{x} \to \boldsymbol{\xi}, \tag{4.27}$$

$$\frac{\partial G}{\partial z} = kG, \qquad when\ z \to 0^-, \zeta = 0, \boldsymbol{x} \not\to \boldsymbol{\xi} \tag{4.28}$$

$$\frac{\partial G}{\partial z} = -\frac{2z}{r^3} + kG, \qquad when\ z \to 0^-, \zeta = 0, \boldsymbol{x} \to \boldsymbol{\xi} \tag{4.29}$$

$$\frac{\partial G}{\partial \zeta} = kG, \qquad when\ z \to 0^-, \zeta = 0, \boldsymbol{x} \to \boldsymbol{\xi} \tag{4.30}$$

In the constant panel method, each panel has a uniform source distribution. All the internal lid panels are exactly on the z = 0 surface while the field points are inside the floater body. Thus, equations (4.28) and (4.29) are better descriptions of the practical model.

In calculating the panel effect on itself, the integral of $-2z/r^3$ will result in 4π. Also please note

that the above four equations are derived based on Noblesse's Green function, i.e. equation (4.26). The Green function (4.26) is different from (4.25) because the choice of $exp(i\omega t)$ or $exp(-i\omega t)$ in the derivation.

4.3 Evaluation of Log Singularity

When the source points are close to field points, we will have a natural log singularity in the Green function. This is occurring when considering the internal free surface panels. The log term can be written as:

$$f = \ln(d - v) \tag{4.31}$$

where $d = \sqrt{(x-\xi)^2 + (y-\eta)^2 + (z+\zeta)^2}$, $v = z + \zeta$.

To evaluate the integral, there are generally two types of approaches. The first one is to calculate the integral directly, called the Direct Approach herein. The other is to calculate the integral about $\ln(d)$, which is the source of the singularity, referred to as the $\ln(d)$ Approach.

4.3.1 Direct Calculation

4.3.1.1 Approach I

Newman[60] adopted the direct approach. He noticed that this function satisfies Laplace equation and constructed a closed surface. The integral across the panel surface plus the integral on the remaining surfaces must be zero. In this way, if we can evaluate the integral across the remaining surfaces, we will naturally get the integral across the panel surface.

More specifically, Newman used the panel surface and the field point to form a pyramid and convert the bottom surface integral into that along the four triangular facets.The derivation herein is based on the panel coordinates and the final results are different from Newman's. The function

f is harmonic in the pyramid region. Green's 2nd identity can be used, then we can get:

$$\int_S (\zeta \nabla f - f \nabla \zeta) \cdot \boldsymbol{n} \; dS + \int_{\sum_{i=1}^{4} T_i} (\zeta \nabla f - f \nabla \zeta) \cdot \boldsymbol{n} \; dS = 0$$

$$L + \sum_{i=1}^{4} L_i = 0$$

On this bottom panel, $\zeta = 0$, $\frac{\partial}{\partial \boldsymbol{n}} = \frac{\partial}{\partial z}$, then

$$L = -\int_S f \; d\xi d\eta$$

$$L_i = \int_{T_i} (\zeta \nabla f - f \nabla \zeta) \cdot \boldsymbol{n} \; dS$$

If the field point is at a finite distance from the panel, ζ in L_i is not zero. However, the log term will become a singularity only if the field point is infinitesimally close to the panel, which makes it necessary to evaluate the log integral in an alternative way. Thus, in this case, we need to assume $\zeta \to 0$ even on the triangular facets. Thus we will have:

$$L_i = \int_{T_i} f \; dS \tag{4.32}$$

Please note that on the triangular surface, the approximate normal vector $\boldsymbol{n}$ is pointing along negative z-axis, i.e. $\frac{\partial}{\partial \boldsymbol{n}} = -\frac{\partial}{\partial z}$ From the above, we need to integrate f along the triangular surface. It will be convenient to complete it in the polar coordinate on the triangular surface. Thus, the coordinate is described in the following way.

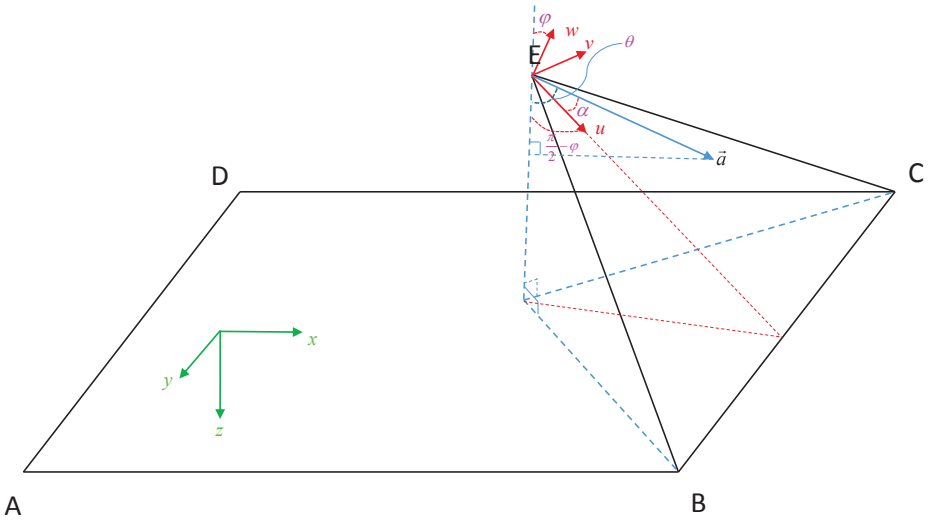

Figure 4.2: Coordinate Setting for Log Singularity

We are more interested in the internal free surface panels. To have a better view of these angles, the panel is flipped over. That is the reason why z-axis is pointing downward.

Assume O-uvw is the Cartesian coordinate on the triangular surface. The w-axis is perpendicular to the surface BCE. We determine u such that u will point to the edge $\overline{BC}$ and the surface u-O-w is perpendicular to the edge $\overline{BC}$. This has ensured that the u-axis is perpendicular to edge $\overline{BC}$ and v-axis is, therefore, determined. The angle between the w-axis and negative z-axis is defined as φ. For an arbitrary vector $\boldsymbol{a}$ on the surface BCE, α is the angle between the vector $\boldsymbol{a}$ and the u axis and θ is the angle between the vector $\boldsymbol{a}$ and the positive z-axis. Naturally, the u-axis becomes the reference axis when converting to the polar coordinate on the surface BCE. In the O-uvw coordinate system, we define B (u_1, v_1), C(u_2, v_2). The line equation can be $Au + Bv = 1$. If in polar coordinate and $u = \rho\cos\alpha$, $v = \rho\sin\alpha$, it is easy to get:

$$\rho(\alpha) = \frac{1}{A\cos\alpha + B\sin\alpha} = \frac{1}{C\cos\beta}$$

where, $C = \sqrt{A^2 + B^2}$, $\beta = \alpha - \delta$, $\delta = \arctan(\frac{B}{A})$. After solving for the following two equations:

$$Au_1 + Bv_1 = 1$$

$$Au_2 + Bv_2 = 1$$

Solve for A, B as:

$$\begin{aligned} A &= \frac{v_2 - v_1}{u_1 v_2 - u_2 v_1} \\ B &= \frac{u_1 - u_2}{u_1 v_2 - u_2 v_1} \end{aligned} \tag{4.33}$$

Based on the geometric relation, we have $\cos\theta = \cos(\frac{\pi}{2} - \varphi)\cos\alpha = \sin\varphi\cos\alpha$.In the discussion below, to distinguish the source point on the quadrilateral panel and those on the triangular facet. We will use r on the triangular surface and d on the quadrilateral.

Therefore, on the triangular surface, this equation can be transformed to:

$$f = \ln[r(1 - \frac{v}{r})] = \ln[r(1 + \cos\alpha\sin\varphi)] \tag{4.34}$$

Then the integral equation will become:

$$\int_{\alpha_1}^{\alpha_2} d\alpha \int_0^{r(\alpha)} \ln[r(1 + \cos\alpha\sin\varphi)] r dr \tag{4.35}$$

If enforcing the assumption that $\zeta \to 0$. Thus, $\varphi \to 0$, $\sin\varphi \approx \varphi$, $\cos\varphi \approx 1$. The final result will be:

$$\begin{aligned} \int_{T_i} f \, dS &= \int_{\alpha_1}^{\alpha_2} d\alpha \int_0^{r(\alpha)} \ln[r(1 + \cos\alpha\sin\varphi)] r dr \\ &= \left\{ -\frac{\tan\beta}{2C^2}[\ln C + \ln(\cos\beta) + \frac{3}{2}] - \frac{\varphi}{2C^2}[\cos\delta \ln[\tan(\frac{\pi}{4} + \frac{\beta}{2})] - \frac{\sin\delta}{\cos\beta}] + \frac{\beta}{2C^2} \right\} \Bigg|_{\beta_1}^{\beta_2} \end{aligned}$$

Finally, we can get the integral of log singularity on the panel by this equation:

$$L = \int_S f \; d\xi d\eta = \sum_{i=1}^{4} \int_{T_i} f \; dS$$

This approach can only deal with the case when the projection of the field point falls into the panel area. In some cases when the panel sizes are slender, the singular effect still exists if the field point locates at the neighboring panels. Thus it will be necessary to evaluate the integral when the field point is close to the panel, leading to the second method belonging to the category of Direct Approach.

4.3.1.2 Approach II

This approach is a simple improvement of Approach I, considering the normal vector effects from the four triangular facets. Recall the initial equation for the surface integral:

$$\int_S (\zeta \nabla f - f \nabla \zeta) \cdot \boldsymbol{n_S} \; dS + \int_{\sum_{i=1}^{4} T_i} (\zeta \nabla f - f \nabla \zeta) \cdot \boldsymbol{n_{T_i}} \; dS = 0$$

After enforcing $\zeta \to 0$, we will have

$$\int_S (-f \nabla \zeta) \cdot \boldsymbol{n_S} \; dS + \int_{\sum_{i=1}^{4} T_i} (-f \nabla \zeta) \cdot \boldsymbol{n_{T_i}} \; dS = 0$$

The relative position of the field point will affect the value of the normal vector. If the normal vectors from the four facets are opposite to the bottom surface. We will have this relationship same with Approach I. If the normal vector of a certain facet is almost the same with the bottom surface, the coefficient of that term will be -1 instead of $+1$. In other words, we have introduced the coefficient in the integral shown as below:

$$L = \int_S f \; d\xi d\eta = \sum_{i=1}^{4} C(i) \int_{T_i} f \; dS$$

If the normal vector of facet T_i is opposite to that of the bottom surface, $C(i) = 1$. Otherwise,

$C(i) = -1$. With this decision process we are able to handle such cases when the field point is infinitesimally close to a certain panel area. This can be shown in an exaggerated figure as below:

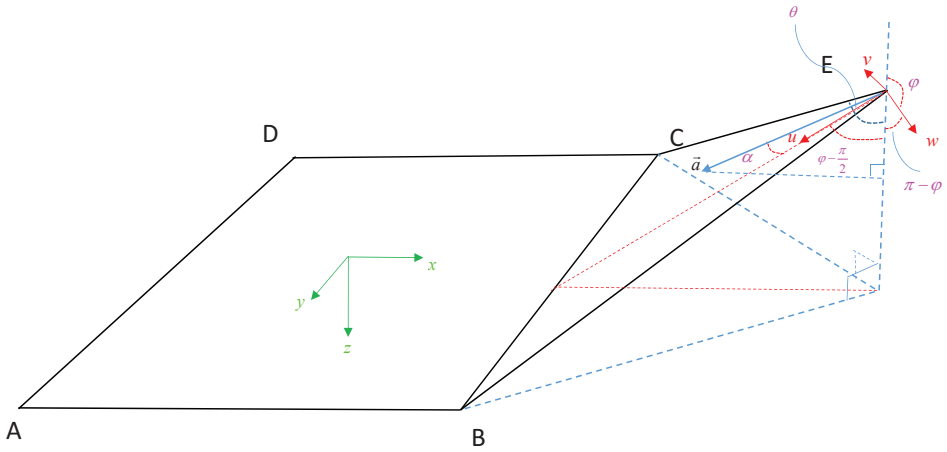

Figure 4.3: Cases When Field Point Outside the Panel Area

4.3.2 ln(d) Approach

The log singularity will be significant when the field point is approaching the image source point. We are interested in the part which cannot be well handled by the Gaussian Quadrature method. The direct method will work for most of the cases. However, in some cases when encountering special panels near but not exactly on the waterline, the panel centers of two panels are close by, thus the log term effect may appear in calculating the interaction coefficient. Such cases may not be well handled by the aforementioned direct methods. We, therefore, proposed alternative methods to handle the special cases.

Note that $\ln(d - v)$ can be written as:

$$\ln(d - v) = \ln(d) + \ln(1 - v/d) \tag{4.36}$$

When $v \to 0$ and d is changing by the source point across the panel area, we can expect that the

geometric shape of the term $\ln(1-v/d)$ is relatively flat. It indicates that the integral of $\ln(1-v/d)$ across the panel surface can be properly handled by the Gaussian Quadrature method. Then our focus can be shifted to the evaluation of the term $\ln(d)$.

If following the similar method to convert the variable to cylindrical coordinate of the panel surface, the integral can be written as:

$$\frac{1}{2}\int_{\alpha_1}^{\alpha_2} d\alpha \int_0^{\rho(\alpha)} \ln[\rho^2+z^2]\rho d\rho = \frac{1}{4}\int_{\alpha_1}^{\alpha_2} d\alpha\ [r^2\ln r^2] - \frac{1}{4}\int_{\alpha_1}^{\alpha_2} \rho^2(\alpha)\ d\alpha - \frac{1}{4}\int_{\alpha_1}^{\alpha_2} d\alpha\ z^2\ln z^2 \tag{4.37}$$

The last two terms on the RHS will have analytical solutions. We will focus on the evaluation method on the first term on the RHS.

$$\frac{1}{4}\int_{\alpha_1}^{\alpha_2} d\alpha\ [r^2\ln r^2] = \frac{1}{4}\int_{\alpha_1}^{\alpha_2} d\alpha\ \rho^2(\alpha)\ln[\rho^2(\alpha)+z^2] + \frac{1}{4}\int_{\alpha_1}^{\alpha_2} d\alpha\ z^2\ln[\rho^2(\alpha)+z^2] \tag{4.38}$$

where,

$$\begin{aligned}\frac{1}{4}\int_{\alpha_1}^{\alpha_2} d\alpha\ \rho^2(\alpha)\ln[\rho^2(\alpha)+z^2] = \frac{1}{4C^2}\tan\beta\ln[\frac{1}{C^2\cos^2\beta}+z^2]\Big|_{\beta_1}^{\beta_2} - \frac{1}{2C^2}\tan\beta\Big|_{\beta_1}^{\beta_2} \\ -\frac{\sqrt{1+C^2z^2}}{2C^2}\arctan(\sqrt{1+C^2z^2}\cot\beta)\Big|_{\beta_1}^{\beta_2}\end{aligned} \tag{4.39}$$

$$\frac{1}{4}\int_{\alpha_1}^{\alpha_2} d\alpha\ z^2\ln[\rho^2(\alpha)+z^2] = \frac{1}{4}\int_{\alpha_1}^{\alpha_2} z^2\ln\rho^2(\alpha) + \frac{1}{4}\int_{\alpha_1}^{\alpha_2} d\alpha z^2\ln[1+\frac{z^2}{\rho^2(\alpha)}] \tag{4.40}$$

Based on the treatment method to the term $\frac{1}{4}\int_{\alpha_1}^{\alpha_2} d\alpha z^2\ln[1+\frac{z^2}{\rho^2(\alpha)}]$, we can have two approaches as well. $\rho(\alpha)$ stands for the distance between the panel center and the point on the panel edge. z the vertical distance of the field point in panel local coordinate. When the field point is approaching the panel surface, it will be natural to assume $\frac{z^2}{\rho^2(\alpha)}$ is relatively small. Thus, we can use a Taylor series or a fast convergent series to represent the term, which are the Approach III and Approach

IV respectively.

4.3.2.1 Approach III

In this approach, we expand $\ln(1+x)$ by Taylor series:

$$\ln(1+x) = \sum_{n=1}^{\infty}(-1)^{n+1}\frac{x^n}{n} \qquad for\ |x|<1 \tag{4.41}$$

Then we will get:

$$\begin{aligned}\ln[1+\frac{z^2}{\rho^2(\alpha)}] &= \sum_{n=1}^{\infty}(-1)^{n+1}\frac{1}{n}\frac{z^{2n}}{\rho^{2n}(\alpha)} \\ &= \sum_{n=1}^{\infty}\frac{(-1)^{n+1}}{n}z^{2n}C^{2n}\cos^{2n}\beta\end{aligned} \tag{4.42}$$

Thus, substitute back to the integral, we will get:

$$\begin{aligned}&\int_{\alpha_1}^{\alpha_2} d\alpha \ln[1+\frac{z^2}{\rho^2(\alpha)}] = \\ &\sum_{n=1}^{\infty}\frac{(-1)^{n+1}}{n}z^{2n}C^{2n}\big[\frac{1}{2^{2n}}\cdot\frac{(2n)!}{n!n!}\beta + \frac{1}{2^{2n-1}}\sum_{k=0}^{n-1}\frac{(2n)!}{k!(2n-k)!}\frac{sin(2n-2k)\beta}{2n-2k}\big]\Big|_{\beta_1}^{\beta_2}\end{aligned} \tag{4.43}$$

Depending on the value of $\frac{z^2}{\rho^2(\alpha)}$, we can choose the value of n. Usually, when $\frac{z^2}{\rho^2(\alpha)}$ is small, $n=3$ will lead to good results. However, when $\frac{z^2}{\rho^2(\alpha)}$ is relatively larger, the approximation cannot handle some cases while 4-node Gaussian quadrature cannot achieve good results either. Such situations motivate us to search for an alternative approach to evaluate the integral.

4.3.2.2 Approach IV

The Taylor expansion has put a strong restriction on x, i.e. $|x|<1$. Such an assumption will restrict the application range of the Taylor expansion approach. To make the series method applicable for a wider range of x, we find an alternative expansion for $\ln(x)$.

$$\ln x = 2\sum_{n=1}^{\infty}\frac{1}{2n-1}(\frac{x-1}{x+1})^{2n-1} \qquad for\ x>0 \tag{4.44}$$

Then we will get:

$$ln[1+\frac{z^2}{\rho^2(\alpha)}]=2\sum_{n=1}^{\infty}\frac{1}{2n-1}(\frac{z^2C^2\cos^2\beta}{2+z^2C^2\cos^2\beta})^{2n-1} \tag{4.45}$$

Therefore, the integral will become:

$$\frac{1}{4}\int_{\alpha_1}^{\alpha_2}d\alpha z^2\ln[1+\frac{z^2}{\rho^2(\alpha)}]=\frac{1}{2}z^2\sum_{n=1}^{\infty}\frac{1}{2n-1}\frac{\sin\beta}{(a+1)^{2n-1}}F_1(\frac{1}{2};2n-1,\frac{3}{2}-2n;\frac{3}{2};\frac{\sin^2\beta}{a+1},\sin^2\beta) \tag{4.46}$$

where, F_1 is the Appell Hypergeometric Function.

The Appell Hypergeometric Function is defined as below:

$$F_1(\alpha;\beta,\beta';\gamma;x,y)=\sum_{m=0}^{\infty}\sum_{n=0}^{\infty}\frac{(\alpha)_{m+n}(\beta)_m(\beta')_n}{m!n!(\gamma)_{m+n}}x^my^n \tag{4.47}$$

where, $(a)_n$ is defined as:

$$(a)_n=\frac{\Gamma(a+n)}{\Gamma(a)} \tag{4.48}$$

where, $\Gamma(a)$ is the Gamma function. This equation looks complicated and has infinitely many terms. Based on our numerical test, its convergence rate is strongly affected by $\sin\beta$. In most of cases, this function converges very fast and is still numerically efficient. Additionally, the adoption of the fourth approach will not significantly affect the total efficiency of the program because this method is used only for some special panels when other methods cannot accurately evaluate them. In other words, Approach IV is less efficient than the rest of the three methods but it is not often used, thus not significantly affecting the whole program.

4.4 Results and Discussion

In this section, we will first verify the accuracy of our method to evaluate the log singularity, then justify the method of subtracting the log singularity from the wavy Green function, finally

evaluate the irregular frequency removal effects.

4.4.1 Log Singularity

As mentioned in the introduction section, Newman[60] did not provide complete details about the assumptions and some other information for the final expression was also not included. To be conservative, we chose some special cases in which Newman's final expression might be valid and applied a systematic trial-and-error approach to tune the parameters until we got similar results with Maple. Afterwards, based on the idea, we have developed our own method for evaluation, ending up with somewhat different expressions. When comparing against Newman's results, not surprisingly, they are very close. The comparison validates our assumptions about Newman's expression and also proves our approach is accurate.

Table 4.1 contains the comparison results for the method I and II in this article with Newman's. As can be seen from the table, the difference is 10^{-7}. We can draw the conclusion that our method will be accurate enough in evaluating the log singularity. Please note that table 4.2 contains the node position vector in the panel coordinate for different cases. The rest three methods are also tested against the first method, they achieve the same accuracy when the field point is infinitesimally close to the image source panel.

Table 4.1: Comparison of Log Singularity in Different Methods

Case	Liu et al.	Newman	Abs Error
1	-1.472113	-1.472113	3.48E-07
2	90.625475	90.625475	-4.12E-07
3	-1.268191	-1.268191	-2.48E-07
4	80.647368	80.647368	-5.39E-07
5	-1.188854	-1.188854	-2.33E-07

Table 4.2: Explanation on Cases Setting

Case	x	y
2x2 Square	[-1, 1, 1, -1]	[-1, -1, 1, 1]
Arbitrary Quadrilateral	[-1, 10, 1, -1]	[-1, -1, 10, 1]
Trapezoid	[-1, 1, 0.1, -0.1]	[-1, -1, 1, 1]
Long rectangular	[-1, 1, 1, -1]	[-1, -1, 20, 20]
Triangle	[-1, 1, 0, 0]	[-1, -1, 1, 1]

To study the range of applicability of the methods discussed in the previous section, we conducted numerical experiments on different cases. The case setting is listed below, the vertical

distance between panel surface and field point will vary from 0 to 1 and the projection of field point onto the panel area will be coincident with the panel center.

Moreover, we also conducted the convergent study for the Gaussian quadrature method, i.e. we keep increasing the node number until the Gaussian quadrature method output converges. The node number increases from 4 until 160000. Such a large number of nodes is required in evaluating the integral for relatively larger panels. In all the cases, we can observe the convergent behavior of the Gaussian quadrature method. As a benchmark value, we choose the value when there are 160000 nodes and compared the output from other methods against the benchmark value.

Also please note that in some cases when the vertical distance is large enough to make Method III diverge, we only plot the comparison results of the other methods. In the legend, "Gau 2pt" indicates the Gaussian node number in one dimension thus it stands for the 4-point Gaussian quadrature method across the panel area. For Taylor series expansion, we adopt the first 5 terms. For the fast convergent series, we also keep the first 5 terms.

Table 4.3: Cases Setting for the Range of Applicability

Case	x	y
0.2x0.2 Square	[-0.1, 0.1, 0.1, -0.1]	[-0.1, -0.1, 0.1, 0.1]
1x1 Square	[-0.5, 0.5, 0.5, -0.5]	[-0.5, -0.5, 0.5, 0.5]
2x2 Square	[-1, 1, 1, -1]	[-1, -1, 1, 1]
20x20 Square	[-10, 10, 10, -10]	[-10, -10, 10, 10]

For 0.2×0.2 panel, the absolute error and relative error plots can be shown as below:

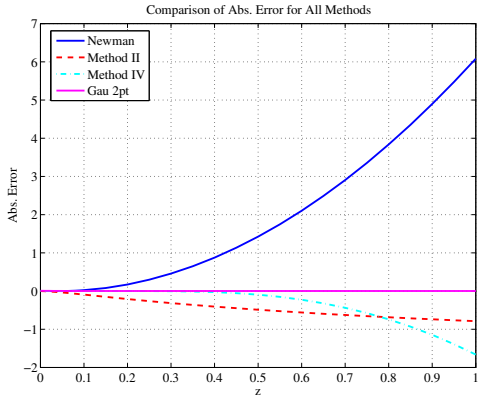

Figure 4.4: Absolute error for 0.2x0.2 panel ($z = 0 \sim 1$)

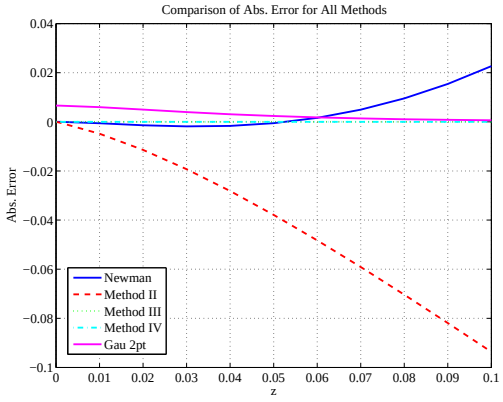

Figure 4.5: Absolute error for 0.2x0.2 panel ($z = 0 \sim 0.1$)

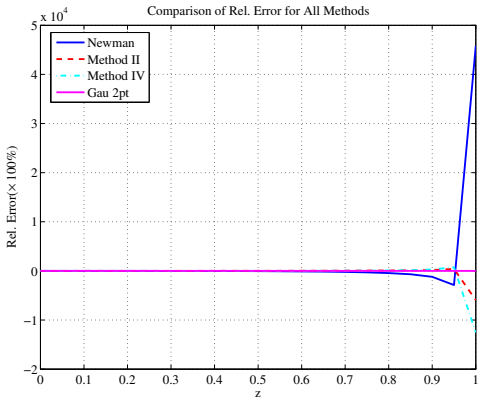

Figure 4.6: Relative error for 0.2x0.2 panel ($z = 0 \sim 1$)

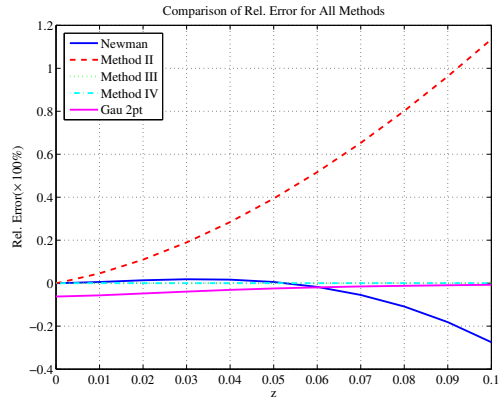

Figure 4.7: Relative error for 0.2x0.2 panel ($z = 0 \sim 0.1$)

For 1×1 panel, the absolute error and relative error plots can be shown as below:

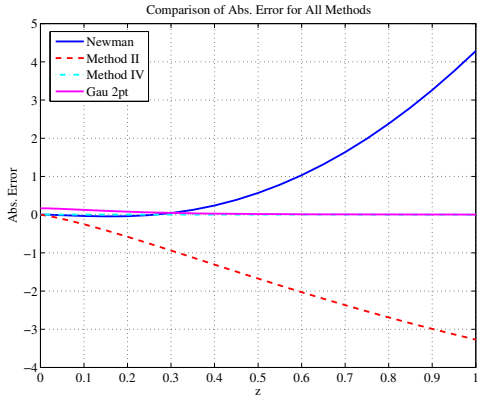

Figure 4.8: Absolute error for 1x1 panel ($z = 0 \sim 1$)

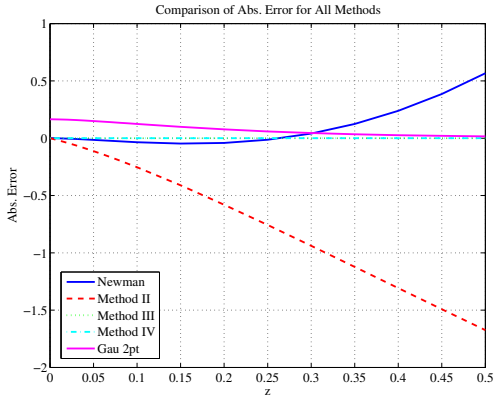

Figure 4.9: Absolute error for 1x1 panel ($z = 0 \sim 0.5$)

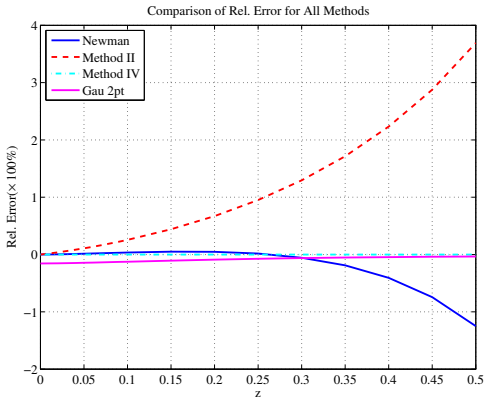

Figure 4.10: Relative error for 1x1 panel ($z = 0 \sim 1$)

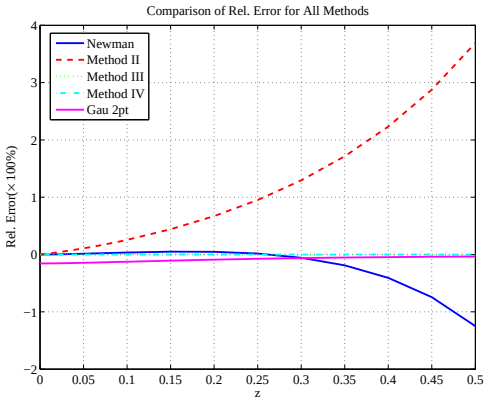

Figure 4.11: Relative error for 1x1 panel ($z = 0 \sim 0.5$)

For 2×2 panel, the absolute error and relative error plots can be shown as below:

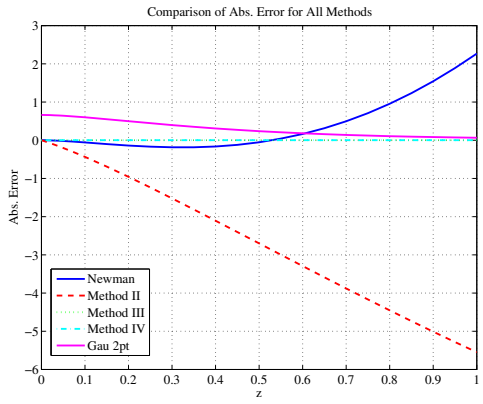

Figure 4.12: Absolute error for 2x2 panel ($z = 0 \sim 1$)

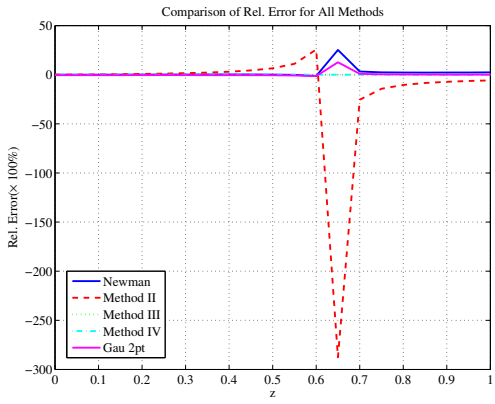

Figure 4.13: Relative error for 2x2 panel ($z = 0 \sim 1$)

For 20×20 panel, the absolute error and relative error plots can be shown as below:

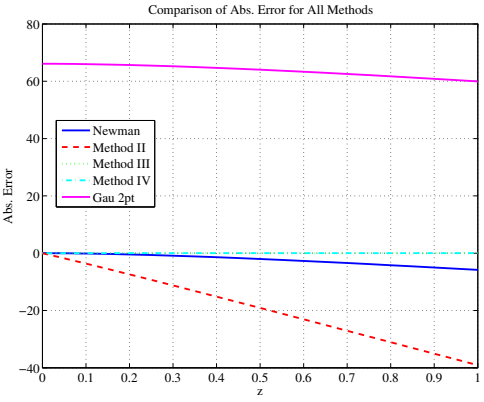

Figure 4.14: Absolute error for 20x20 panel ($z = 0 \sim 1$)

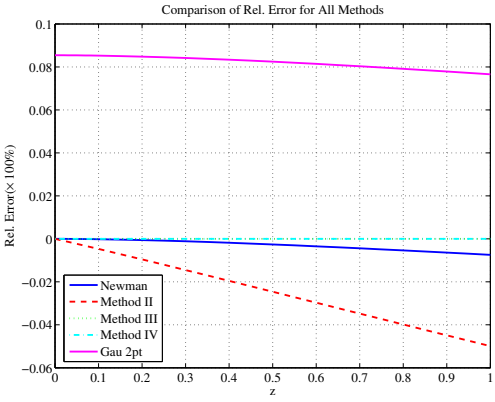

Figure 4.15: Absolute error for 20x20 panel ($z = 0 \sim 1$)

As we may find from the plots, for smaller panels, the 4-point Gaussian quadrature method can achieve relatively higher accuracy for a larger value of z. For $z \to 0$, the 4-point Gaussian quadrature method will be less accurate than the other methods, which have achieved similar accuracy.

When the panel area is growing, the 4-point Gaussian quadrature method gradually shows the

discrepancy compared with the others. Meanwhile, Method IV is relatively more accurate than the rest for a larger range of z. Second to Method IV is Method III, which shares the similar applicable range but will diverges when the vertical distance z is large enough to weaken the assumptions.

To sum up, when the vertical distance z is relatively larger than the square root of panel area, the 4-point Gaussian quadrature method will be adopted. Otherwise, the rest methods are adopted to handle the cases based on the relative position of the field point to the panel.

4.4.2 Integral of R_0

Since the log singularity was evaluated analytically, one may be curious about the function shape of R_0 after subtracting the log integral from it. This subsection will illustrate the shape and justify a proper numerical method to evaluate R_0. The numerical evaluation method for R_0 is from Telste and Noblesse [10].

Figures 4.16 to 4.19 illustrate the function value of $R_0 - ln(d - v)$ across a unit square panel.

As shown in Figures 4.16 to 4.19, if the panel size is small, a 4-node Gaussian quadrature method can still give accurate results. However, if the panel is of a larger size, the wavy behavior will nullify the 4-node Gaussian quadrature. To balance the accuracy and efficiency, it is preferable to construct smaller panels for the internal lid surface. Moreover, please note that in implementing the Gaussian quadrature method, the input is dimensionless. The variable related to length is multiplied by $f = \omega^2 L/g$, where ω is wave frequency, L is the wave length, g the gravity constant. For a floater with a large L, when wave frequency ω is relatively higher, the node position could be amplified. Therefore, the 4-node quadrature method may not produce accurate enough results. Nevertheless, the shorter wave may not lie in the range of interest for such floaters in sea-keeping analysis if the panel size is properly set in the geometric model.

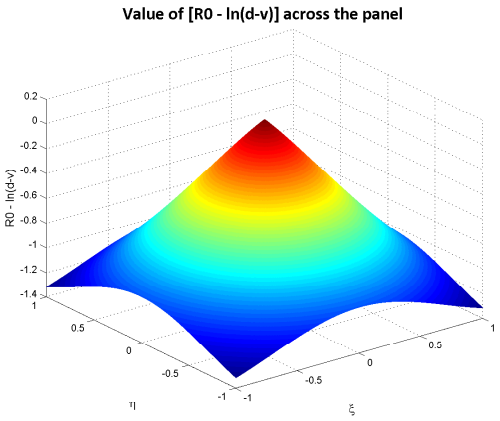

Figure 4.16: Shape of $R_0 - ln(d-v)$ for 2x2 panel

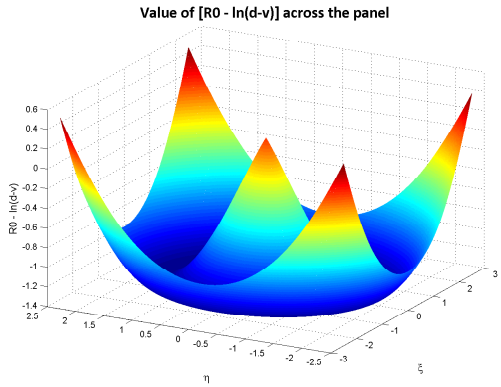

Figure 4.17: Shape of $R_0 - ln(d-v)$ for 5x5 panel

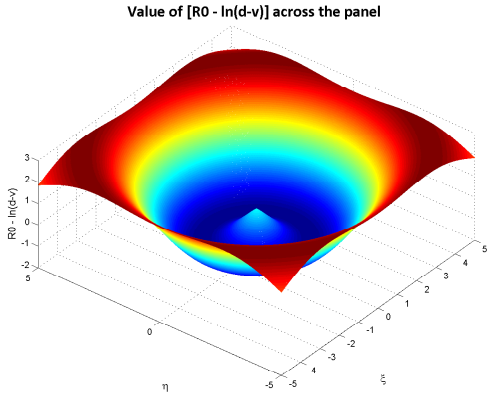

Figure 4.18: Shape of $R_0 - ln(d-v)$ for 10x10 panel

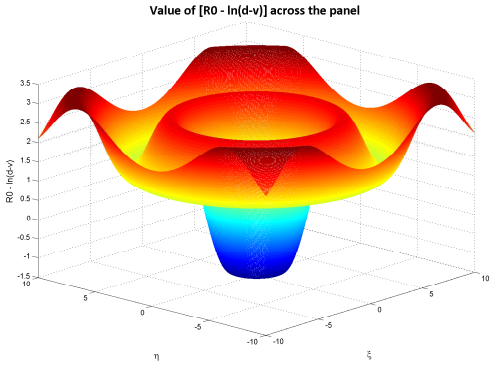

Figure 4.19: Shape of $R_0 - ln(d-v)$ for 20x20 panel

4.4.3 Irregular Frequency Removal Effect

The accurate numerical evaluation of log singularity is important to eliminate the irregular frequency effect. The subsection will demonstrate the irregular frequency removal effects for single-body and multi-body case. The results are generated by MDL-MultiDYN, an in-house program developed by Marine Dynamic Laboratory, Texas A&M University. This program is

a redesigned program based on MDL HydroD by Guha[111]. It is able to conduct multi-body analysis with log singularity evaluation and an irregular frequency removal module.

To validate, we have simulated several cases which were known to have irregular frequency effects and will discuss each one of them in this section. The cases are listed in the following table.

Table 4.4: Floater Particulars

	L	B	T	k_{xx}	k_{yy}	k_{zz}
Mini Box Barge	20	10	5	1	1	1
Box Barge	80	20	10	20	5	20
Cylinder Dock	40	40	20	1	1	1
Square Column	90	90	40	1	1	1
Wigley Hull	3	0.6	0.19	0.24	0.75	0.75
BOBO	187.325	32.156	6.685	12.86241	46.8313	46.8313
Bob Hope	269.45	32.258	8.795	11.44610	66.58380	66.58380

We will first provide the figure of the floater, followed by some results which demonstrate the irregular frequencies are successfully removed. For multi-body cases, the term "separation" is defined as the horizontal distance from one vessel coordinate origin to another.

When coming to the verification of the ships, we also output the results from WAMIT to demonstrate that the effectiveness of our irregular frequency removal module. Figures 4.94 to 4.97 are the results for the ship Bob Hope. The irregular frequency effect is not significant. However, it is still removed.

Figures 4.99 to 4.104 show the results for ship BOBO. In the single body case, the irregular

frequency effect is very significant in some components in the added mass matrix, for example, A13, A33 etc. For this case, we also find the irregular frequency effects exist in the drift forces of the floater. The results in the heave drift force and pitch drift force are also presented here to demonstrate the effectiveness of our method.

Figures 4.106 to 4.111 are the results when ship BOBO is next to the ship Bob Hope. The separation distance is 3 meters. Similar to the mini-box-barge case, the results prove that the irregular frequency effect will confuse the resonance in the relatively higher frequency range. It must be removed to achieve a more accurate prediction of the hydrodynamic responses.

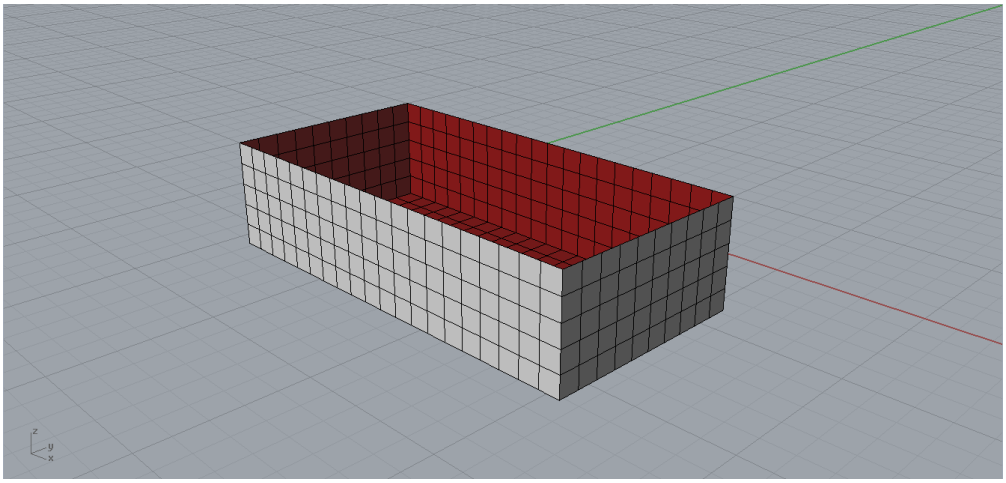

Figure 4.20: Perspective view of mini box barge

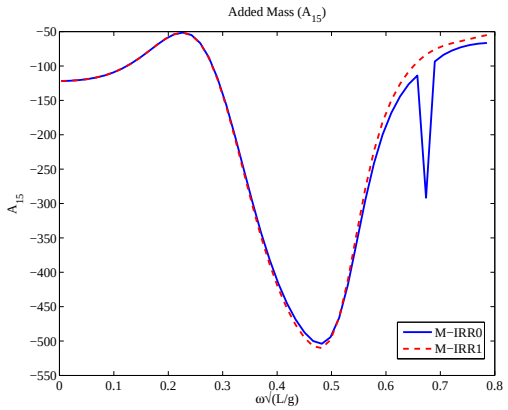

Figure 4.21: Added mass A15 vs frequency $\omega\sqrt{L/g}$

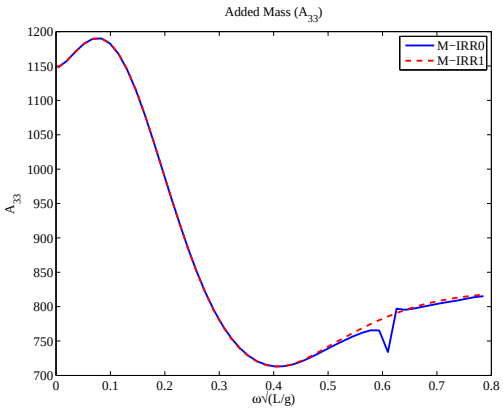

Figure 4.22: Added mass A33 vs frequency $\omega\sqrt{L/g}$

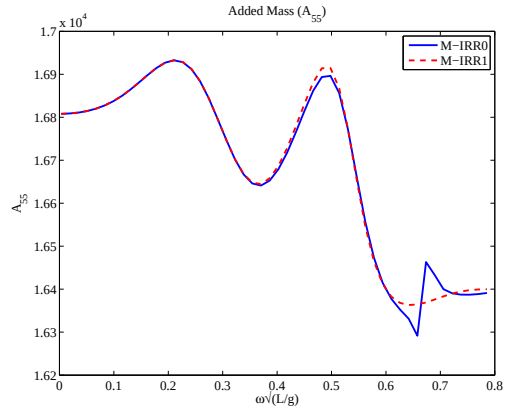

Figure 4.23: Added mass A55 vs frequency $\omega\sqrt{L/g}$

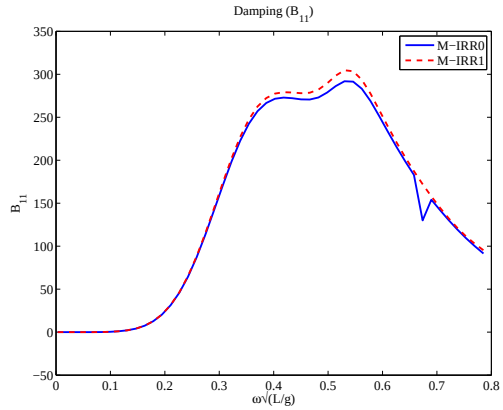

Figure 4.24: Damping B11 vs frequency $\omega\sqrt{L/g}$

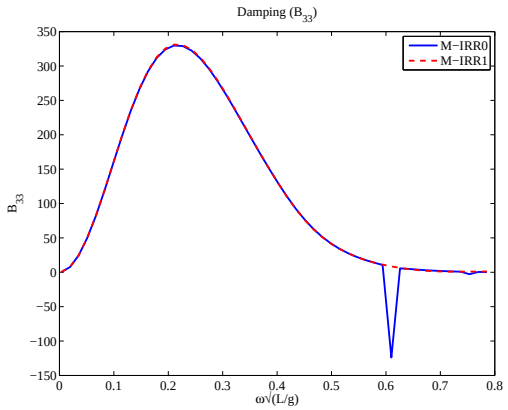

Figure 4.25: Damping B33 vs frequency $\omega\sqrt{L/g}$

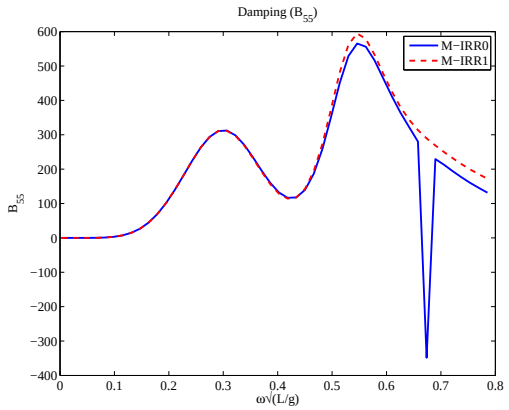

Figure 4.26: Damping B55 vs frequency $\omega\sqrt{L/g}$

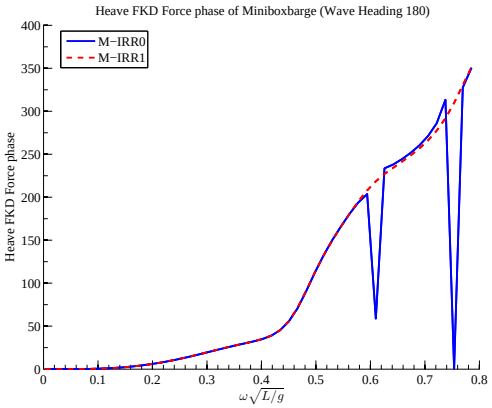

Figure 4.27: Heave FKD force phase vs frequency $\omega\sqrt{L/g}$

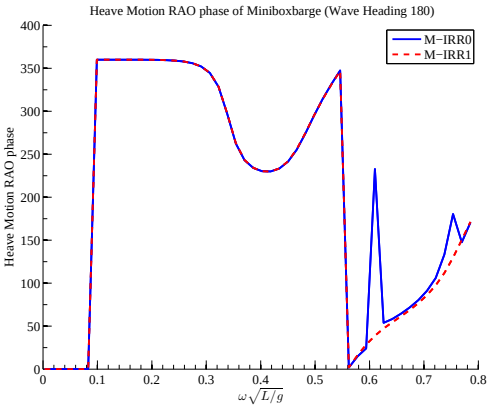

Figure 4.28: Heave RAO phase vs frequency $\omega\sqrt{L/g}$

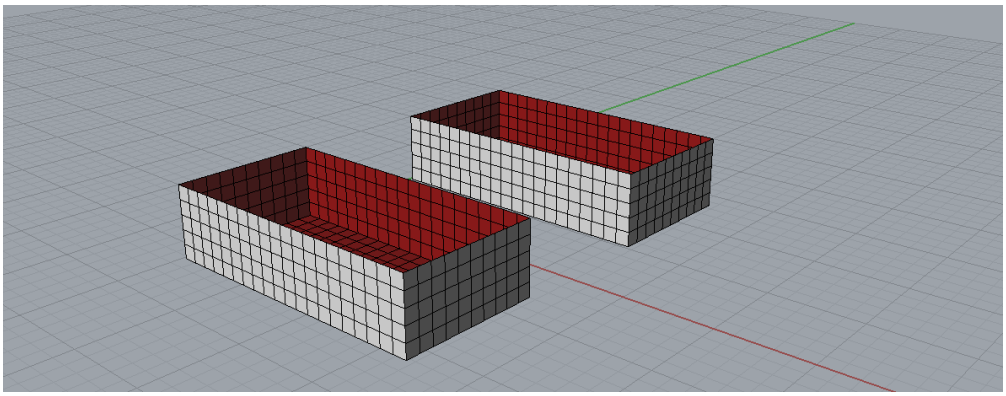

Figure 4.29: Perspective view of two mini box barges (separation 10m)

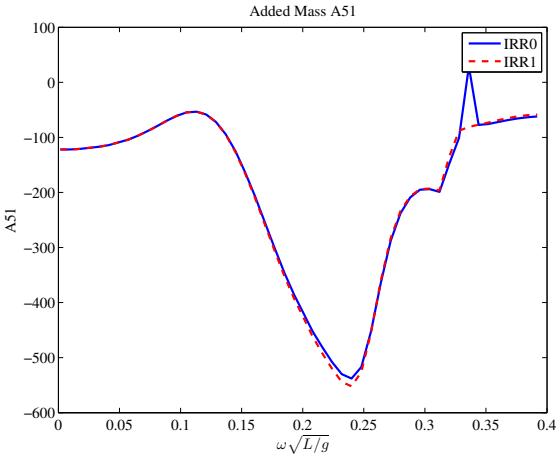

Figure 4.30: Added mass A51 vs frequency $\omega\sqrt{L/g}$

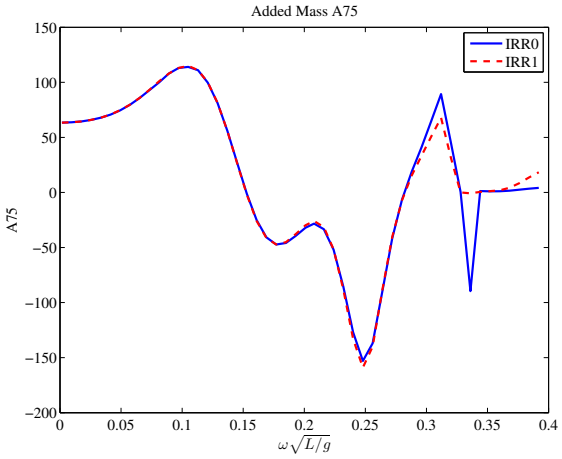

Figure 4.31: Added mass A75 vs frequency $\omega\sqrt{L/g}$

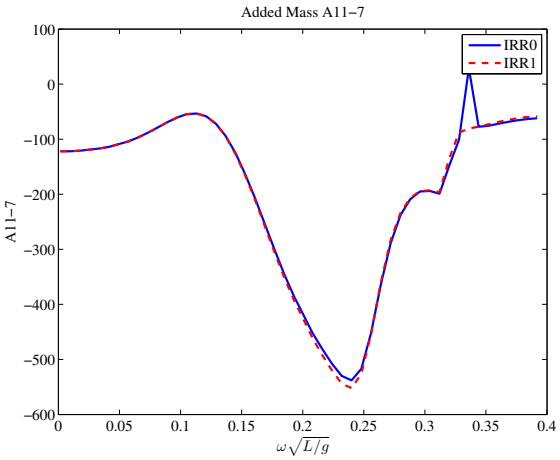

Figure 4.32: Added mass A11-7 vs frequency $\omega\sqrt{L/g}$

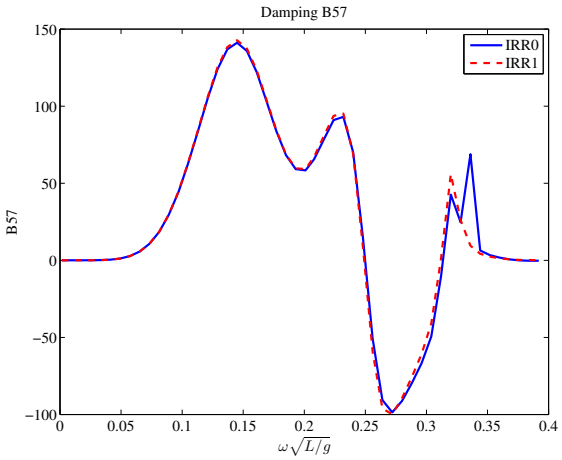

Figure 4.33: Damping B57 vs frequency $\omega\sqrt{L/g}$

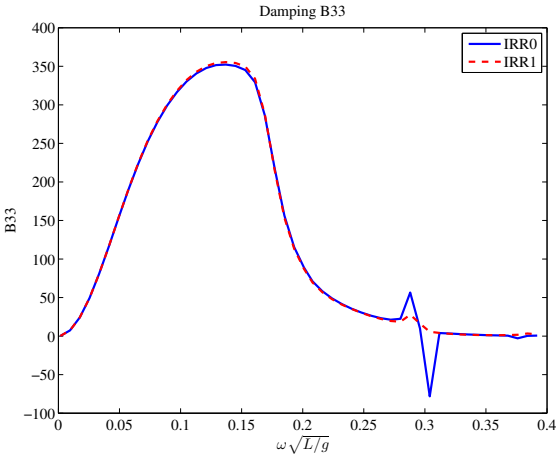

Figure 4.34: Damping B33 vs frequency $\omega\sqrt{L/g}$

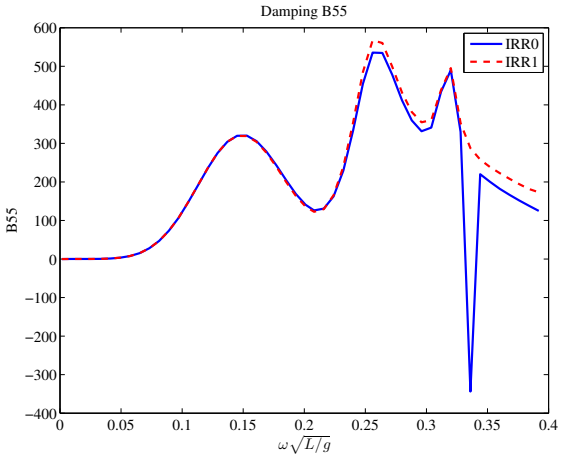

Figure 4.35: Damping B55 vs frequency $\omega\sqrt{L/g}$

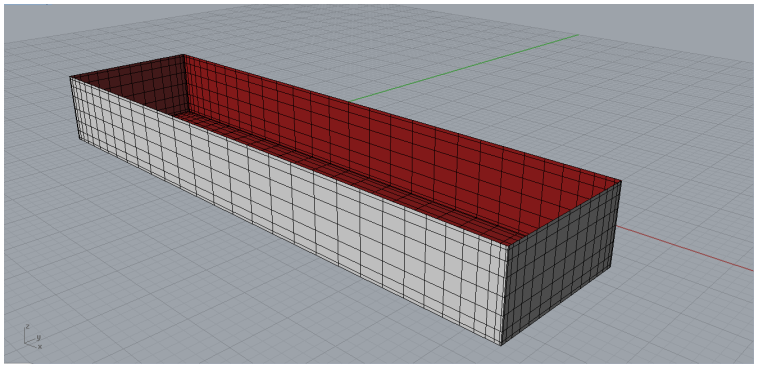

Figure 4.36: Perspective view of box barge

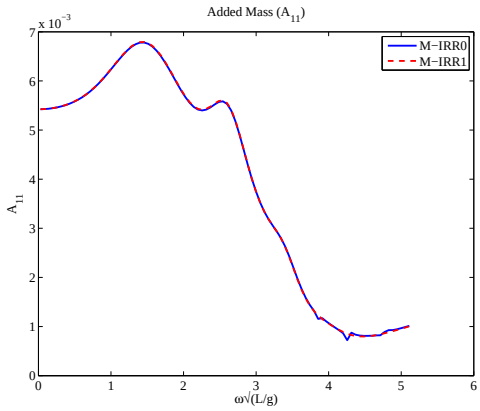

Figure 4.37: Added mass A11 vs frequency $\omega\sqrt{L/g}$

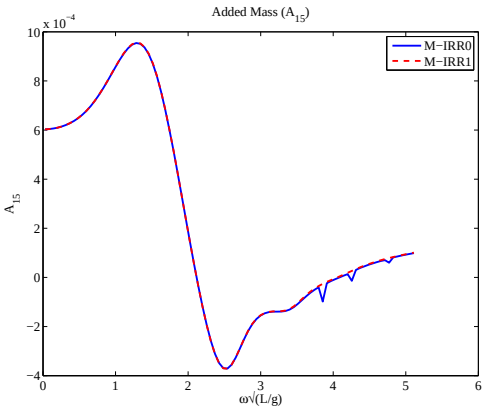

Figure 4.38: Added mass A15 vs frequency $\omega\sqrt{L/g}$

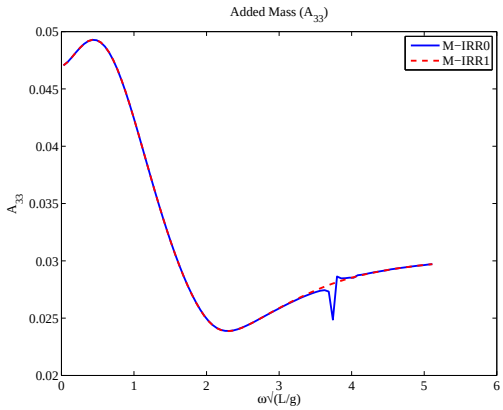

Figure 4.39: Added mass A33 vs frequency $\omega\sqrt{L/g}$

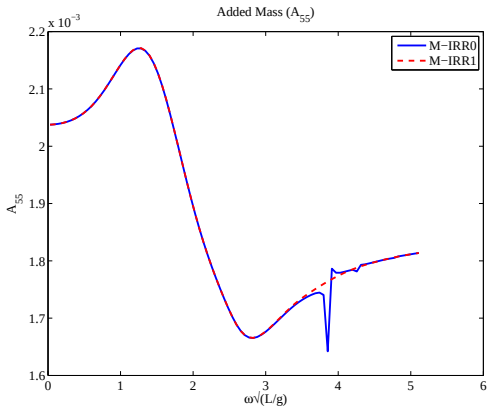

Figure 4.40: Added mass A55 vs frequency $\omega\sqrt{L/g}$

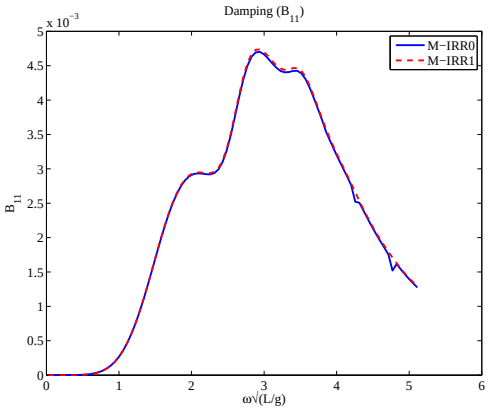

Figure 4.41: Damping B11 vs frequency $\omega\sqrt{L/g}$

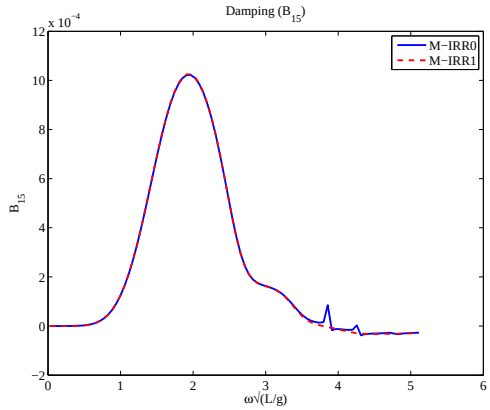

Figure 4.42: Damping B15 vs frequency $\omega\sqrt{L/g}$

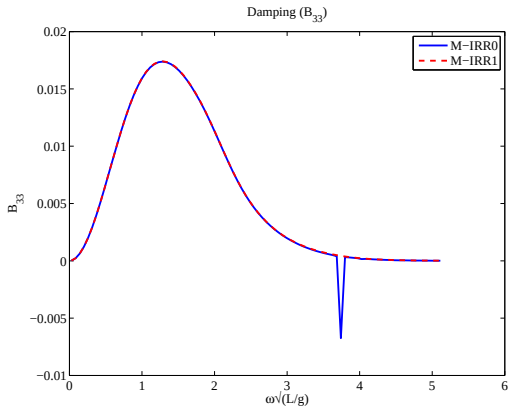

Figure 4.43: Damping B33 vs frequency $\omega\sqrt{L/g}$

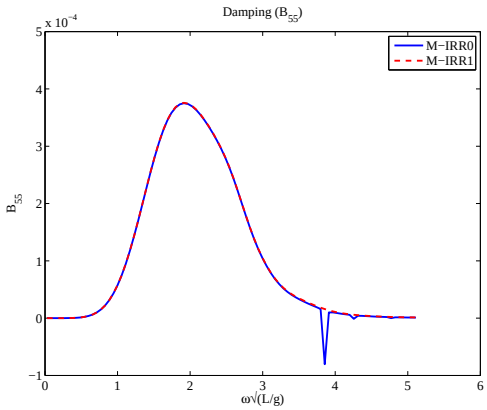

Figure 4.44: Damping B55 vs frequency $\omega\sqrt{L/g}$

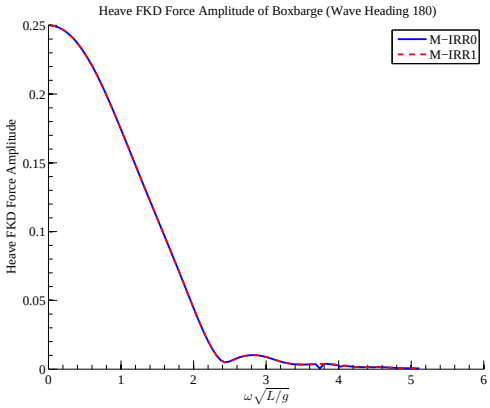

Figure 4.45: Heave FKD force vs frequency $\omega\sqrt{L/g}$

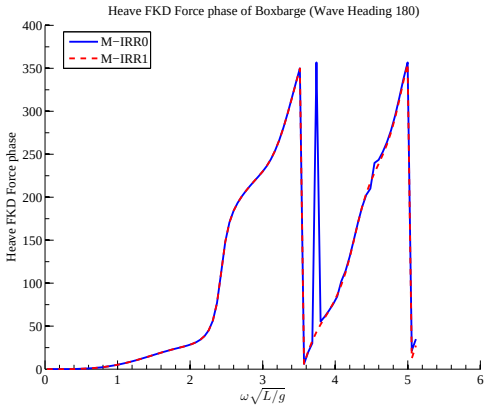

Figure 4.46: Heave FKD force phase vs frequency $\omega\sqrt{L/g}$

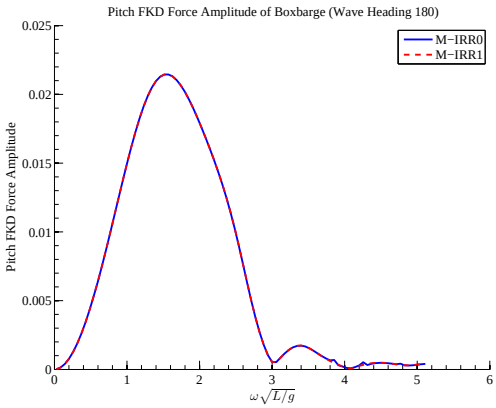

Figure 4.47: Pitch FKD force vs frequency $\omega\sqrt{L/g}$

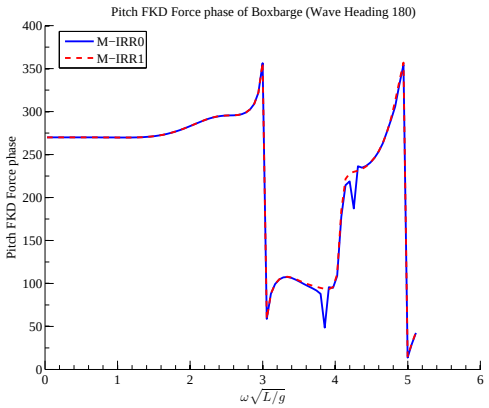

Figure 4.48: Pitch FKD force phase vs frequency $\omega\sqrt{L/g}$

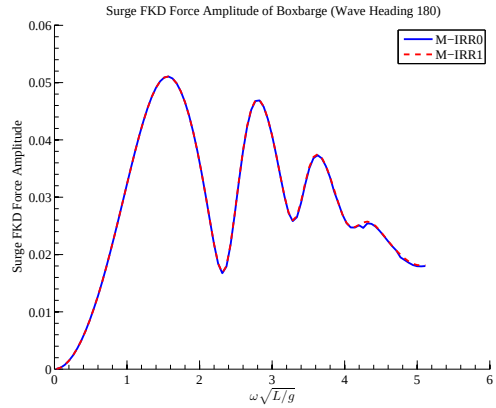

Figure 4.49: Surge FKD force vs frequency $\omega\sqrt{L/g}$

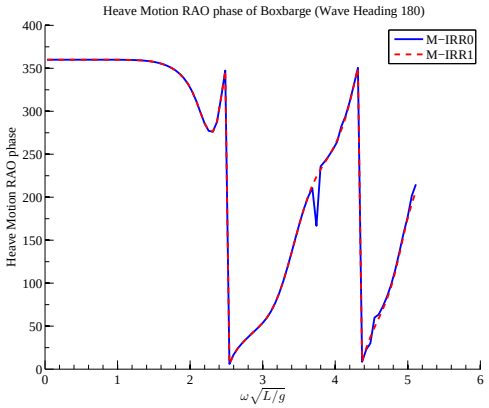

Figure 4.50: Heave RAO phase vs frequency $\omega\sqrt{L/g}$

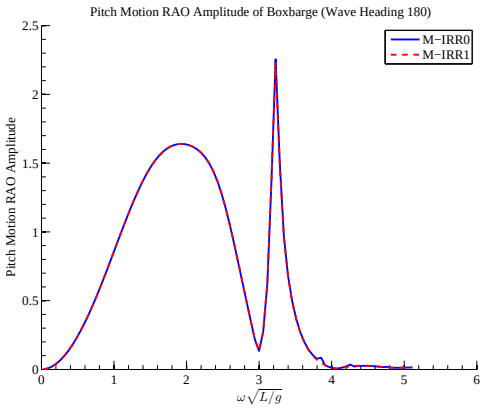

Figure 4.51: Pitch RAO vs frequency $\omega\sqrt{L/g}$

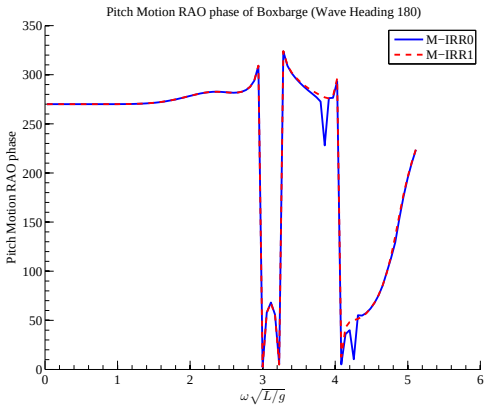

Figure 4.52: Pitch RAO phase vs frequency $\omega\sqrt{L/g}$

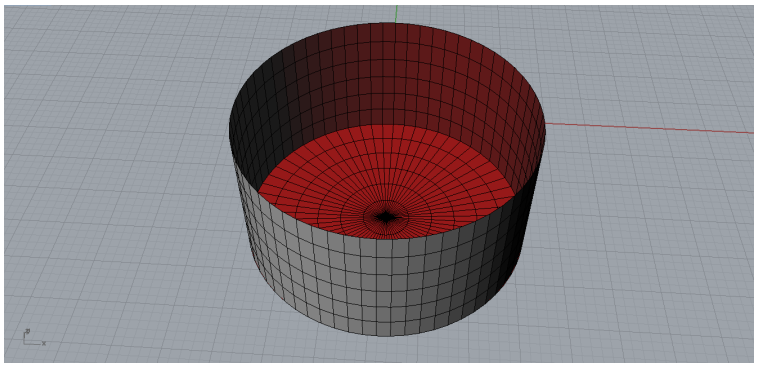

Figure 4.53: Perspective view of cylinder dock

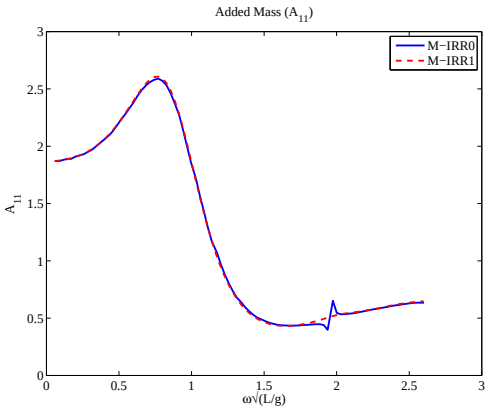

Figure 4.54: Added mass A11 vs frequency $\omega\sqrt{L/g}$

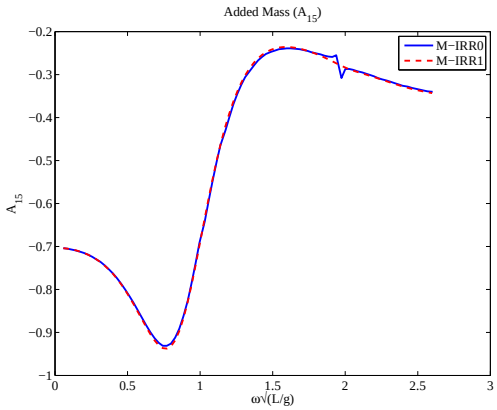

Figure 4.55: Added mass A15 vs frequency $\omega\sqrt{L/g}$

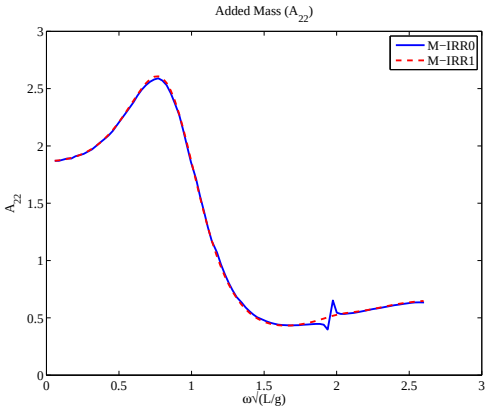

Figure 4.56: Added mass A22 vs frequency $\omega\sqrt{L/g}$

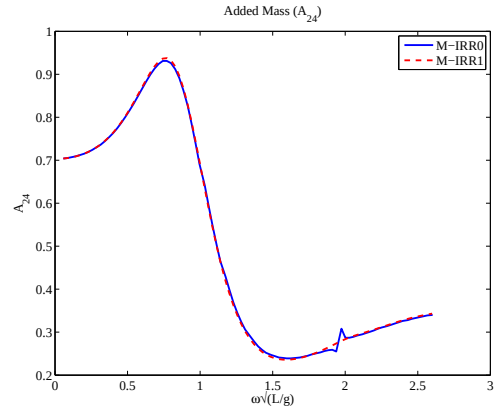

Figure 4.57: Added mass A24 vs frequency $\omega\sqrt{L/g}$

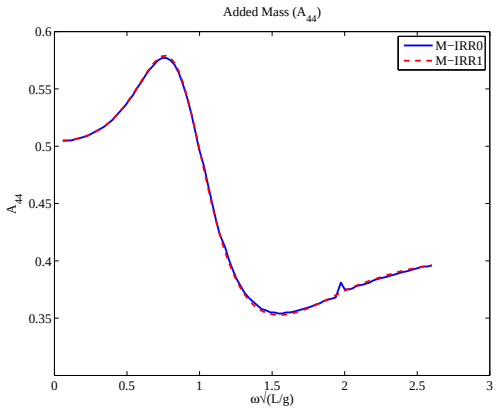

Figure 4.58: Added mass A44 vs frequency $\omega\sqrt{L/g}$

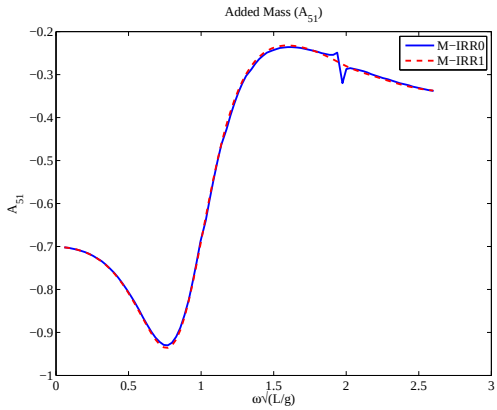

Figure 4.59: Added mass A51 vs frequency $\omega\sqrt{L/g}$

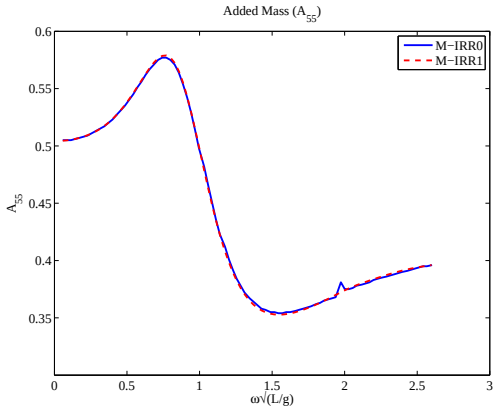

Figure 4.60: Added mass A55 vs frequency $\omega\sqrt{L/g}$

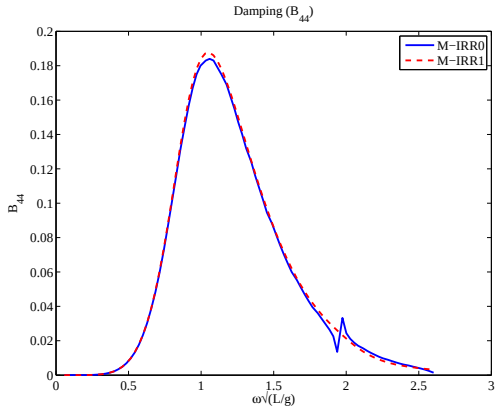

Figure 4.61: Damping B44 vs frequency $\omega\sqrt{L/g}$

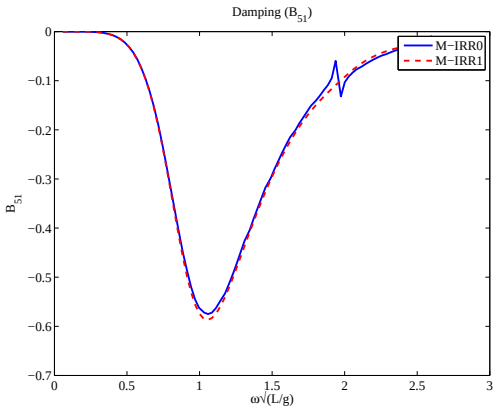

Figure 4.62: Damping B51 vs frequency $\omega\sqrt{L/g}$

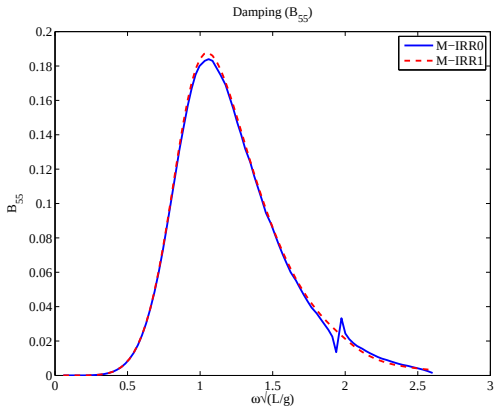

Figure 4.63: Damping B55 vs frequency $\omega\sqrt{L/g}$

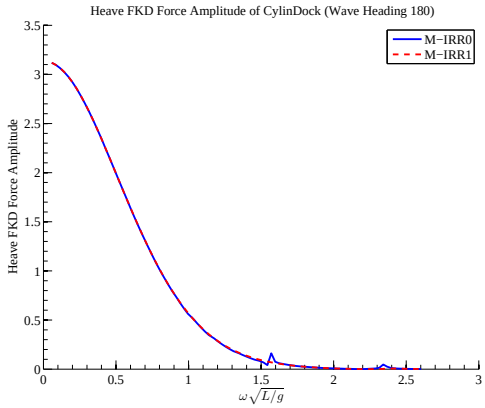

Figure 4.64: Heave FKD force vs frequency $\omega\sqrt{L/g}$

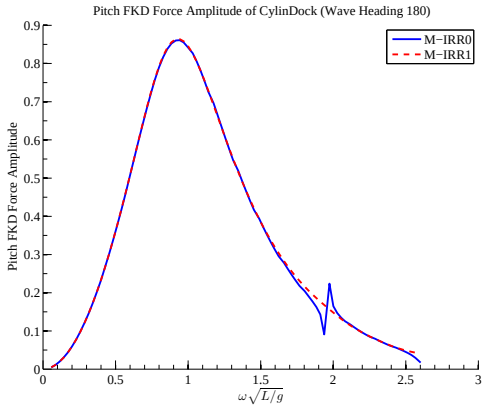

Figure 4.65: Pitch FKD force vs frequency $\omega\sqrt{L/g}$

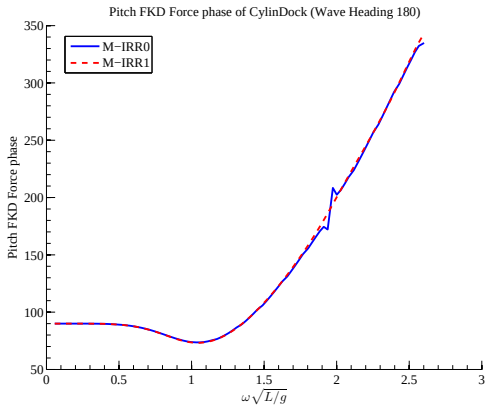

Figure 4.66: Pitch FKD force phase vs frequency $\omega\sqrt{L/g}$

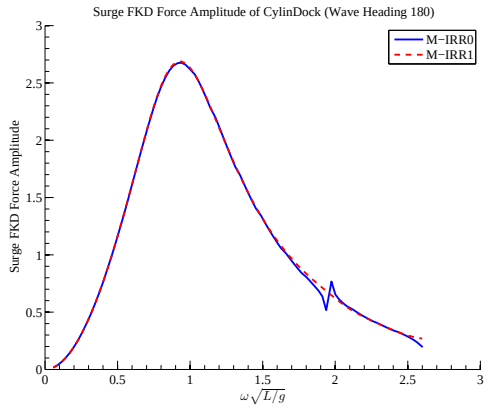

Figure 4.67: Surge FKD force vs frequency $\omega\sqrt{L/g}$

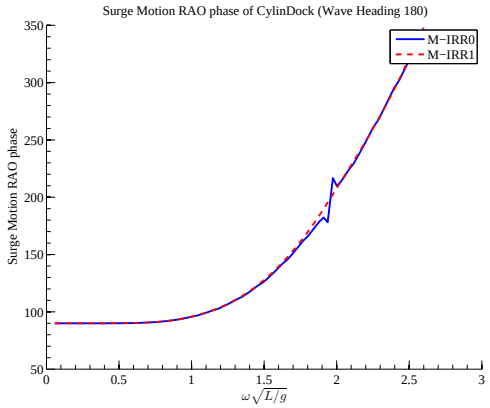

Figure 4.68: Surge RAO vs frequency $\omega\sqrt{L/g}$

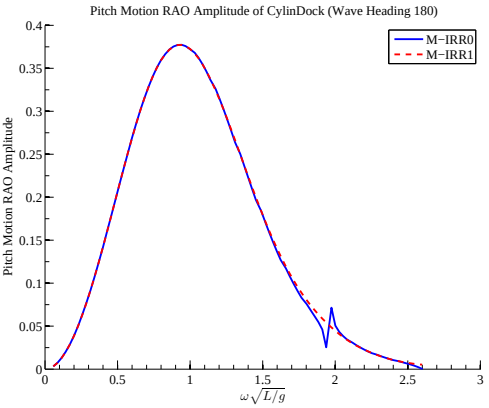

Figure 4.69: Pitch RAO vs frequency $\omega\sqrt{L/g}$

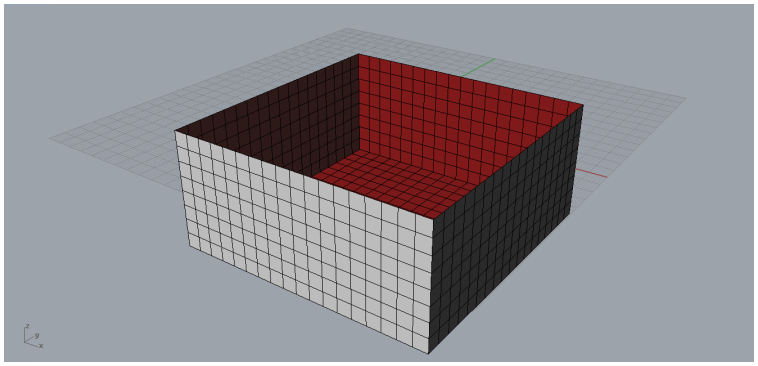

Figure 4.70: Perspective view of square column

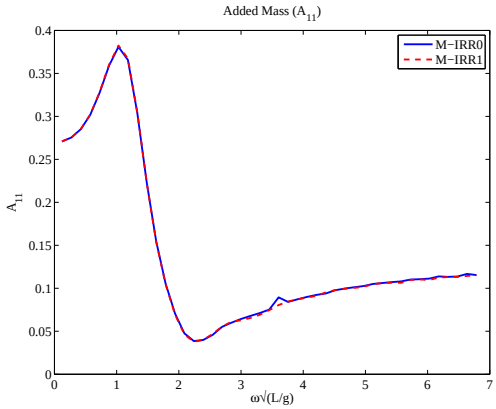

Figure 4.71: Added mass A11 vs frequency $\omega\sqrt{L/g}$

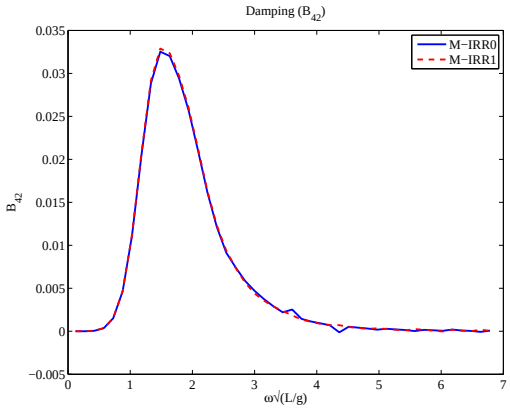

Figure 4.72: Damping B42 vs frequency $\omega\sqrt{L/g}$

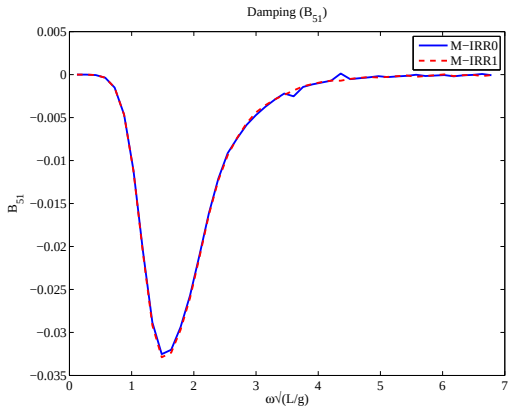

Figure 4.73: Damping B51 vs frequency $\omega\sqrt{L/g}$

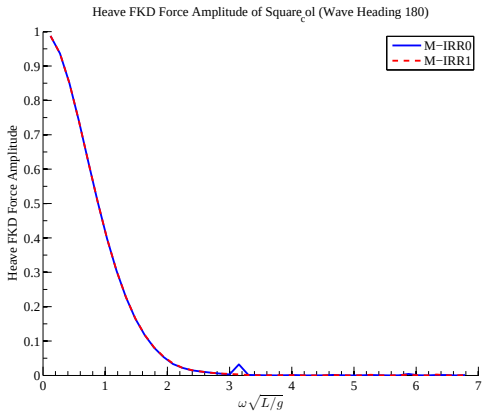

Figure 4.74: Pitch RAO vs frequency $\omega\sqrt{L/g}$

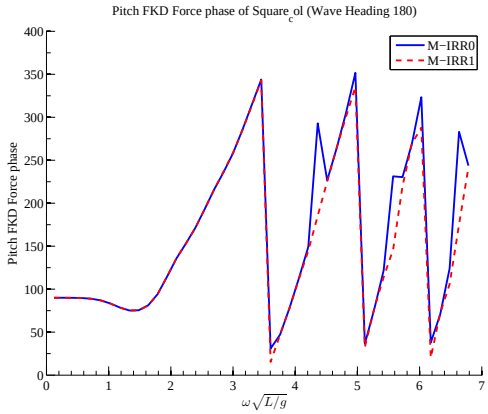

Figure 4.75: Pitch FKD force phase vs frequency $\omega\sqrt{L/g}$

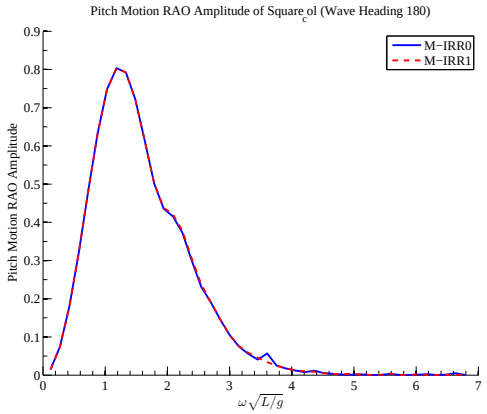

Figure 4.76: Pitch RAO vs frequency $\omega\sqrt{L/g}$

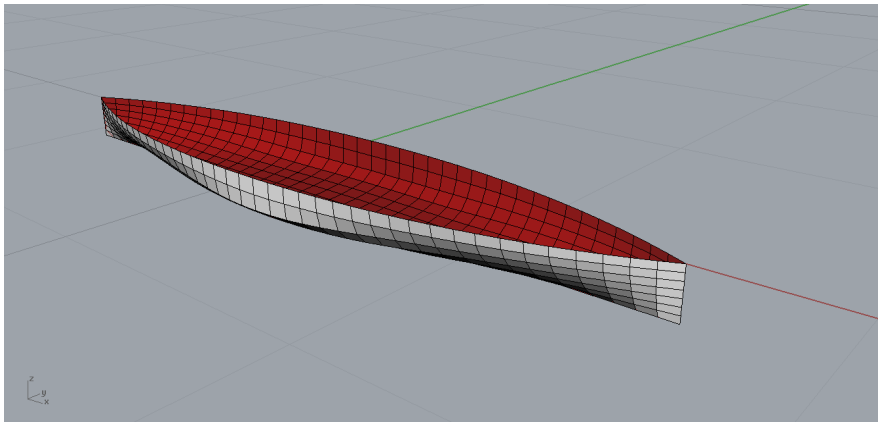

Figure 4.77: Perspective view of Wigley hull

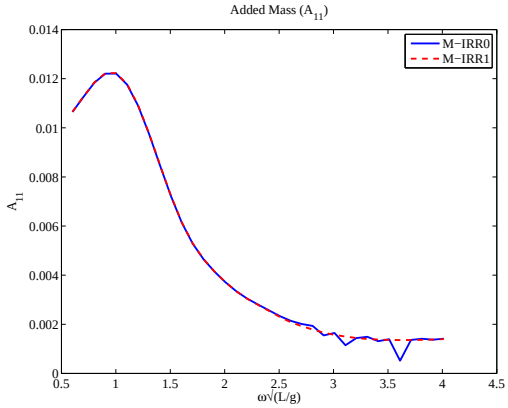

Figure 4.78: Added mass A11 vs frequency $\omega\sqrt{L/g}$

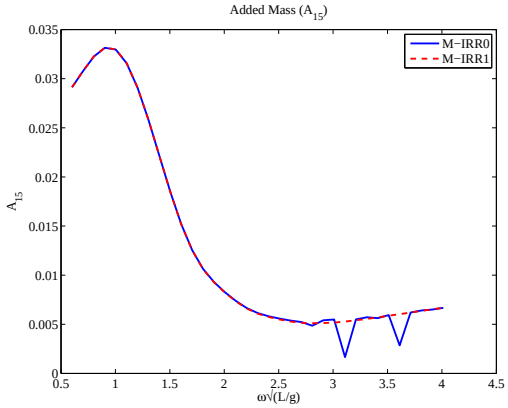

Figure 4.79: Added mass A15 vs frequency $\omega\sqrt{L/g}$

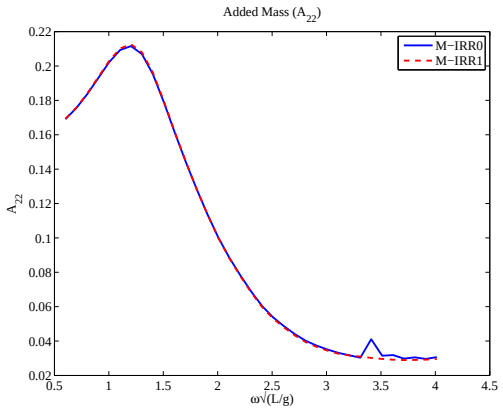

Figure 4.80: Added mass A22 vs frequency $\omega\sqrt{L/g}$

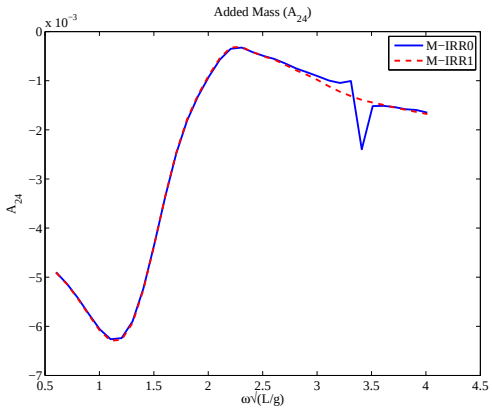

Figure 4.81: Added mass A24 vs frequency $\omega\sqrt{L/g}$

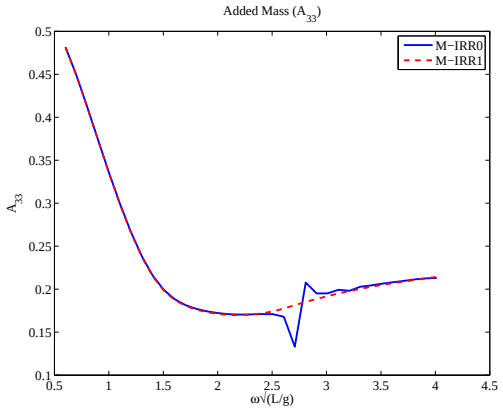

Figure 4.82: Added mass A33 vs frequency $\omega\sqrt{L/g}$

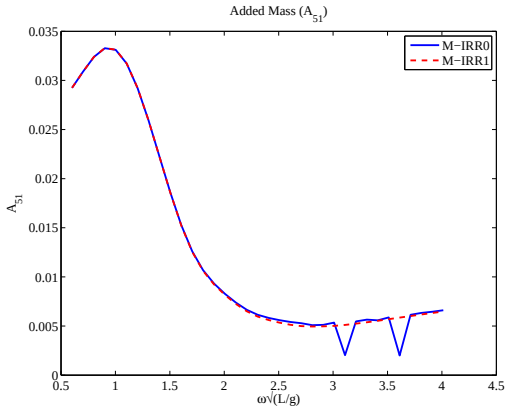

Figure 4.83: Added mass A51 vs frequency $\omega\sqrt{L/g}$

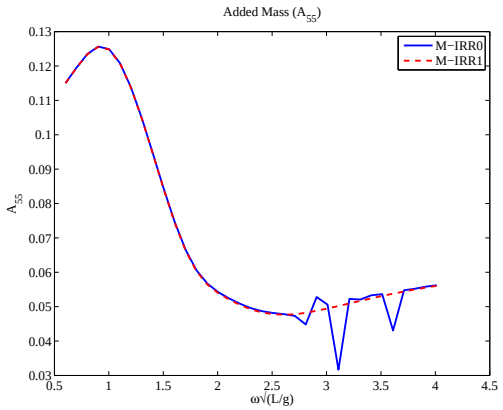

Figure 4.84: Added mass A55 vs frequency $\omega\sqrt{L/g}$

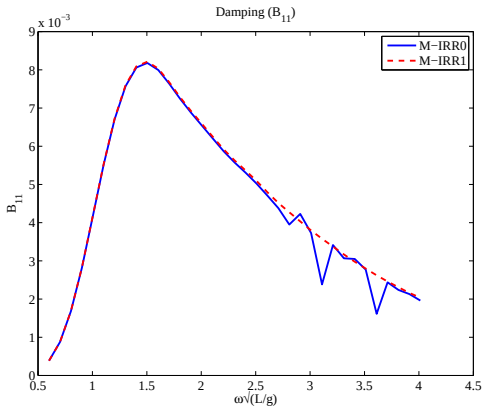

Figure 4.85: Damping B11 vs frequency $\omega\sqrt{L/g}$

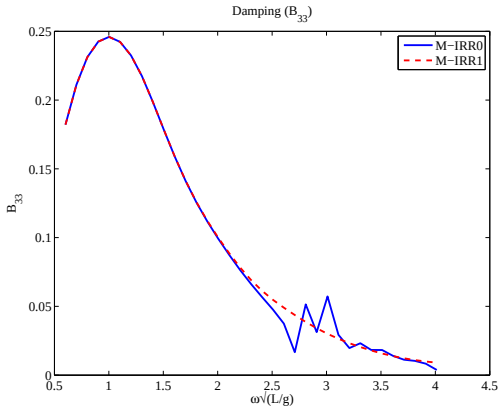

Figure 4.86: Damping B33 vs frequency $\omega\sqrt{L/g}$

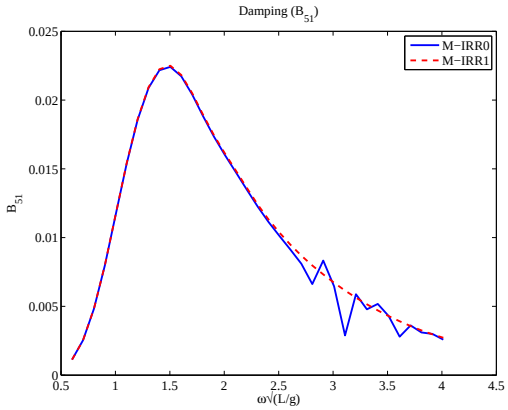

Figure 4.87: Damping B51 vs frequency $\omega\sqrt{L/g}$

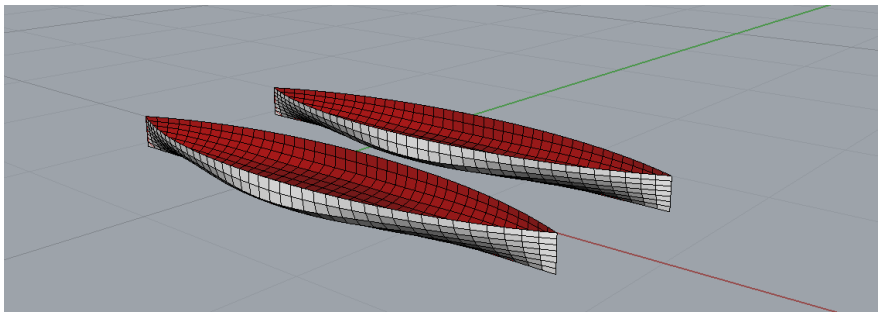

Figure 4.88: Perspective view of 2 Wigley hulls (separation 1m)

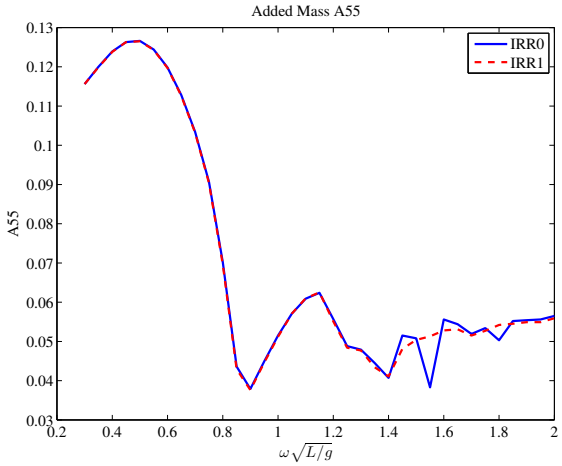

Figure 4.89: Added mass A55 vs frequency $\omega\sqrt{L/g}$

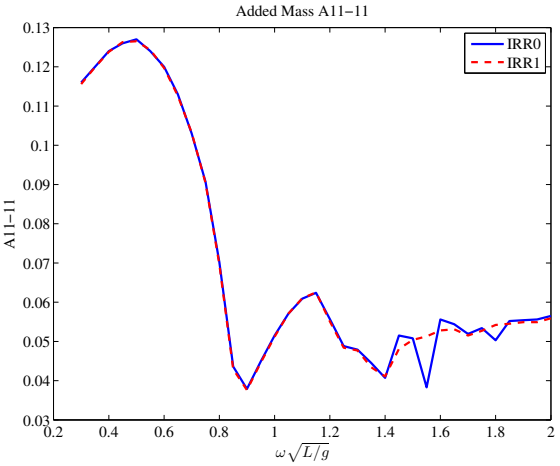

Figure 4.90: Added mass A11-11 vs frequency $\omega\sqrt{L/g}$

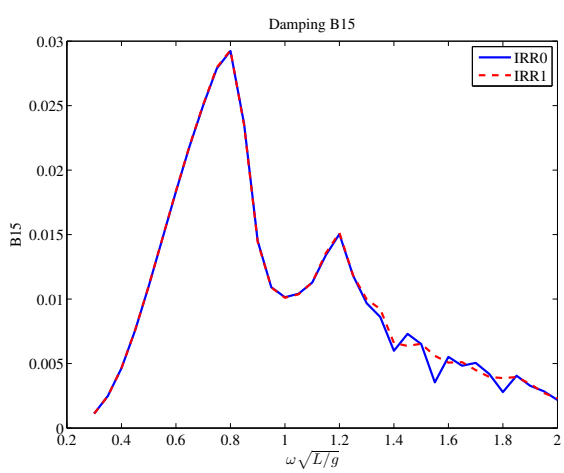

Figure 4.91: Damping B15 vs frequency $\omega\sqrt{L/g}$

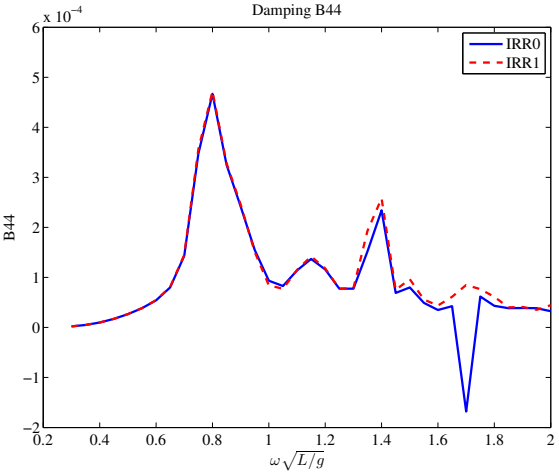

Figure 4.92: Damping B44 vs frequency $\omega\sqrt{L/g}$

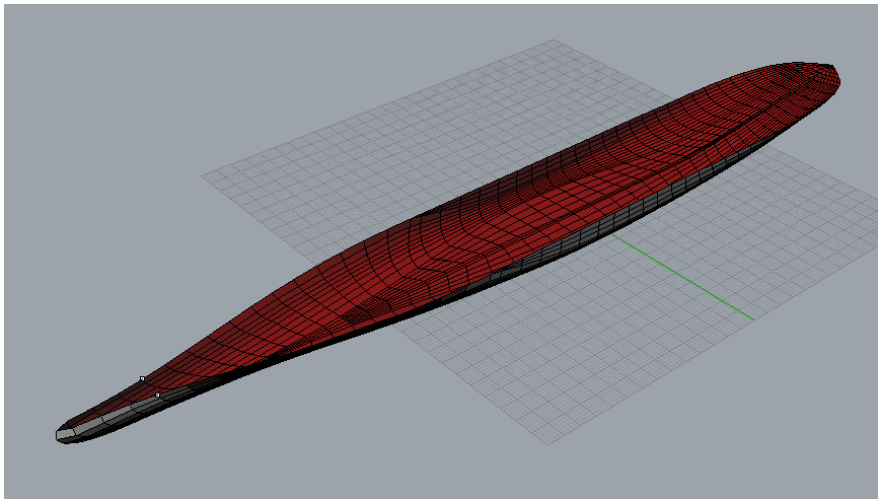

Figure 4.93: Perspective View of Bob Hope

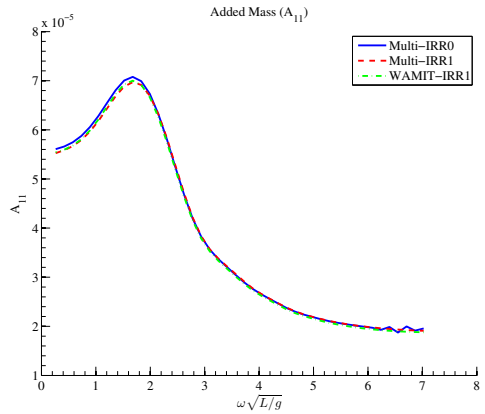

Figure 4.94: Added Mass A11 vs Frequency $\omega\sqrt{L/g}$

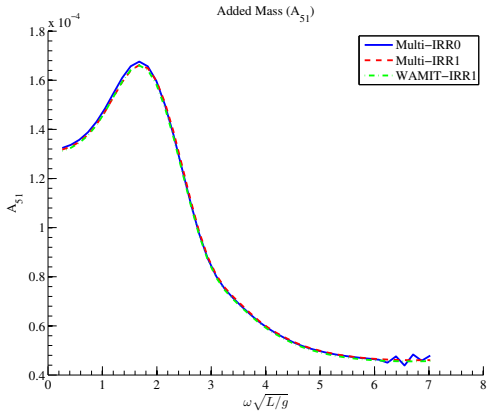

Figure 4.95: Added Mass A51 vs Frequency $\omega\sqrt{L/g}$

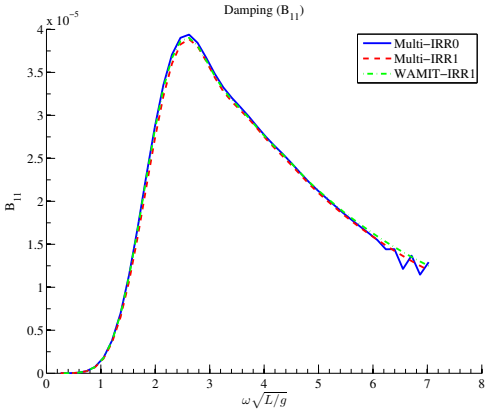

Figure 4.96: Added Mass B11 vs Frequency $\omega\sqrt{L/g}$

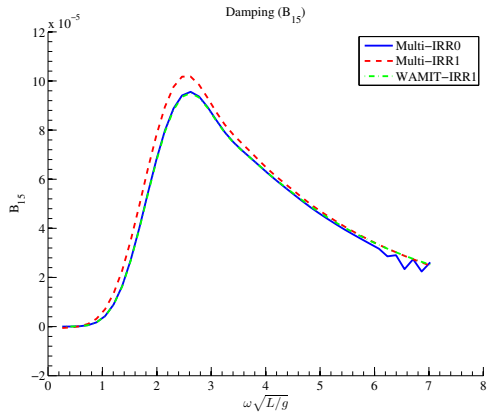

Figure 4.97: Added Mass B15 vs Frequency $\omega\sqrt{L/g}$

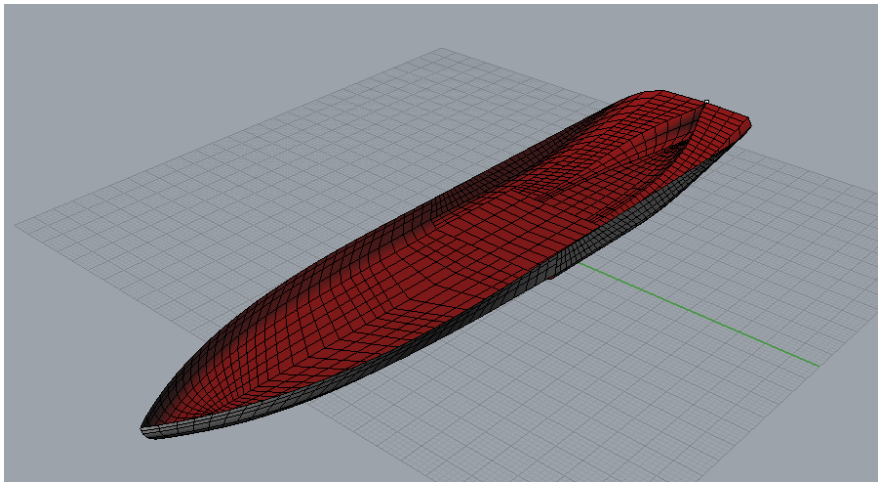

Figure 4.98: Perspective View of BOBO

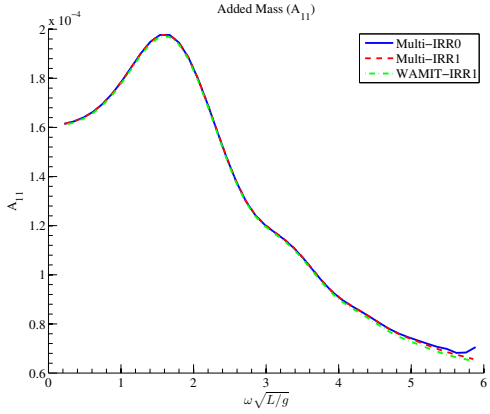

Figure 4.99: Added Mass A11 vs Frequency $\omega\sqrt{L/g}$

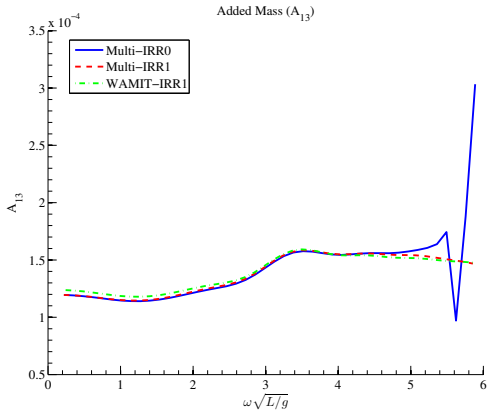

Figure 4.100: Added Mass A13 vs Frequency $\omega\sqrt{L/g}$

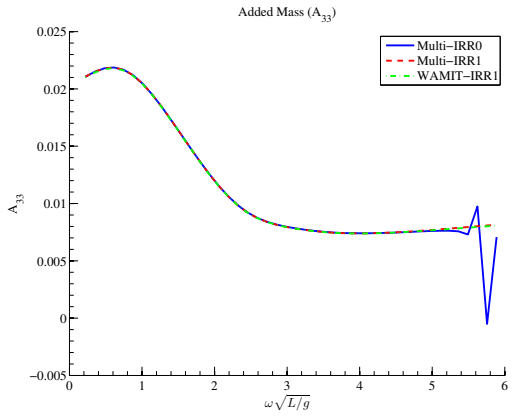

Figure 4.101: Added Mass A33 vs Frequency $\omega\sqrt{L/g}$

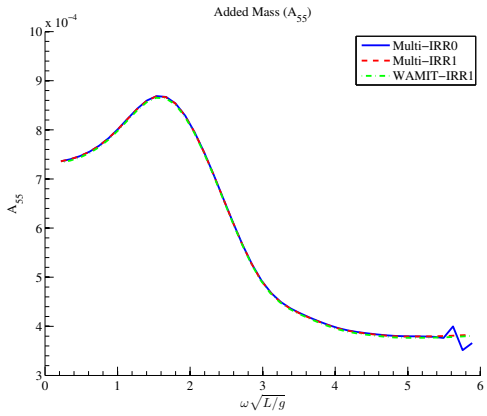

Figure 4.102: Added Mass A55 vs Frequency $\omega\sqrt{L/g}$

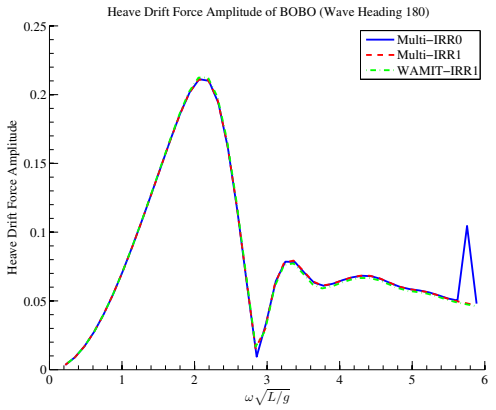

Figure 4.103: Heave Drift Force vs Frequency $\omega\sqrt{L/g}$

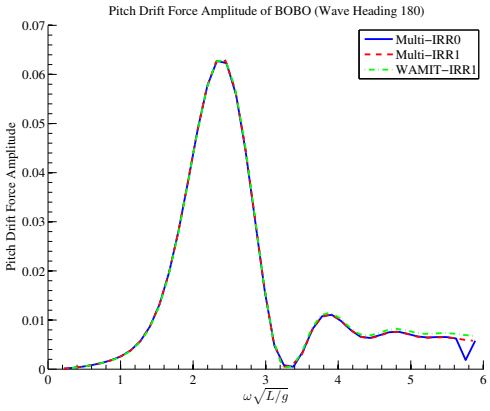

Figure 4.104: Pitch Drift Force vs Frequency $\omega\sqrt{L/g}$

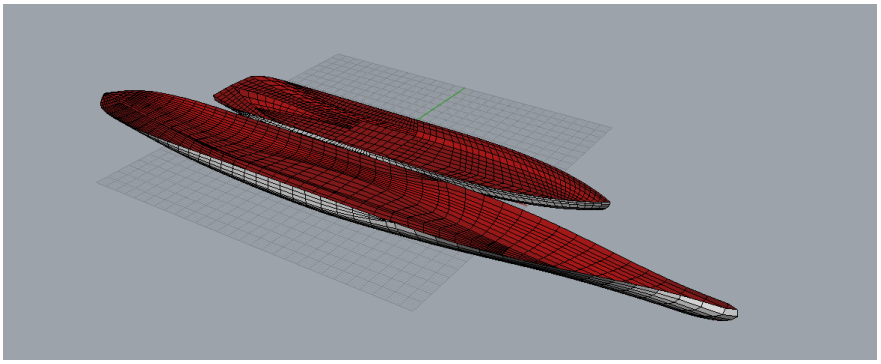

Figure 4.105: Perspective View of Bob Hope-BOBO (separation 3m)

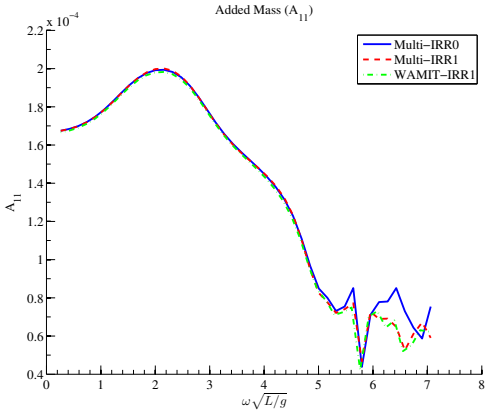

Figure 4.106: Added Mass A11 vs Frequency $\omega\sqrt{L/g}$

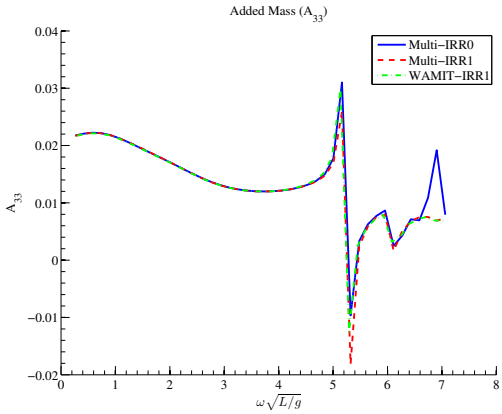

Figure 4.107: Added Mass A33 vs Frequency $\omega\sqrt{L/g}$

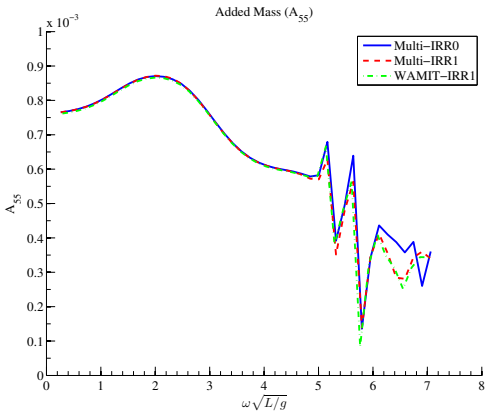

Figure 4.108: Added Mass A55 vs Frequency $\omega\sqrt{L/g}$

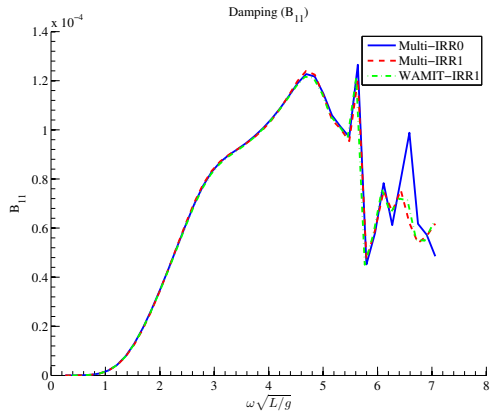

Figure 4.109: Added Mass B11 vs Frequency $\omega\sqrt{L/g}$

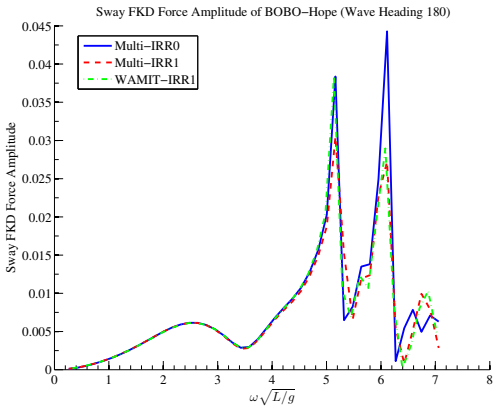

Figure 4.110: Sway FKD Force vs Frequency $\omega\sqrt{L/g}$

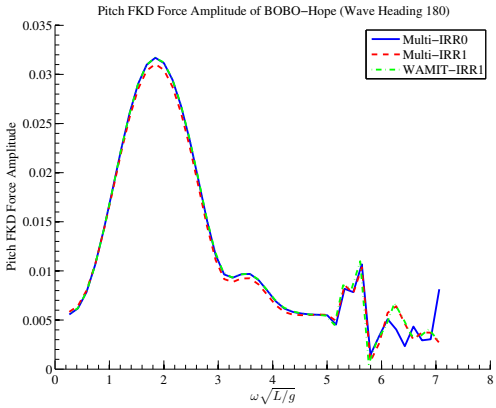

Figure 4.111: Pitch FKD Force vs Frequency $\omega\sqrt{L/g}$

5. 2ND ORDER PROBLEM [1]

5.1 Theory and Formula

In this chapter, we will discuss about the 2nd order force and its time average.

When we are calculating forces or moments, we will use the following equations:

$$\vec{F} = -\iint_S P\,\vec{n}\,dS = -(\iint_{S_m} + \iint_{\Delta S})P\,\vec{n}\,dS$$
$$\vec{M} = -\iint_S P[(\vec{X} - \vec{X}_0) \times \vec{n}]dS = -(\iint_{S_m} + \iint_{\Delta S})P[(\vec{X} - \vec{X}_0) \times \vec{n}]dS$$

where, S_m indicates the wet surface of the floater below $\bar{z} = 0$ when in equilibrium position. If we mark the waterline when the floater is in equilibrium position, then ΔS is the wet area between the wave elevation ζ and the marked waterline when the floater is moving. Mathematically, ΔS is the wet area between $z = \eta_3 + \eta_4 Y' - \eta_5 X'$ and wave elevation ζ.

When we substitute the perturbation relationships in Chapter 3 into the equations above, we will get the corresponding 0th, 1st, 2nd order forces and moments. Please note that the integral in the area ΔS is of order $o(\epsilon^2)$, as discussed in Appendix B.

[1] Part of the chapter is reprinted with permission from "Suppression of Irregular Frequency Effect in Hydrodynamic Problems and Free-Surface Singularity Treatment" by Yujie Liu, Jeffrey Falzarano, 2017. *Journal of Offshore Mechanics and Arctic Engineering*, Vol.139 051101 pages 1-16. Copyright 2017 by ASME.

The equations of $\vec{F}, \vec{M}$ can be:

$$\begin{aligned}
\vec{F} &= -\iint_S P\,\vec{n}\,dS \\
&= -\iint_{S_m} (P^{(0)} + \epsilon P^{(1)} + \epsilon^2 P^{(2)})(\vec{n}^{(0)} + \epsilon\vec{n}^{(1)} + \epsilon^2\vec{n}^{(2)})dS - \iint_{\Delta S} P\,\vec{n}\,dS \\
&= \vec{F}^{(0)} + \epsilon\vec{F}^{(1)} + \epsilon^2\vec{F}^{(2)} \\
\vec{M} &= -\iint_S P[(\vec{X} - \vec{X}_0) \times \vec{n}]dS \\
&= -\iint_{S_m} (P^{(0)} + \epsilon P^{(1)} + \epsilon^2 P^{(2)})[(\vec{X'} + \vec{\eta} + \vec{\alpha} \times \vec{X'} + \epsilon^2 H\vec{X'}) \times (\vec{n'}^{(0)} + \epsilon\vec{n'}^{(1)} + \epsilon^2\vec{n'}^{(2)})]dS \\
&\quad - \iint_{\Delta S} P[(\vec{X} - \vec{X}_0) \times \vec{n}]dS \\
&= \vec{M}^{(0)} + \epsilon\vec{M}^{(1)} + \epsilon^2\vec{M}^{(2)}
\end{aligned} \tag{5.1}$$

$P^{(0)}, P^{(1)}, P^{(2)}$ can be obtained as:

$$\begin{aligned}
P^{(0)} &= -\rho g z|_{S_m} \\
P^{(1)} &= -\rho\frac{\partial\Phi^{(1)}}{\partial t} - \rho g(\eta_3^{(1)} + \eta_4^{(1)}Y' - \eta_5^{(1)}X') \\
P^{(2)} &= -\rho\frac{\partial\Phi^{(2)}}{\partial t} - \rho\frac{1}{2}\vec{\nabla}\Phi^{(1)} \cdot \vec{\nabla}\Phi^{(1)} - \rho g\vec{k} \cdot (\vec{\eta}^{(2)} + \vec{\alpha}^{(2)} \times \vec{X'} + H\vec{X'}) \\
&\quad - \rho\frac{\partial}{\partial t}\vec{\nabla}\Phi^{(1)}(\vec{\eta}^{(1)} + \vec{\alpha}^{(1)} \times \vec{X'})
\end{aligned}$$

where, H is defined as:

$$H = \begin{bmatrix}
-\frac{1}{2}(\eta_5^{(1)^2} + \eta_6^{(1)^2}) & 0 & 0 \\
\eta_4^{(1)}\eta_5^{(1)} & -\frac{1}{2}(\eta_4^{(1)^2} + \eta_6^{(1)^2}) & 0 \\
\eta_4^{(1)}\eta_6^{(1)} & \eta_5^{(1)}\eta_6^{(1)} & -\frac{1}{2}(\eta_4^{(1)^2} + \eta_5^{(1)^2})
\end{bmatrix}$$

To sum up, the expressions of forces for the sea keeping problem are as below:

$$
\begin{aligned}
\vec{F}^{(0)} &= \rho g V \vec{k} \\
\vec{F}^{(1)} &= -\rho g A_{wp}(\eta_3^{(1)} + \eta_4^{(1)} y_f - \eta_5^{(1)} x_f)\vec{k} + \iint_{S_m} \rho \frac{\partial \Phi^{(1)}}{\partial t} \vec{n'} dS \\
\vec{F}^{(2)} &= \vec{\alpha}^{(1)} \times \vec{F}^{(1)} \\
&\quad + \iint_{S_m} \frac{1}{2} \rho \vec{\nabla} \Phi^{(1)} \cdot \vec{\nabla} \Phi^{(1)} \, \vec{n'} dS \\
&\quad + \rho g[-x_f A_{wp} \eta_4^{(1)} \eta_6^{(1)} - y_f A_{wp} \eta_5^{(1)} \eta_6^{(1)} - \frac{1}{2} Z_0 A_{wp} (\eta_4^{(1)^2} + \eta_5^{(1)^2})]\vec{k} \\
&\quad + \iint_{S_m} \rho [\frac{\partial}{\partial t} \vec{\nabla} \Phi^{(1)} \cdot (\vec{\eta}^{(1)} + \vec{\alpha}^{(1)} \times \vec{X'})] \vec{n'} dS \\
&\quad - \int_{C_{wl}} dl \, \frac{1}{2} \, \rho g \zeta_r^{(1)^2} \vec{n'} \frac{1}{\sqrt{1 - n_3'^2}} \\
&\quad + \iint_{S_m} \rho \frac{\partial \Phi^{(2)}}{\partial t} \, \vec{n'} dS - \rho g (A_{wp} \eta_3^{(2)} + y_f A_{wp} \eta_4^{(2)} - x_f A_{wp} \eta_5^{(2)}) \vec{k}
\end{aligned}
$$

The expressions of the moments are:

$$
\begin{aligned}
\vec{M}^{(0)} &= \rho g y_{CB} V \vec{i} - \rho g x_{CB} V \vec{j} \\
\vec{M}^{(1)} &= \iint_{S_m} (\rho \frac{\partial \Phi^{(1)}}{\partial t})(\vec{X'} \times \vec{n'}) dS \\
&\quad + \rho g [x_{CB} V \eta_6^{(1)} + V \eta_2^{(1)} - y_f A_{wp} \eta_3^{(1)} - I_{YY}^A \eta_4^{(1)} - z_{CB} V \eta_4^{(1)} + I_{XY}^A \eta_5^{(1)}] \vec{i} \\
&\quad + \rho g [y_{CB} V \eta_6^{(1)} - V \eta_1^{(1)} + x_f A_{wp} \eta_3^{(1)} + I_{XY}^A \eta_4^{(1)} - z_{CB} V \eta_5^{(1)} - I_{XX}^A \eta_5^{(1)}] \vec{j} \\
\vec{M}^{(2)} &= - \rho g V [\eta_4^{(1)} \eta_6^{(1)} \frac{I_{XY}^A}{V} + \eta_5^{(1)} \eta_6^{(1)} \frac{I_{YY}^A}{V} + \eta_5^{(1)} \eta_6^{(1)} z_{CB} + \frac{1}{2} (\eta_4^{(1)^2} - \eta_6^{(1)^2}) y_{CB} \\
&\quad + \frac{1}{2} (\eta_4^{(1)^2} + \eta_5^{(1)^2}) y_f Z_0 \frac{A_{wp}}{V} - x_{CB} \eta_4^{(1)} \eta_5^{(1)} + \eta_1^{(1)} \eta_6^{(1)}] \vec{i} \\
&\quad + \rho g V [\eta_4^{(1)} \eta_6^{(1)} (z_{CB} + \frac{I_{XX}^A}{V}) + \eta_5^{(1)} \eta_6^{(1)} \frac{I_{XY}^A}{V} - \frac{1}{2} x_{CB} (\eta_6^{(1)^2} - \eta_5^{(1)^2}) \\
&\quad + \frac{1}{2} (\eta_4^{(1)^2} + \eta_5^{(1)^2}) x_f Z_0 \frac{A_{wp}}{V} - \eta_2^{(1)} \eta_6^{(1)}] \vec{j} \\
&\quad + \rho g V [-\eta_4^{(1)} \eta_6^{(1)} y_{CB} + \eta_5^{(1)} \eta_6^{(1)} x_{CB} + \eta_1^{(1)} \eta_4^{(1)} + \eta_2^{(1)} \eta_5^{(1)}] \vec{k} \\
&\quad + \vec{\alpha}^{(1)} \times \vec{M}^{(1)} + \vec{\eta}^{(1)} \times \vec{F}^{(1)} \\
&\quad - \int_{C_{wl}} dl \frac{1}{2} \rho g \zeta_r^{(1)^2} (\vec{X'} \times \vec{n'}) \frac{1}{\sqrt{1 - n_3'^2}} \\
&\quad + \iint_{S_m} [\frac{1}{2} \rho (\vec{\nabla} \Phi^{(1)} \cdot \vec{\nabla} \Phi^{(1)}) + \rho (\frac{\partial}{\partial t}) \vec{\nabla} \Phi^{(1)} (\vec{\eta}^{(1)} + \vec{\alpha}^{(1)} \times \vec{X'})] (\vec{X'} \times \vec{n'}) dS \\
&\quad + \iint_{S_m} \rho \frac{\partial \Phi^{(2)}}{\partial t} (\vec{X'} \times \vec{n'}) dS \\
&\quad + \rho g [V \eta_2^{(2)} - A_{wp} y_f \eta_3^{(2)} - (I_{YY}^A + V z_{CB}) \eta_4^{(2)} + I_{XY}^A \eta_5^{(2)} + V x_{CB} \eta_6^{(2)}] \vec{i} \\
&\quad + \rho g [-V \eta_1^{(2)} + A_{wp} x_f \eta_3^{(2)} + I_{XY}^A \eta_4^{(2)} - (I_{XX}^A + V z_{CB}) \eta_5^{(2)} + V y_{CB} \eta_6^{(2)}] \vec{j}
\end{aligned}
$$

where,

$$\zeta_r^{(1)} = \zeta^{(1)} - (\eta_3 + \eta_4 Y' - \eta_5 X')$$
$$I_{XY}^A = -\iint_{S_m} Y'X'n_3' dS = \iint_{S_m} Y'X' dxdy$$
$$I_{XX}^A = -\iint_{S_m} X'X'n_3' dS = \iint_{S_m} X'X' dxdy$$
$$I_{YY}^A = -\iint_{S_m} Y'Y'n_3' dS = \iint_{S_m} Y'Y' dxdy$$

When the floater has a small forward speed, the expressions for the forces will be:

$$\vec{F}^{(0)} = \rho g V \vec{k}$$
$$\vec{F}^{(1)} = -\rho g A_{wp}(\eta_3^{(1)} + \eta_4^{(1)} y_f - \eta_5^{(1)} x_f)\vec{k} + \iint_{S_m} \rho(\frac{\partial}{\partial \bar{t}} - U\frac{\partial}{\partial \bar{x}})\overline{\Phi}_{rel}^{(1)} \vec{n'} dS$$
$$\begin{aligned}\vec{F}^{(2)} = {} & \vec{\alpha}^{(1)} \times \vec{F}^{(1)} \\ & + \iint_{S_m} \frac{1}{2}\rho \vec{\nabla}\overline{\Phi}_{rel}^{(1)} \cdot \vec{\nabla}\overline{\Phi}_{rel}^{(1)} \vec{n'} dS \\ & + \rho g[-x_f A_{wp}\eta_4^{(1)}\eta_6^{(1)} - y_f A_{wp}\eta_5^{(1)}\eta_6^{(1)} - \frac{1}{2}Z_0 A_{wp}(\eta_4^{(1)^2} + \eta_5^{(1)^2})]\vec{k} \\ & + \iint_{S_m} \rho[(\frac{\partial}{\partial \bar{t}} - U\frac{\partial}{\partial \bar{x}})\vec{\nabla}\Phi_{rel}^{(1)} \cdot (\vec{\eta}^{(1)} + \vec{\alpha}^{(1)} \times \vec{X'})]\vec{n'} dS \\ & - \int_{C_{wl}} dl \, \frac{1}{2} \rho g \zeta_r^{(1)^2} \vec{n'} \frac{1}{\sqrt{1 - n_3'^2}} \\ & + \iint_{S_m} \rho(\frac{\partial}{\partial \bar{t}} - U\frac{\partial}{\partial \bar{x}})\bar{\Phi}_{rel}^{(2)} \vec{n'} dS - \rho g(A_{wp}\eta_3^{(2)} + y_f A_{wp}\eta_4^{(2)} - x_f A_{wp}\eta_5^{(2)})\vec{k}\end{aligned}$$

The expressions of the moments become:

$$
\begin{aligned}
\vec{M}^{(0)} &= \rho g y_{CB} V \vec{i} - \rho g x_{CB} V \vec{j} \\
\vec{M}^{(1)} &= \iint_{S_m} [\rho(\frac{\partial}{\partial \bar{t}} - U\frac{\partial}{\partial \bar{x}})\overline{\Phi}^{(1)}_{rel}](\vec{X}' \times \vec{n'}) dS \\
&\quad + \rho g[x_{CB} V \eta_6^{(1)} + V\eta_2^{(1)} - y_f A_{wp}\eta_3^{(1)} - I^A_{YY}\eta_4^{(1)} - z_{CB}V\eta_4^{(1)} + I^A_{XY}\eta_5^{(1)}]\vec{i} \\
&\quad + \rho g[y_{CB} V \eta_6^{(1)} - V\eta_1^{(1)} + x_f A_{wp}\eta_3^{(1)} + I^A_{XY}\eta_4^{(1)} - z_{CB}V\eta_5^{(1)} - I^A_{XX}\eta_5^{(1)}]\vec{j} \\
\vec{M}^{(2)} &= -\rho g V[\eta_4^{(1)}\eta_6^{(1)}\frac{I^A_{XY}}{V} + \eta_5^{(1)}\eta_6^{(1)}\frac{I^A_{YY}}{V} + \eta_5^{(1)}\eta_6^{(1)} z_{CB} + \frac{1}{2}(\eta_4^{(1)^2} - \eta_6^{(1)^2}) y_{CB} \\
&\quad + \frac{1}{2}(\eta_4^{(1)^2} + \eta_5^{(1)^2}) y_f Z_0 \frac{A_{wp}}{V} - x_{CB}\eta_4^{(1)}\eta_5^{(1)} + \eta_1^{(1)}\eta_6^{(1)}]\vec{i} \\
&\quad + \rho g V[\eta_4^{(1)}\eta_6^{(1)}(z_{CB} + \frac{I^A_{XX}}{V}) + \eta_5^{(1)}\eta_6^{(1)}\frac{I^A_{XY}}{V} - \frac{1}{2}x_{CB}(\eta_6^{(1)^2} - \eta_5^{(1)^2}) \\
&\quad + \frac{1}{2}(\eta_4^{(1)^2} + \eta_5^{(1)^2}) x_f Z_0 \frac{A_{wp}}{V} - \eta_2^{(1)}\eta_6^{(1)}]\vec{j} \\
&\quad + \rho g V[-\eta_4^{(1)}\eta_6^{(1)} y_{CB} + \eta_5^{(1)}\eta_6^{(1)} x_{CB} + \eta_1^{(1)}\eta_4^{(1)} + \eta_2^{(1)}\eta_5^{(1)}]\vec{k} \\
&\quad + \vec{\alpha}^{(1)} \times \vec{M}^{(1)} + \vec{\eta}^{(1)} \times \vec{F}^{(1)} \\
&\quad - \int_{C_{wl}} dl \frac{1}{2}\rho g \zeta_r^{(1)^2}(\vec{X}' \times \vec{n'}) \frac{1}{\sqrt{1 - n_3'^2}} \\
&\quad + \iint_{S_m} [\frac{1}{2}\rho(\vec{\nabla}\overline{\Phi}^{(1)}_{rel} \cdot \vec{\nabla}\overline{\Phi}^{(1)}_{rel}) + \rho(\frac{\partial}{\partial \bar{t}} - U\frac{\partial}{\partial \bar{x}})\vec{\nabla}\overline{\Phi}^{(1)}_{rel}(\vec{\eta}^{(1)} + \vec{\alpha}^{(1)} \times \vec{X}')](\vec{X}' \times \vec{n'}) dS \\
&\quad + \iint_{S_m} [\rho(\frac{\partial}{\partial \bar{t}} - U\frac{\partial}{\partial \bar{x}})\overline{\Phi}^{(2)}_{rel}](\vec{X}' \times \vec{n'}) dS \\
&\quad + \rho g[V\eta_2^{(2)} - A_{wp} y_f \eta_3^{(2)} - (I^A_{YY} + V z_{CB})\eta_4^{(2)} + I^A_{XY}\eta_5^{(2)} + V x_{CB}\eta_6^{(2)}]\vec{i} \\
&\quad + \rho g[-V\eta_1^{(2)} + A_{wp} x_f \eta_3^{(2)} + I^A_{XY}\eta_4^{(2)} - (I^A_{XX} + V z_{CB})\eta_5^{(2)} + V y_{CB}\eta_6^{(2)}]\vec{j}
\end{aligned}
$$

In the expressions of $\vec{F}^{(2)}$ and $\vec{M}^{(2)}$, there exist the terms $\vec{F}^{(1)}$ and $\vec{M}^{(1)}$. In our investigation, there may be some issues in the identity equation in Salvesen[112]. Then the expression $\vec{F}^{(1)}$ and $\vec{M}^{(1)}$ containing the radiation forces may lead to some issues in the end. Thus, we choose not to substitute the expressions of $\vec{F}^{(1)}$ and $\vec{M}^{(1)}$ herein into $\vec{F}^{(2)}$ and $\vec{M}^{(2)}$. The alternative expressions of $\vec{F}^{(1)}$ and $\vec{M}^{(1)}$ can be found via the equations of motion, resulted from the conservation of momentum and angular momentum.

$$\vec{F}^{(1)} = m\frac{d^2\vec{\eta}^{(1)}}{dt^2} + m\frac{d^2\vec{\alpha}^{(1)}}{dt^2} \times \vec{X}'_g - \vec{F}^{(1)}_{ex}$$
$$\vec{M}^{(1)} = \iiint_V dm\vec{X}' \times \frac{d^2}{dt^2}(\vec{\eta}^{(1)} + \vec{\alpha}^{(1)} \times \vec{X}') - \vec{X}'_g \times (-mg\vec{k}) - \vec{T}^{(1)} - (\vec{X}_F - \vec{X}_0) \times \vec{F}^{(1)}_{ex}$$

where, $\vec{X}'_g$ is the gravity center of the floater, $\vec{F}^{(1)}_{ex}$ is the 1st-order external force, $\vec{X}_F$ is the application point of the force $\vec{F}^{(1)}_{ex}$, $\vec{X}_0$ is the origin of the vessel translating coordinate, $\vec{T}^{(1)}$ is the 1st-order external moment.

In the expressions of $\vec{F}^{(2)}$, $\vec{M}^{(2)}$, we may notice there exist the 2nd-order potential $\overline{\Phi}^{(2)}_{rel}$ and the 6 DOF motions $\eta^{(2)}_j, j = 1 \sim 6$. However, up to this step, we have not solved for the terms except the 2nd-order incident potential. To dig out more information from the 2nd-order forces and moments, we choose to take the time average of $\vec{F}^{(2)}$ and $\vec{M}^{(2)}$ so that $\overline{\Phi}^{(2)}_{rel}$ and $\eta^{(2)}_j (j = 1 \sim 6)$ will vanish while the contribution from the 1st-order terms remains.

5.2 Results and Discussion

In this section, we will compare the results from MDL Multi DYN against those from WAMIT version 5 and version 6.

From the Figure 5.1 and 5.2, we can conclude that the results from MDL Multi DYN are in a good agreement with WAMITv5 except for the resonance region. It may be due to the difference in the numerical implementations (definitions of panel centroid, matrix solver etc) between the two programs.

Based on the comparison between the zero-speed case and the nonzero-speed case in Figure 5.3, we may find that the peak of the curve is slightly shifted to the lower frequency region. The amplitude is enhanced in the heave and roll direction, which implies that the nonlinear phenomenon may be more likely to happen.

We need to assume the forward speed is small or the floater is a slender body in order to use the approximation method to evaluate the nonzero speed case. It is interesting to find the upper limit within which the approach can still provide effective results.

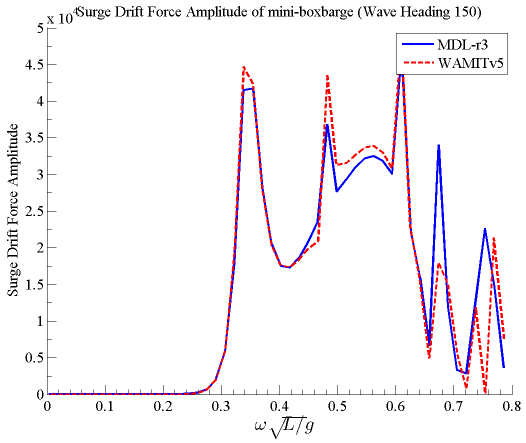

(a) Surge Drift Force vs $\omega\sqrt{L/g}$

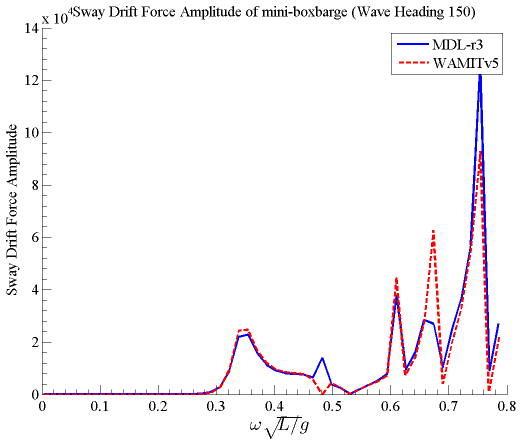

(b) Sway Drift Force vs $\omega\sqrt{L/g}$

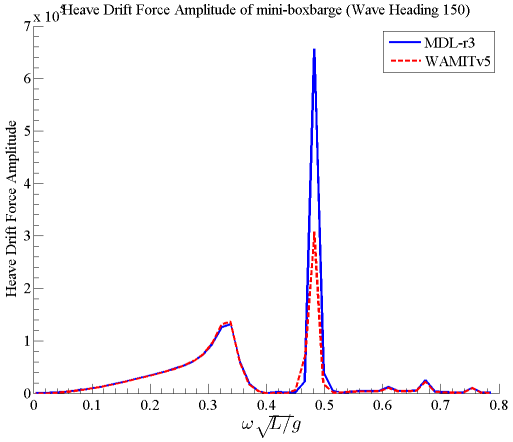

(c) Heave Drift Force vs $\omega\sqrt{L/g}$

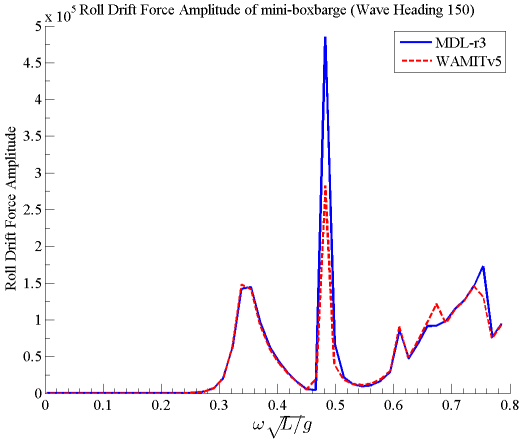

(d) Roll Drift Force vs $\omega\sqrt{L/g}$

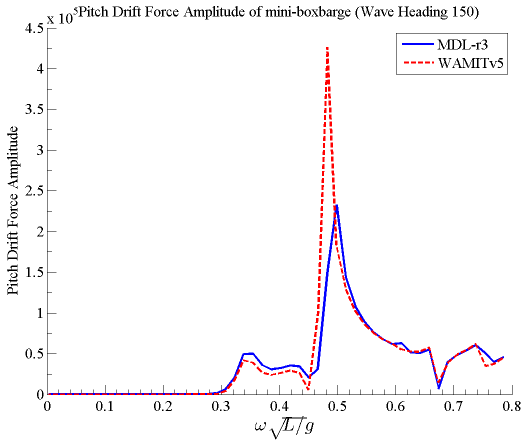

(e) Pitch Drift Force vs $\omega\sqrt{L/g}$

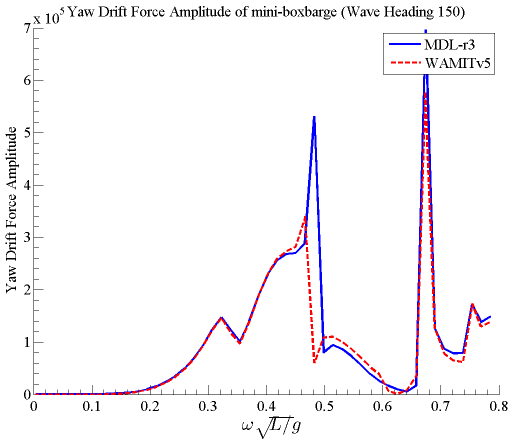

(f) Yaw Drift Force vs $\omega\sqrt{L/g}$

Figure 5.1: A Comparison of one Mini Box Barge MDL (MDL Multi DYN vs WAMITv5): Drift Force when Wave Heading Angle = 150

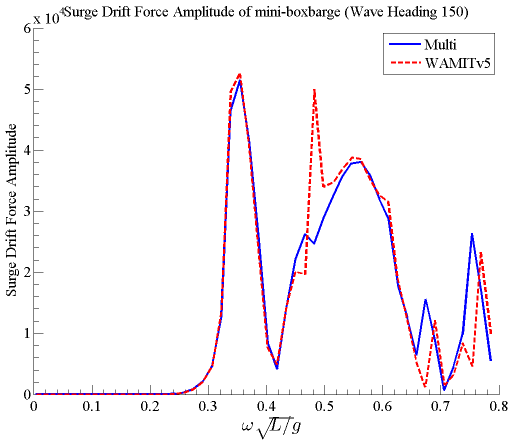

(a) Surge Drift Force vs $\omega\sqrt{L/g}$

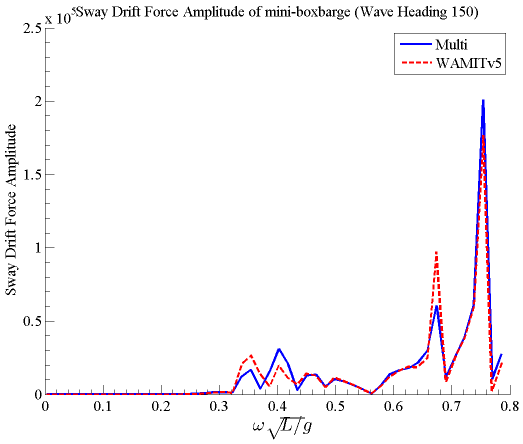

(b) Sway Drift Force vs $\omega\sqrt{L/g}$

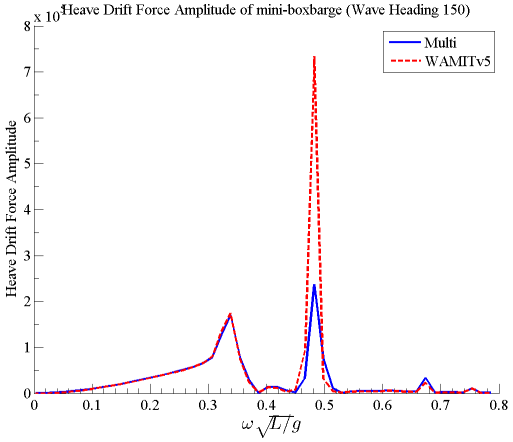

(c) Heave Drift Force vs $\omega\sqrt{L/g}$

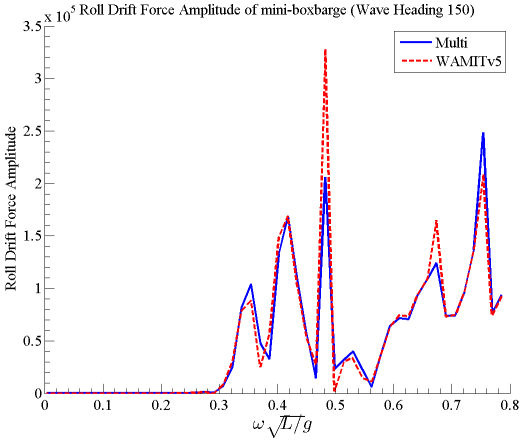

(d) Roll Drift Force vs $\omega\sqrt{L/g}$

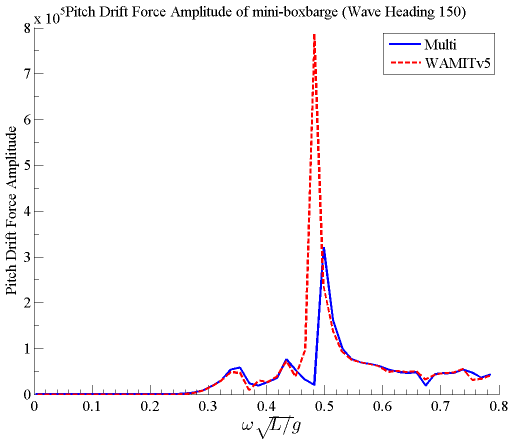

(e) Pitch Drift Force vs $\omega\sqrt{L/g}$

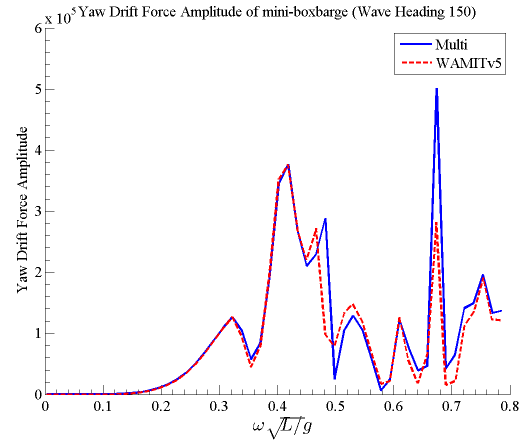

(f) Yaw Drift Force vs $\omega\sqrt{L/g}$

Figure 5.2: A Comparison of Two Mini Box Barges (MDL Multi DYN vs WAMITv5): Drift Force when Wave Heading Angle = 150, Separation Dist = 20

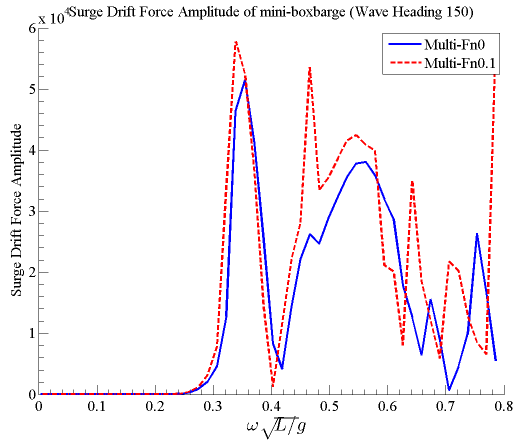

(a) Surge Drift Force vs $\omega\sqrt{L/g}$

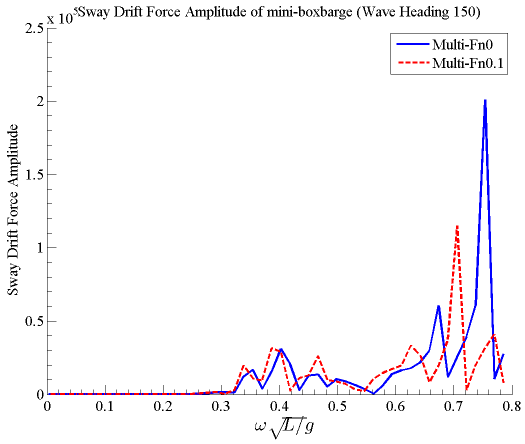

(b) Sway Drift Force vs $\omega\sqrt{L/g}$

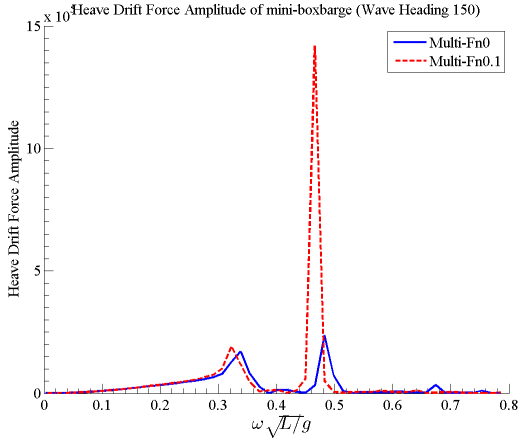

(c) Heave Drift Force vs $\omega\sqrt{L/g}$

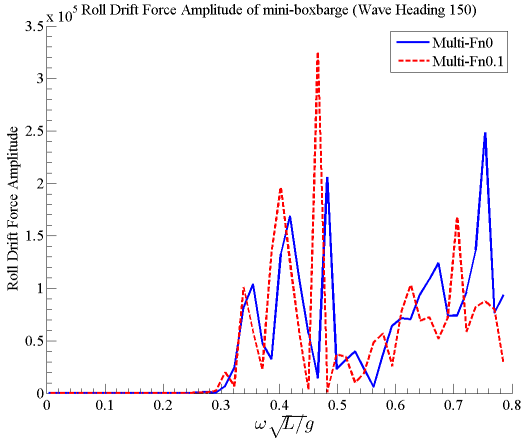

(d) Roll Drift Force vs $\omega\sqrt{L/g}$

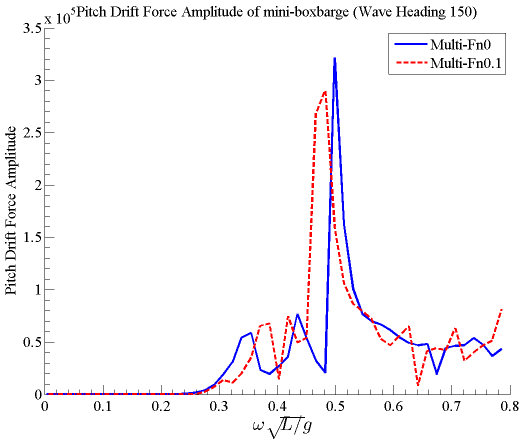

(e) Pitch Drift Force vs $\omega\sqrt{L/g}$

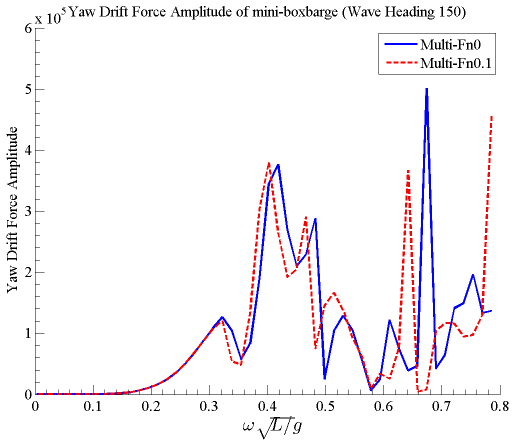

(f) Yaw Drift Force vs $\omega\sqrt{L/g}$

Figure 5.3: A Comparison of Two Mini Box Barges (Fn = 0 vs Fn = 0.1): Body 1 Drift Force when Wave Heading Angle = 150, Separation Dist = 20

When activating the module to remove the irregular frequencies, we conduct the comparisons of the results from MDL Multi DYN and WAMITv6 with or without the irregular frequency removal module. The cases include one box barge, two box barges, one hemisphere and one cylinder dock. "Multi" stands for the results from our in-house program MDL Multi DYN. IRR0 indicates the module of irregular frequency removal is off. IRR1 means that the module is activated.

In Figure 5.4, the results in the heave and pitch direction are consistent except near the resonant frequencies whether IRR = 0 or IRR = 1. In the surge direction, the result (IRR1) from WAMITv6 began to show some discrepancies while the result (IRR1) from MDL Multi DYN generally follows the trend of the curve when IRR equals 0.

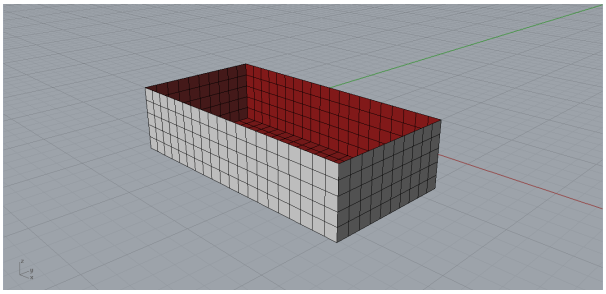

(a) Overview of One Mini Box Barge

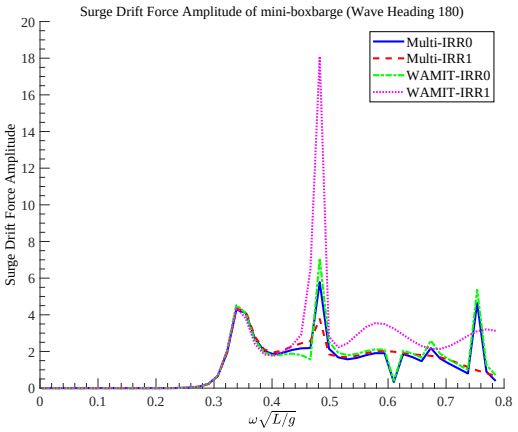

(b) Surge Drift Force vs $\omega\sqrt{L/g}$

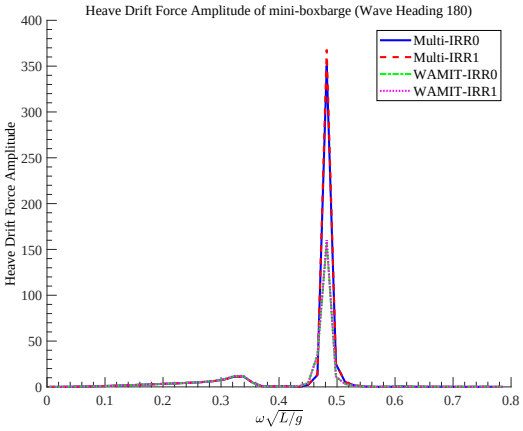

(c) Heave Drift Force vs $\omega\sqrt{L/g}$

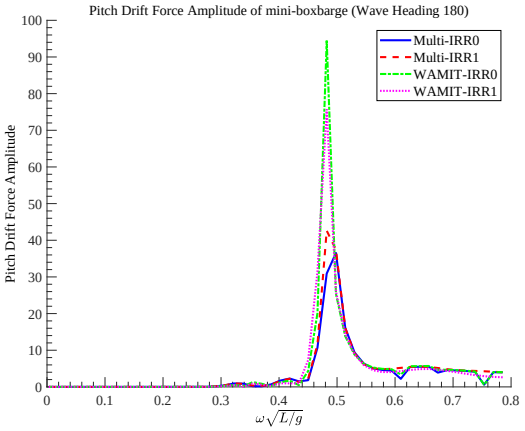

(d) Pitch Drift Force vs $\omega\sqrt{L/g}$

Figure 5.4: A Comparison of One Mini Box Barge: Drift Force when Wave Heading Angle = 180

In Figure 5.5, we can observe a similar pattern with the single body case.

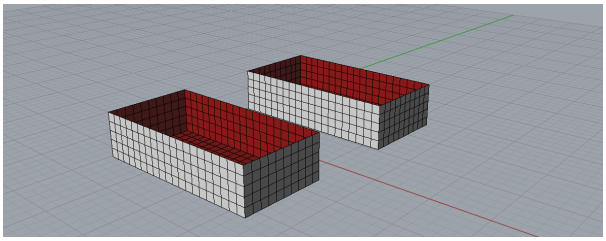

(a) Overview of Two Mini Box Barges

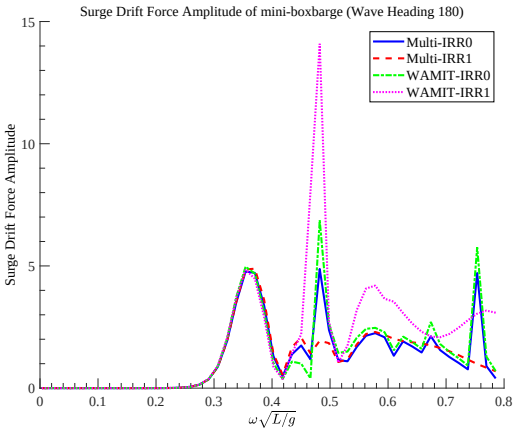

(b) Surge Drift Force vs $\omega\sqrt{L/g}$

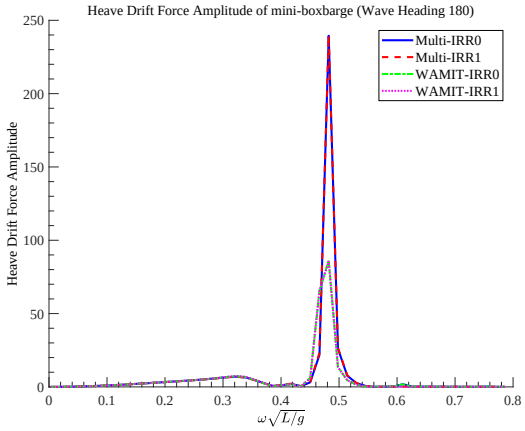

(c) Heave Drift Force vs $\omega\sqrt{L/g}$

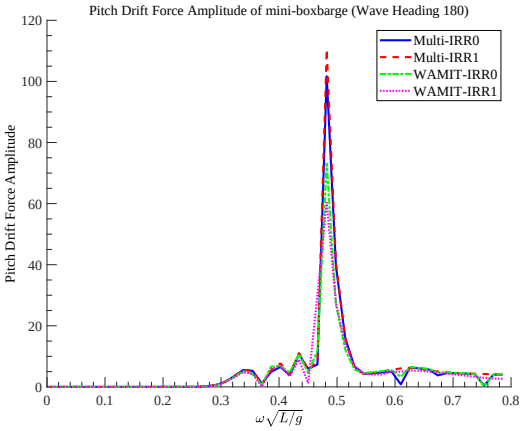

(d) Pitch Drift Force vs $\omega\sqrt{L/g}$

Figure 5.5: A Comparison of Two Mini Box Barges: Body 1 Drift Force when Wave Heading Angle = 180, Separation Dist = 20

In Figure 5.6, the results of MDL Multi DYN and WAMITv6 are in an excellent agreement. In the surge direction, there are some discrepancies in the relatively higher frequencies. The result from WAMITv6 approaches 0 when the non-dimensional radian frequency is about 2.8. Additionally, the predicted curve from MDL Multi DYN touches 0 when the radian frequency equals 2.5 and goes up afterwards, following the general trend of the results when IRR = 0. However, the values of the drift forces at the higher frequencies are relatively small. The difference between MDL Multi DYN and WAMITv6 may not be that important. Nevertheless, from this results (especially

the surge force), we need to be aware that the irregular frequency effect may be significant in the higher frequency range for the drift forces or moments.

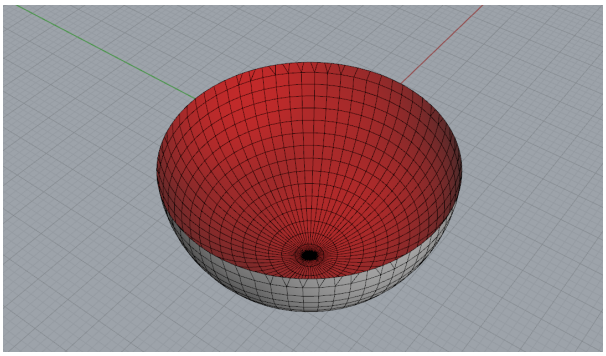

(a) Overview of One Hemisphere

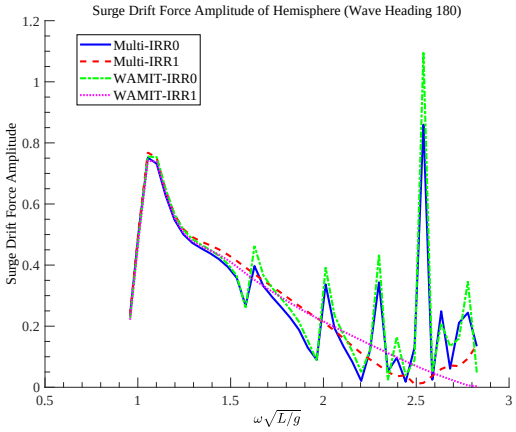

(b) Surge Drift Force vs $\omega\sqrt{L/g}$

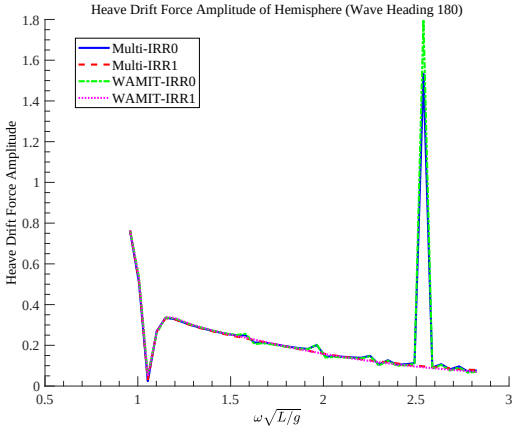

(c) Heave Drift Force vs $\omega\sqrt{L/g}$

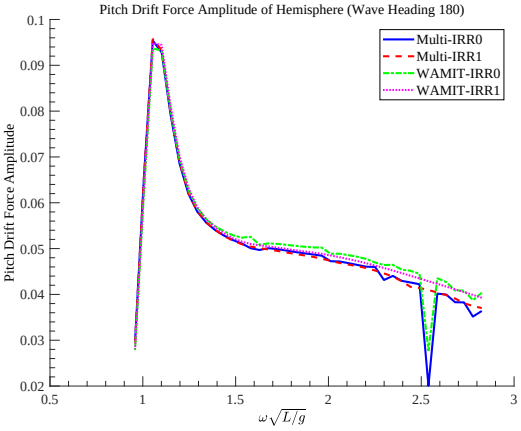

(d) Pitch Drift Force vs $\omega\sqrt{L/g}$

Figure 5.6: A Comparison of One Hemisphere: Drift Force when Wave Heading Angle = 180

In Figure 5.7, an excellent agreement between MDL Multi DYN and WAMITv6 is achieved in the heave and pitch directions whether IRR is 0 or 1. In the surge direction, the results when IRR = 0 are highly consistent. After IRR is set to be 1, the predicted curves are consistent in lower frequencies and seemingly have captured the trend of the results when IRR = 0 in the range of relatively higher frequencies. However, the discrepancy began to appear. It may be because

WAMITv6 uses a different boundary condition along the waterline or a different formula in removing the irregular frequencies.

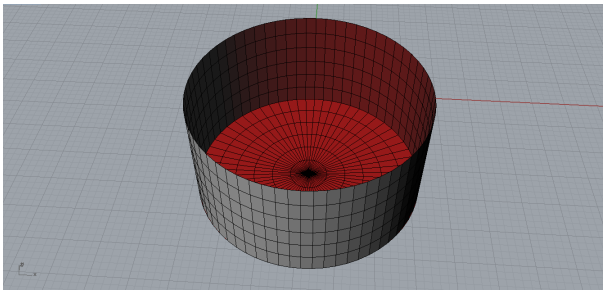

(a) Overview of One Cylindrical Dock

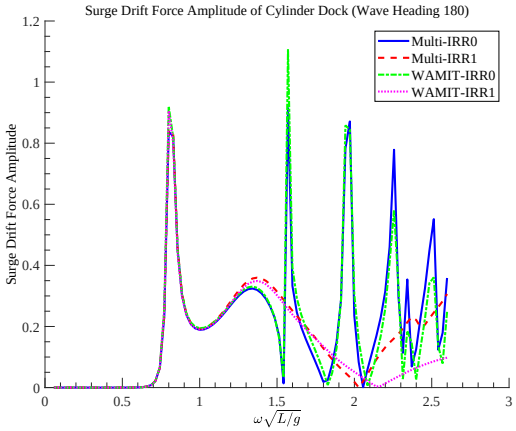

(b) Surge Drift Force vs $\omega\sqrt{L/g}$

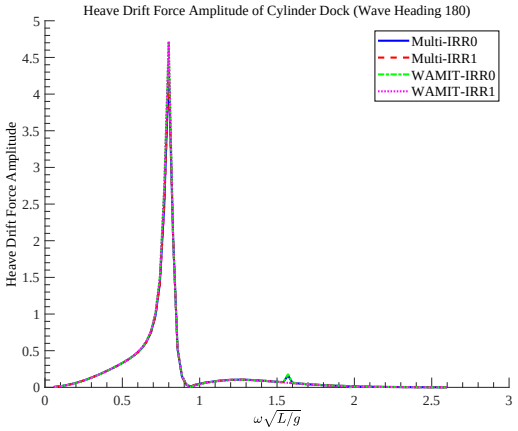

(c) Heave Drift Force vs $\omega\sqrt{L/g}$

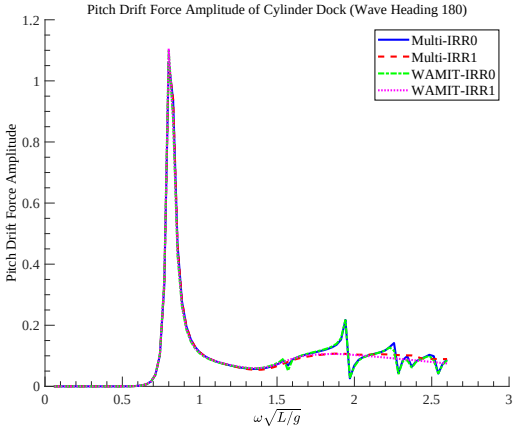

(d) Pitch Drift Force vs $\omega\sqrt{L/g}$

Figure 5.7: A Comparison of One Cylinder Dock: Drift Force when Wave Heading Angle = 180

To conclude, the results of the mean drift force from our in-house program MDL Multi DYN are highly consistent with WAMITv6 if we do not activate the irregular frequency removal module. If we have removed the irregular frequency effects, the results are consistent in the range of relatively lower frequencies. However, a discrepancy can be observed in the range of relatively

higher frequencies. This may be due to different formula or numerical techniques for the irregular frequency removal problem. To further validate the predicted results, we may need to use the experimental data.

Additionally, we demonstrate that the effects of irregular frequency may be significant in the relatively higher frequencies in the mean drift forces or moments. In practice, we may need to conduct a comparative study for the cases with or without the irregular frequency removal module, to ensure that the conclusion is more reliable.

6. IMPROVEMENT OF MEAN DRIFT FORCE CALCULATION [1]

In this chapter, we discuss the technique to improve the accuracy of the mean drift force. We have tried up to 16 methods. All of the methods showed some dependency on the geometry of the floater or the complexity of the fluid domain, except one method. The method is mathematically reasonable and shows very good performance after the convergence tests. That is the method we will discuss about. The mathematical investigation will be presented. We will prove the validity of the method and provide the convergence tests. In the end, we will conclude that it is necessary to use the improved method, which is theoretically more accurate though the experimental data is needed for the further validation.

6.1 Relative Wave Elevation

The Cartesian coordinate setting is indicated in Figure 6.1:

[1] Part of the section is reprinted with permission from "Improvement on the Accuracy of Mean Drift Force Calculation" by Yujie Liu, Jeffrey Falzarano, 2017. *Proceedings of the ASME 2017 36th International Conference on Ocean, Offshore and Arctic Engineering* pages 1-13. Copyright 2017 by ASME.

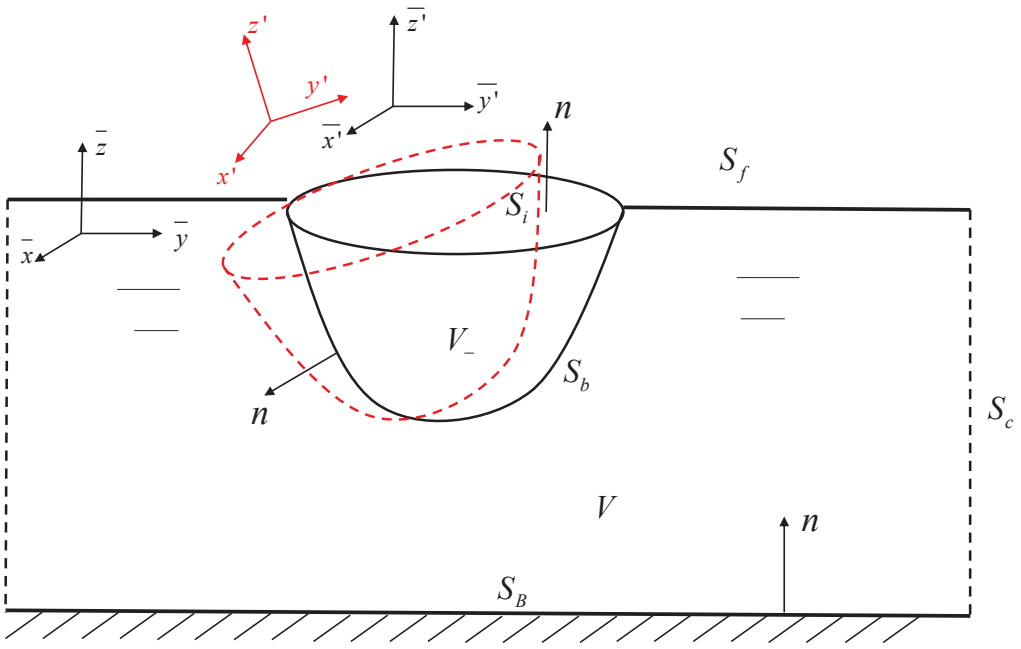

Figure 6.1: Coordinate Setting

where, n is the normal vector on a certain surface, positive when pointing outward into the fluid domain. S_B is the bottom surface, which is described by $z = -h$. S_b is the body surface. S_f is the free surface, which can be described by $z = \zeta(x, y, t)$. S_c is the control surface in the far field. S_i is the internal free surface. V is the fluid domain. V_- is the internal domain of the floater.

The calculation of the mean drift forces is a way to dig out more information from the first order problem. The formula of the mean drift forces contains only the first order terms. Thus, we

only need to solve for the first order problem. The governing equations are as below:

$$\nabla^2\Phi^{(1)} = 0 \qquad in\ fluid\ domain \tag{6.1}$$

$$-\frac{1}{g}\frac{\partial^2\Phi^{(1)}}{\partial t^2} = \frac{\partial\Phi^{(1)}}{\partial z} \qquad on\ z = 0 \tag{6.2}$$

$$\vec{n'}\cdot\vec{\nabla}\Phi^{(1)} = \vec{n'}\cdot[\dot{\vec{\eta}}^{(1)} + (\dot{\vec{\alpha}}^{(1)}\times\vec{X'})] \qquad at\ body\ surface \tag{6.3}$$

$$\lim_{r\to\infty} r(\frac{\partial\Phi^{(1)}}{\partial r} - ik\Phi^{(1)}) = 0 \qquad at\ control\ surface \tag{6.4}$$

$$\frac{\partial\Phi^{(1)}}{\partial z} = 0 \qquad on\ z = -h \tag{6.5}$$

where, $\Phi^{(1)}$ is the first order potential. $\dot{\vec{\eta}}^{(1)}$, $\dot{\vec{\alpha}}^{(1)}$ stand for the translational displacements and the rotational angles, $\vec{X'}$ is the vector in the vessel equilibrium coordinate, $\vec{n'}$ is the normal vector on the body surface.

In the above equations, we use the combined free surface boundary condition, integrating the kinematic and dynamic free surface boundary conditions. The dynamic boundary condition correlates the wave elevation with the potential value, which is as below:

$$Z^{(1)} = -\frac{1}{g}\frac{\partial\Phi^{(1)}}{\partial t} \tag{6.6}$$

If reaching the steady state, we can assume $\Phi^{(1)} = \phi^{(1)}exp(i\omega t)$ and $Z^{(1)} = \zeta^{(1)}exp(i\omega t)$. Thus the dynamic free surface boundary condition can be converted into:

$$\zeta^{(1)} = -\frac{i\omega\phi^{(1)}}{g} \tag{6.7}$$

In the expressions of the drift forces, the terms resulted from the relative wave elevation are:

$$\vec{F}_{rel} = -\int_{C_{wl}} dl\ \frac{1}{2}\epsilon^2 \rho g \vec{n'} \frac{\zeta_r^{(1)^2}}{\sqrt{1-n_3'^2}} + o(\epsilon^3) \tag{6.8}$$

$$\begin{aligned}\vec{M}_{rel} &= -\iint_{\Delta S} P[(\vec{X}-\vec{X}_0)\times\vec{n'}]dS \\ &= -\int_{C_{wl}} dl \frac{1}{2}\epsilon^2 \rho g \zeta_r^{(1)^2} (\vec{X'}\times\vec{n'}) \frac{1}{\sqrt{1-n_3'^2}} + o(\epsilon^3)\end{aligned} \tag{6.9}$$

where, the relative wave elevation is defined as $\zeta_r^{(1)} = \zeta^{(1)} - (\eta_3^{(1)} + \eta_4^{(1)}Y' - \eta_5^{(1)}X')$. To evaluate the terms regarding the relative wave elevation, we need to calculate the absolute wave elevation by the equation 6.7. Herein, we are interested in the wave elevation along the waterline of the floater. If we can calculate the potential value on the waterline, the wave elevation will be naturally found.

To find the wave elevation along the waterline, we need to find the corresponding potential value according to the relationship for the first order problem. Herein we are using the source formula to calculate the potential value inside the fluid domain.

$$\phi(\boldsymbol{x}) = \frac{1}{4\pi}\sum_{j=1}^{N}\sigma_j \iint_{\Delta S} G(\boldsymbol{x};\boldsymbol{\xi})dS_{\boldsymbol{\xi}} \qquad \boldsymbol{x}\in S_b \& \boldsymbol{x}\in V \tag{6.10}$$

where, the Green function by Noblesse[9] is used in the calculation:

$$G = \frac{1}{r} + \frac{1}{r'} + 2f^*[R_0(h,v) - i\pi J_0(h)exp(v)] \tag{6.11}$$

where, $f^* = \omega^2 L/g$, $\rho = [(x-\xi)^2+(y-\eta)^2]^{\frac{1}{2}}$, $r = [\rho^2+(z-\zeta)^2]^{\frac{1}{2}}$, $r' = [\rho^2+(z+\zeta)^2]^{\frac{1}{2}}$, $h = f^*\rho$, $v = f^*(z+\zeta)$, J_0 is Bessel function of the first kind at order 0, R_0 is the function defined in Telste and Noblesse[10]. In the limiting case when $d \to 0$, $R_0 = -ln(d-v) + ln(2) - \gamma$ with error $O(d\,ln(d))$.

If writing in the matrix form, the equation to solve for the potential value is:

$$[\phi] = [BETA][\sigma] \tag{6.12}$$

where, $\beta_{ij} = \frac{1}{4\pi} \iint_{\Delta S} G(\boldsymbol{x}; \boldsymbol{\xi}) dS_{\boldsymbol{\xi}}$, which is the element in the ith row and jth column of the matrix [BETA].

We need to find the source strength based on the body boundary condition first. Afterward, the potential value at an arbitrary spatial point can be calculated based on the equation 6.10. To finish that, the integral to decide β_{ij} needs to be evaluated. In calculating the integral, we will use the method in Hess and Smith[4] for the part resulted from $1/r + 1/r'$ and the Gaussian quadrature method for the wavy Green function, which is dependent on the frequency.

6.2 The Singular Problem

We encounter some difficulties in evaluating the integral resulted from the Green function when the field point locates on the edge of the waterline panel. When the field point is exactly on the edge of the waterline panel, we will get a NaN (Not a Number) for the potential value at the waterline point. When the field point is very close to the panel surface (about 10^{-6}), we will get an Inf (Infinity). We are using the in-house program MDL Multi DYN, based on FORTRAN. MDL Multi DYN is the program for the hydrodynamic analysis of multiple floaters developed by Liu[107][105]. It is the redesigned version based on the program for a single body analysis by Guha[114]. This observation implies that we may not be able to set the field point on the edge of the waterline panel. Alternative methods need to be sought to accurately calculate the potential value on the waterline.

More exactly, we need to find an approach to accurately calculate the potential value at the waterline. The potential is the sum of the incident potential, diffraction and radiation potential. For the incident potential, it is easy to find the value because the expression of the incident potential is explicitly given. The incident potential value is not NaN or Inf. The NaN or Inf comes from the diffraction potential or the radiation potential.

After further investigation, the method of Hess and Smith leads to the NaN or Inf. It is a result of $0/0$ or $1/0$ in FORTRAN. Here we will cite the expression to evaluate the integral of $1/r$ as

below:

$$
\begin{aligned}
&\iint_{\Delta Sj} \frac{1}{r} dS \\
&= [\frac{(x-x_1)(y_2-y_1)-(y-y_1)(x_2-x_1)}{d_{12}} \ln \frac{r_1+r_2+d_{12}}{r_1+r_2-d_{12}} \\
&+ \frac{(x-x_2)(y_3-y_2)-(y-y_2)(x_3-x_2)}{d_{23}} \ln \frac{r_2+r_3+d_{23}}{r_2+r_3-d_{23}} \\
&+ \frac{(x-x_3)(y_4-y_3)-(y-y_3)(x_4-x_3)}{d_{34}} \ln \frac{r_3+r_4+d_{34}}{r_3+r_4-d_{34}} \\
&+ \frac{(x-x_4)(y_1-y_4)-(y-y_4)(x_1-x_4)}{d_{41}} \ln \frac{r_4+r_1+d_{41}}{r_4+r_1-d_{41}}] \\
&- |z|[\arctan(\frac{m_{12}e_1-h_1}{zr_1}) - \arctan(\frac{m_{12}e_2-h_2}{zr_2}) \\
&+ \arctan(\frac{m_{23}e_2-h_2}{zr_2}) - \arctan(\frac{m_{23}e_3-h_3}{zr_3}) \\
&+ \arctan(\frac{m_{34}e_3-h_3}{zr_3}) - \arctan(\frac{m_{34}e_4-h_4}{zr_4}) \\
&+ \arctan(\frac{m_{41}e_4-h_4}{zr_4}) - \arctan(\frac{m_{41}e_1-h_1}{zr_1})]
\end{aligned} \tag{6.13}
$$

where,

$$
\begin{aligned}
d_{12} &= \sqrt{(x_2-x_1)^2+(y_2-y_1)^2} \\
d_{23} &= \sqrt{(x_3-x_2)^2+(y_3-y_2)^2} \\
d_{34} &= \sqrt{(x_4-x_3)^2+(y_4-y_3)^2} \\
d_{41} &= \sqrt{(x_1-x_4)^2+(y_1-y_4)^2} \\
m_{12} &= \frac{y_2-y_1}{x_2-x_1} \quad m_{23} = \frac{y_3-y_2}{x_3-x_2} \\
m_{34} &= \frac{y_4-y_3}{x_4-x_3} \quad m_{41} = \frac{y_1-y_4}{x_1-x_4} \\
r_k &= \sqrt{(x-x_k)^2+(y-y_k)^2+z^2}, k = 1,2,3,4 \\
e_k &= z^2+(x-x_k)^2, k = 1,2,3,4 \\
h_k &= (y-y_k)(x-x_k), k = 1,2,3,4
\end{aligned}
$$

We choose to study one single panel only as indicated below:

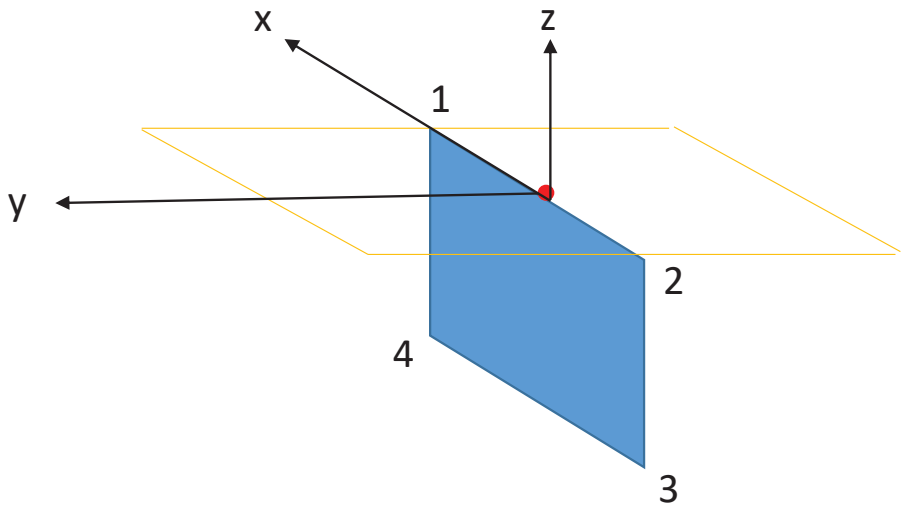

Figure 6.2: View of a Square Panel

After we apply the equation 6.13, we find the first term in RHS (Right Hand Side) of the expression of the equation 6.13 is causing NaN or Inf. Then the question comes: why we will get NaN or Inf? Is it because of the singular behavior of the function or the computer round-off errors? We, therefore, need to study the convergence behavior of the first term. After the transformation, the problem is equivalent to finding the limit of $x \ln x$ when $x \to 0$. Apparently, the limit of $x \ln x$ exists and is zero. To view the function property, we also plot the function value on the surface enclosed by the yellow frame in Figure 6.2. The contour of the function value distribution can be shown below. Please note that we let b equal to the first term of the integral.

$$b = \frac{(x - x_1)(y_2 - y_1) - (y - y_1)(x_2 - x_1)}{d_{12}} \ln \frac{r_1 + r_2 + d_{12}}{r_1 + r_2 - d_{12}} \tag{6.14}$$

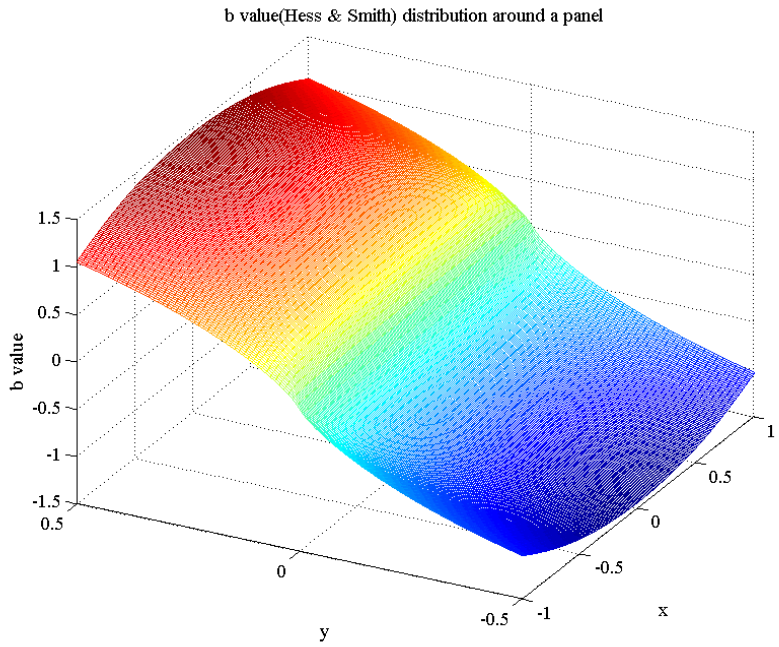

Figure 6.3: Distribution of the Function Value B

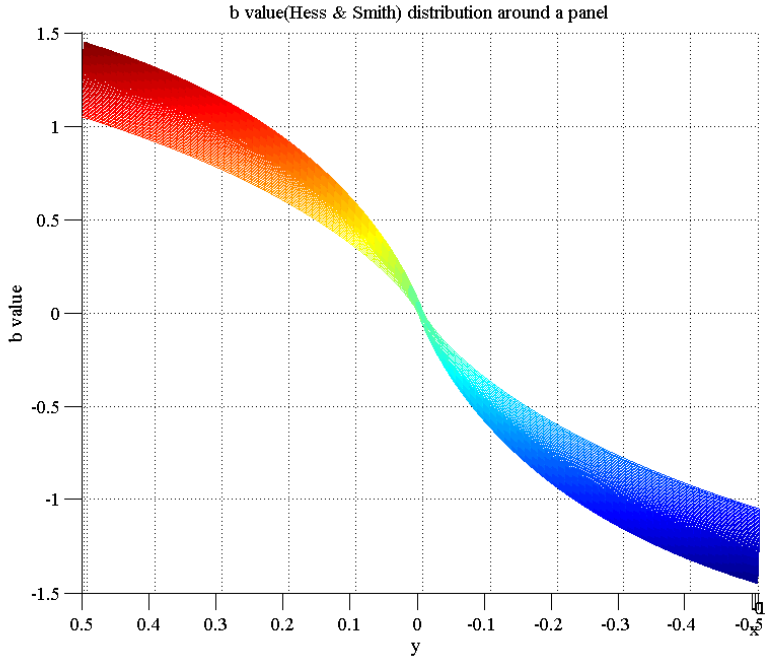

Figure 6.4: Distribution of the Function Value B

We may notice that the value of the term b is approaching 0 when the field point is approaching the panel edge. This has validated that the limit of the term exists and equals 0. Also, we notice that the slope of the function near the panel edge does not vary so quickly and the function value has an approximate linear relationship with the distance along the normal direction of the panel. This inspires us that we may be able to use the extrapolation method to calculate the potential value on the waterline.

6.3 The Extrapolation Method

In the previous section, we are inspired by the function property and want to try the extrapolation method to calculate the integral. To illustrate how to use the extrapolation method, Figure 6.5 is introduced. The yellow part stands for the waterline panel. Point A represents the centroid of the panel. Point B is located on the waterline. Point C is apart from the panel, along the normal direction of the panel. As a note, in the commercial software WAMIT, the potential value at the waterline panel centroid (e.g. point A) is used to represent the value at the field point (e.g. B) on the waterline.

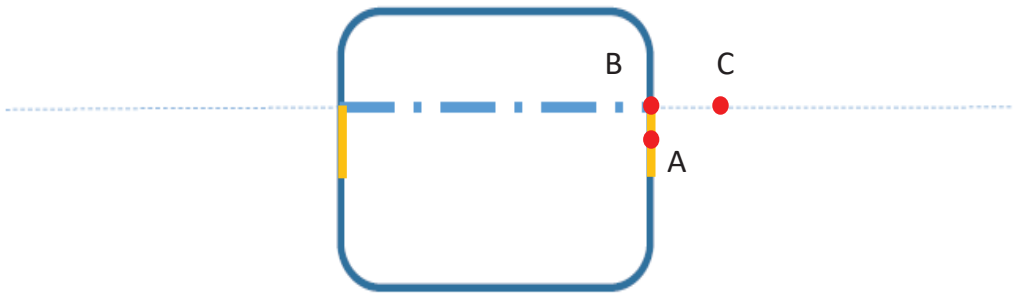

Figure 6.5: Illustration of the Extrapolation Method

The objective is to calculate the integral value when the field point is located at point B. However, due to the difficulty mentioned before, we need to find the alternative method. Herein, we are

using the extrapolation method to calculate the integral value. We will calculate the integral value at point C and use that value to extrapolate the integral value at B. We cannot use the value at point A because the waterline panel size will vary from case to case, which introduces some uncertainty to the extrapolation method. The formula can be written as below:

$$\begin{aligned}\iint_{\Delta S} G(B)dS = \iint_{\Delta S} G(C)dS + (x_B - x_C)\iint_{\Delta S} \frac{\partial G}{\partial x}(C)dS \\ + (y_B - y_C)\iint_{\Delta S} \frac{\partial G}{\partial y}(C)dS \\ + (z_B - z_C)\iint_{\Delta S} \frac{\partial G}{\partial z}(C)dS \end{aligned} \tag{6.15}$$

As a result, the value of some elements in the matrix [BETA] is changed. The extrapolation method is only used when calculating the panel effect on the field point which is locating on the panel itself.

To validate the extrapolation method, we plot the contour of the integral value for the different field points. The integral is the surface integral of the Green function G. We spread the arrays of field points on the surfaces in blue indicated by Figure 6.6. In such a way, we can create the 3D mesh plot with xOy plane located on the blue surface and the z axis representing the integral value. We will first present the results for a square panel (2×2), then the results for another square panel (0.2×0.2).

Figure 6.6 is the illustration of the square panel (2×2).

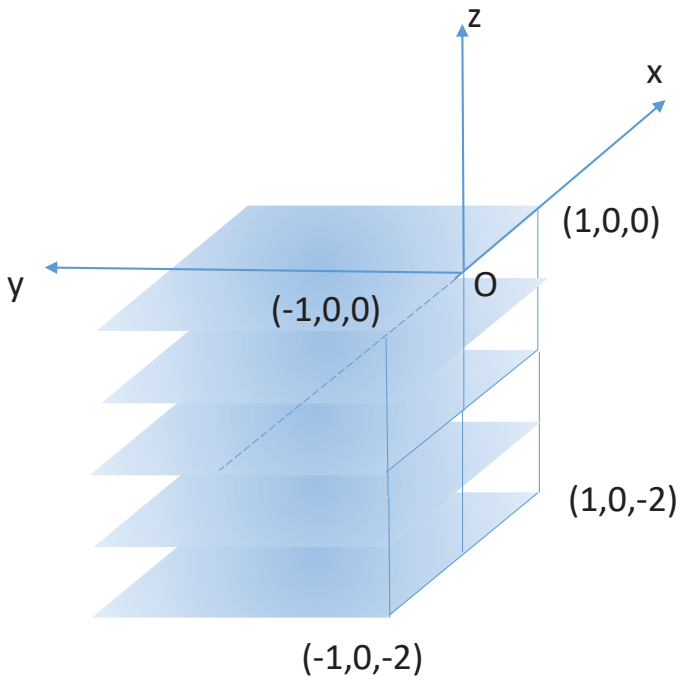

Figure 6.6: Illustration of the Panel and the Locations of the Field Points

The information of the array of the field points is listed in Table 6.1.

Table 6.1: Information of the Field Points for Panel 2×2

X	Nx	Y	Ny	ω
[-1, 1]	200	[0.0001, 0.5]	100	1

where, X means the range of the x-axis, Nx is the number of points along the x-axis. Similar rules apply for Y and Ny. ω is the radian frequency. The effect of the wavy Green function part will be weakened when the radian frequency is relatively lower. Thus, we choose $\omega = 1$ herein.

In Figure 6.7 to 6.16, we will illustrate the integral value for the term $1/r$ and the real part of the Green function G. The imaginary part of the Green function has a fairly small slope, thus we will present the results of the real part only.

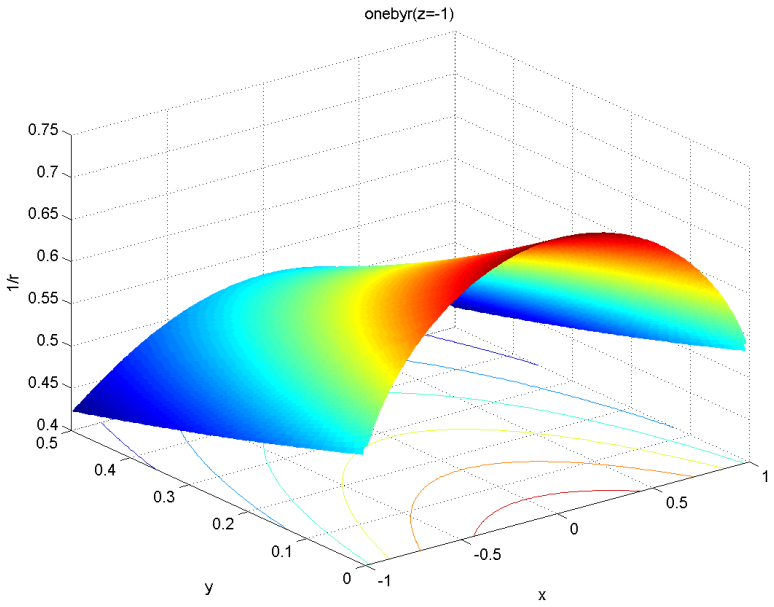

Figure 6.7: Integral Value of $1/r$ on the Surface When z = -1

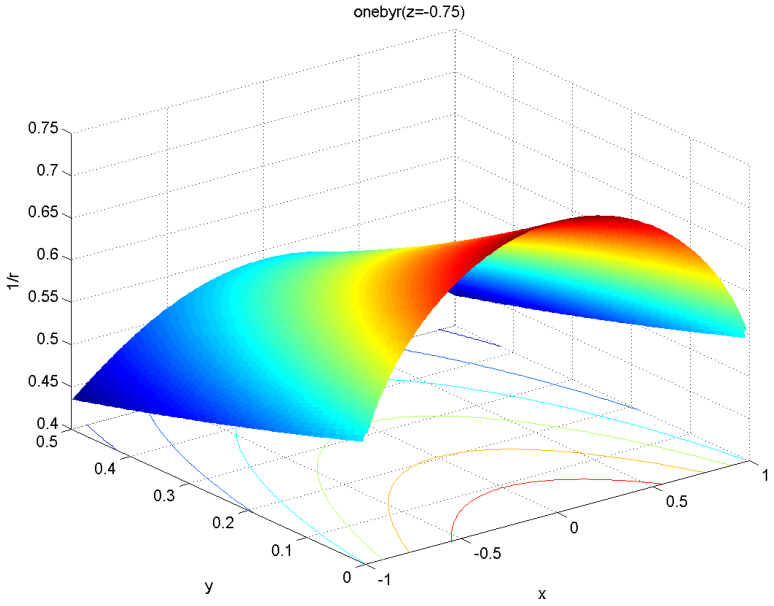

Figure 6.8: Integral Value of $1/r$ on the Surface When z = -0.75

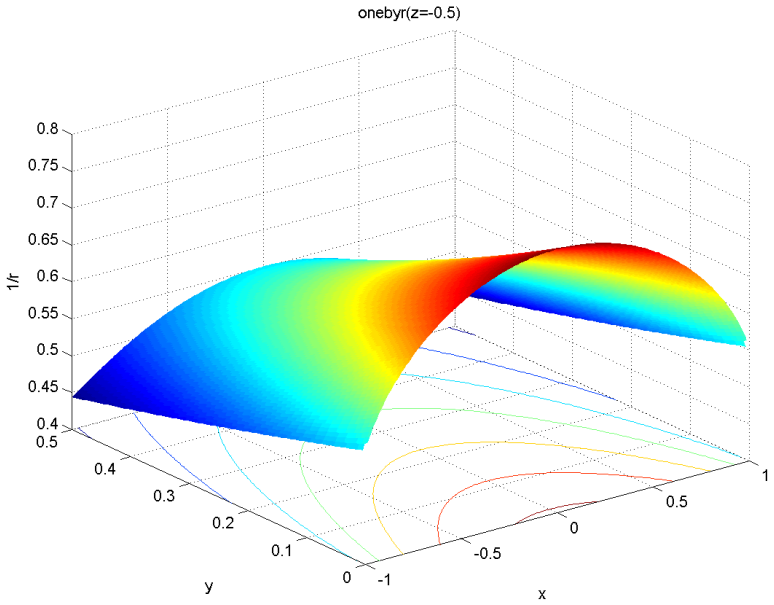

Figure 6.9: Integral Value of $1/r$ on the Surface When z = -0.5

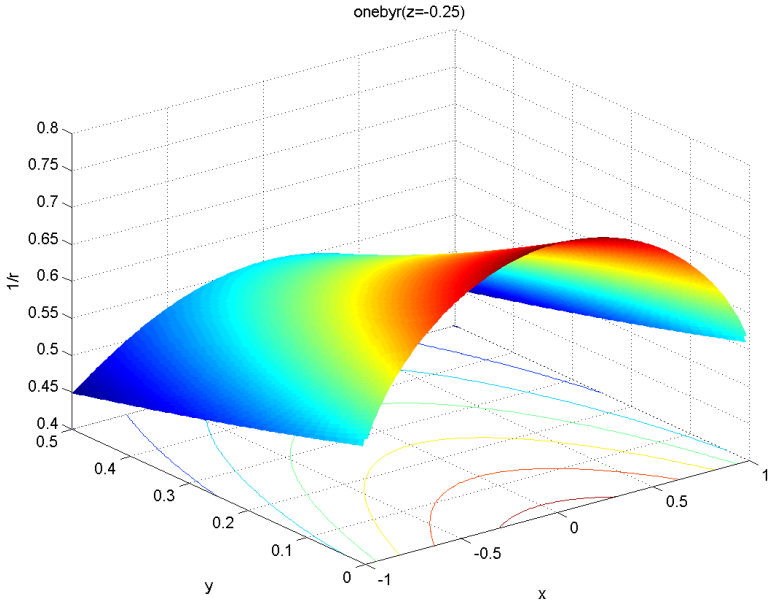

Figure 6.10: Integral Value of $1/r$ on the Surface When z = -0.25

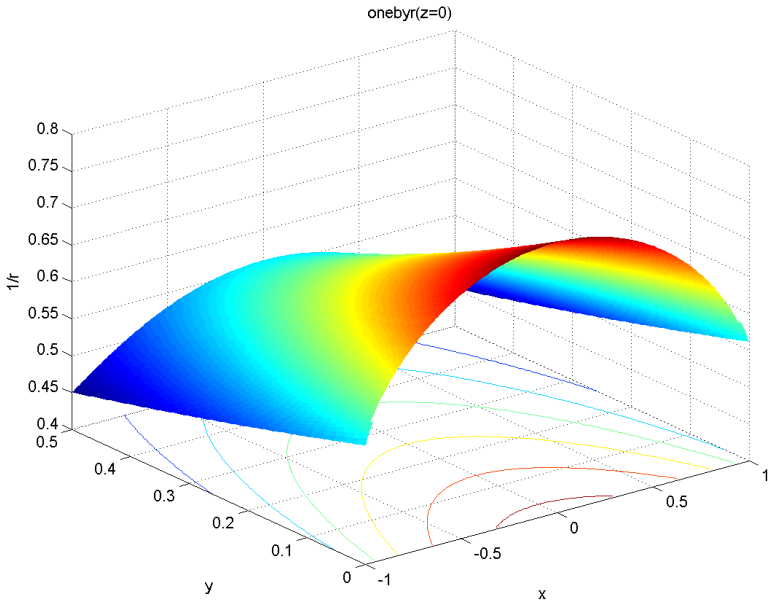

Figure 6.11: Integral Value of $1/r$ on the Surface When z = 0

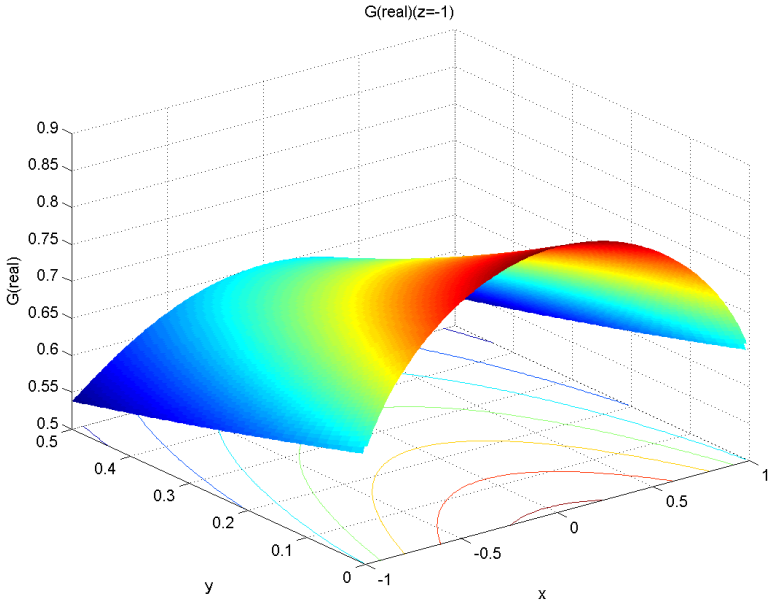

Figure 6.12: Integral Value of G on the Surface When z = -1

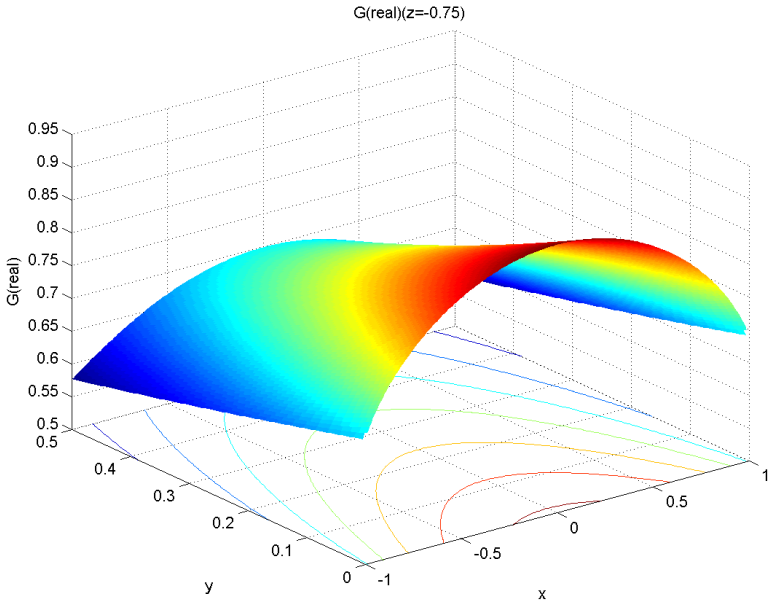

Figure 6.13: Integral Value of G on the Surface When z = -0.75

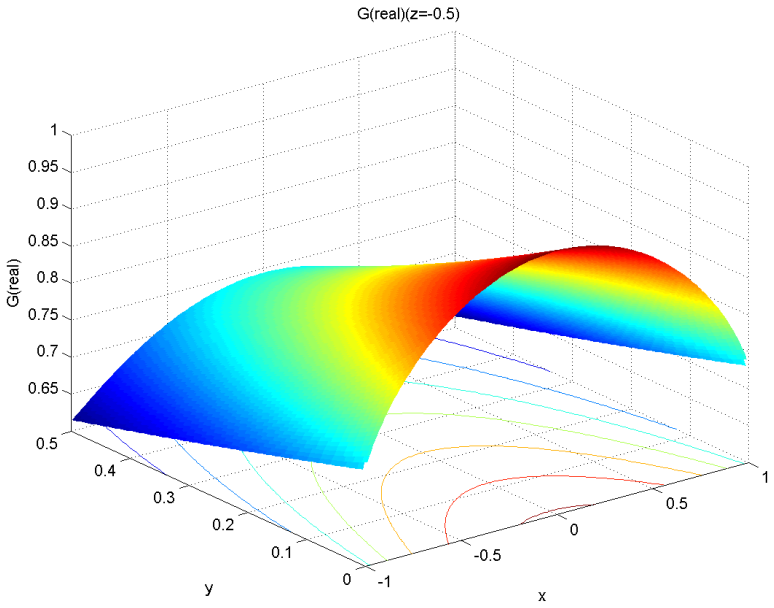

Figure 6.14: Integral Value of G on the Surface When z = -0.5

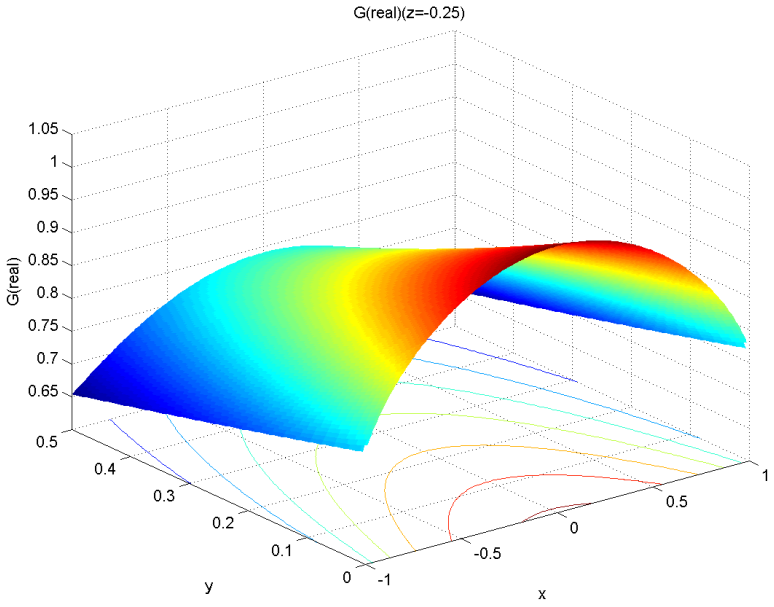

Figure 6.15: Integral Value of G on the Surface When z = -0.25

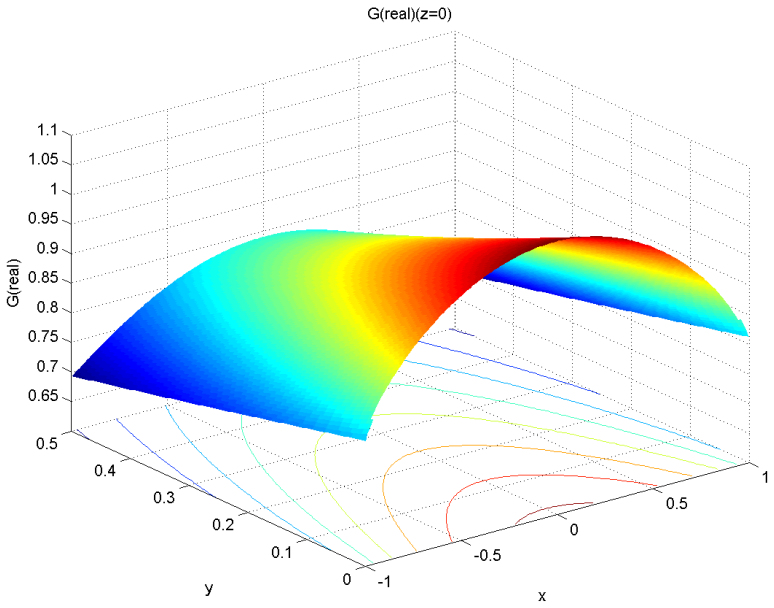

Figure 6.16: Integral Value of G on the Surface When z = 0

Figure 6.7 to 6.16 show that the frequency independent part is dominating in the integral value. The integral value of the Green function G is approximately linearly varying with respect to the distance normal to the panel, including the case when $x = 0$, y is increasing. To be conservative, we will also examine whether the same conclusion is valid for a smaller panel. Because near the waterline, we usually use smaller panel to make the integral more accurate. Herein, we choose the panel size to be $0.2x0.2$. The information of the field points are listed in Table 6.2.

Table 6.2: Information of the Field Points for Panel 0.2×0.2

X	Nx	Y	Ny	ω
[-0.1, 0.1]	200	[0.0001, 0.1]	100	1

The results for the integral of the $1/r$ and the Green function G on the panel 0.2×0.2 are shown in Figure 6.17 to 6.26.

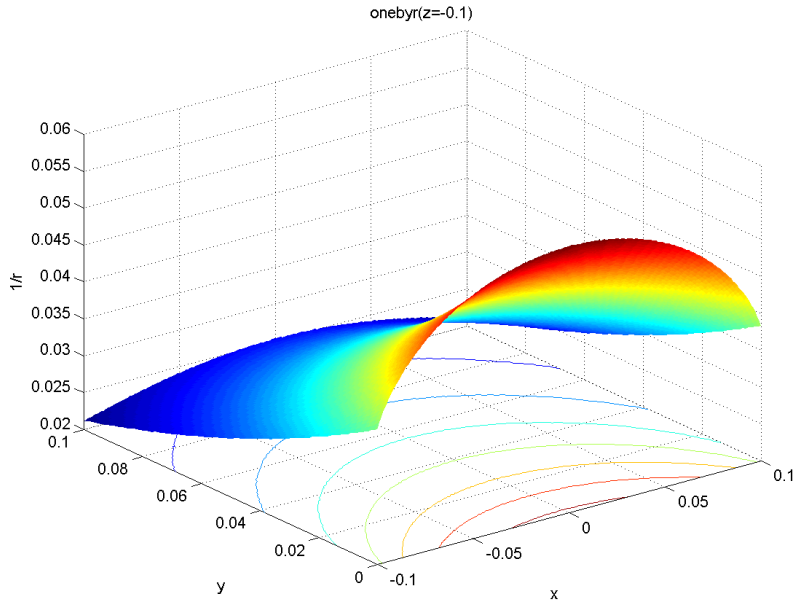

Figure 6.17: Integral Value of $1/r$ on the Surface When z = -1

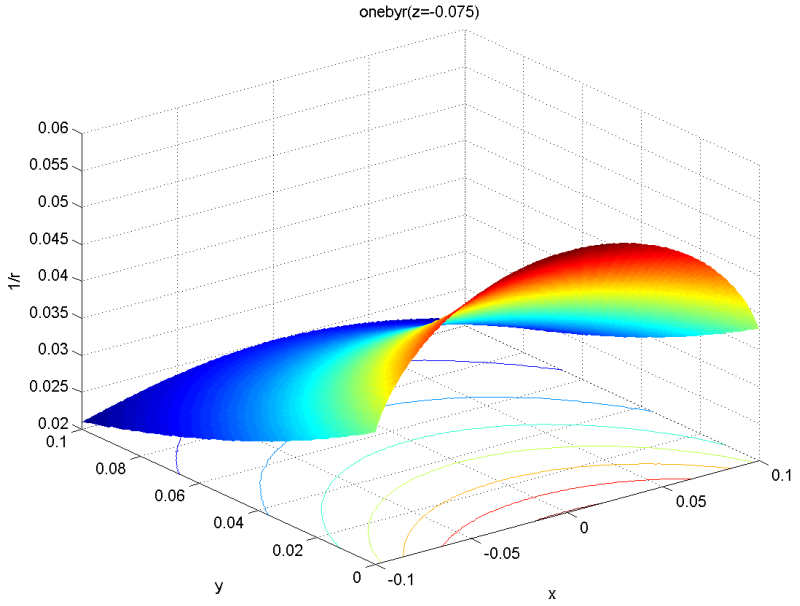

Figure 6.18: Integral Value of $1/r$ on the Surface When z = -0.75

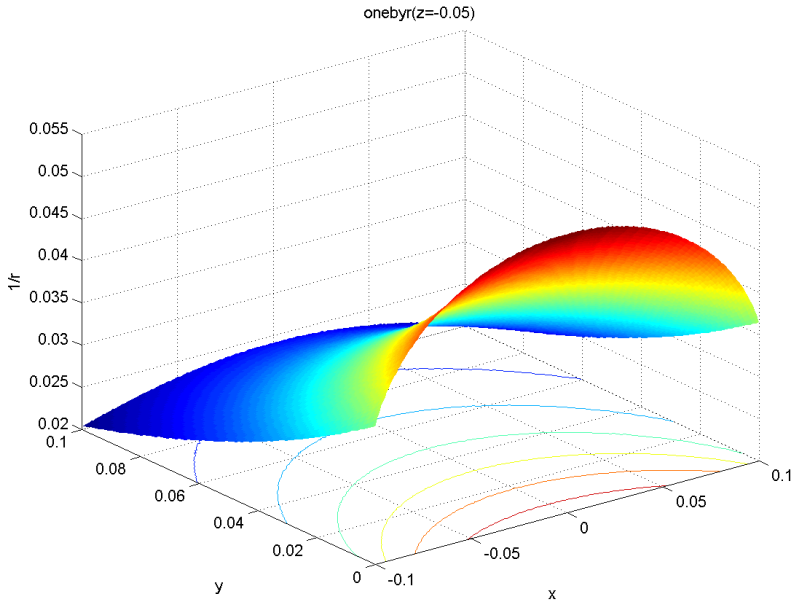

Figure 6.19: Integral Value of $1/r$ on the Surface When z = -0.5

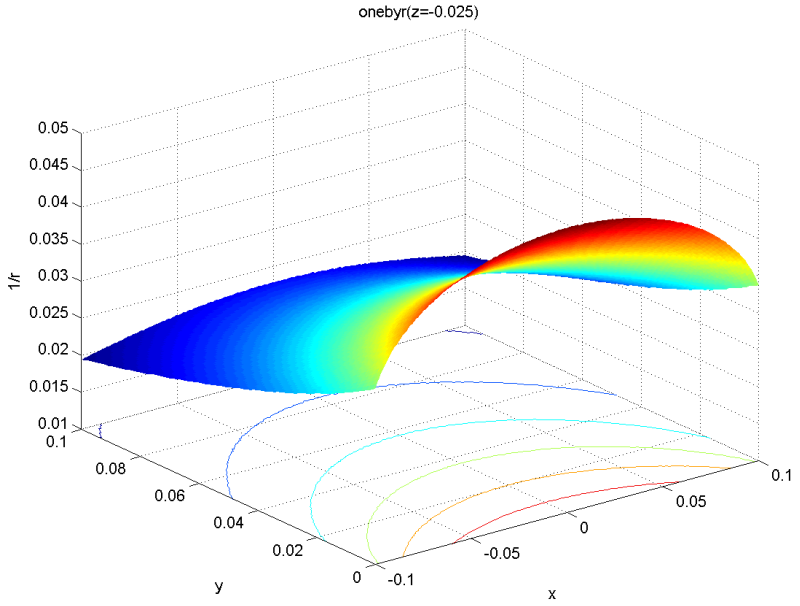

Figure 6.20: Integral Value of $1/r$ on the Surface When z = -0.25

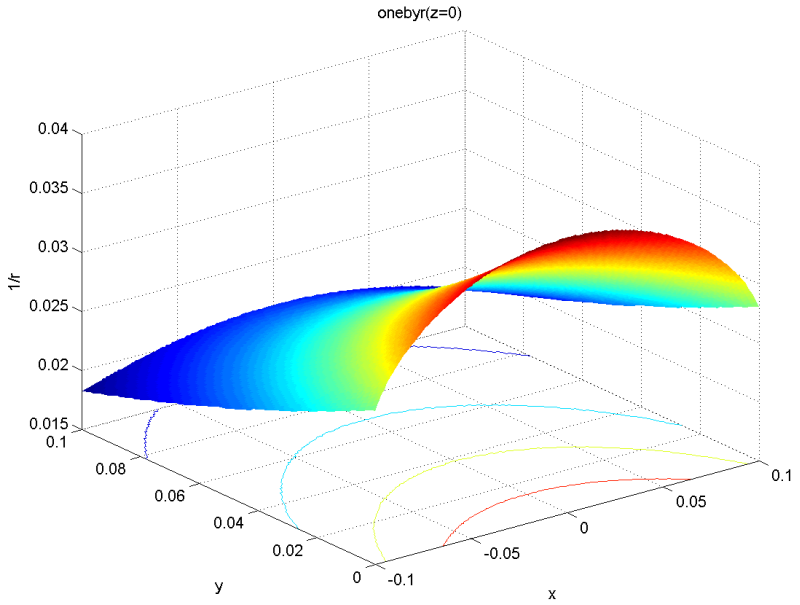

Figure 6.21: Integral Value of $1/r$ on the Surface When z = 0

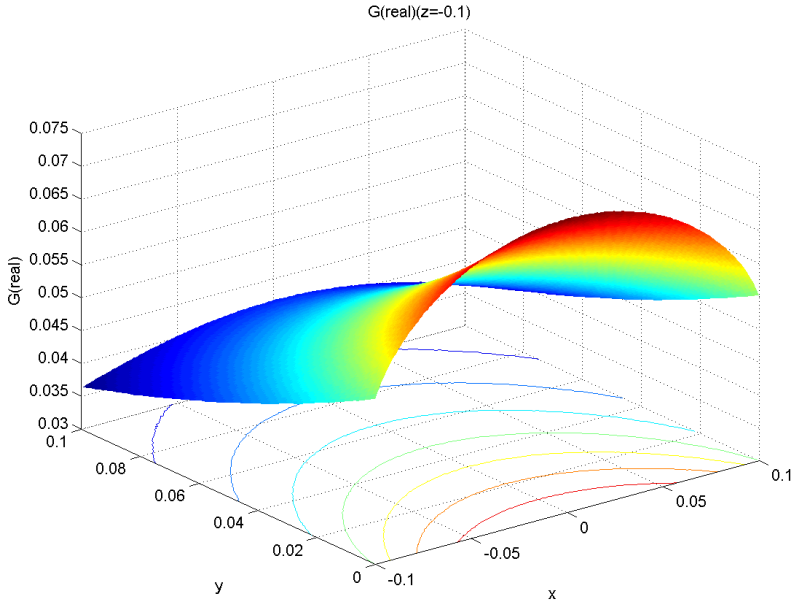

Figure 6.22: Integral Value of G on the Surface When z = -1

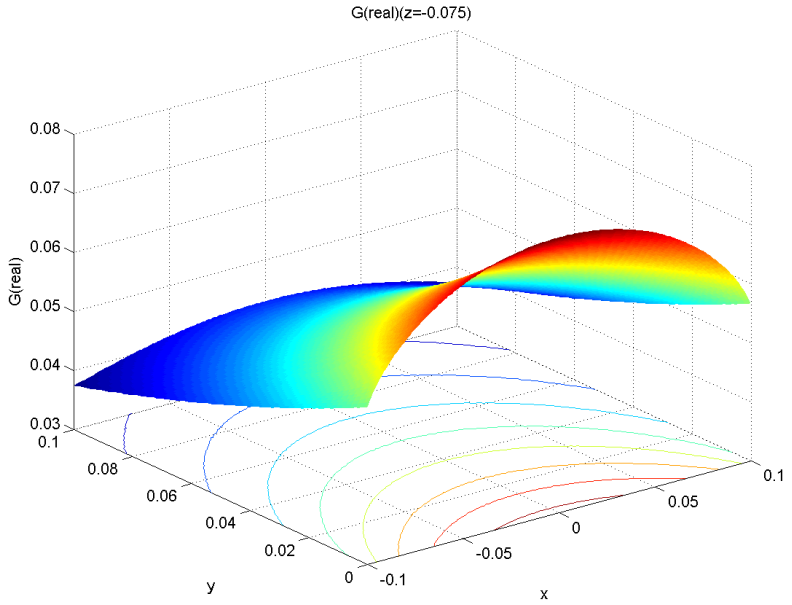

Figure 6.23: Integral Value of G on the Surface When z = -0.75

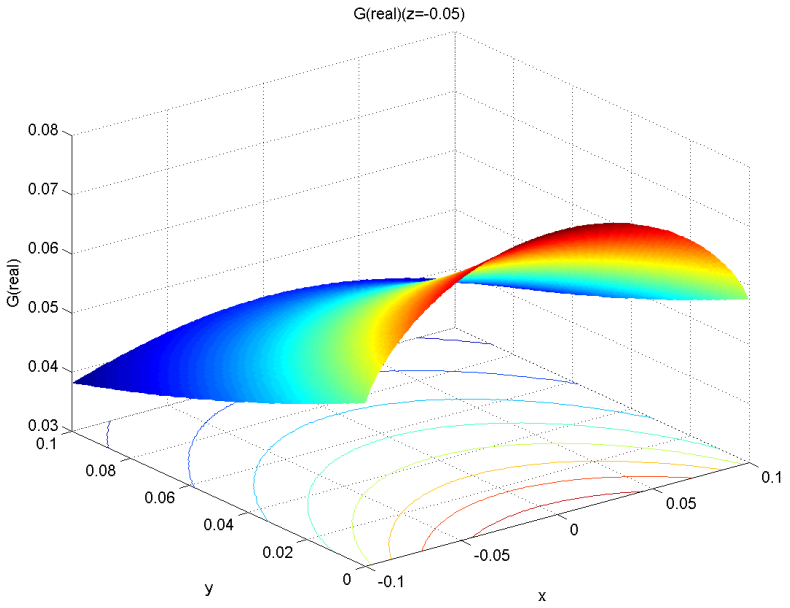

Figure 6.24: Integral Value of G on the Surface When z = -0.5

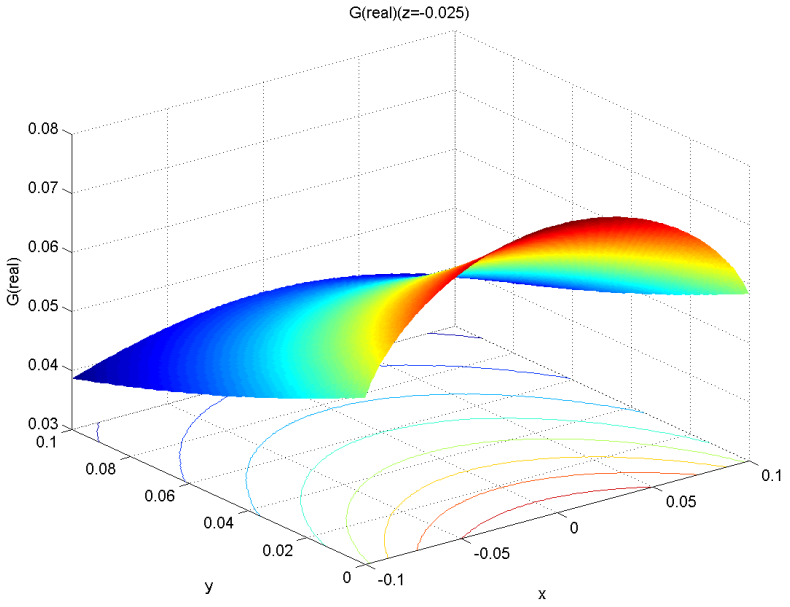

Figure 6.25: Integral Value of G on the Surface When z = -0.25

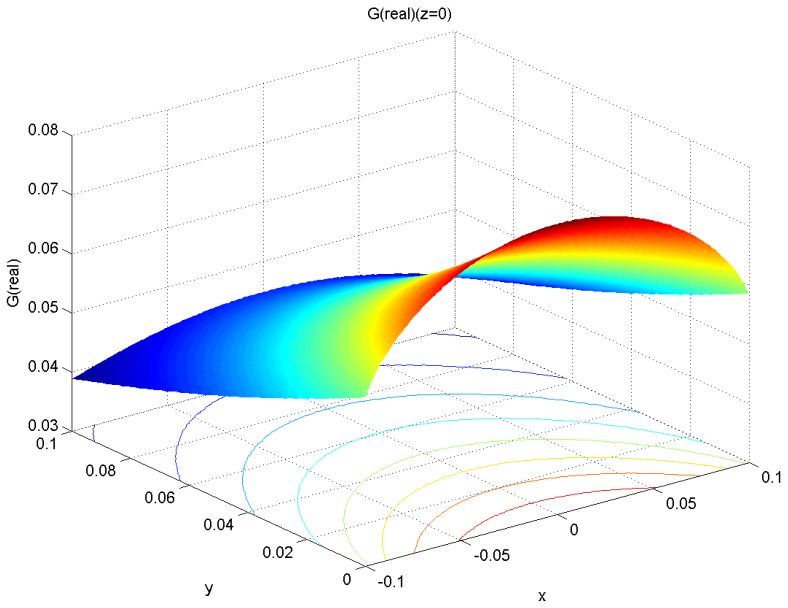

Figure 6.26: Integral Value of G on the Surface When z = 0

From the Figure 6.17 to 6.26, we will reach the same conclusions. Thus, the extrapolation method will be a good alternative approach to find the integral value when the field point is located on the edge of the panel. Adopting this method, we will examine the results of the drift forces.

6.4 Results and Discussions

In this section, we will benchmark our results against the industry standard software (WAMIT). If we use the same approach as WAMIT, the results from our in-house program will be consistent. If we use the theoretically more accurate approach discussed in the previous section, the results from WAMIT will converge to our in-house program MDL Multi DYN when we use smaller waterline panels in WAMIT.

First, we will study the case of the mini box barge, which is shown in Figure 6.27.

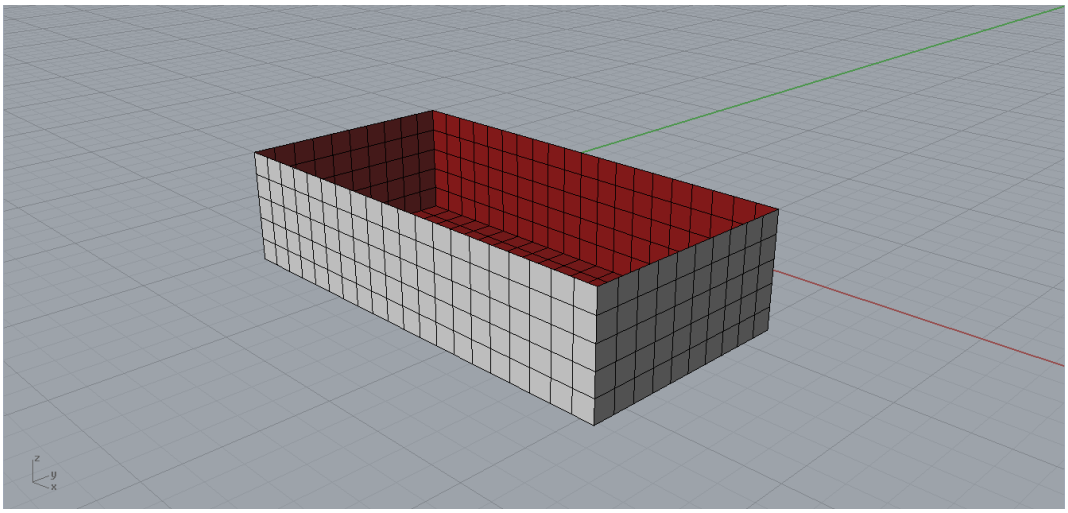

Figure 6.27: Perspective View of Mini Box Barge

When we choose the same method with WAMIT to evaluate the wave elevation, the results are shown as below. Herein, we use the head sea condition.

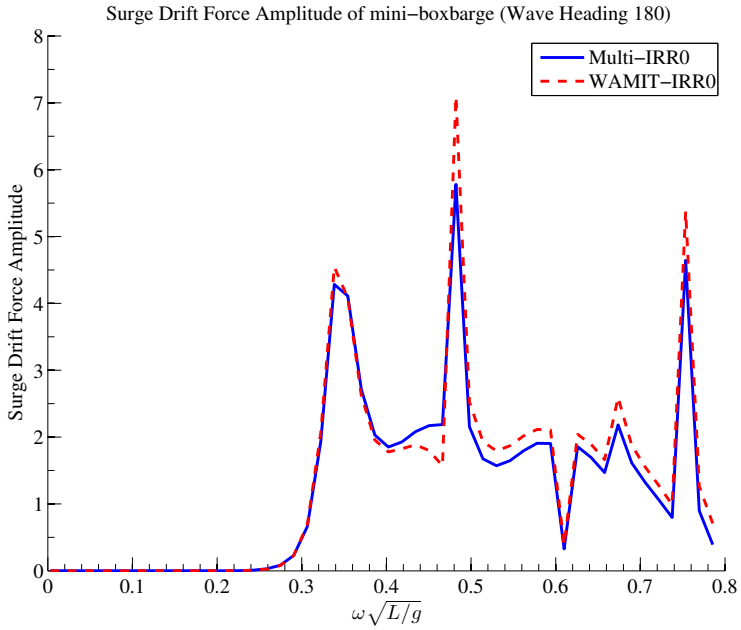

Figure 6.28: Drift Force in Surge Direction of Mini Box Barge

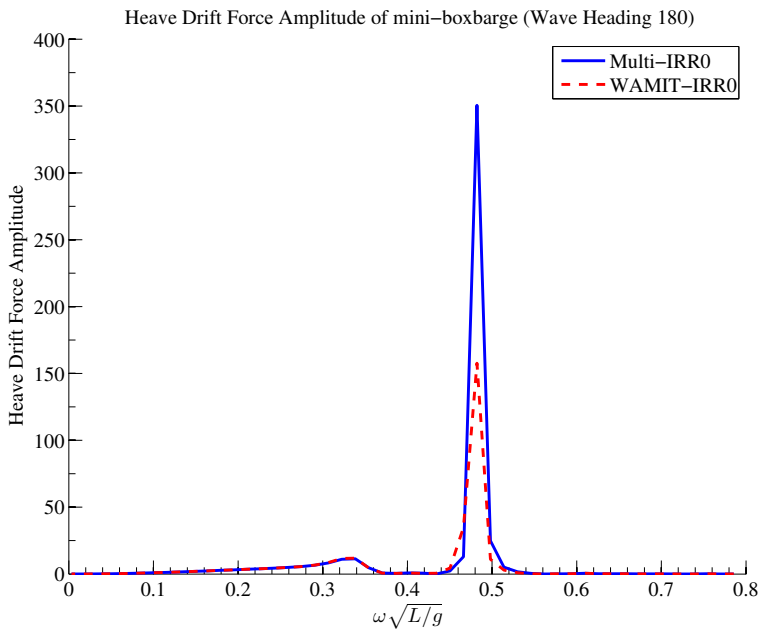

Figure 6.29: Drift Force in Heave Direction of Mini Box Barge

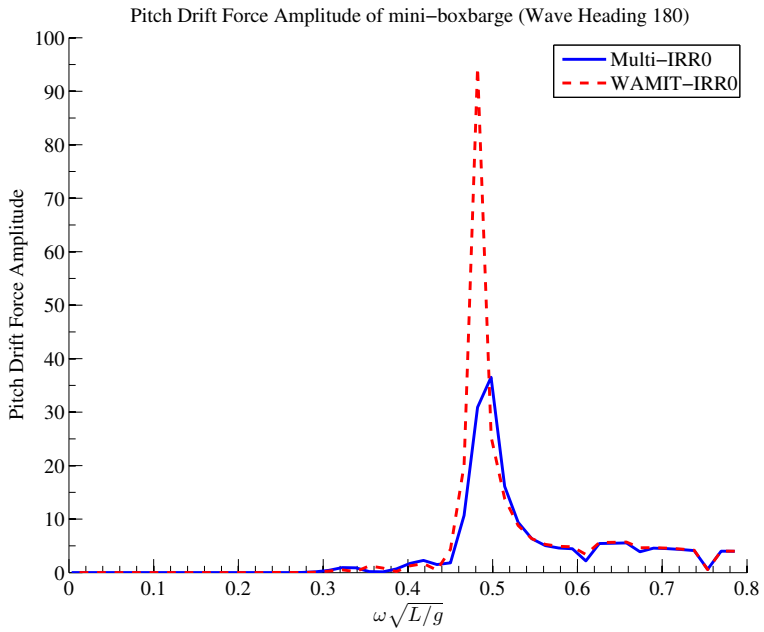

Figure 6.30: Drift Force in Pitch Direction of Mini Box Barge

From the Figure 6.28 to 6.30, we can conclude that if using the same method, the results from MDL Multi DYN and WAMIT are consistent except the amplitude at the resonance frequency. The reason of the discrepancy is still under investigation.

To validate the effectiveness of the method discussed in this paper, we will choose 3 different sizes of the waterline panels for the simulations in WAMIT. The dimension of the panel is defined in Figure 6.31. In MDL Multi DYN, we will choose the waterline panel size to be 1×1 (Length $\times$ Width) while in WAMIT, the following sizes are used: 1×1 (500 panels), 1×0.4 (560 panels), 1×0.1 (560 panels). Herein, we changed the head sea condition to the oblique sea. The wave heading angle is 150 degrees from the positive x axis. Please note that we are interested in the size effect of the waterline panels. To control the influence of other parameters, we split the waterline panels (1×1) into different sizes.

Figure 6.31: Waterline Panel Size

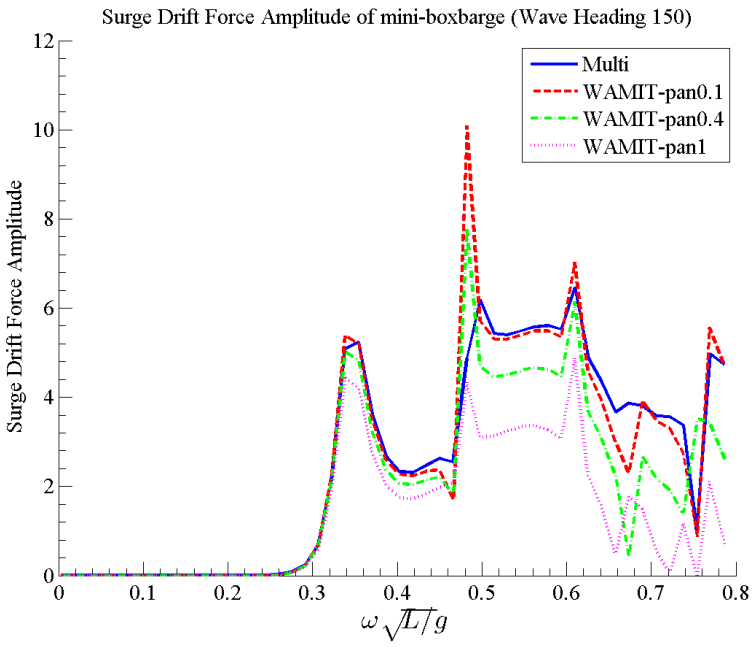

Figure 6.32: Drift Force in Surge Direction of Mini Box Barge

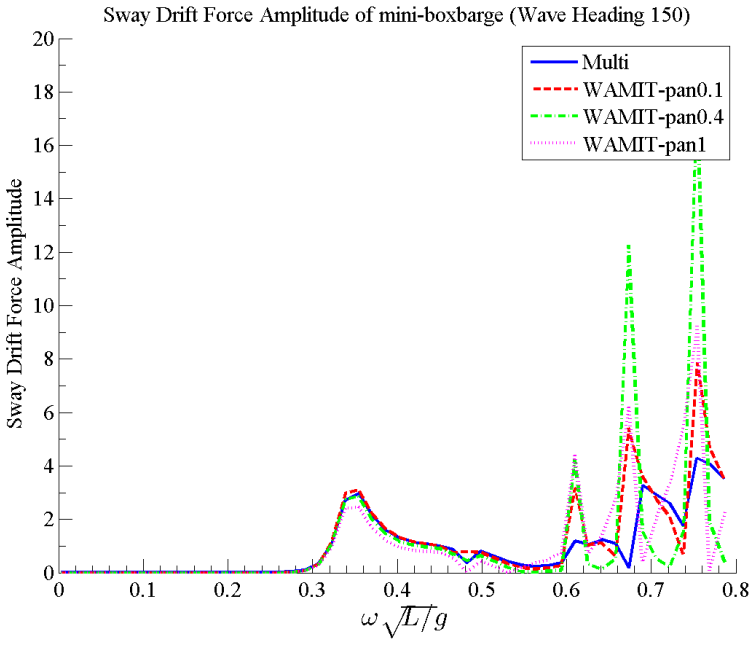

Figure 6.33: Drift Force in Sway Direction of Mini Box Barge

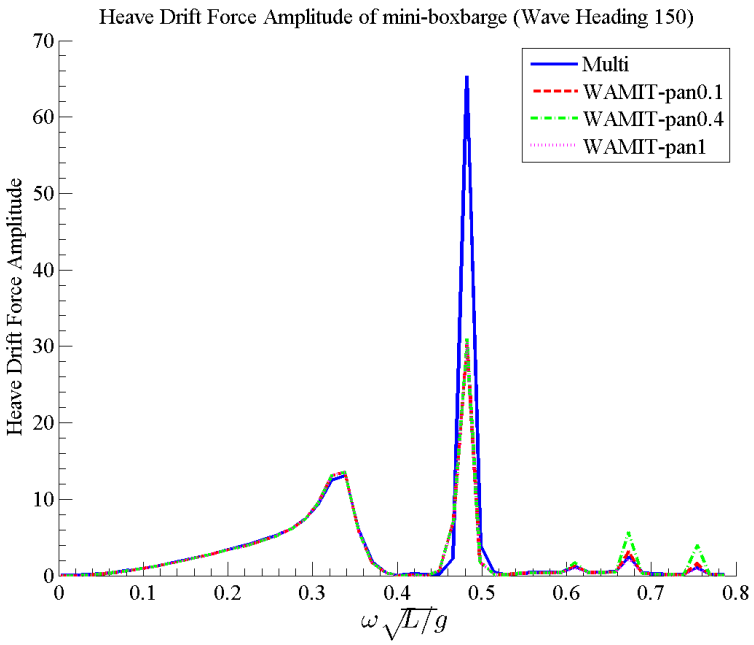

Figure 6.34: Drift Force in Heave Direction of Mini Box Barge

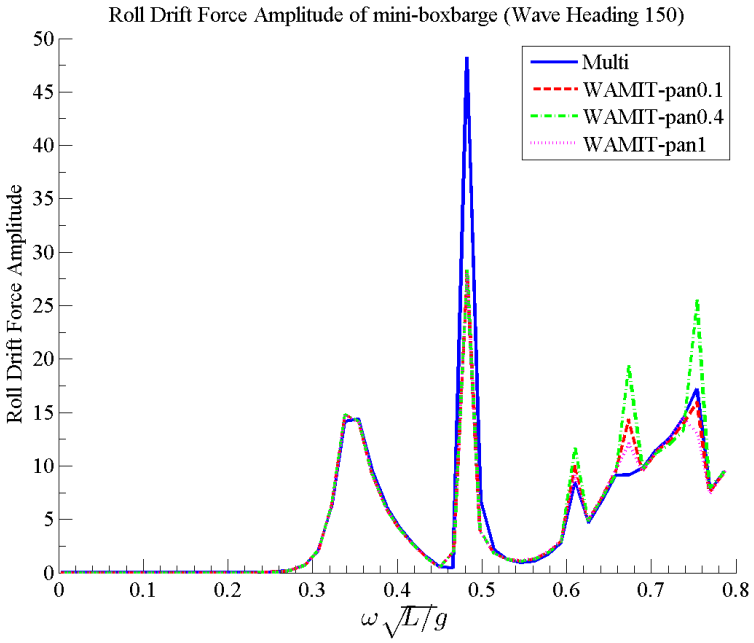

Figure 6.35: Drift Force in Roll Direction of Mini Box Barge

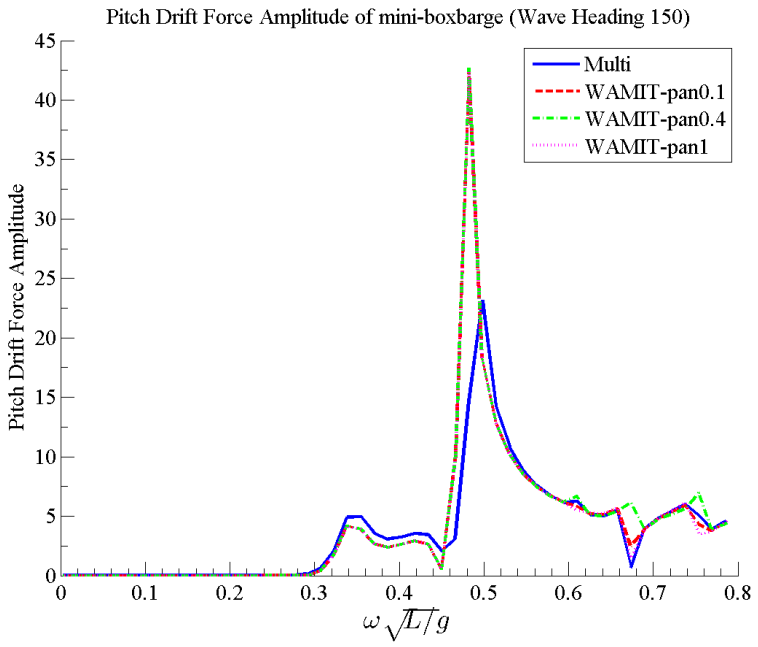

Figure 6.36: Drift Force in Pitch Direction of Mini Box Barge

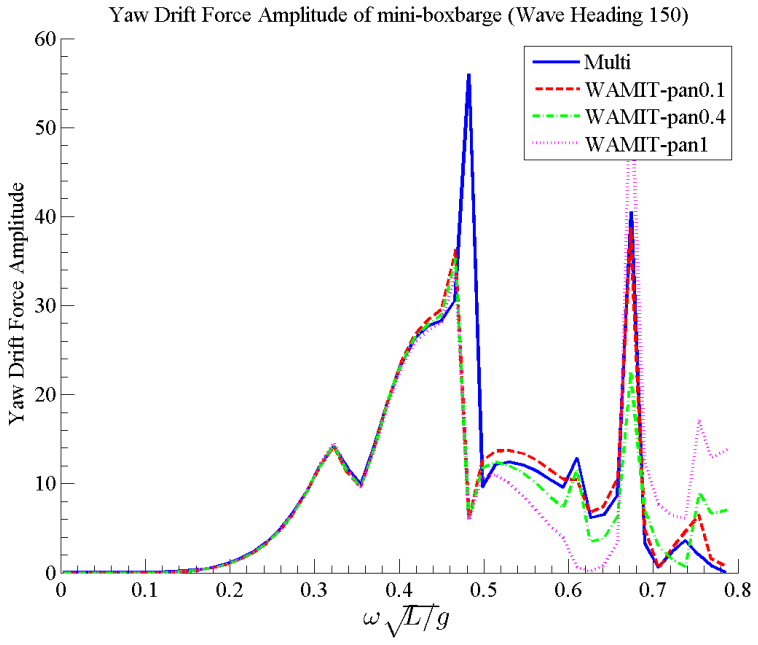

Figure 6.37: Drift Force in Yaw Direction of Mini Box Barge

We may observe in Figure 6.32 to 6.37, the results from WAMIT will converge to MDL Multi DYN when the width of the waterline panel gets smaller and smaller. The comparisons validate the effectiveness of our method. Herein, the "orignal method" refers to the approach used in WAMIT, i.e. using the potential at the waterline panel centroid to calculate the absolute wave elevation. The "improved method" indicates the method we are discussing. We use the extrapolation method to calculate the some of the matrix element to evaluate the potential at the waterline.

It is important to use the improved method to calculate the absolute wave elevation. Because in some cases, the discrepancy is significant between the results from the original method and those from the improved. We may notice the difference in the relatively higher frequency in Figure 6.32, 6.33 and 6.37.

In Figure 6.32, if using the original method, we will underestimate the drift forces unless we use tiny panels near the waterline. Sometimes, we may not have a reliable estimate about how small the panel should be and may have a wrong estimation. For example, the panel size 1×1 is usually small enough. However, for the case of the mini box barge, only when the panel size is 1×0.1, the results from the original method are close enough to the improved method.

In Figure 6.33, we tend to overestimate the drift force in the sway direction if using the original method to calculate the absolute wave elevation. As can be seen from Figure 6.33, if using the panel 1×1, the amplitude of the drift force resulted from the original method is larger than those from the improved method in the relatively higher frequency range. When we choose to use smaller panels, for instance, 1×0.4, we expect to get more accurate results. However, in this case, the resulting amplitude is becoming much higher, as indicated in green dashed line. Until we choose the panel size to be 1×0.1, the results are gradually converging to those from the improved method. This case also proves that sometimes it is hard to decide whether the waterline panel is small enough to obtain theoretically more accurate results. It is necessary to use the improved approach.

In Figure 6.37, we may find the discrepancy as well. When choosing the panel size 1×1, the results from the original method are overestimated in some frequency range and underestimated in some other frequency range. When the panel size is getting smaller, the results are converging to

those from the improved method.

To conclude, the results from the improved method are theoretically more accurate. It is more robust and efficient compared to the original method.

7. STUDY OF THE SIDE-BY-SIDE BOX BARGES PROBLEM

In this chapter, we apply the CFD approach and the potential method to study the wave elevation inside the gap. Firstly, we briefly describe the experiment conducted by Dr Zhao from the University of Western Australia. Secondly, we apply the CFD approach to study the gap elevation and identify the physical mechanism happening inside. Thirdly, we conduct the simulation in our in-house program, MDLMultiDYN, to dig out information about the problem using the potential method. Our program is based on the potential theory, which neglects the viscosity and rotational properties of the fluid.

7.1 Description of the Experiment

In this section, we briefly describe the experiment of the side-by-side box barges. The more detailed description can be found in Zhao[115] [102].

The model test was conducted in the Deepwater Wave Basin at Shanghai Jiao Tong University, China. The scale was 1:60. The experiment was well designed and the focus was on the gap resonance by choosing identical box barges with round corners (radius = 0.083 m). The two box barges are also fixed to a gantry so that they are rigidly fixed. The dimensions of the box barge are listed below:

Dimension	Value (m)
Length	3.333
Breadth	0.767
Depth	0.425
Gap Width	0.067

Table 7.1: Dimensions of the Box Barge and Gap Width

We have obtained part of the experimental data. In this section, we use the model test conducted in head waves and study the wave elevation.

7.2 Observations using CFD

To understand the physical mechanism in the problem of two box barges side-by-side, the simulation in CFD (Computational Fluid Dynamics) is needed to examine the flow field around the gap at or near the resonant frequencies. Herein, we adopt the commercial software STAR-CCM+ Version 12.06 as the tool to model the experiment. We model the head sea condition in regular waves and pick one frequency near the resonant frequencies. We adopt VOF (Volume Of Fluid) method[116][117] to model the free surface of the waves and the $k-\epsilon$ model for the turbulence.

7.2.1 Setup of the Case

The dimension of the box barge is the same with the model adopted in the experiment. Therefore, we set up the domain following the recommendations of STAR-CCM+ tutorial and perform a convergence study of the parameters.

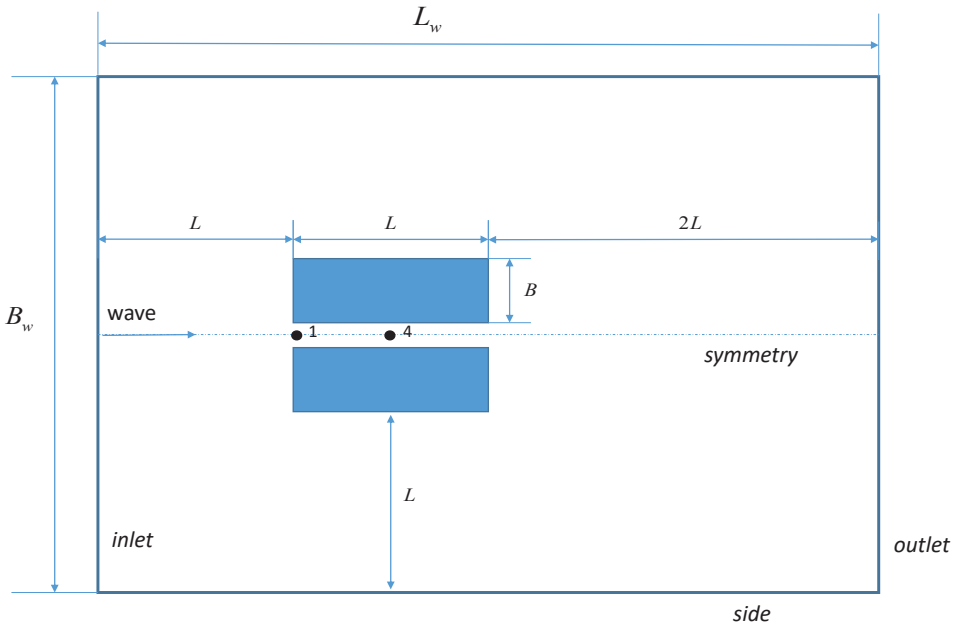

Figure 7.1: Dimensions of Wave Basin (Top View)

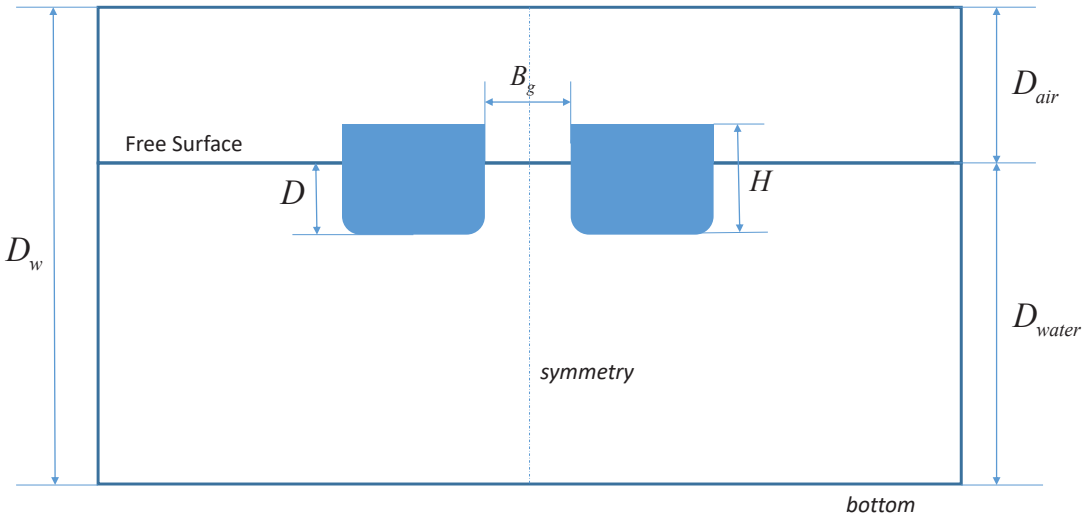

Figure 7.2: Dimensions of Wave Basin (Side View)

The distance between the wave inlet and the bow of the box barges is one ship length (L). The outlet boundary is 2L away from the stern of the box barges. The side wall is set as symmetry plane in STAR-CCM+, which is one ship length away from the ship. Based on the observations of the experiment, the flow inside the gap is relatively mild with an increased amplitude. We may assume the phenomenon is symmetric. In this figure, we use the dot-point line to indicate the location of the symmetric plane.

The time step is set based on this equation:

$$\Delta t = \frac{P}{2.4n} \tag{7.1}$$

where, P is the wave period and n is the number of grid inside one wave length. If we set X size of the grid to be 1/80 of the wave length, the value of n is 80. In our case, the wave frequency is 6.41 rad/s and the wave length λ is 1.5m, according to the assumption of deep water. The wave

amplitude A is 0.03m. Then $A/L = 0.02$ and deep water wave steepness $H/(gT^2) = 0.0064 << 1$. To ensure the deep water assumption, the depth of the fluid domain D_{water} is set to be 1.5m, which is larger than the half wave length $\lambda/2$. The depth of the air domain D_{air} is 0.5m.

STAR-CCM+ provides some options to specify the boundary conditions. The velocity inlet boundary condition is assigned to the upstream ("inlet"), downstream ("outlet"), side and bottom boundaries. The symmetric boundary condition is assigned to the symmetry plane. The pressure outlet boundary condition is assigned to the top boundary. A forcing zone [118] is applied at the upstream, downstream and side boundaries in order to eliminate the reflection of the waves at the boundaries. The forcing zone length is one wave length λ at the inlet and outlet boundaries, is 0.6λ at the side boundary.

When the two box barges are placed inside the wave basin, several mesh refinement zones are adopted to refine the mesh around the gap and the two box barges, also ensuring the mesh is changing gradually from a high density zone and a low density zone. The final settings of the mesh for the free surface and the gap are obtained by a series of convergence tests. The processes are discussed in the following sections.

To benchmark the results against the experimental data, we choose wave gauge 1 through 4. The wave gauges locate in the upstream location relative to wave gauge 5, 6, 7. It may requires less time for the upstream region to reach the steady state, compared with the downstream region.

7.2.2 Convergence Tests of Regular Waves

In this case, we generate the regular waves in the wave basin. First, we need to make sure the regular wave is properly generated. Thus, a convergence test is conducted to ensure the convergence and a 2D wave profile.

7.2.2.1 Grid Size

Herein, we will compare the time series of the wave elevation at wave 4 and wave contours from the different settings of meshes.

After about 8s, the waves inside the wave basin reaches approximately steady state.

Case	$\lambda/\Delta x$
A1	160
A2	100
A3	80
A4	40
A5	20

Table 7.2: Cases for the Convergence Test of Regular Waves

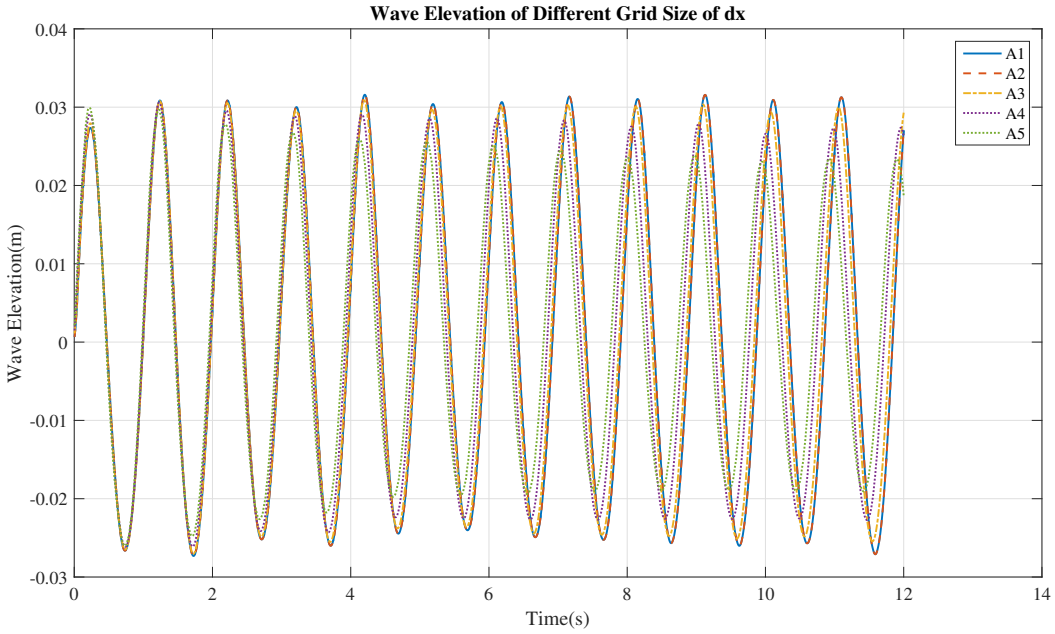

Figure 7.3: Time Series of Wave Elevation at (0, 0) for A1, A2, A3, A4, A5

We can observe that when we choose the setting of case A2, the results are independent of the grid size.

7.2.2.2 Number of Inner Iterations

In STAR-CCM+, the user needs to specify the number of inner iterations for each time step. This parameter is important in ensuring the accuracy of the result at each time step. We will investigate the time series at $(0, 0)$ and the wave profiles at different locations to decide the proper number of inner iterations.

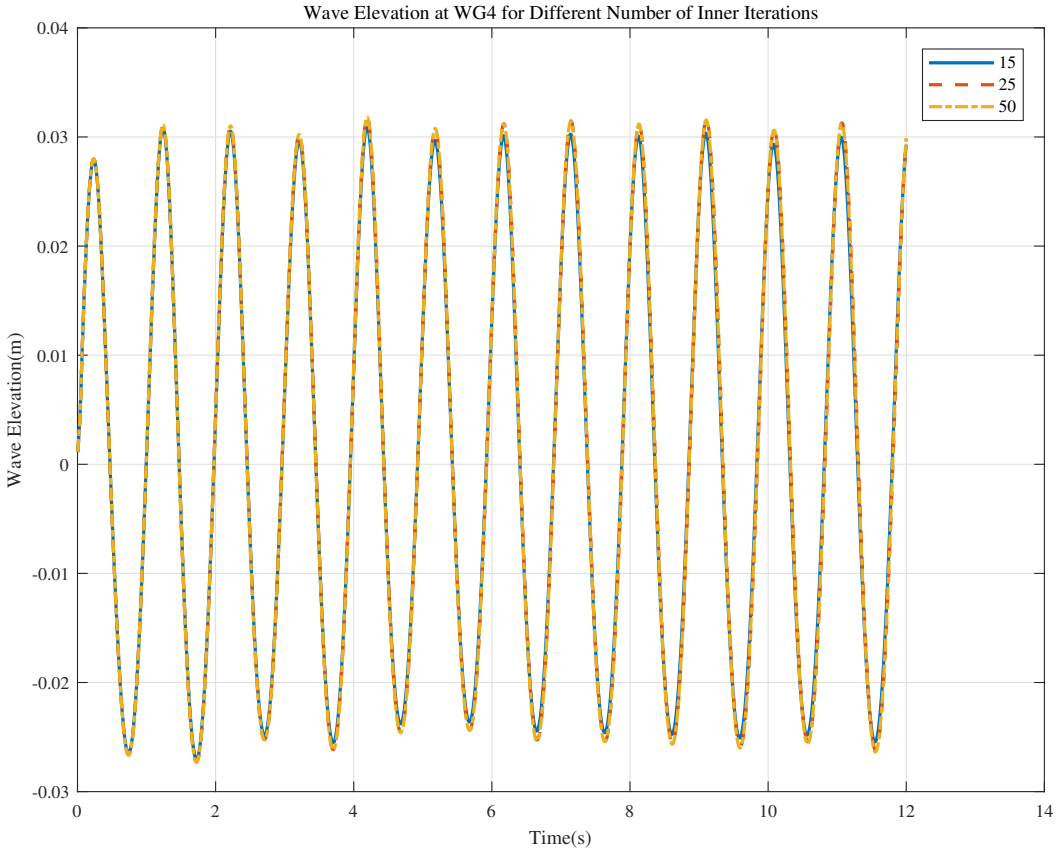

Figure 7.4: Time Series of Wave Elevation at (0, 0) for Different Number of Inner Iterations

From the time series, we may find small differences in the amplitudes between the blue curve and the other two curves. When the number of the inner iterations is set to be 25, the results are independent of this parameter. Thus, we set the number of inner iterations to be 25. After the ship is added into the domain, we will increase the number based on the number of cells in the domain.

We also plot the wave profiles passing through $(0, 0)$ at time $12s$ for different numbers of inner iterations.

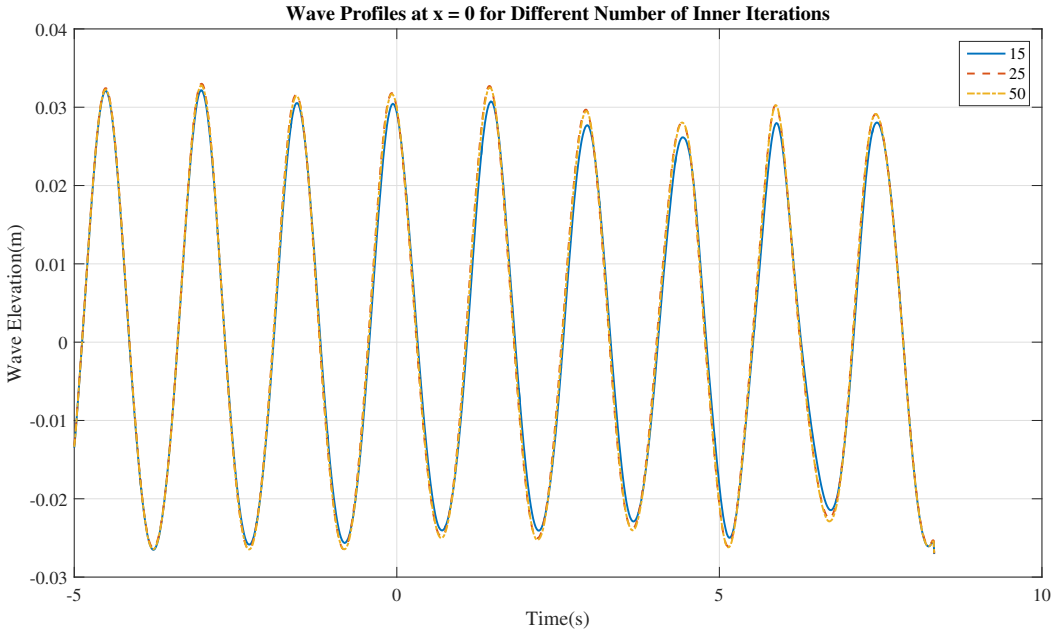

Figure 7.5: Wave Profiles for Different Numbers of Inner Iterations

A similar pattern is observed. It is reasonable to set the number of inner iterations to be 25. After adjusting the grid size, the number of inner iterations and other parameters, we observe the trough is relatively shallower compared against the peak. This phenomenon is also observed in the Finnegan[119], Duz[120] about the generation of regular waves. It may be due to the nonlinearity of the Navier-Stokes equations. When the wave is propagating away from the wave maker, it may begin to show some nonlinear properties in the profiles.

7.2.2.3 Region of Interest

The forcing function is adopted at the boundaries of the domain. The forcing function will affect the wave profile in the domain near the boundary. To study the wave interaction problem, we need to make sure the wave is 2D in the region of interest. Therefore, we plot the wave profiles at different locations when the simulation time is at $12s$.

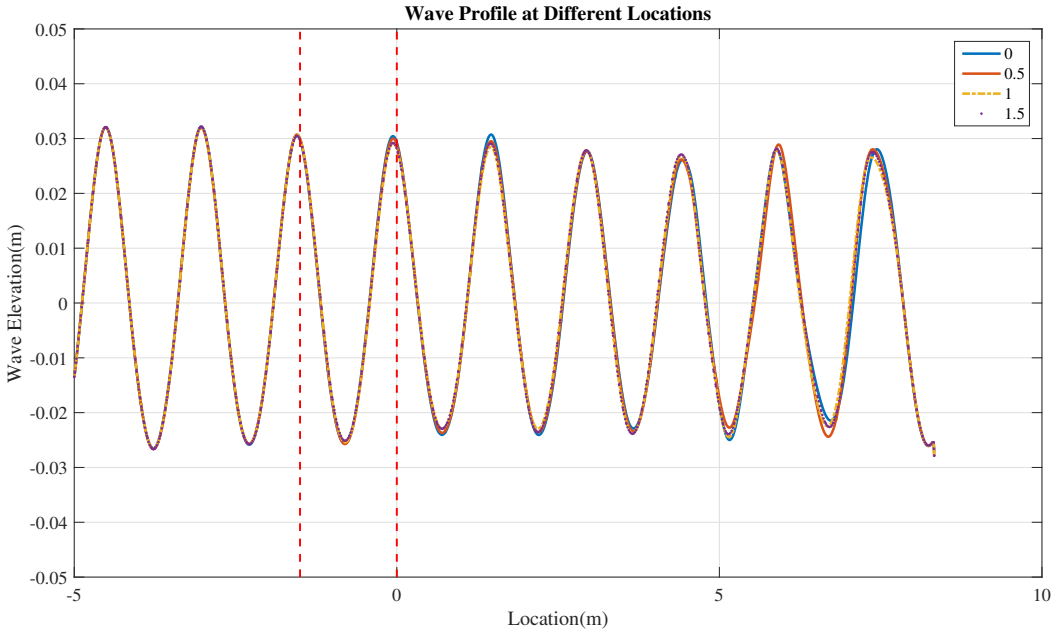

Figure 7.6: Wave Profiles at Different Locations (0, 0.5, 1, 1.5)

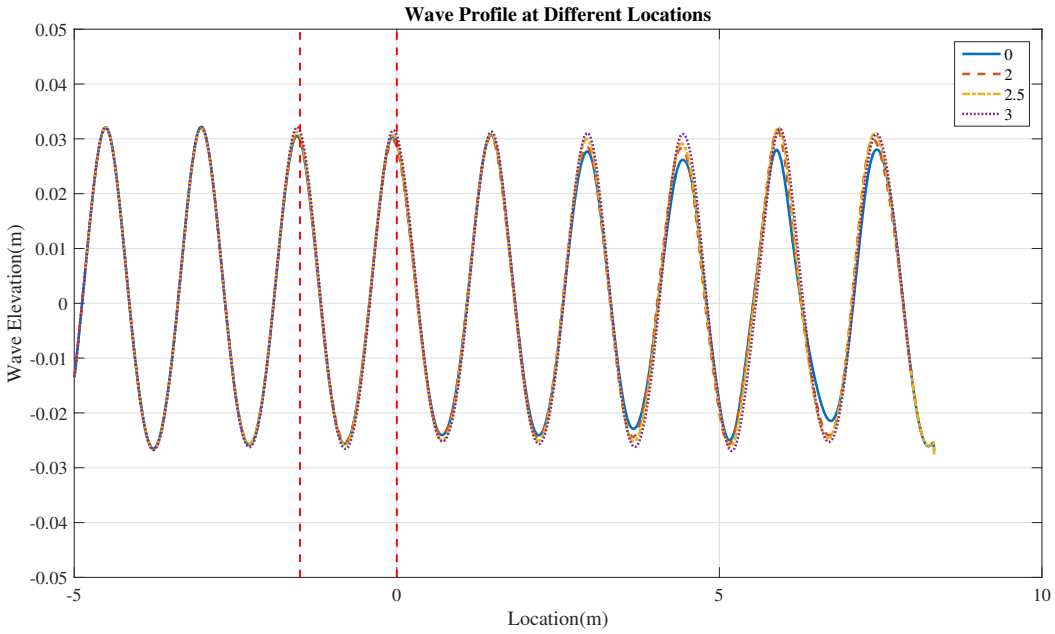

Figure 7.7: Wave Profiles at Different Locations (0, 2, 2.5, 3)

In the figures, the number 0 stands for the wave profile right at the symmetry plane, which is at the middle of the wave basin. The number 0.5 is the wave profile which is 0.5m apart from the symmetry plane. The same definition applies for the rest of the numbers. When the separation distance is 3m, the wave profile is very near the forcing zone. The red vertical dashed lines indicate the region we are interested in. The side walls of the box barge locates at 0.034m and 0.767m from the symmetry plane.

From the comparisons, we may conclude that the wave can be considered as 2D in the region of interest. In the down stream part, there are some differences in the amplitudes of the wave profiles when the separation distance is larger than 2. However, that discrepancy happens far away from the region of interest. We assume that the discrepancy will not affect the results. We will also validate the assumption after we put the box barges inside the domain by testing different widths of the wave basin.

7.2.3 Convergence Tests of Wave Elevation in Gap

After placing the two box barges in the wave basin, we need to find the proper mesh density to make the results converge. In the convergence tests, we adjust the mesh density around the gap and around the two vessels simultaneously. We choose the settings in case A2 to model the free surface far away from the two box barges. Below is the table of the settings for the smallest control surface around the gap. When the mesh density is adjusted, the other control volumes for the gap and those for the box barges are changed accordingly.

Case	$\lambda/\Delta x$ or $\lambda/\Delta y$	$\lambda/\Delta z$
B1	160	1000
B2	320	1000

Table 7.3: Cases for the Convergence Test of Wave Elevation inside Gap

Firstly, we compare the time series of the wave elevation at the two wave gauges.

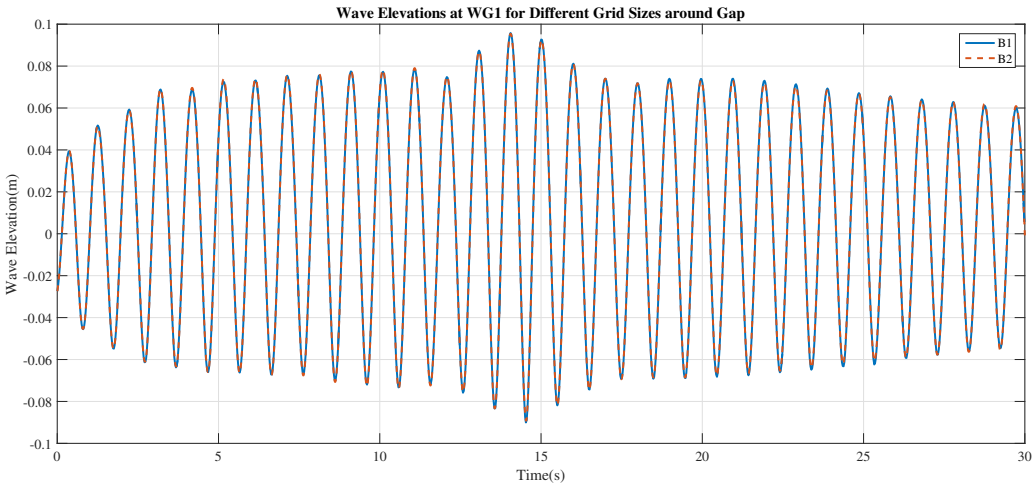

Figure 7.8: Time Series of Wave Elevation at WG1 for Different Grid Sizes

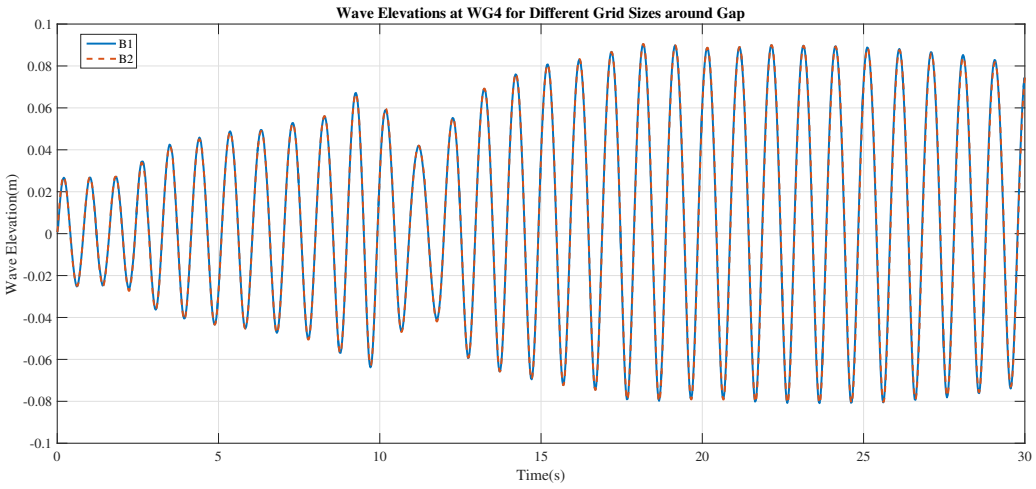

Figure 7.9: Time Series of Wave Elevation at WG4 for Different Grid Sizes

We can observe that the two curves are identical. Thus, we choose the settings in case B1 to continue the following study.

Secondly, we validate the assumption that the wave can be considered as 2D wave in the region of interest. We choose the width of the computational domain to be 4m and 6m. Please note that

the width of the wave basin is twice the width of the computational domain. Because we adopted the assumption of symmetry. The width in the legend of the figures indicates the width of the computational domain.

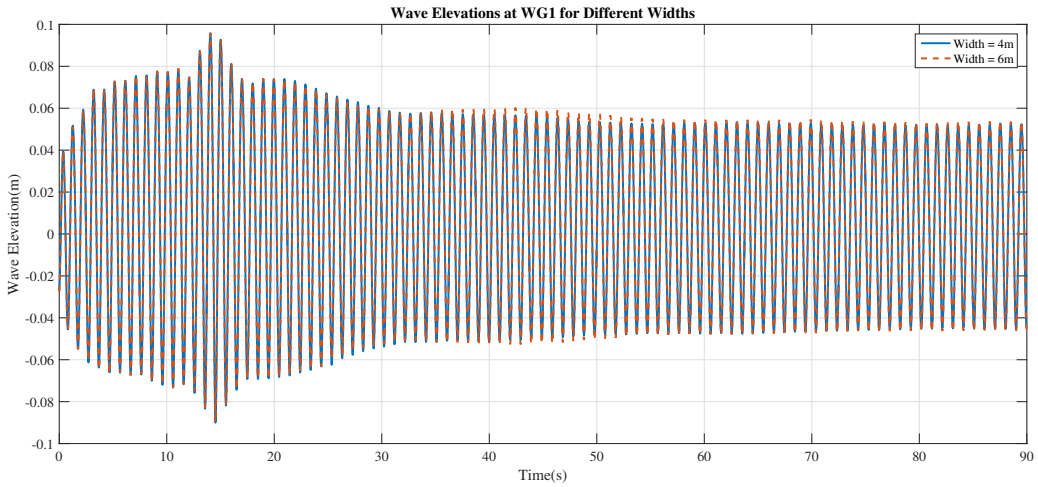

Figure 7.10: Time Series of Wave Elevation at WG1 for Different Widths

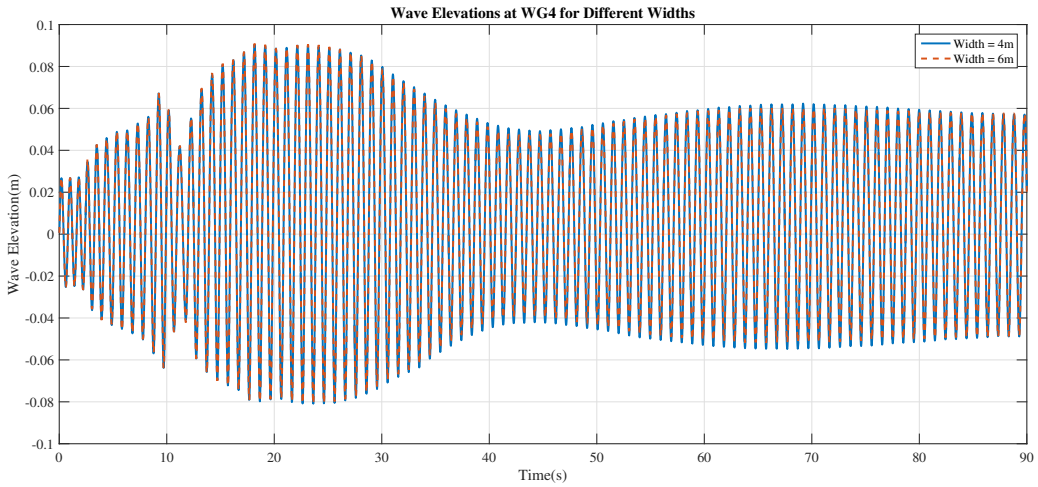

Figure 7.11: Time Series of Wave Elevation at WG4 for Different Widths

The two time series are almost identical except that in the range from 40s to 55s, there are very small discrepancies. When the two curves reach the steady state, they are exactly on top of each other.

7.2.4 Results and Conclusions

In this section, we benchmark the results from STAR-CCM+ with the experimental data and visualize the flow field inside the gap.

7.2.4.1 Comparisons of Wave Elevation RAO

From STAR-CCM+, we obtain the time series of the wave elevation at the wave gauges 1 to 4. We need to select the part after the flow field reaches a steady state. In simulating the regular waves without the box barges, we find that it takes about 8s. In the simulation with the box barges, we keep elongating the total simulation time until the steady state is reached.

Below are the plots of the time series of the wave elevation at wave gauges 1 and 4. When the time series at the two wave gauges reach a steady state, the wave elevation at wave gauges 2 and 3 are also steady. Due to the similarity, here we show the time series at wave gauges 1 and 4 only. In comparing the results from CFD, experiments, potential method, we will present the results for wave gauges 2 and 3.

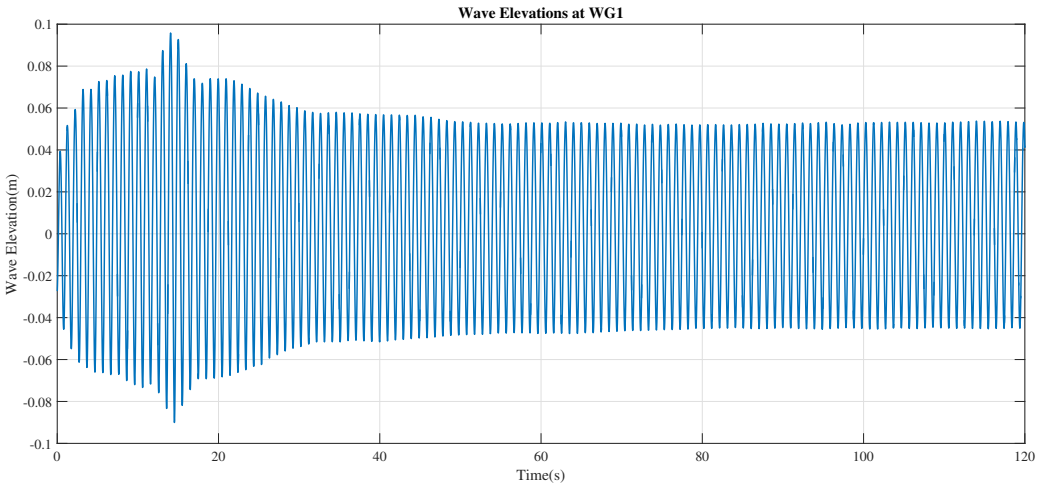

Figure 7.12: Time Series of Wave Elevation at WG1 (0-120s)

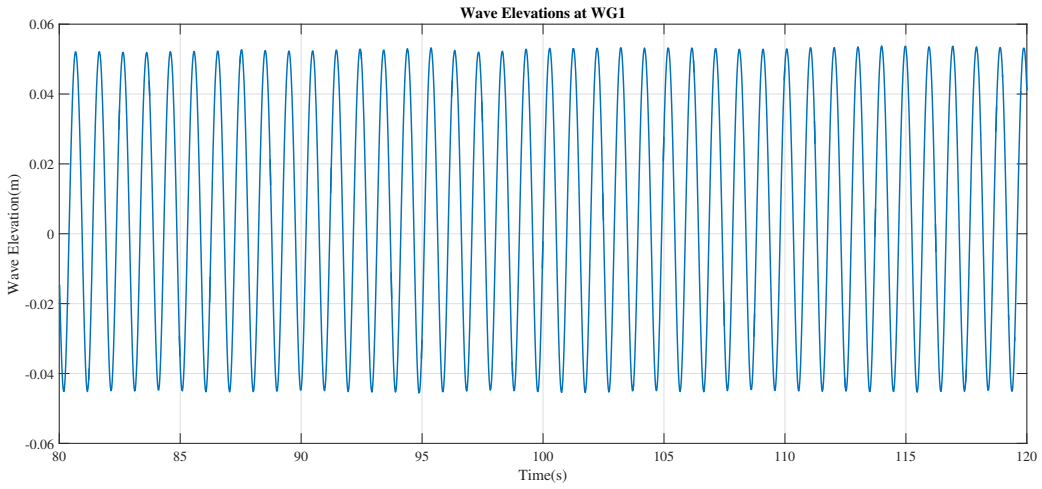

Figure 7.13: Time Series of Wave Elevation at WG1 (80-120s)

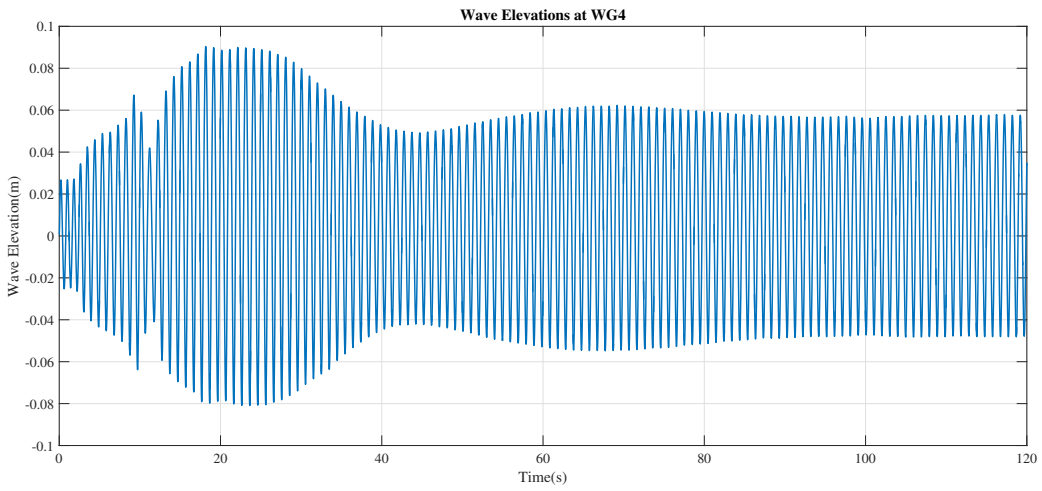

Figure 7.14: Time Series of Wave Elevation at WG4 (0-120s)

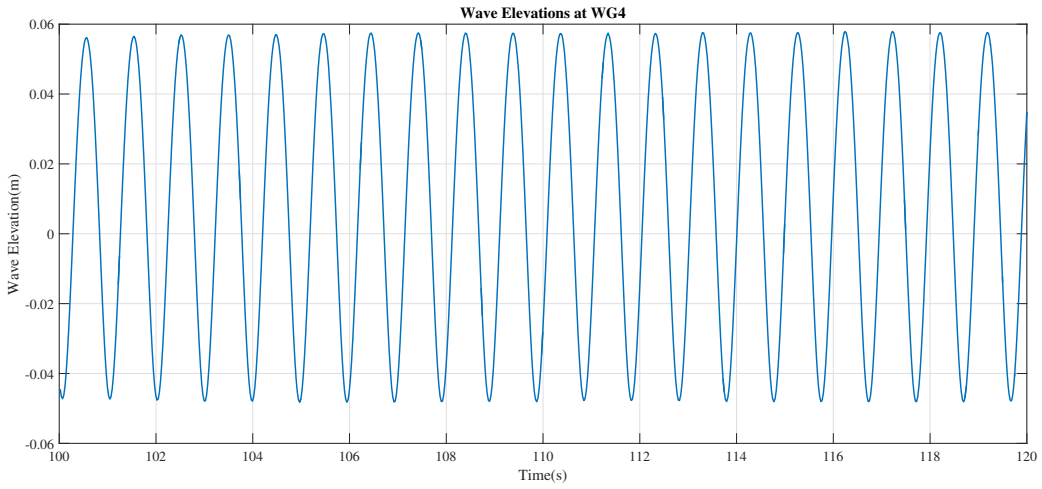

Figure 7.15: Time Series of Wave Elevation at WG4 (100-120s)

From the time series, we can find the minimum, maximum, average time series of wave amplitudes and wave periods. We use the average wave amplitude to find the RAO and use the error bar to denote the minimum and maximum of the wave amplitudes and wave periods.

The comparisons of the results from STAR-CCM+, experiments and the panel method are shown below. The vertical error bars denote the minimum and maximum wave amplitudes in the selected time series. The horizontal bars are the minimum and maximum radian frequencies. We use the way to denote the uncertainty in the CFD simulation by using STAR-CCM+.

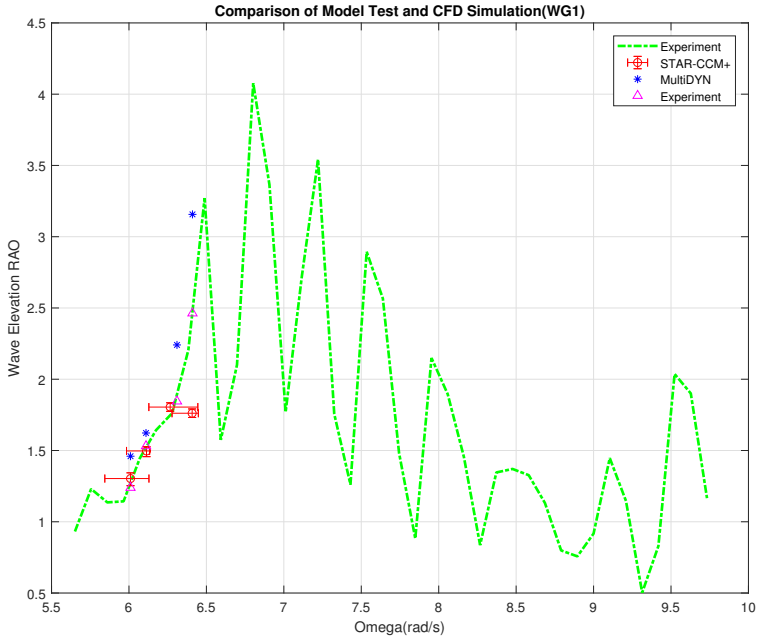

Figure 7.16: Comparisons of Wave Elevation RAO at Gauge 1

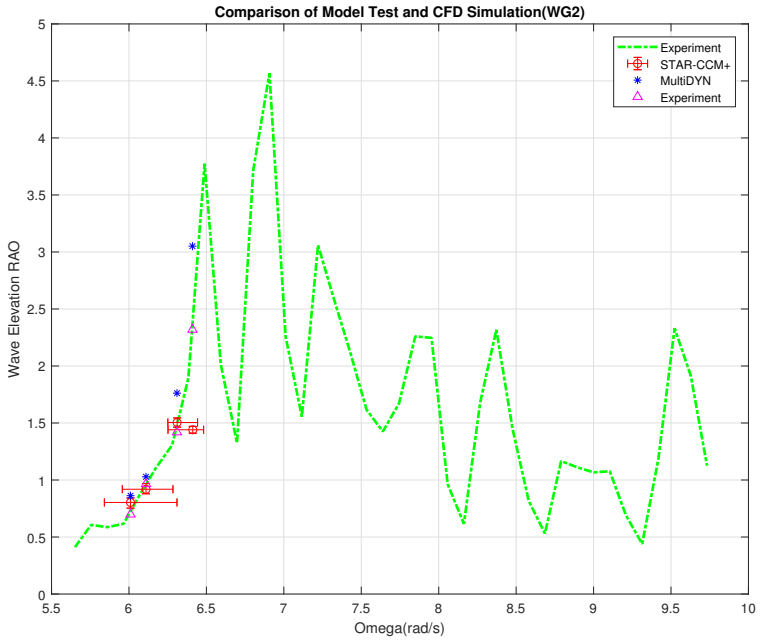

Figure 7.17: Comparisons of Wave Elevation RAO at Gauge 2

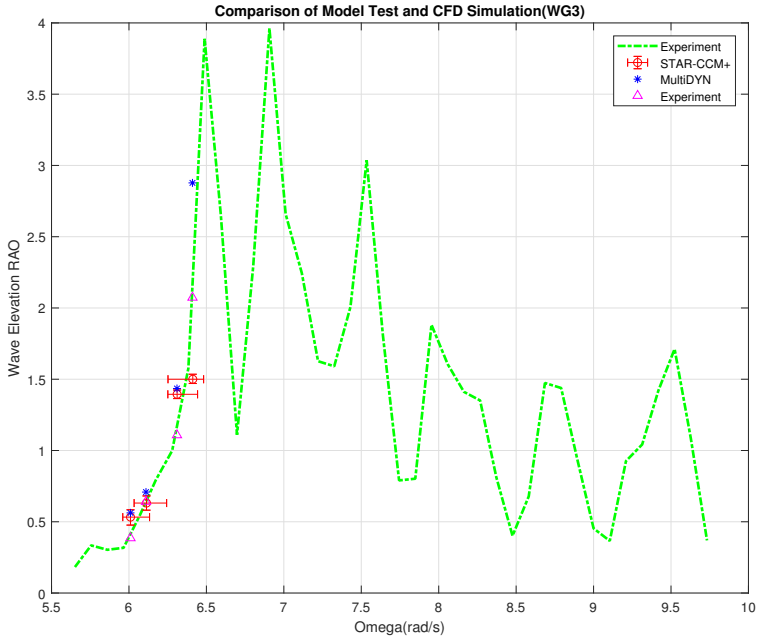

Figure 7.18: Comparisons of Wave Elevation RAO at Gauge 3

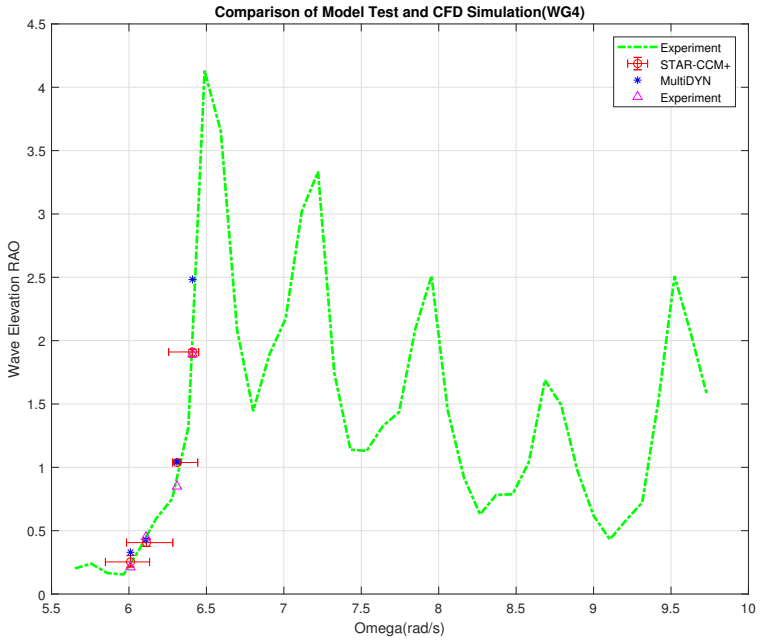

Figure 7.19: Comparisons of Wave Elevation RAO at Gauge 4

The results of the panel methods are from our in-house program, MDLMultiDYN. The wave elevation is over predicted by the potential method compared with the STAR-CCM+ and the experiment. In the range of relatively lower frequencies, the average wave elevation RAOs at the wave gauges are consistent with the experimental data if considering the uncertainties. At radian frequency $6.41rad/s$, we may notice the discrepancy. However, because the period we choose is 0.98s, a difference 0.02 leads to a noticeable discrepancy for the radian frequency. When considering the uncertainty in the CFD simulation, we may find the results at wave gauge 1 through 4 are in good agreement with the experimental data. This confirms the simulation is reliable for further investigation.

7.2.4.2 Vector Plots of the Cross Section inside Gap

Additionally, to understand the physical phenomenon inside the gap, we create a vector field to visualize the flow field on the cross sections along the gap and transversely across the gap. Below is the figure to indicate the cross sections at wave gauges 1 and 4. This is a top view of the cross sections. The red line indicates the cross section along the gap and orange line is across the gap. To avoid the confusion of the air velocity, we set the Z coordinate of the cross section to be from -0.35m to -0.05m.

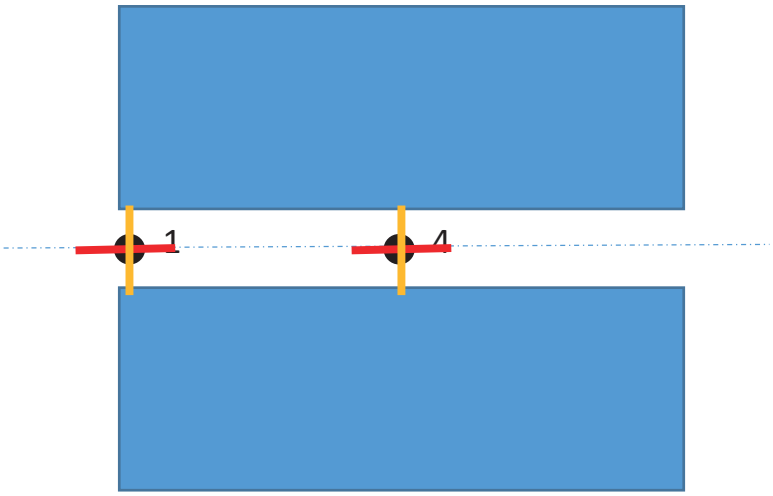

Figure 7.20: Cross Sections of the Vector Plots

Herein we extract some of the vector field at different simulation time at wave gauge 4 to illustrate the physical process. The arrows display the direction of the flow and the color indicates the amplitude of the flow velocity. The vector field is created at the round corner of the box barge. Because of the symmetry, we only show the vector plot for one box barge. The vertical line indicates the symmetry plane.

The mesh is indicated in the following figure:

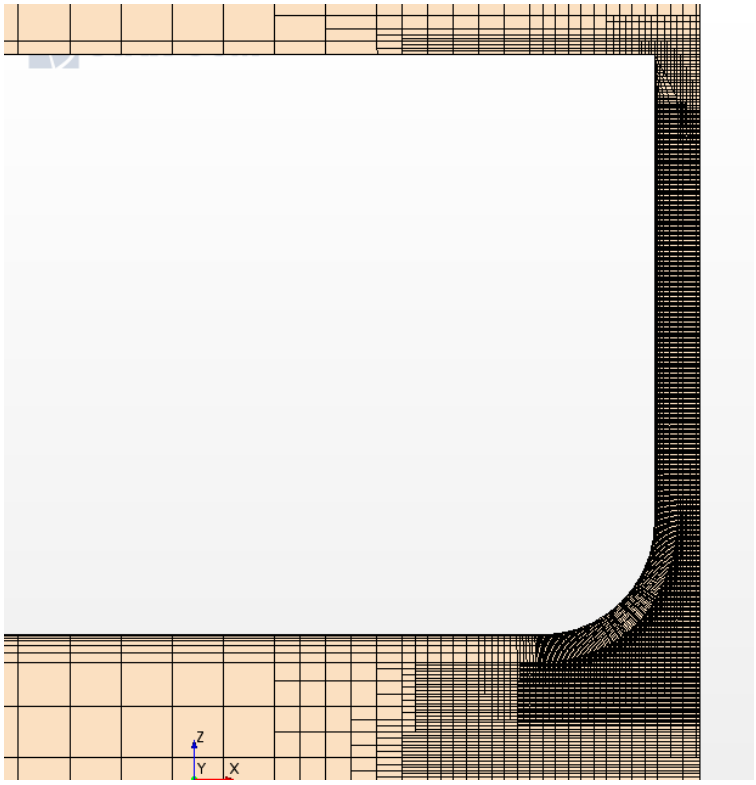

Figure 7.21: Mesh Near the Gap

At 117.93s, the cross section is like this:

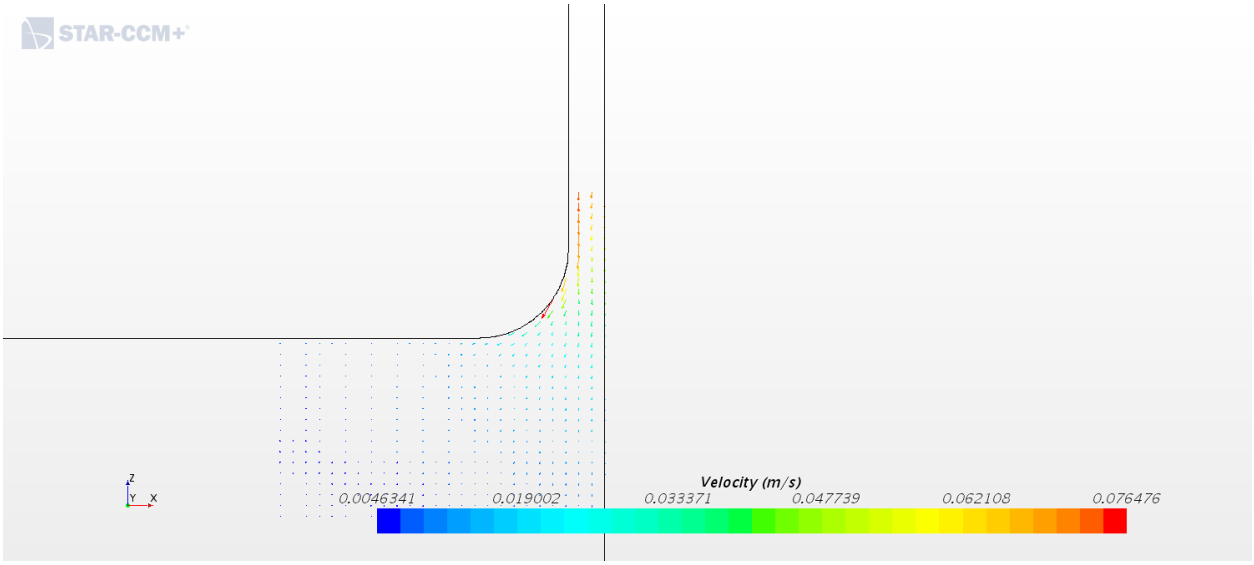

Figure 7.22: Vector Plot at 117.93s

The flow inside the gap has a tendency to move downward. The velocity of the flow around the round corner is the largest relative to the other locations.

As the flow moves downward, at 118.025s, the vector field is like that in the following figure.

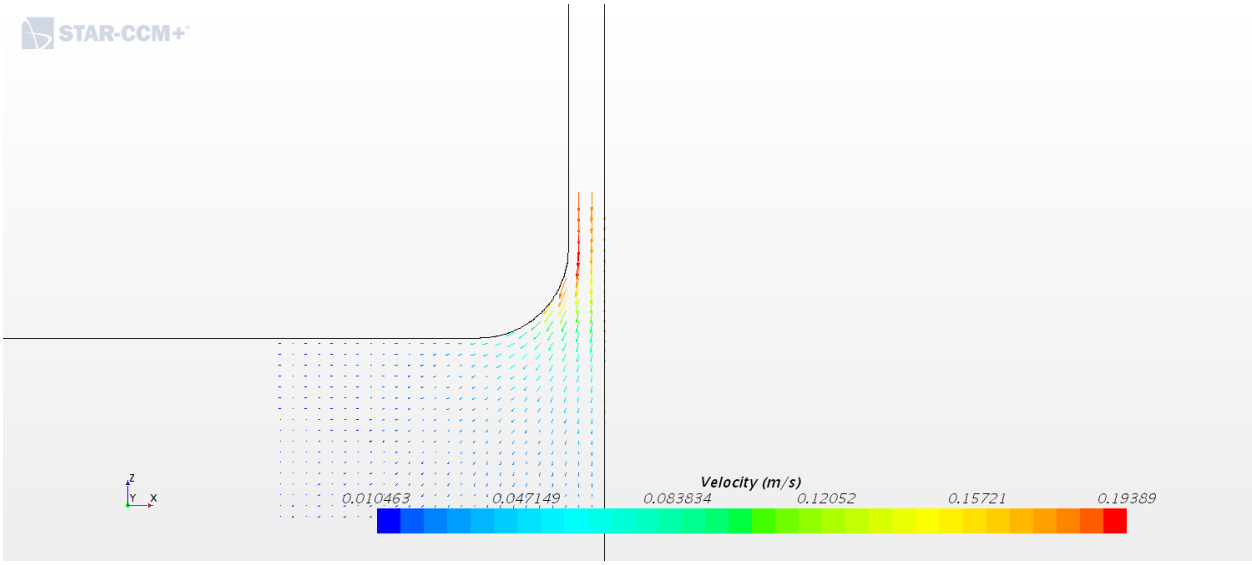

Figure 7.23: Vector Plot at 118.025s

The velocity of the fluid next to the ship hull is relatively larger. It means that the flow at the ship hull will first move downward. Soon after that, the fluid inside the gap begins to move together to the bottom of the box barge. The velocity profile at 118.275s is shown as below:

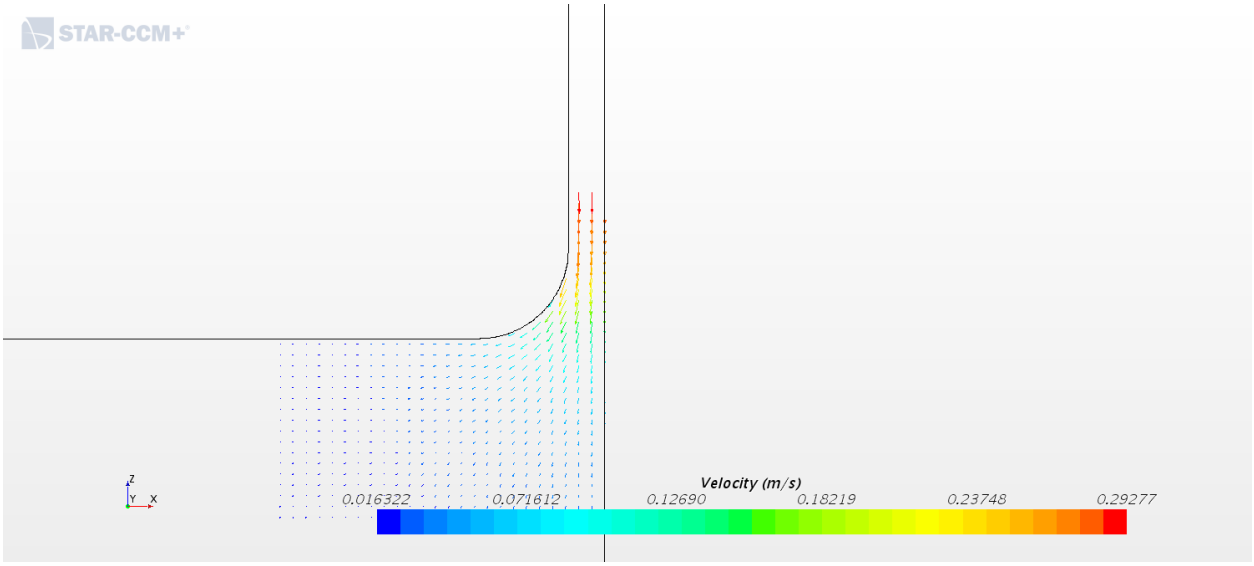

Figure 7.24: Vector Plot at 118.275s

Due to the periodicity of the wave, the fluid inside the gap will also move upward. Initially, the velocity of fluid field is relatively larger at the center of the gap. It means that when the fluid moves upward, the fluid at the center moves first. The profile is shown as below:

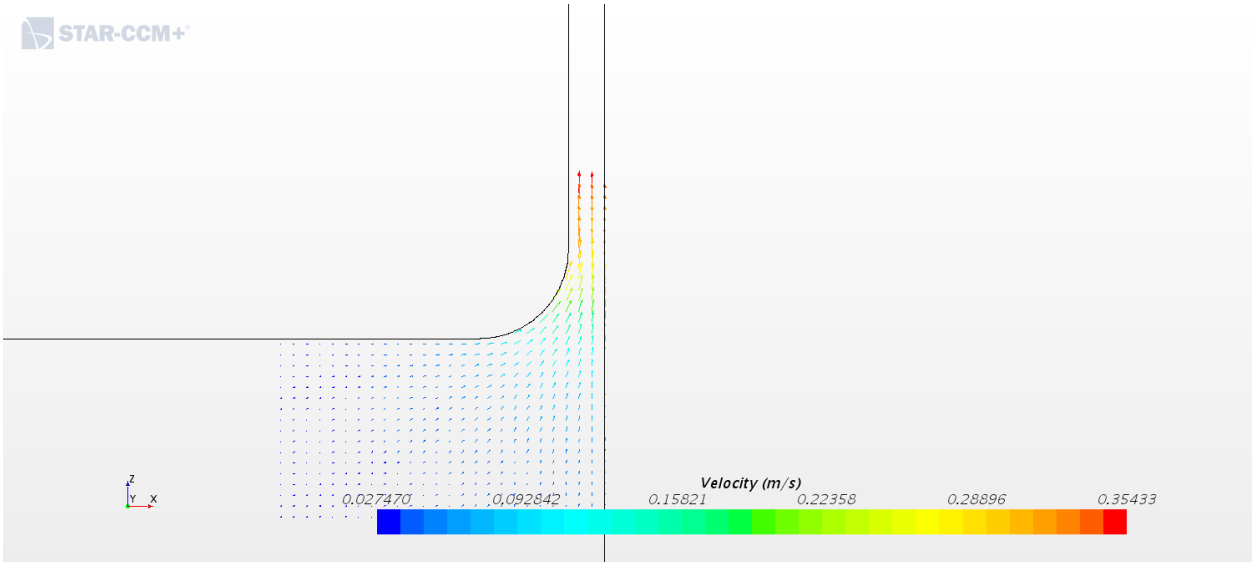

Figure 7.25: Vector Plot at 118.57s

After that, the fluid next to the ship hull begins to have a larger velocity shown as below:

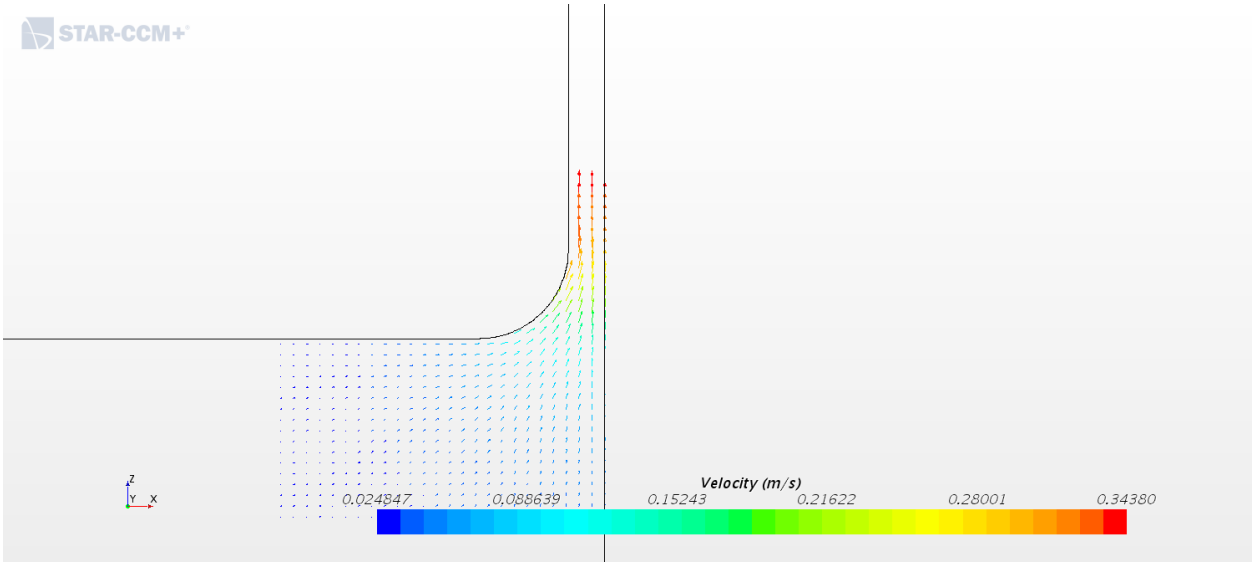

Figure 7.26: Vector Plot at 118.615s

When the maximum velocity drops down, the fluid next to the ship hull will slow down first. From the following figure, we can see the velocity of the fluid at the center is relatively bigger until the start of the next period.

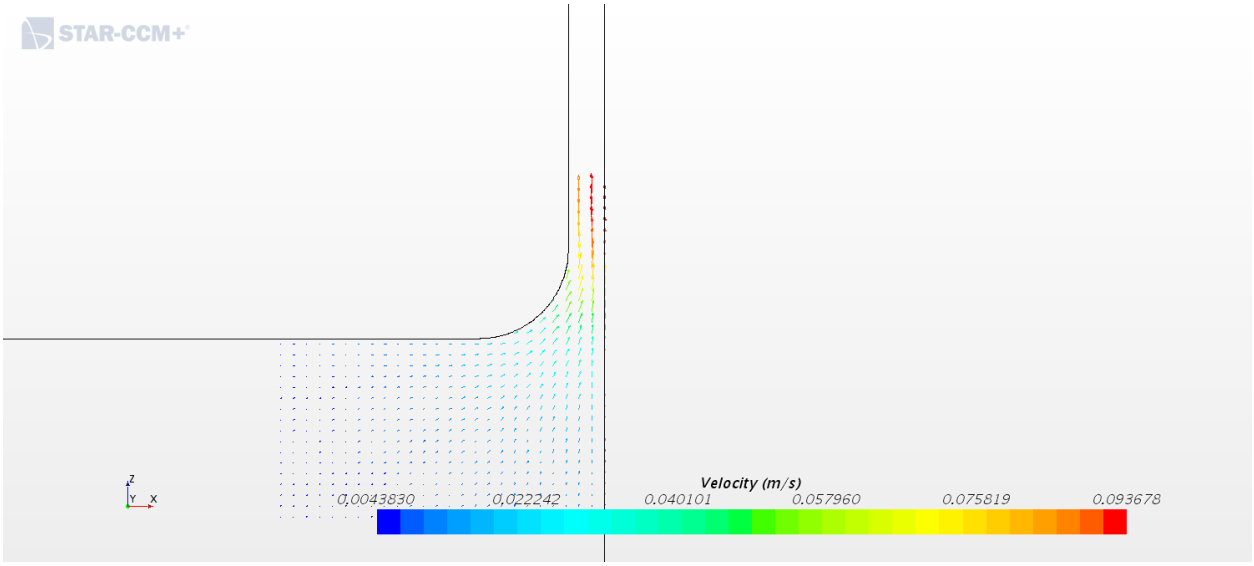

Figure 7.27: Vector Plot at 118.85s

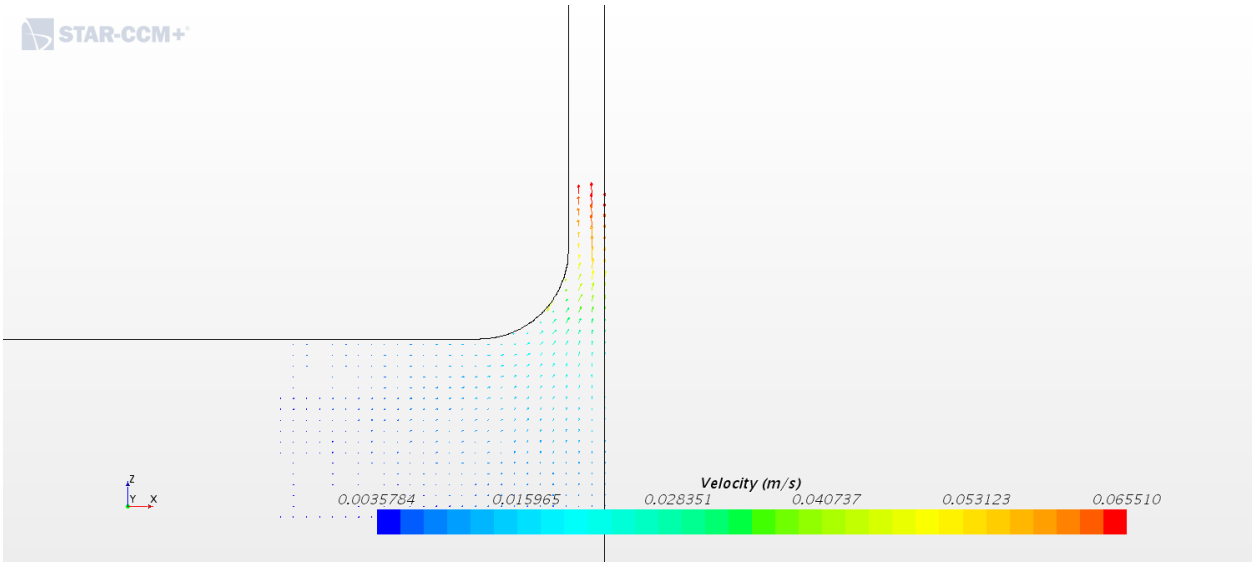

Figure 7.28: Vector Plot at 118.88s

In the beginning of the next period, the fluid next to the ship hull shows similar pattern as before. It moves up/down first and then repeats the whole process again. Below is the figure to show the start of the next period.

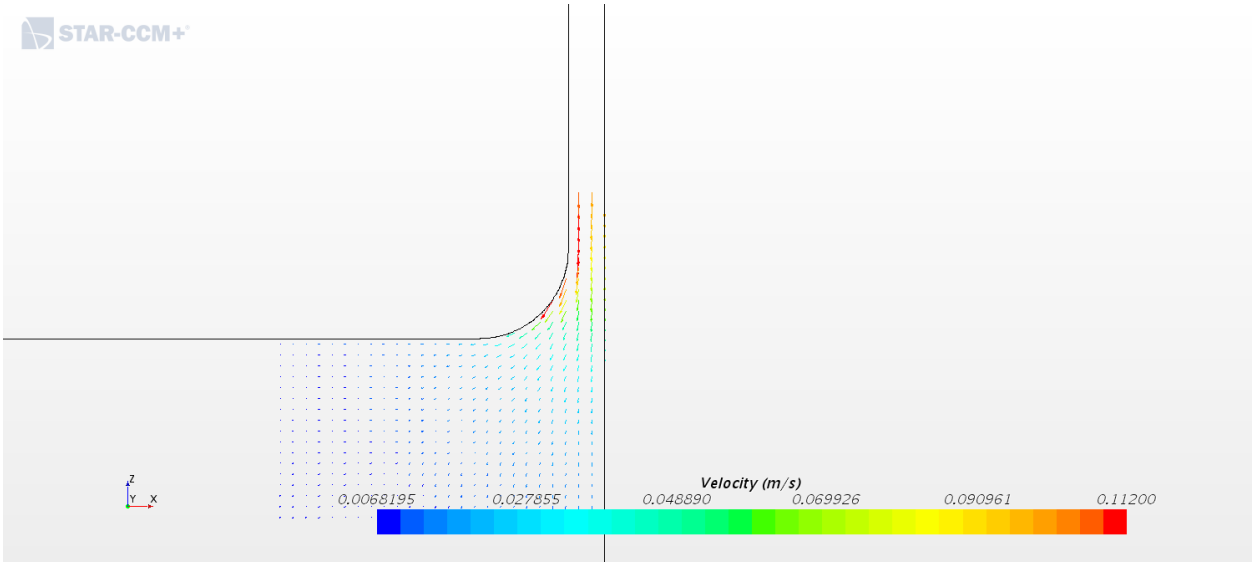

Figure 7.29: Vector Plot at 118.945s

7.2.4.3 Comparisons of Pressure Contour of the Ship Hull

In this section, we will compare the pressure contour in the frequency domain from MDLMultiDYN and STAR-CCM+. Below are the results from STAR-CCM+:

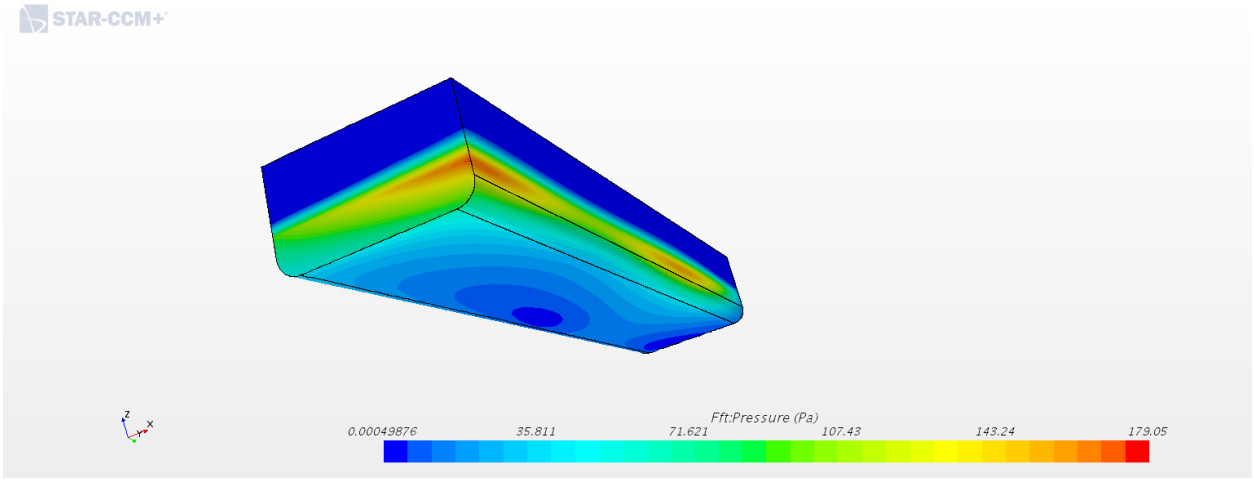

Figure 7.30: Pressure Contour ($\omega = 6.41$ rad/s) from STAR-CCM+

We may find from the figures that near the waterline, there are approximately two peak values

(indicated by the red area).

If we view the pressure contour from the bottom of the ship hull near the stern, we will get this pressure contour.

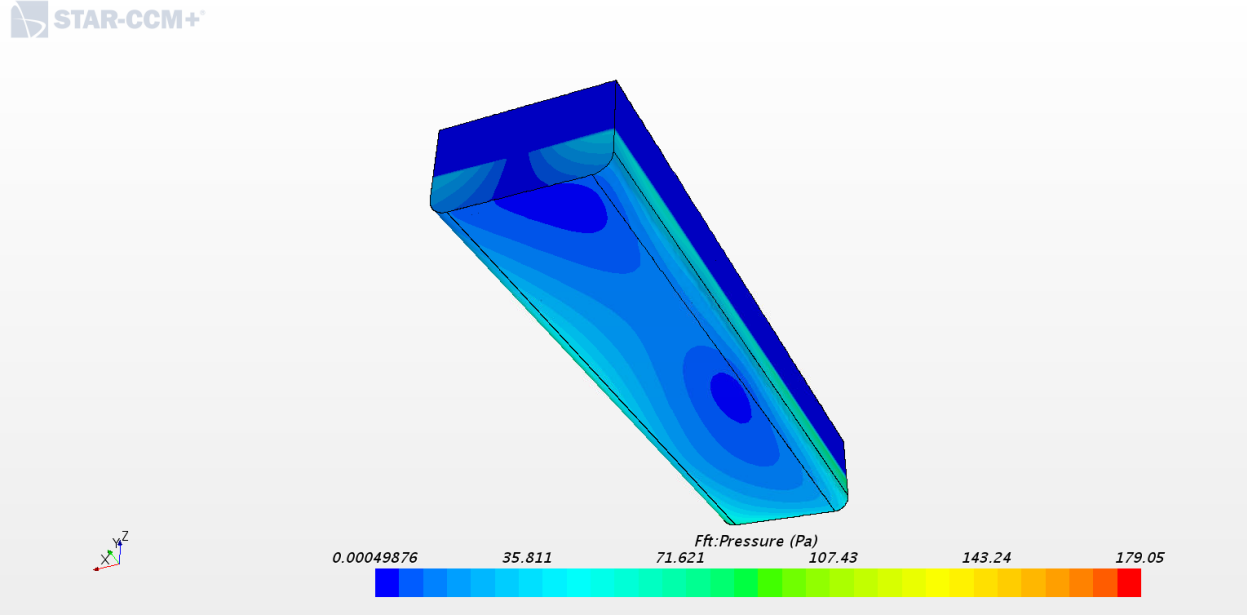

Figure 7.31: Pressure Contour ($\omega = 6.41$ rad/s) from STAR-CCM+

We can clearly identify that there are two troughs on the bottom (indicated by dark blue), near which the pressure value reaches the local minimum.

The results from MDLMultiDYN are as below:

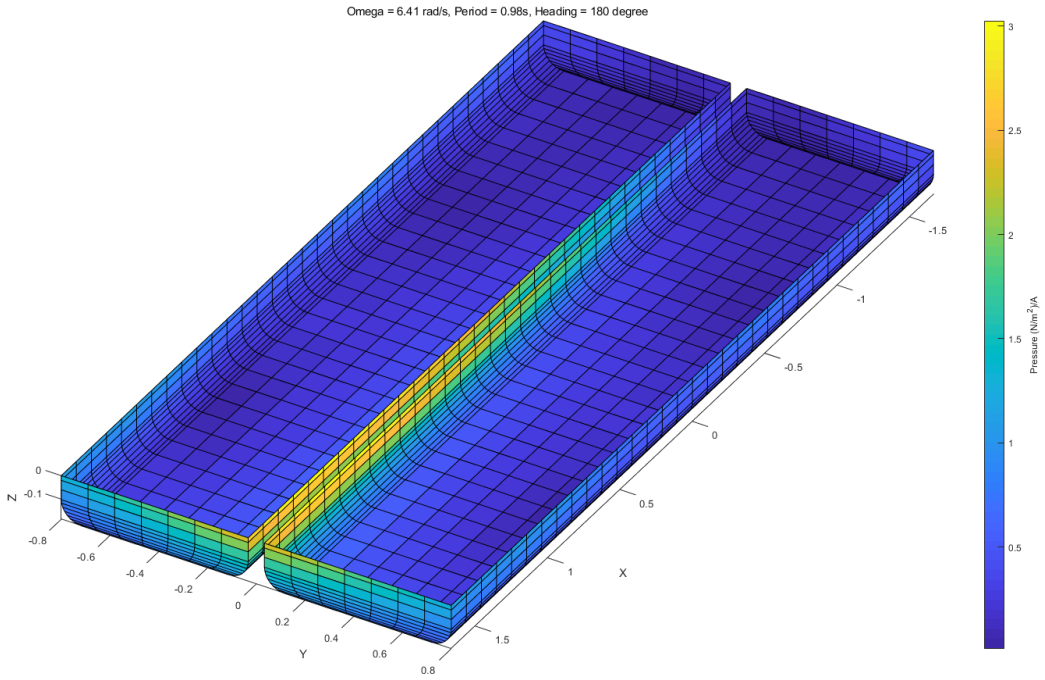

Figure 7.32: Pressure Contour ($\omega = 6.41$ rad/s) from MDLMultiDYN

Please note that the displayed part is the ship hull under water while the displayed part from STAR-CCM+ is the whole ship hull. We find the pressure distribution has a similar pattern near the bow of the ships. It reaches a peak value at the entrance of the gap region. However, there does not exist the other peak near the middle of the ship. The difference is seemingly caused by the viscous effect in the simulations in CFD.

If we view the ship from the bottom and near the stern, we may observe a similar pattern with that in STAR-CCM+. The locations of the two troughs are close to those observed in the simulations from STAR-CCM+.

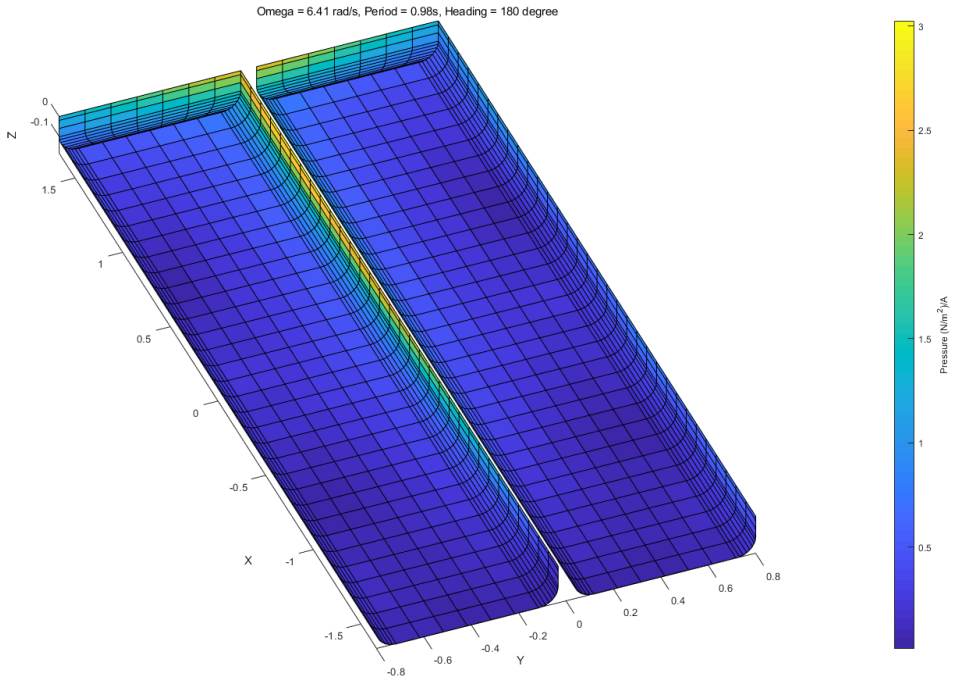

Figure 7.33: Pressure Contour ($\omega = 6.41$ rad/s) from MDLMultiDYN

From the comparisons, we may conclude that in this case, the observations from the potential method are similar to that in CFD. Thus, by using the tools based on the potential method, we may dig out useful information about the patterns of the pressure distribution on the ship hull.

7.2.4.4 Conclusion

From the comparisons of the results, we can conclude that the CFD simulation is a useful tool to simulate the side-by-side offloading problem. At the wave frequency we choose, the results are consistent with the experimental data.

After visualizing the fluid domain inside the gap, we find the fluid next to the ship hull have the tendency to move before the remainder of the fluid at the cross section. It also quickly slows down due to the viscosity. The fluid at the center of the gap seems to have a time lag relative to the fluid next to the ship hull. Wave breaking and fluid separation are not observed in this case. Therefore, we can conclude that in this case, the dominant effect to damp out the wave energy is the surface

friction on the ship hull.

Finally, the comparisons of the pressure contours show the similarity and the differences between the results from the potential method and the CFD approach. Despite the difference, the information from the potential method will still be helpful to the initial evaluation of the design.

7.3 Observations using Potential Method

7.3.1 Wave Elevation along the Gap

After obtaining the model test data, we simulated the model in both MDL Multi DYN and WAMITv6 and obtained similar results. Here is the comparison of the wave elevation at wave gauge 4.

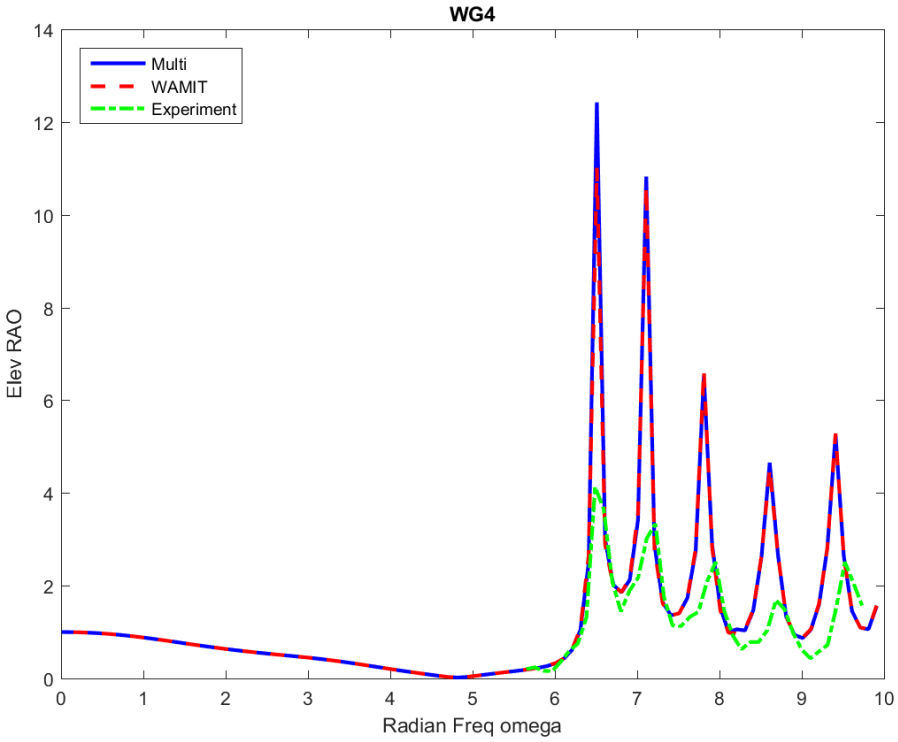

Figure 7.34: Comparisons of Wave Elevation at Gauge 4

We may observe from the figure that the tools based on the potential method over predict the

wave amplitude. The resonance frequencies of the experimental data seemingly have a shift compared against the simulation results. It is of interest to study the wave elevation inside the gap at different frequencies. Thus, we generated 2655 field points inside the gap and the corresponding contour of the wave elevation RAO formed by those points. We find that different modes of resonance appear at different frequencies. In the range of radian frequencies ($\omega = 6.51 - 9.91 rad/s$), we observe 10 modes of the resonance. Herein we present the first three modes of the gap resonance. The rest modes share the same pattern.

The figures show that along the gap, a standing wave is seemingly formed. At the first mode, only one antinode exists in the middle of the gap. From the figure, it is hard to identify the exact locations of the nodes, which seem to locate at the two ends of the gap. A similar pattern applies for the second and the third modes. However, for different modes, the locations of the nodes seem distinguished from each other. It means the region where forms the standing wave is different at different resonant frequencies.

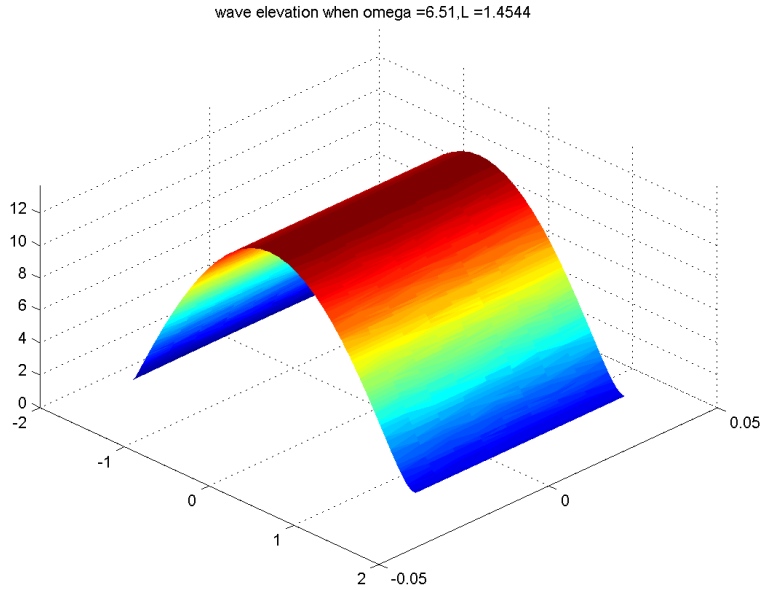

Figure 7.35: 1st Mode of Resonance inside the Gap

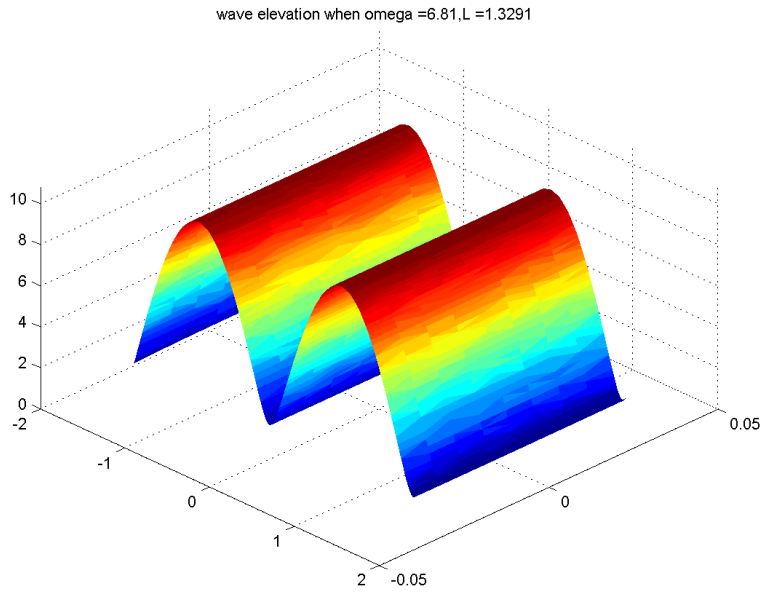

Figure 7.36: 2nd Mode of Resonance inside the Gap

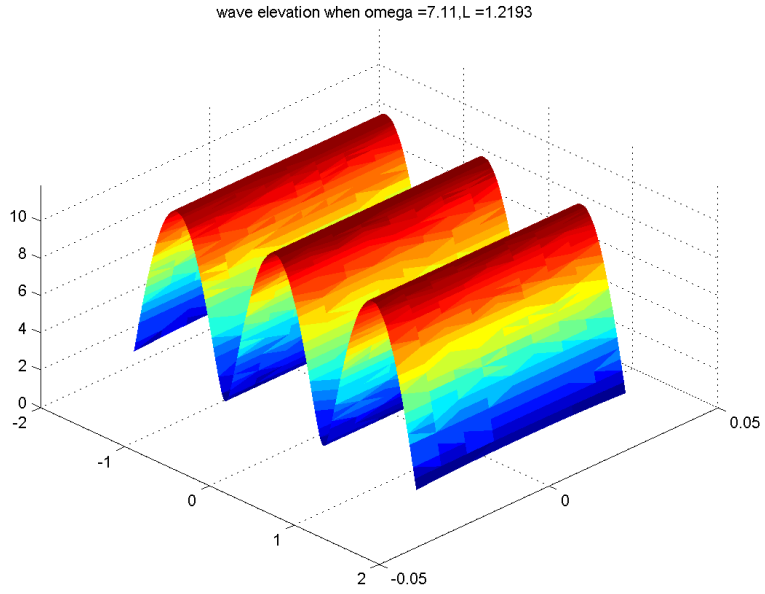

Figure 7.37: 3rd Mode of Resonance inside the Gap

7.3.2 Pressure Contour of the Ship Hull

Meanwhile, to study the effect on the ship hull, we generate the plots of the amplitude of the total pressure on the ship. We have also generated such plots caused by the incident waves and diffracted waves separately. We may find the patterns of the pressure are consistent with the wave elevation. The pressure in the following figures is contributed by the sum of the incident potential and the diffraction potential.

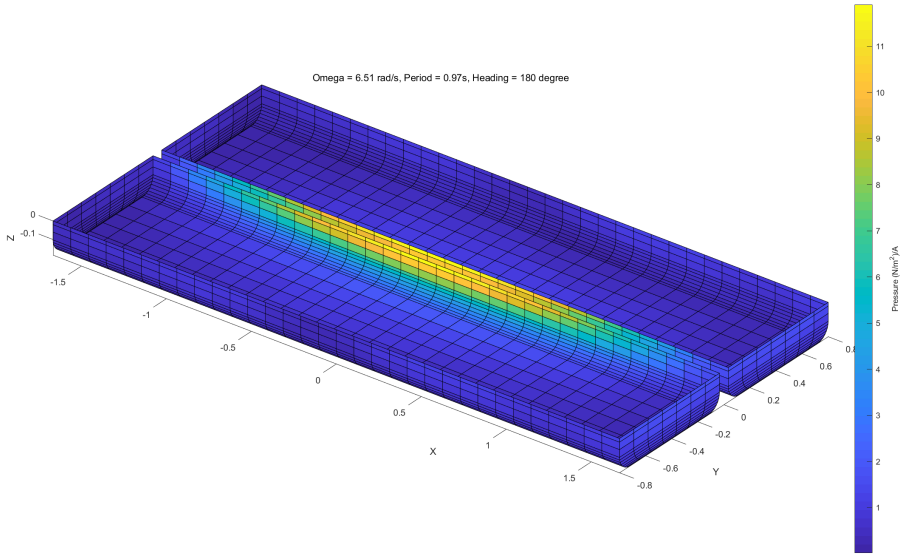

Figure 7.38: Pressure Distribution at 1st Mode of Resonance inside the Gap

We may find the pressure distribution is corresponding to the wave elevation RAO along the gap. The amplitude of the pressure reaches a maximum where the wave elevation RAO is the largest. The two box barges share a similar pattern, which is indicating the symmetry of the phenomenon. Similar patterns can be found in the pressure plots at the second and third mode of resonances.

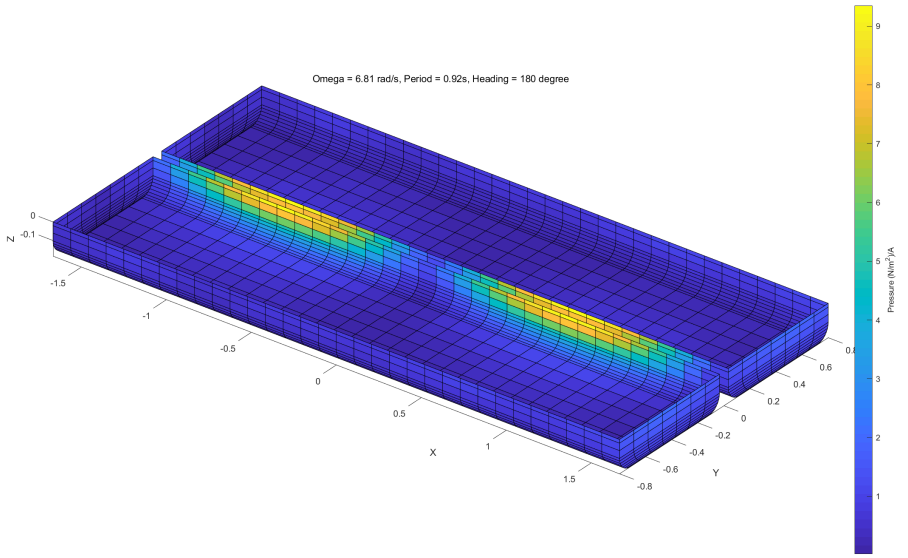

Figure 7.39: Pressure Distribution at 2nd Mode of Resonance inside the Gap

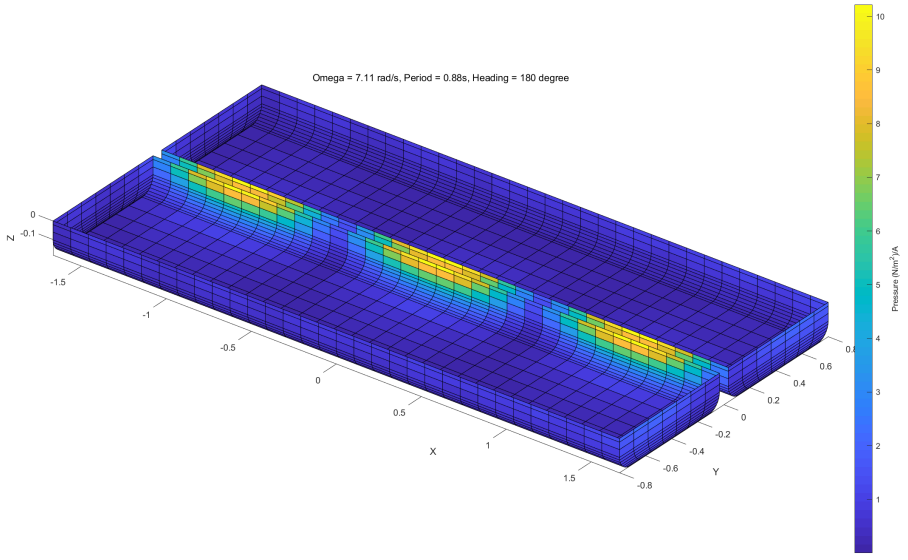

Figure 7.40: Pressure Distribution at 3rd Mode of Resonance inside the Gap

To study the effects of incident potential and diffraction potential separately, we also generate the contour plots of the two types of potentials.

The plots of pressure distribution caused by the incident potential are listed below:

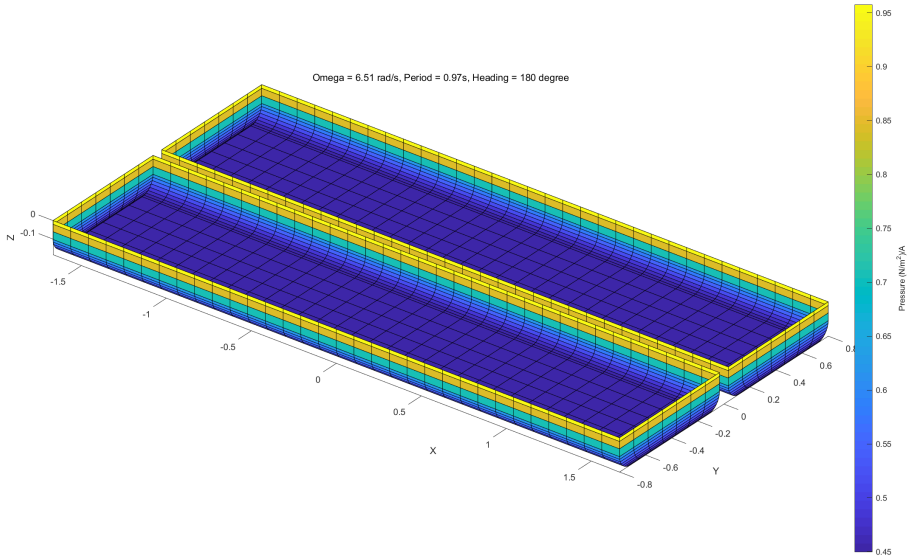

Figure 7.41: Pressure Distribution by Incident Potential at 1st Mode of Gap Resonance

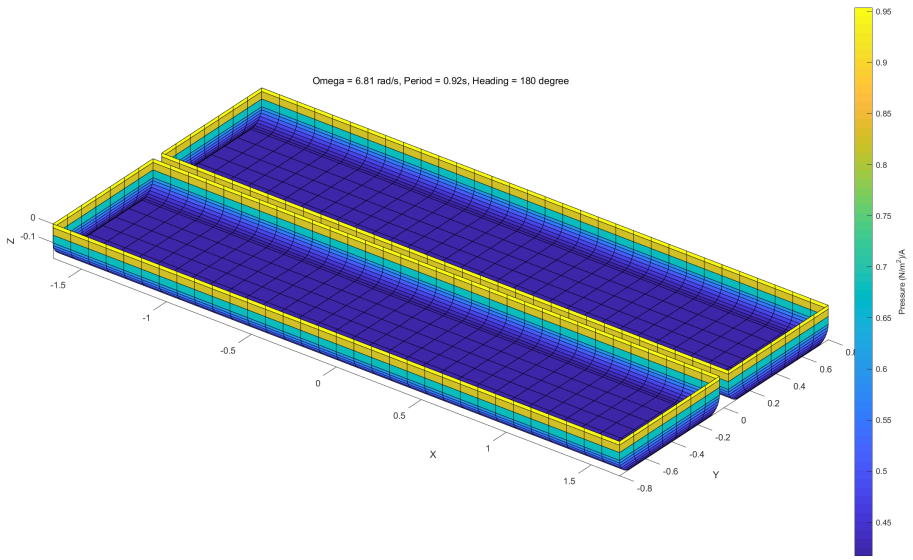

Figure 7.42: Pressure Distribution by Incident Potential at 2nd Mode of Gap Resonance

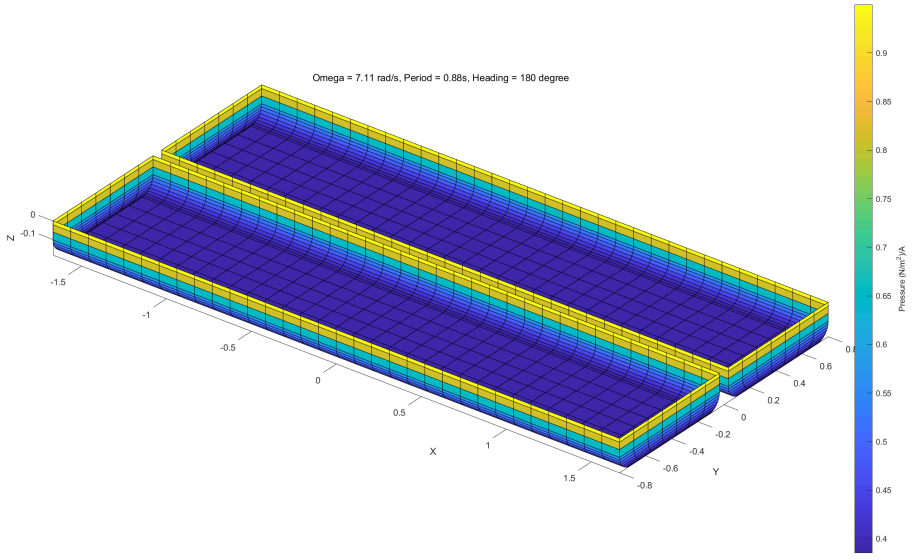

Figure 7.43: Pressure Distribution by Incident Potential at 3rd Mode of Gap Resonance

The figures show that the amplitude of the pressure caused by the incident waves is relatively larger near the water free surface, smaller at the bottom. The patterns are the same for the three resonant frequencies, which is indicating that the diffraction pressure is the dominant effect in the total pressure.

The plots of pressure distribution caused by the diffraction potential are listed below:

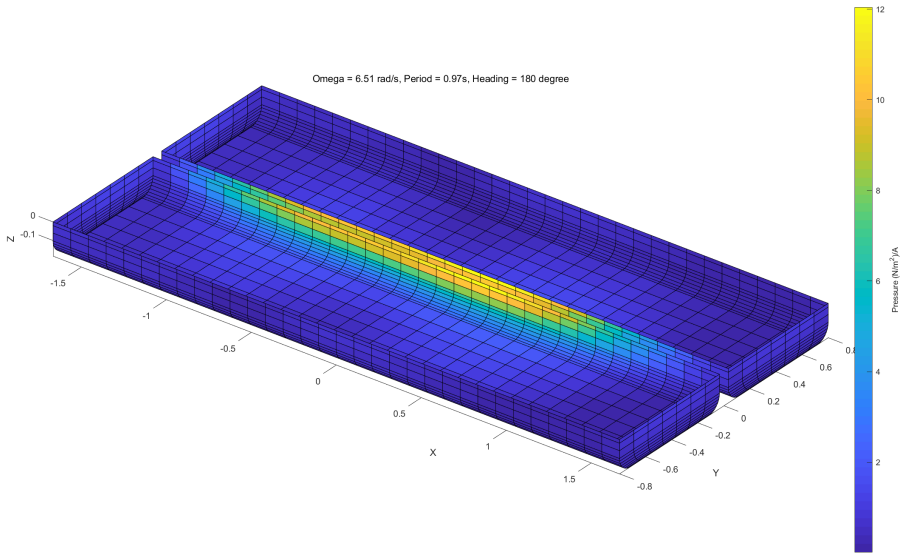

Figure 7.44: Pressure Distribution by Diffraction Potential at 1st Mode of Gap Resonance

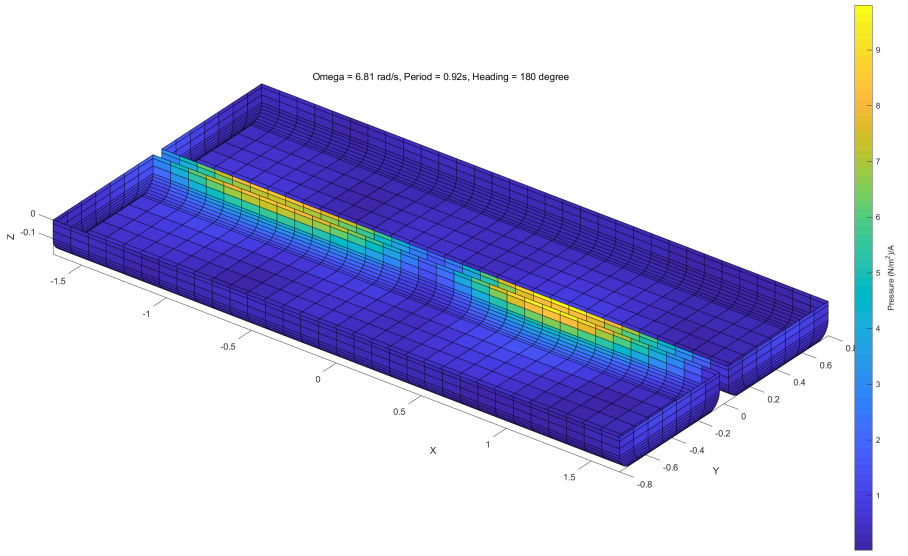

Figure 7.45: Pressure Distribution by Diffraction Potential at 2nd Mode of Gap Resonance

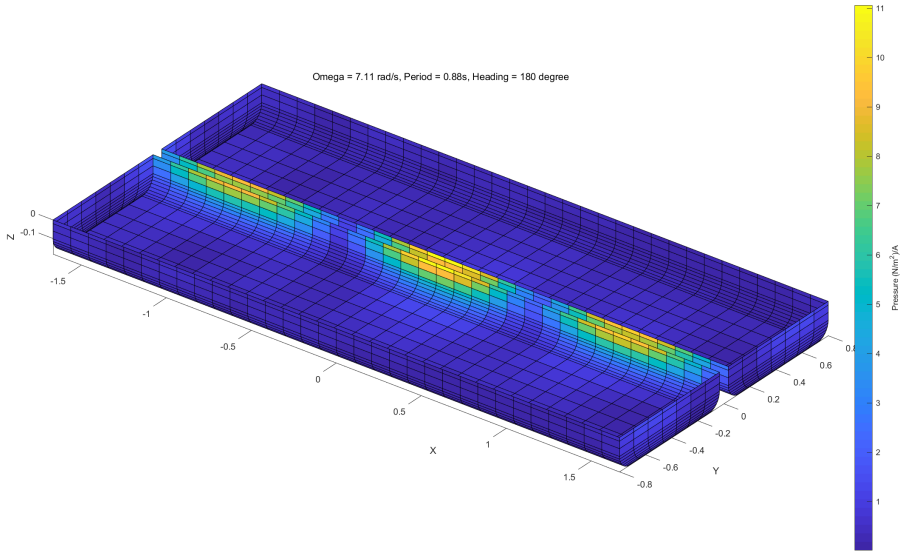

Figure 7.46: Pressure Distribution by Diffraction Potential at 3rd Mode of Gap Resonance

From the plots, we confirm that the pressure resulted from the diffraction potential is the doiminant component in the total pressure.

7.3.3 Velocity Contour of the Ship Hull

Additionally, we also generated the plots of the amplitude of the velocity induced by diffraction potential on the hull and its three components. We may find that the components $d\phi/dy, d\phi/dz$ share similar patterns with the amplitude of the wave elevation along the gap free surface. The distribution of $d\phi/dx$ is consistent with the wave theory. The x-component of the velocity reaches maximum at the node of the wave profile. A symmetric distribution is observed as well.

Below are the plots about the amplitudes of the x-components of velocity.

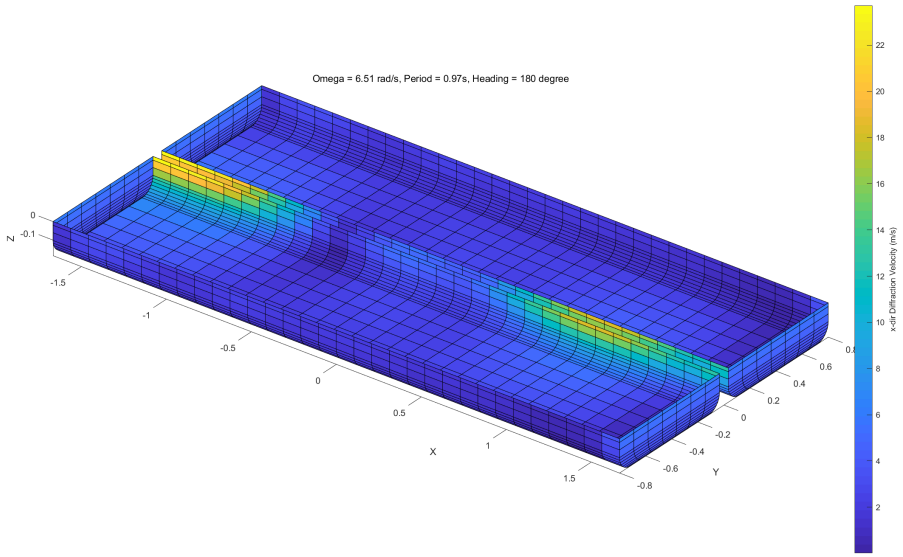

Figure 7.47: Distribution of $d\phi/dx$ at 1st Mode of Resonance inside the Gap

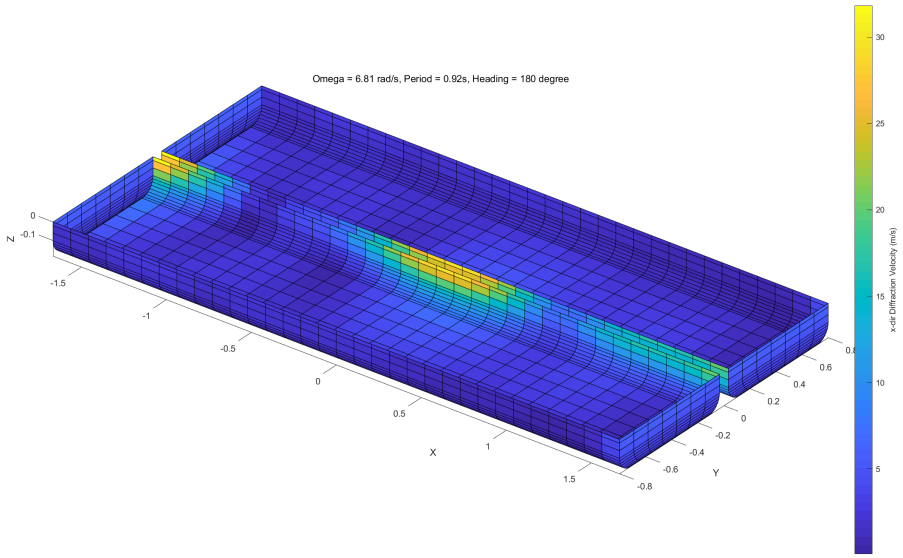

Figure 7.48: Distribution of $d\phi/dx$ at 2nd Mode of Resonance inside the Gap

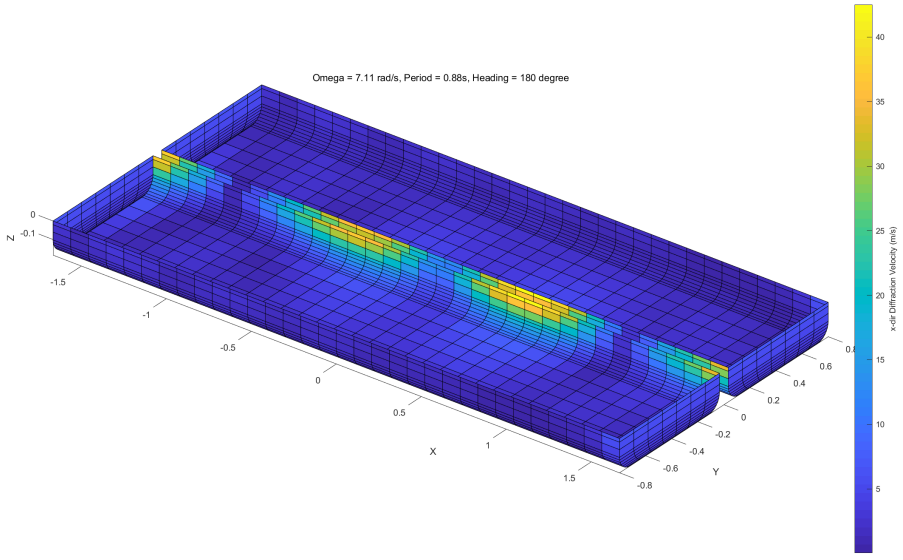

Figure 7.49: Distribution of $d\phi/dx$ at 3rd Mode of Resonance inside the Gap

Below are the plots about the amplitudes of the y-components of velocity.

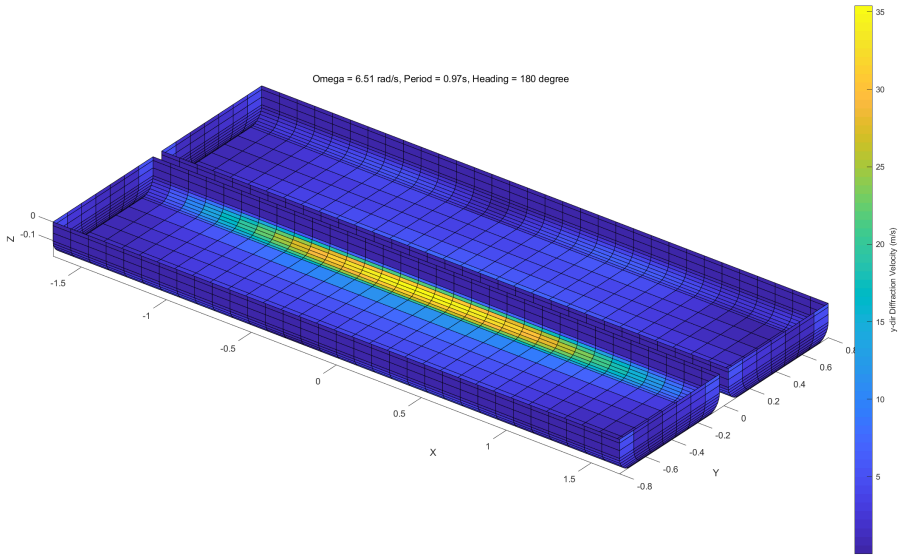

Figure 7.50: Distribution of $d\phi/dy$ at 1st Mode of Resonance inside the Gap

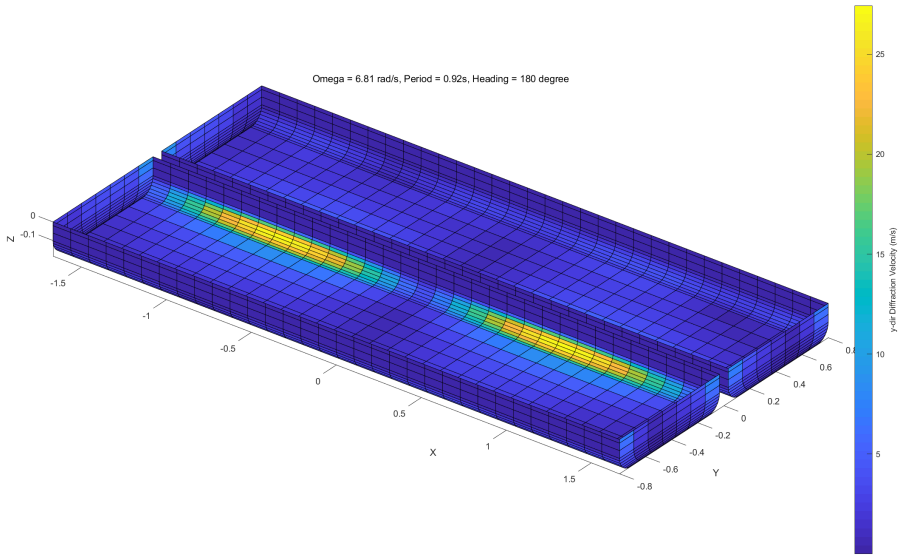

Figure 7.51: Distribution of $d\phi/dy$ at 2nd Mode of Resonance inside the Gap

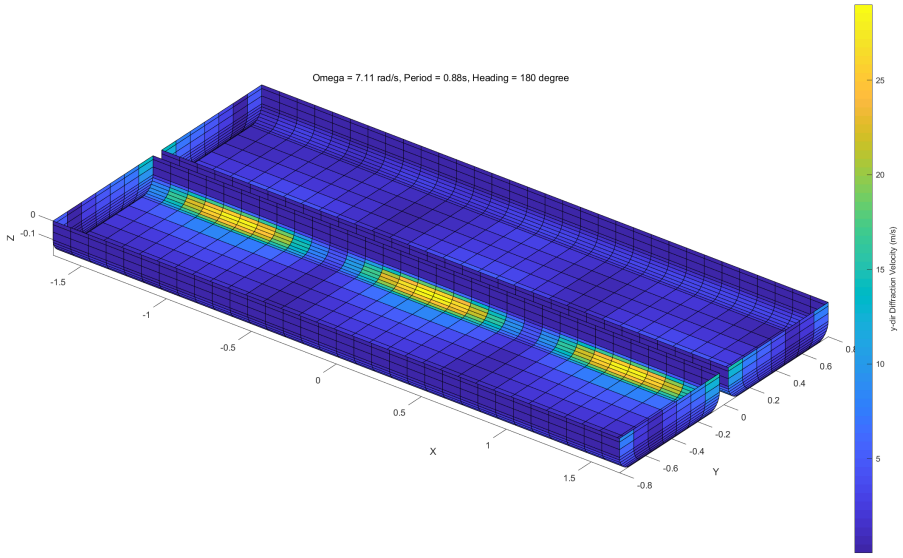

Figure 7.52: Distribution of $d\phi/dy$ at 3rd Mode of Resonance inside the Gap

Below are the plots about the amplitudes of the z-components of velocity.

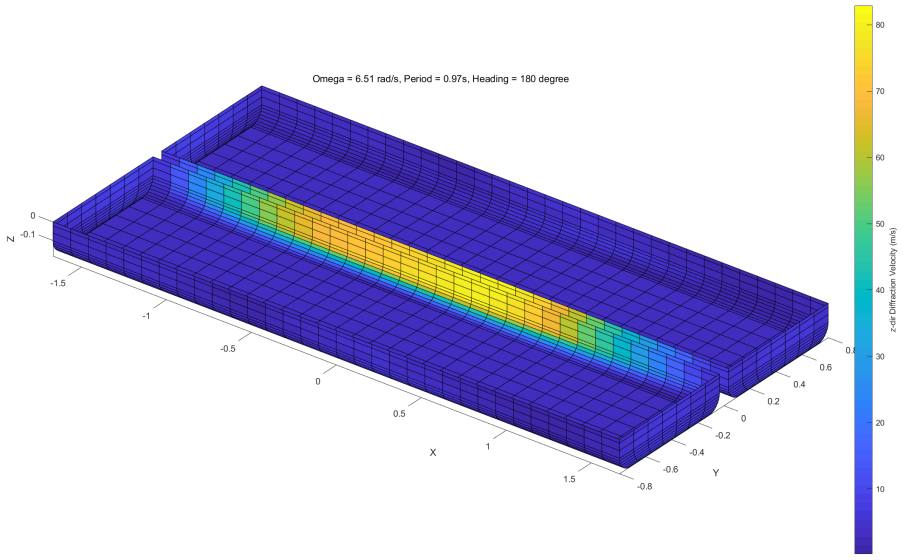

Figure 7.53: Distribution of $d\phi/dz$ at 1st Mode of Resonance inside the Gap

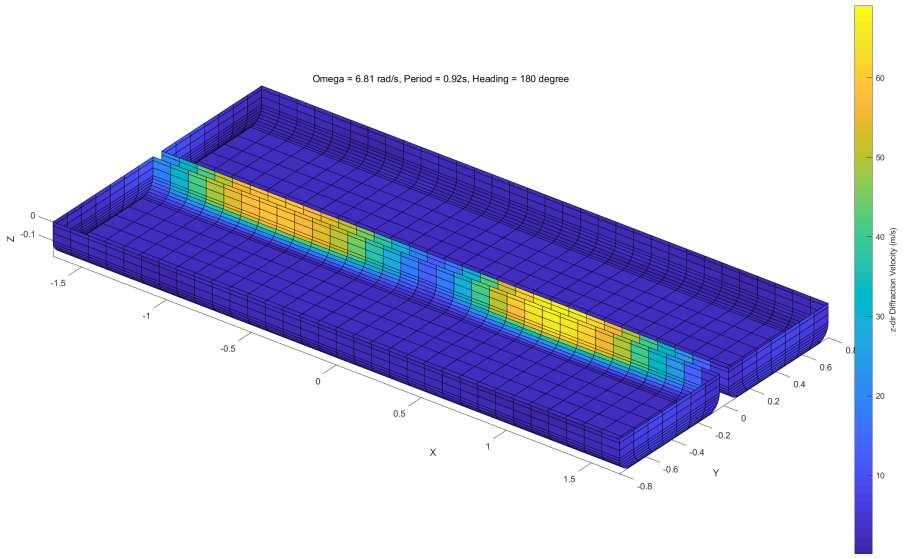

Figure 7.54: Distribution of $d\phi/dz$ at 2nd Mode of Resonance inside the Gap

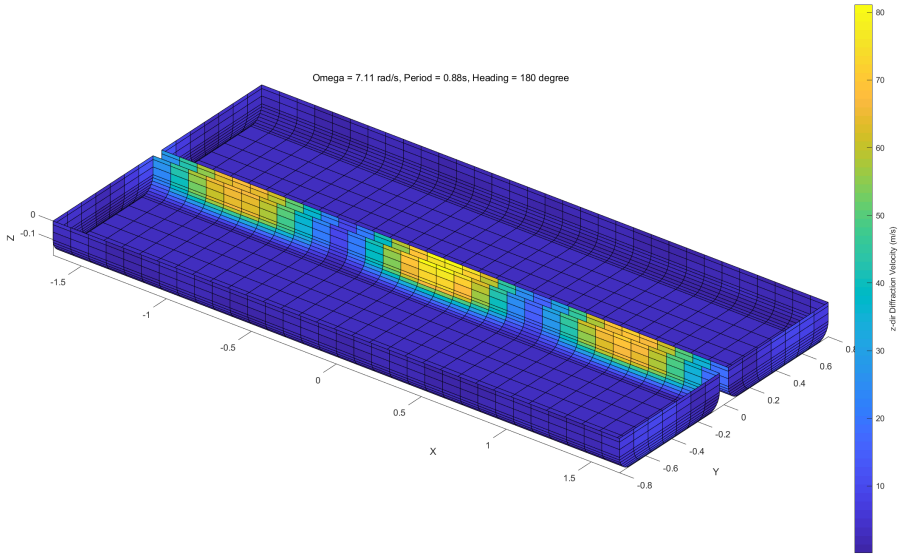

Figure 7.55: Distribution of $d\phi/dz$ at 3rd Mode of Resonance inside the Gap

From the contour plots of the velocity distributions from CFD, we may speculate on the possible physical mechanism inside and near the gap. When the resonance occurs, the amplitude of the oscillating velocity can be quite high. We can imagine that the fluid particles will repeatedly move quickly into the gap and away from it. As a result, the y- and z- components of the velocity have large amplitudes. If the corner is round, the separation phenomenon may not be so obvious. If the corner is sharp, it is easy to understand that the separation will occur because the fluid is passing by a blunt body at a relatively high speed. In this case, the generation of the vorticity will take away part of the energy inside the gap, which may damp the wave elevation along the gap.

7.3.4 Conclusion

To conclude, at the resonant frequencies, a seemingly standing wave is observed inside the gap. The wave elevation RAO is apparently over predicted by the potential method. The distribution of the amplitude of the total pressure is corresponding to the wave elevation. The amplitude of the pressure reaches a local maximum where the wave elevation RAO reaches a peak value. The total pressure is contributed by the incident potential and the diffraction potential, of which the diffraction potential is dominant.

As for the distribution of the amplitude of velocities, it is consistent with the wave elevation RAO inside the gap. The amplitudes of the y- and z- components of the velocities reach the maximum where the wave elevation RAO reaches a peak value. Alternatively, if there are three antinodes inside the gap, there will be three locations where the amplitudes of the y- and z- components of the velocities reach the peak value. The amplitudes of the x-component of the velocity reach a peak value at the nodes, which is consistent with the wave theory.

Therefore, the results of the potential methods provide some insights about the phenomenon happening inside the gap. However, the viscosity and rotational properties of fluid are neglected. The predicted wave elevation RAO is too high compared to the experiments. Naturally, the other relevant predictions may also be too high.

8. ARTIFICIAL DAMPING METHODS

In this section, we discuss the previous works on artificial damping methods and also describe our proposed method. Before proceeding to the derivation, we review the formulas for the 1st order seakeeping problem, which is the basis of the damping methods.

The nonlinear kinematic and dynamic boundary conditions are:

$$\frac{\partial \zeta}{\partial t} + \frac{\partial \Phi}{\partial x}\frac{\partial \zeta}{\partial x} + \frac{\partial \Phi}{\partial y}\frac{\partial \zeta}{\partial y} = \frac{\partial \Phi}{\partial z} \qquad at\ z = \zeta(x, y, t) \tag{8.1}$$

$$\frac{\partial \Phi}{\partial t} + \frac{1}{2}\vec{\nabla}\Phi \cdot \vec{\nabla}\Phi + g\zeta = C - \frac{p_a}{\rho} \qquad at\ z = \zeta(x, y, t) \tag{8.2}$$

After applying the perturbation technique and Taylor expansion as discussed before, we will obtain the 1st order equation as below:

$$\frac{\partial \zeta^{(1)}}{\partial t} = \frac{\partial \Phi^{(1)}}{\partial z} \qquad at\ z = 0 \tag{8.3}$$

$$\frac{\partial \Phi^{(1)}}{\partial t} + g\zeta^{(1)} = 0 \qquad at\ z = 0 \tag{8.4}$$

In solving for the Green function, we usually merge the two equations to get the combined free surface boundary condition:

$$\frac{1}{g}\frac{\partial^2 \Phi^{(1)}}{\partial t^2} + \frac{\partial \Phi^{(1)}}{\partial z} = 0 \qquad at\ z = 0 \tag{8.5}$$

With the Green function, we solve for the source strength using the body boundary condition.

$$\vec{n'} \cdot \vec{\nabla}\Phi^{(1)} = \vec{n'} \cdot V^{(1)} \qquad at\ body\ surface \tag{8.6}$$

By assuming steady state, we can apply the following equations and make the equations inde-

pendent of time t.

$$\Phi^{(1)} = Re\{\phi^{(1)} e^{i\omega t}\}$$

$$V_{\boldsymbol{n}} = Re\{v_{\boldsymbol{n}} e^{i\omega t}\}$$

$$\zeta^{(1)} = Re\{\zeta^{A(1)} e^{i\omega t}\}$$

Then the body boundary condition becomes:

$$\frac{\partial \phi^{(1)}}{\partial n_{\boldsymbol{x}}} = -\frac{1}{2}\sigma(\boldsymbol{x}) + \frac{1}{4\pi}\iint_{S_b} \sigma(\boldsymbol{\xi}) \frac{\partial G(\boldsymbol{x};\boldsymbol{\xi})}{\partial n_{\boldsymbol{x}}} dS_{\boldsymbol{\xi}} = v_n \tag{8.7}$$

Afterwards, substituting the source strength on the body into the following equation, we will obtain the potential at any point inside or on the boundary of the fluid domain:

$$4\pi\phi^{(1)}(\boldsymbol{x}) = \iint_{S_b} \sigma(\boldsymbol{\xi}) G(\boldsymbol{x};\boldsymbol{\xi}) dS_{\boldsymbol{\xi}},\ \boldsymbol{x} \in S_b \cup V \tag{8.8}$$

Using the equation (8.4), we will be able to find the wave elevation on the linearized free surface. The equation for the complex amplitude is as below:

$$\zeta^{A(1)} = -\frac{i\omega\phi^{(1)}}{g} \tag{8.9}$$

The nondimensional form is:

$$\overline{\zeta}^{A(1)} = \frac{\zeta^{A(1)}}{A} = -\frac{i\omega\phi^{(1)}}{Ag} \tag{8.10}$$

where, A is the wave amplitude.

When we observe a very high wave elevation, the potential value at the point of interest is naturally large. To reduce the wave elevation, it is straightforward to put a rigid lid on the gap as discussed in Buchner[25]. A rigid lid may be too strong a restriction on the gap free surface. Later, the damping lid method was proposed [92]. The wave elevation along the gap is reduced

especially at resonant frequencies. When we add damping terms on the gap free surface, we are changing the source strength on the body panels and then the potentials throughout the domain. If we can decompose the domain into several parts and control the interfaces of the subdomains. We may also achieve a reduced wave elevation. Different types of the domain decomposition methods were discussed in Faltinsen[84], Liu[86], etc. In the following two sections, we discuss the mathematical concepts of the lid method and the domain decomposition method.

8.1 The Domain Decomposition Method

The domain decomposition method breaks down the original solution domain (fluid domain herein) into several parts. It leads to a system of integral equations on the interfaces of the domains, also known as the transmission interfaces. The concept can be illustrated in the figures below:

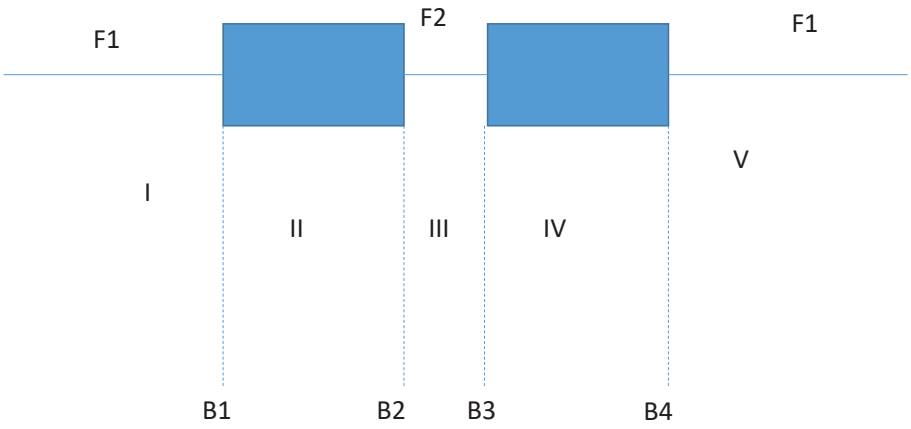

Figure 8.1: Example Configuration for Domain Decomposition Method

This figure is to illustrate the idea of the method. It may have some differences from the discussions in different papers. $F1, F2, F3$ stand for the free surfaces around the floaters. I, II, III, IV, V are the subdomains. $B1, B2, B3, B4$ are the interfaces between the subdomains. Proper transmission conditions need to be specified on the interfaces $B1, B2, B3, B4$. In Faltinsen[84], the authors

introduced admissible functions on the interfaces. Then they solved the problem in different domains separately. In Liu[86], a dissipation boundary condition is introduced in the gap free surface $F2$ and also on $B1, B4$. The boundary condition restricted the transmission of energy from domain to domain, in order to ensure a reasonable wave elevation inside the gap.

The change in the solution system can be illustrated as below:

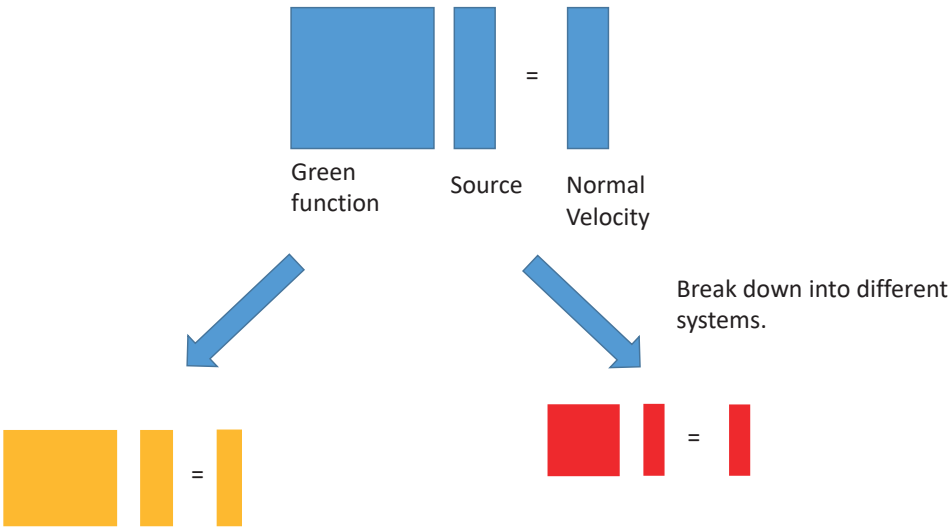

Figure 8.2: Solution System for Domain Decomposition Method

This method is mainly applied in the 2D problem. If considering the 3D case, one may need to decide where to place the interfaces of the domains and also tune the unknown damping coefficients on the transmission boundary conditions to make the simulated wave elevation consistent with the experimental data.

8.2 The Lid Method

The lid method is also an effective method to damp out the wave elevation of the gap free surface. It can be applied in 2D and 3D problem. The methods are already included in some commercial software, for example, WADAM and HydroSTAR.

This method modifies the boundary condition on part of the free surface. To consider the change in the equation system, the part of the free surface needs to be panelized and the source strength on the panels need to be solved. That may be the reason why it is called "lid method". The concept can be shown below:

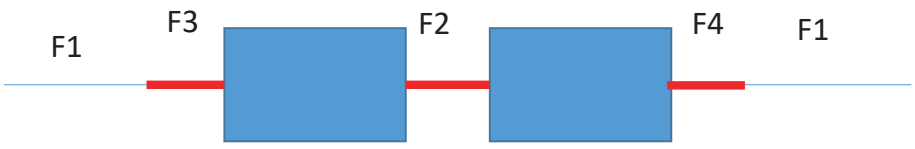

Figure 8.3: Example Configuration for Damping Lid Method

In the figure, $F1$ stands for the part of the free surface without damping. $F2, F3, F4$ are the parts, on which the damping terms may be included. Typically, only $F2$ is panelized. Sometimes, $F3, F4$ or some places inside the fluid domain is also panelized to incorporate the damping effect.

The mathematical essence of this method is to introduce more unknowns, constructing a bigger matrix. It is similar to the irregular frequency removal method (see Chapter 4 for more details). The concept can be shown in Figure 8.4.

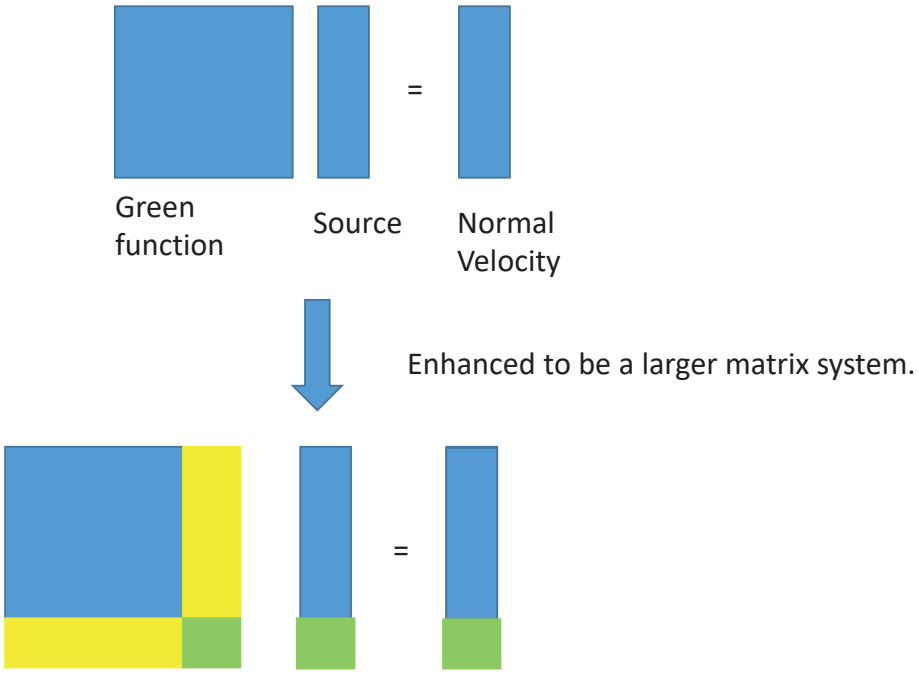

Figure 8.4: Solution System for Damping Lid Method

8.2.1 The Newtonian Damping Method

There are two similar techniques belonging to this category. One is the Newtonian cooling method. This method was discussed in Kim[33], Markeng[101]. The damping effect is enforced on the first order kinematic free surface condition. We have the modified kinematic free surface boundary condition:

$$\frac{\partial \zeta^{(1)}}{\partial t} = \frac{\partial \Phi^{(1)}}{\partial z} \qquad at\ z = 0 \tag{8.11}$$

$$\frac{\partial \Phi^{(1)}}{\partial t} + g\zeta^{(1)} = 0 \qquad at\ z = 0 \tag{8.12}$$

$$\frac{\partial \zeta^{(1)}}{\partial t} = \frac{\partial \Phi^{(1)}}{\partial z} - a\zeta^{(1)} + \frac{b}{g}\Phi^{(1)} \qquad at\ z = 0 \tag{8.13}$$

where, a, b are the coefficients to denote the linear relationship. According to Markeng[101], we can select a, b so that the dispersion relationship remains the same. Herein we will explore the process to decide on the value or the relationship between a, b, the coefficients in equation 8.13.

If using the original dynamic boundary condition and the modified kinematic free surface boundary condition 8.13, we get the modified combined free surface boundary condition:

$$\frac{\partial^2 \Phi^{(1)}}{\partial t^2} + g\frac{\partial \Phi^{(1)}}{\partial z} + a\frac{\partial \Phi^{(1)}}{\partial t} + b\Phi^{(1)} = 0 \tag{8.14}$$

In deriving the dispersion relationship, we assume $\Phi^{(1)}$ satisfies $\Phi^{(1)}(x, z, t) = X(x)Z(z)T(t)$. Substituting the equation into the combined free surface boundary condition, we have:

$$T'' + g\frac{Z'}{Z}T + aT' + bT = 0 \tag{8.15}$$

From the Laplace equation and the bottom boundary condition, we know Z satisfies $Z' = kZ$, where k is the wave number. The above equation becomes:

$$T'' + gkT + aT' + bT = 0 \tag{8.16}$$

Mathematically, we need to solve for this equation to find the solution for T. Here we are reverse engineering the previous references. Thus, we may introduce some assumptions to explore the relationship. If T satisfies $T' = i\omega T$, $T'' = -\omega^2 T$, we obtain the equation about the wave frequency ω:

$$-\omega^2 + gk + i\omega a + b = 0 \tag{8.17}$$

Then we have:

$$\omega^2 - i\omega a - \frac{a^2}{4} = gk + b - \frac{a^2}{4}$$
$$\omega = \pm\sqrt{gk + b - \frac{a^2}{4}} + i\frac{a}{2} \tag{8.18}$$

If $b = a^2/4$, $\omega = \sqrt{gk} + ia/2$, where the real part of ω is $\sqrt{gk}$. If we take $a = 2\mu, b = \mu^2$, we get the exactly same equations as in Markeng[101] as below:

$$\frac{\partial \zeta^{(1)}}{\partial t} = \frac{\partial \Phi^{(1)}}{\partial z} - 2\mu\zeta^{(1)} + \frac{\mu^2}{g}\Phi^{(1)} \qquad at\ z = 0 \tag{8.19}$$

When calculating the wave elevation, the dynamic free surface boundary condition may be applied to calculate the wave elevation.

$$\zeta^{(1)} = -\frac{1}{g}\frac{\partial \Phi^{(1)}}{\partial t} = -\frac{i\omega}{g}\Phi^{(1)} \tag{8.20}$$

If we take the $\omega = \sqrt{gk} + ia/2$, the wave elevation becomes:

$$\zeta^{(1)} = -\frac{i\sqrt{gk}}{g}\Phi^{(1)} + \frac{\mu}{g}\Phi^{(1)} \tag{8.21}$$

When tuning the value of μ against the experimental data, we are almost directly changing value of wave elevation.

Additionally, the combined free surface boundary condition becomes:

$$\frac{\partial \Phi^{(1)}}{\partial z} = \frac{1}{g}\left[\omega^2 - 2i\omega\mu - \mu^2\right]\Phi^{(1)} = \frac{(\omega - i\mu)^2}{g}\Phi^{(1)} \tag{8.22}$$

To consider the change of the free surface boundary condition, the gap surface needs to be panelized. The above formula will be applied in the surface integral to solve for the source strength.

To conclude, the Newtonian damping method provides an approach to adjust the wave elevation

inside the gap. A different free surface boundary condition is applied inside the gap. If applying the same Green function, a lid is needed along the gap free surface. The introduction of the damping terms will affect both the equation system to solve for the potential value or the source strength and the calculation of the wave elevation. To decide on a reasonable damping coefficient, one needs to tune it against the experimental data. This is a mathematical way to modify the method based on potential theory. The process to derive the revised dispersion relationship may not be strictly accurate. Additionally, if the wave frequency has a imaginary part, the waves may not be periodic in time.

8.2.2 XB Chen's Damping Method

Another very promising approach is the method proposed by Chen [93]. The damping force is applied in the dynamic free surface boundary condition. The amplitude of the force is proportional to the amplitude of the velocity on the free surface.

The formula is as below:

$$\vec{F} = -\mu\vec{V} \tag{8.23}$$

In the dynamic free surface boundary condition, if we apply the damping force, the equation becomes:

$$(\frac{\partial}{\partial t} + \vec{V}\cdot\vec{\nabla})\vec{V} = -\vec{\nabla}(\frac{P}{\rho} + gz) - \mu\vec{V} \qquad on\ z = \zeta(x,y,t) \tag{8.24}$$

If assuming ideal flow, the velocity can be expressed in terms of the potential as $\vec{V} = \vec{\nabla}\Phi$. Then the equation is:

$$(\frac{\partial}{\partial t} + \vec{\nabla}\Phi\cdot\vec{\nabla})\vec{\nabla}\Phi = -\vec{\nabla}(\frac{P}{\rho} + gz) - \mu\vec{\nabla}\Phi \tag{8.25}$$

$$\frac{\partial \Phi}{\partial t} + \frac{1}{2}\vec{\nabla}\Phi \cdot \vec{\nabla}\Phi + \frac{P}{\rho} + g\zeta + \mu\Phi = C(t) \qquad on\ z = \zeta(x, y, t) \tag{8.26}$$

Making the same choice for pressure P and the constant $C(t)$, we can extract the first order $o(\epsilon)$ part of the dynamic free surface boundary condition:

$$\frac{\partial \Phi^{(1)}}{\partial t} + g\zeta^{(1)} + \mu\Phi^{(1)} = 0 \qquad on\ z = 0 \tag{8.27}$$

The wave elevation becomes:

$$\begin{aligned} \zeta^{(1)} &= -\frac{1}{g}(\mu\Phi^{(1)} + \frac{\partial \Phi^{(1)}}{\partial t}) \\ &= -\frac{\mu + i\omega}{g}\Phi^{(1)} \\ &= -\frac{i\omega}{g}\Phi^{(1)} - \frac{\mu}{g}\Phi^{(1)} \end{aligned} \tag{8.28}$$

If substituting the wave elevation into the kinematic free surface boundary condition, we obtain a combined formula:

$$-\frac{1}{g}\frac{\partial}{\partial t}(\mu\Phi^{(1)} + \frac{\partial \Phi^{(1)}}{\partial t}) = \frac{\partial \Phi^{(1)}}{\partial z} \tag{8.29}$$

Rearranging the terms, we obtain:

$$\begin{aligned} \frac{\partial \Phi^{(1)}}{\partial z} &= \frac{\omega^2}{g}(1 - i\frac{\mu}{\omega})\Phi^{(1)} \\ &= \frac{\omega^2}{g}\Phi^{(1)} - i\frac{\omega\mu}{g}\Phi^{(1)} \end{aligned} \tag{8.30}$$

Applying the similar technique, we can get the relationship that ω and k satisfy:

$$\omega^2 - gk - i\omega\mu = 0 \tag{8.31}$$

Solving for ω, we get:

$$\omega = \pm\sqrt{gk - \frac{\mu^2}{4}} + \frac{i\mu}{2} \tag{8.32}$$

The real part of the wave frequency is no longer $\sqrt{gk}$ and ω contains an imaginary part as well.

In this method, the free surface boundary condition inside the gap is also changed. Thus, the gap surface needs to be panelized. The damping coefficient has changed the matrix to solve for the potential value or the source strength. It also appears in the formula 8.28 to calculate the wave elevation. Intuitively speaking, when we want to consider the damping effect, we deduct a portion from the original wave elevation. However, if we consider the term related to damping effect, we have also changed the value of the potential. It is indicating that we probably need to tune the damping coefficient for several rounds to make the simulation results match the experimental data.

This method is an alternative approach to modify the wave elevation mathematically. It has changed the dispersion relationship inside the gap surface and the dynamic free surface boundary condition. When applying this method, one needs to decide where is the damping zone and how large it is. The choices may depend on the experience of the user.

8.3 Damping Wall Method

8.3.1 Motivation

Considering the disadvantages of the above methods, two questions come: can we develop a method which does not require the user to specify where the damping zone or damping lid is? Can we use the information of the potential method without damping to identify the damping coefficients?

Let's review the physical processes first. In the potential method, the fluid is assumed to be ideal flow, which is inviscid and irrotational. The energy dissipation caused by the viscous effect is neglected in the results generated by the potential method. However, in reality, the fluid is viscous and rotational.

When comparing the results by potential method and the experimental data, we may attribute

the discrepancies to the differences in the assumptions of the fluid property. Therefore, we say that it may be the viscous effects that damps out the wave elevation.

In the damping lid method, the free surface boundary condition inside the gap is directly controlled to ensure a reasonable wave elevation. It is a straight forward approach to adjust the wave elevation. In this way, the distribution of the potential value will be affected by the change in the free surface boundary condition.

In the domain decomposition method, the fluid domain is broken down into several parts. The transmission of the energy is controlled on the interfaces of the subdomains and the damping condition is also enforced on the free surface inside the gap. As a result, the wave elevation is ensured to be reasonable and the potential throughout the domain is likely to be altered.

The two types of approaches provide feasible ways to modify the matrix structure to solve for the source strength of the potential value on the ship hull. Through the modifications, a reasonable wave elevation can be obtained.

In the potential method without damping, the body boundary condition will determine the source strength or the potential value on the ship hull. In Chen [93], the authors discuss the damping condition on the ship hull near the gap. The damping condition was also adopted in coastal engineering to model the partial reflection of a wall. In the sloshing problem, a uniform damping effect is applied on the tank surface to adjust the motion RAO of the floater [121]. The partial reflection is an alternative way to incorporate the damping effect of the system.

Inspired by the discussion of the partial reflection in Chen[93], we introduce damping effects of different intensities on the ship hull surface. The intensity is determined by the active level of the fluid nearby.

Enlightened by the domain decomposition method and based on the observation of the contour plots through the potential method, we break the ship hull surface into three parts: the vertical walls near the gap, middle parts and vertical walls away from the gap. It can be shown as below:

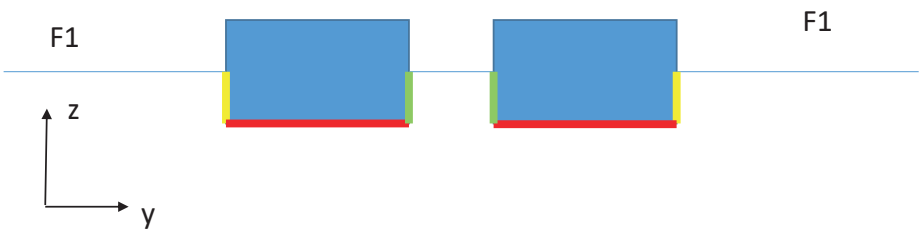

Figure 8.5: Concept of the Proposed Method

In the figure, the green part stands for the vertical wall near the gap. The yellow part is the vertical wall far from the gap. The red part indicates the rest part of the ship. In 2D, the red part only includes the bottom of the ship. In 3D cases, it also includes the stern and bow in the middle region.

8.3.2 Damping Wall Method

8.3.2.1 Formula

We will incorporate the damping term into the body boundary condition by using this formula:

$$\frac{\partial \phi^{(1)}}{\partial n_{\boldsymbol{x}}} = v_n - i\mu\frac{\omega^2}{g}\phi \qquad at\ body\ surface \tag{8.33}$$

If we include the damping term in the body boundary condition, the formula will change into:

$$\frac{\partial \phi^{(1)}}{\partial n_{\boldsymbol{x}}} = -\frac{1}{2}\sigma(\boldsymbol{x}) + \frac{1}{4\pi}\iint_{S_b}\sigma(\boldsymbol{\xi})\big[\frac{\partial G(\boldsymbol{x};\boldsymbol{\xi})}{\partial n_{\boldsymbol{x}}} + i\mu\frac{\omega^2}{g}G(\boldsymbol{x};\boldsymbol{\xi})\big]dS_{\boldsymbol{\xi}} = v_n \tag{8.34}$$

In our case, we assume the damping coefficient μ is a function of location y and the incident wave frequency ω: $\mu = \mu(y,\omega)$. y is adopted to decompose the ship hull into 3 parts and μ will stay constant on each of the three parts of the ship hull given the frequency. We decide which region a panel falls into based on the location of its centroid. The values of μ on different regions can be different.

8.3.2.2 Determination of Ratios

Therefore, to consider the different damping effects on the three sections of the ships, we assume the damping coefficients satisfy a ratio of $a : b : c$. To decide the damping coefficients in the equation, we multiply a constant μ to the ratio. Then the damping coefficients are $a\mu$, $b\mu$, $c\mu$. Consequently, we need to decide the value of μ and the ratio of the damping coefficients $a : b : c$.

In this method, we assume that the panels belonging to one section share the same damping coefficient. It is similar to adding an average damping to the section. If we assume the damping effect is positively correlated to the prediction through the potential method, we may use the ratio of the potential values to help decide the ratio of the damping coefficients.

In generating the results for wave frequencies ranging from $6.01 \sim 9.91$ rad/s, we can obtain the potential value for each panel at each frequency. Herein, we assume the average effect can be achieved by two types of ratios. One ratio is obtained in this way: first summing up the potential value at each section for all frequencies, then find the mean value of the potential for each section and finally calculate the ratio. We may name it as "ratio of the mean".

The other ratio can be named as "ratio of the max mean". Firstly, we compute the mean of the potential values for each section at a certain frequency. Then we find the ratio for each frequency. If we denote the ratio as the format "1:x:y" and y > x > 1, we can eventually find the ratio with the largest value of y. That ratio is our final selection. Please note that we will always divide each number in a ratio by the smallest number so that the ratio has 1 as the minimum value. This is a rule to notation to describe the possible relationship between the damping effects on different sections.

Herein, we provide two possible types of ratios for reference. The ratios reflect the difference in the average potential value. In practice, other types of ratios can be defined as well. The values in the ratios will affect the amplitudes of the kernel functions discussed below. The bigger number inside a ratio will lead to a smaller amplitude of the kernel function.

8.3.2.3 Kernel Function

The ratios of the potential values on the 3 sections indicate the average active level of the fluid close to the different sections. However, based on the observations, the active level is frequency dependent. In other words, at some frequencies, especially the resonant frequencies, the amplitude of the wave elevation or the velocity of fluid inside the gap is relatively larger.

We may assume when the fluid has a relatively larger velocity, the friction effect can cause more energy loss to the system. In other words, the damping effect is positively correlated with the activity of the system. Generally, the damping effect becomes significant when reaching the resonant frequencies and it may grow with the increasing wave radian frequency. Because the velocity amplitude of the fluid particles is growing as the frequency increases.

To consider the resonance effects, we propose to apply the Gaussian kernel function in the function of the damping coefficient μ. The formula of μ is expressed as:

$$\mu = \sum_{i}^{res} A_i exp[-k(\omega - \omega_i^{res})] \tag{8.35}$$

where, "res" stands for "resonance". The number of the terms is equal to the number of resonant frequencies observed. A_i is the amplitude of the kernel functions. k is the decay ratio and ω_i^{res} is the resonant frequencies.

In this equation, ω_i^{res} is determined from the results of the MDLMultiDYN without the non-potential flow damping effect. The unknowns are all the A_i and the decaying factor k.

Given the experimental data, we may adjust the value of A_i and k to make sure the results from the wall damping methods are consistent. We can first tune the amplitude of the kernel function for the result of each resonant frequency separately. Then by adjusting the value of k, we make the results at other frequencies consistent. In the next section, we will demonstrate the effectiveness of the wall damping method.

8.3.3 Results

Herein, we will mainly study the wave elevation at the wave gauge 4, which is located at the center of the gap. We apply the methods to the cases in both head sea and beam sea conditions to prove the effectiveness. Herein, we choose the "ratio of the max mean" as an example. It is equivalent to choose the other ratio, the steps remain the same. The difference may lie in the expressions of the kernel functions.

8.3.3.1 Head Sea Condition

After running the case using our in-house program MDLMultiDYN, the ratios are obtained as in the table below:

Ratio	a	b	c
Ratio of the Mean	1	2.5	11
Ratio of the Max Mean	1	3	22

Table 8.1: Ratios of the Potential Values on the 3 Sections

By tuning the parameters, we find the values of A are 0.0005, 0.0010, 0.0016, 0.0026, 0.0032 and the value of k is 26.

The damping constant curve of μ becomes:

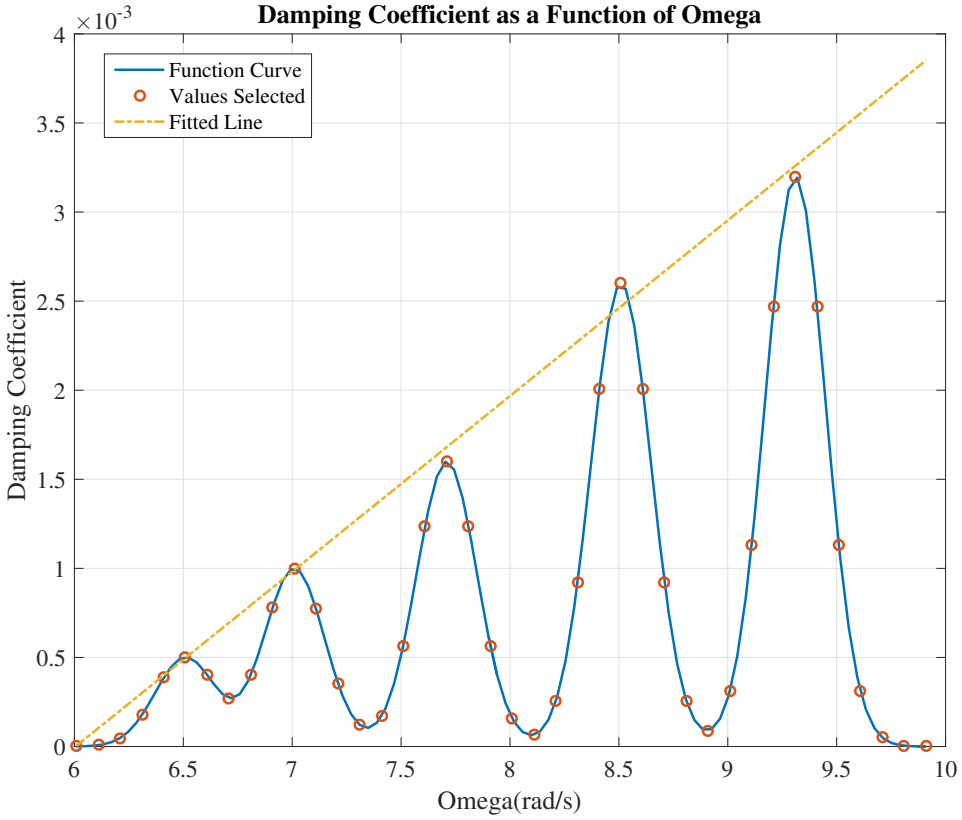

Figure 8.6: Damping Coefficient vs Wave Frequency

The circles on the curve indicate the values we selected at each frequency, which is adopted in the simulation of the MDLMultiDYN. While plotting the curve, we find that the amplitudes at or near the resonant frequencies almost follow a linear relationship. On top of the curve, we also plot the fitted curve of the amplitudes. It shows that the linear curve fits well.

Applying the damping constants, we find the damping coefficient on each section at each frequency. After incorporating the damping effects, we can obtain the damped curve.

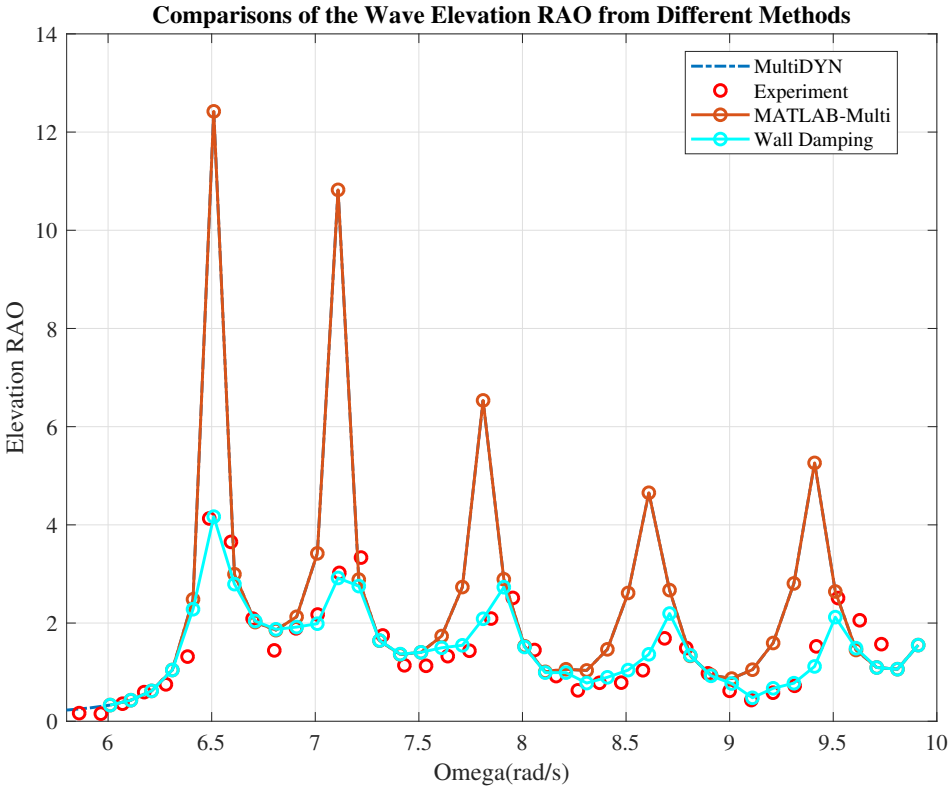

Figure 8.7: Comparisons of Results from Modified Potential Method

From the comparisons, we can observe that the damped curve is consistent with the experimental data. The method is effective in generating a reasonable wave elevation.

In the method, we have to choose 6 parameters. Based on the linear relationship of the amplitudes at the resonant frequencies, we may just need to tune 3 parameters: the amplitudes at 2 resonant frequencies and the parameter k. Thus, we select the amplitudes at the minimum and maximum resonant frequencies to tune and apply the fitted curve to obtain the damping constant for other amplitudes. Below is the curve to show the difference between tuning 5 points and 2 points.

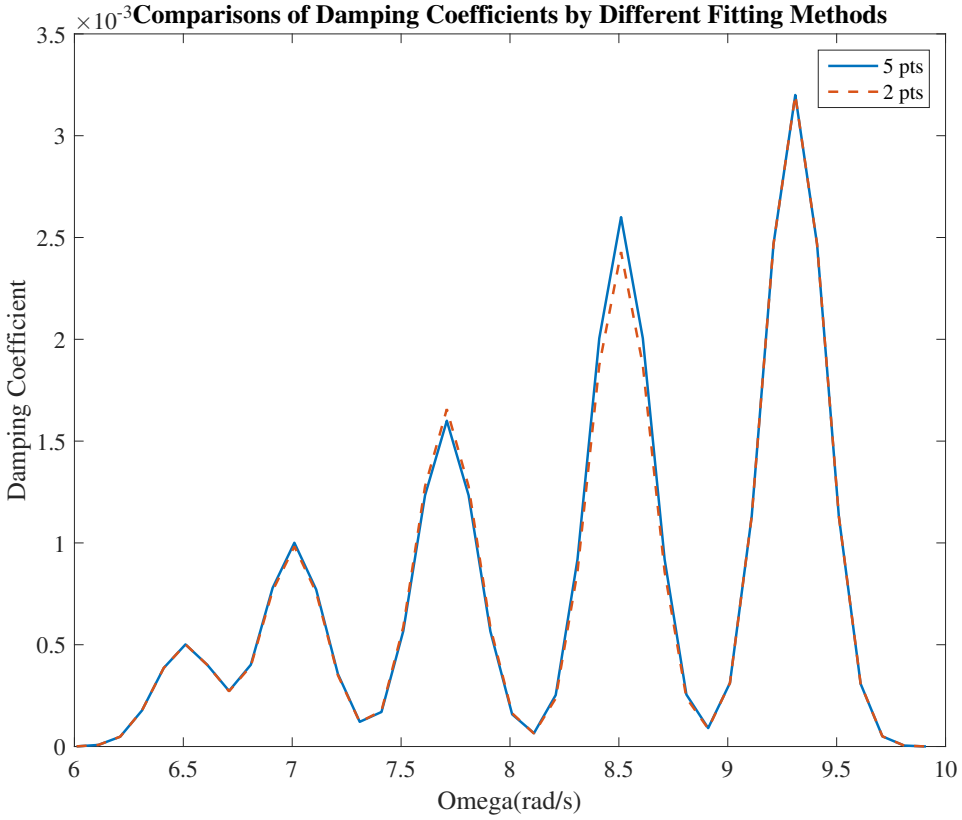

Figure 8.8: Comparisons of Damping Constants from Independent Tuning and Linear Fitting

Applying the fitted curve, we obtain the curve using the modified potential method. It is approximately the same with that when adjusting the five amplitudes independently.

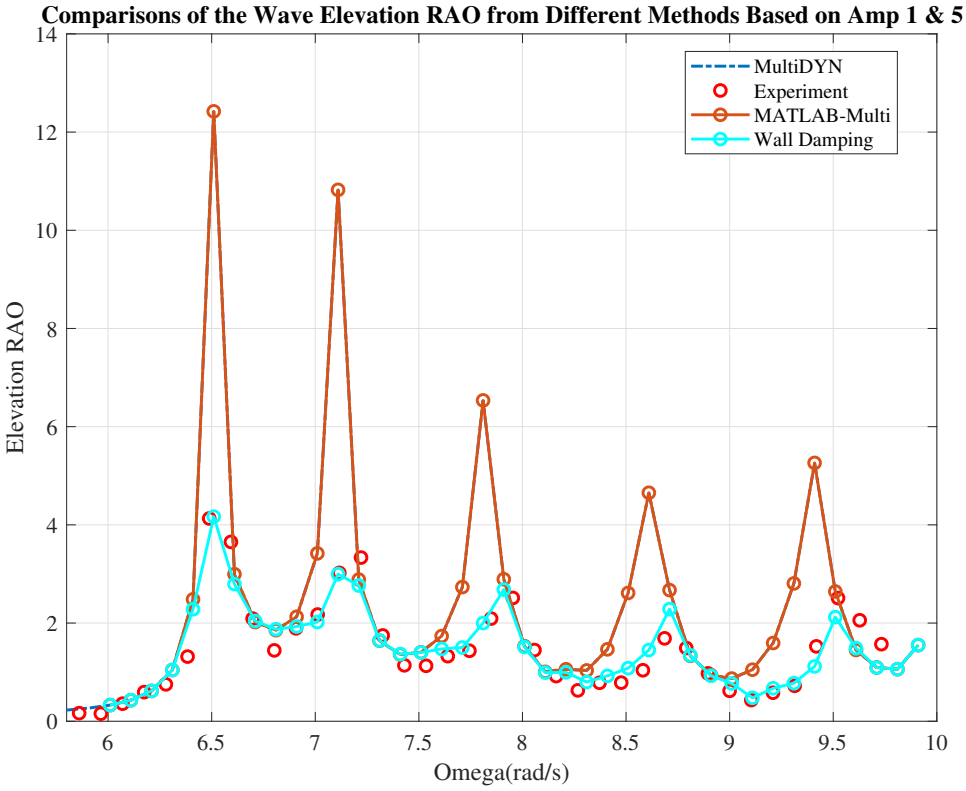

Figure 8.9: Comparisons of Results from Modified Potential Method When Tuning 2 Amplitudes

8.3.3.2 Beam Sea Condition

Similarly, we can obtain the ratios based on the results from the potential method.

Ratio	a	b	c
Ratio of the Mean	2.4	1	3.7
Ratio of the Max Mean	3.5	1	7.6

Table 8.2: Ratios of the Potential Values on the 3 Sections

By tuning the parameters, we find the values of A are 0.0014, 0.0020, 0.0032, 0.0042, 0.0054 and the value of k is 15.

The damping constant curve of μ becomes:

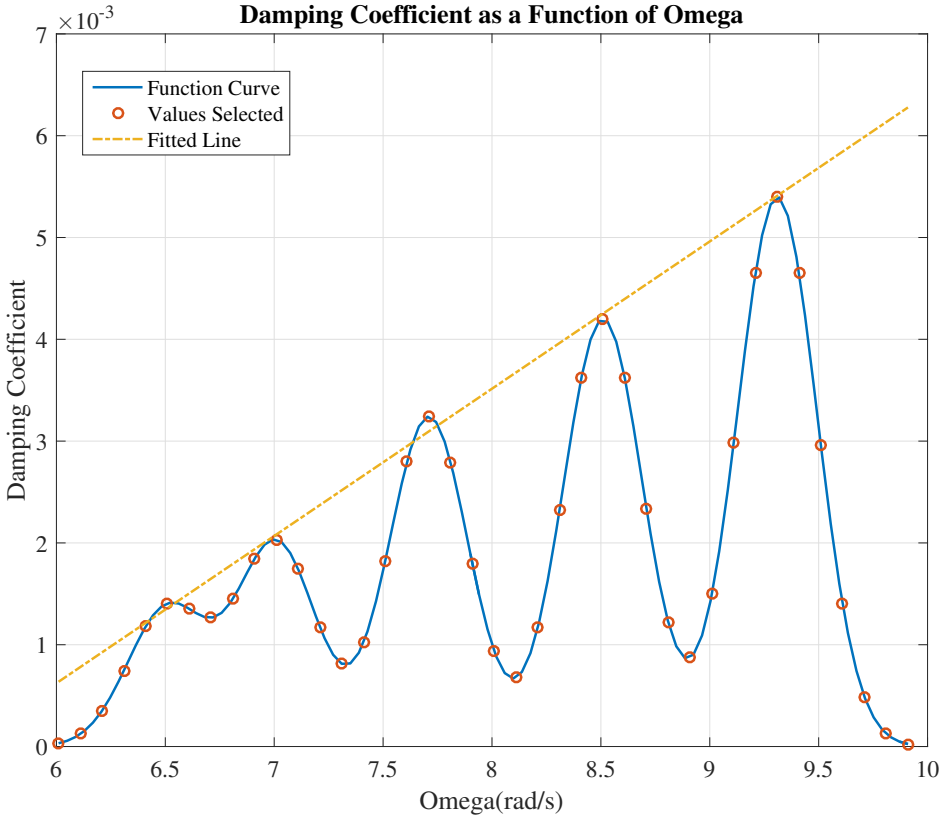

Figure 8.10: Damping Coefficient vs Wave Frequency

Considering the damping effects, we can obtain the results for the modified potential method:

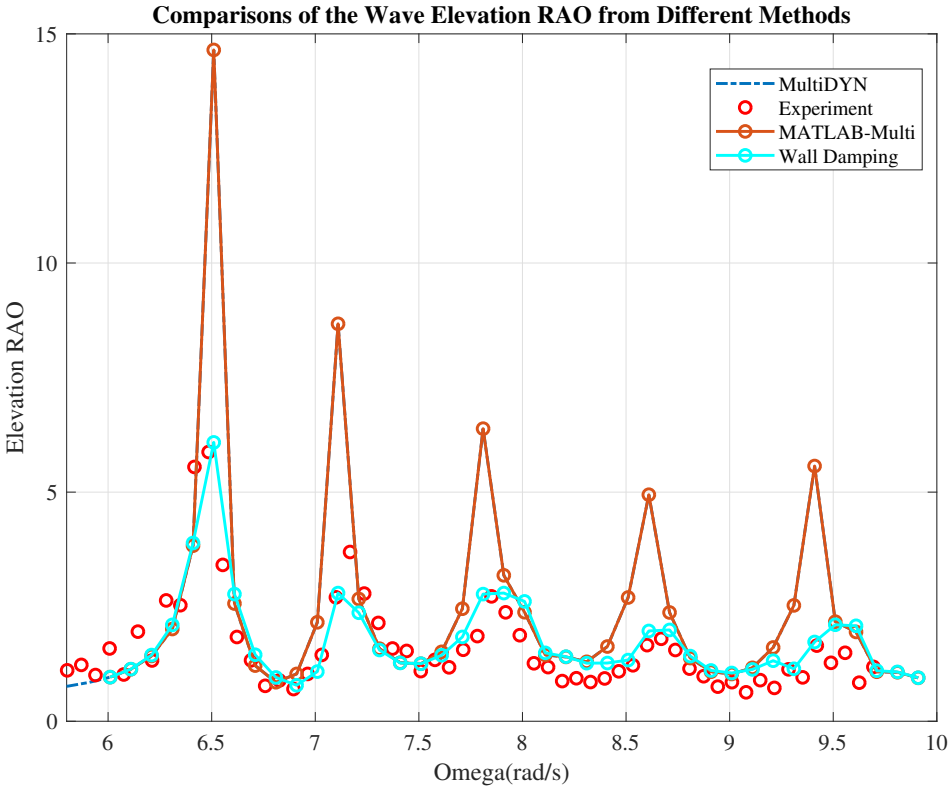

Figure 8.11: Comparisons of Results from Modified Potential Method

If we choose the 3 parameters to tune, we obtain the curves of the damping coefficients:

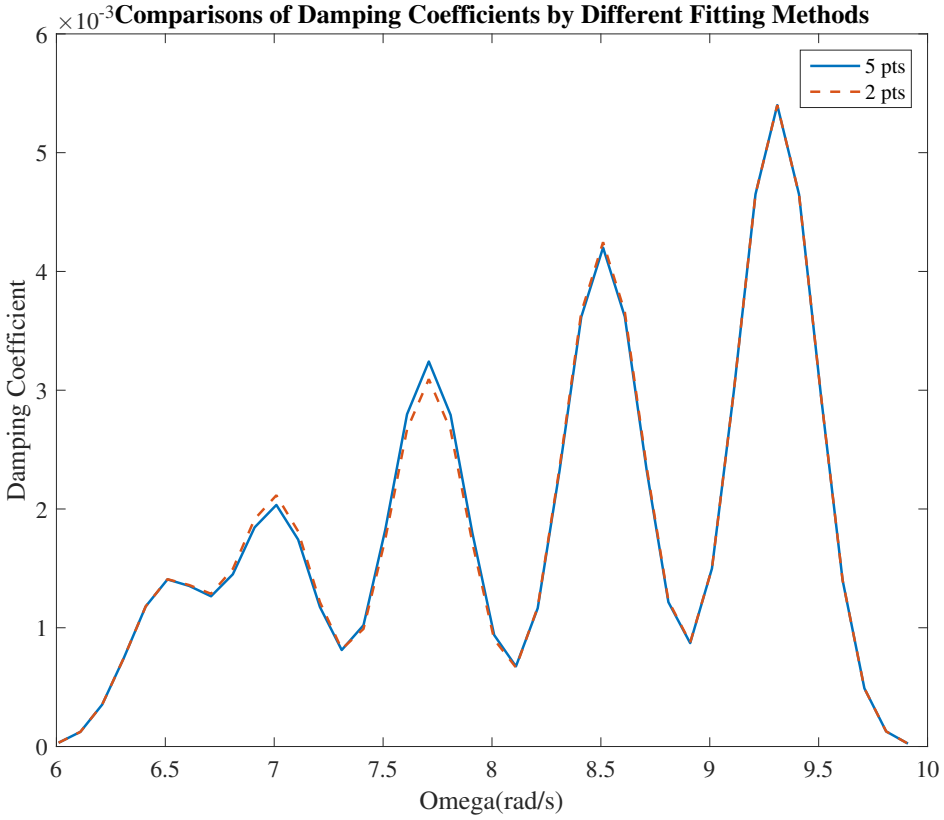

Figure 8.12: Comparisons of Damping Constants from Independent Tuning and Linear Fitting

Applying the damping constants by fitting the 3 parameters, we obtain the results from the modified potential method. Not surprisingly, the results are almost the same with those by fitting 5 parameters.

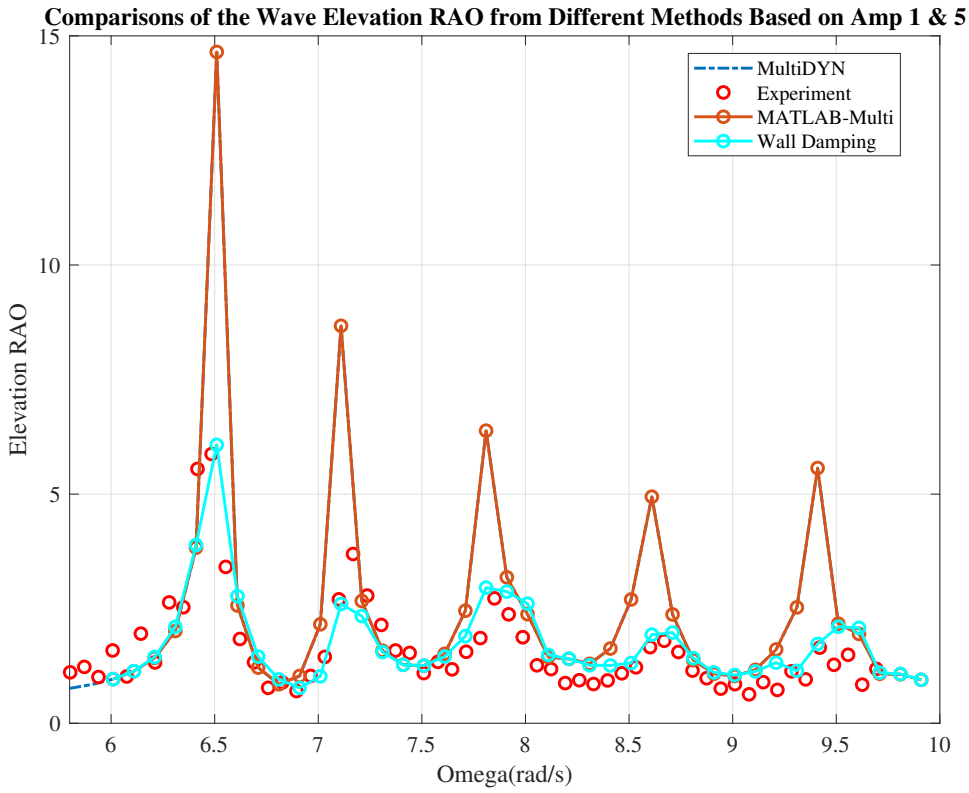

Figure 8.13: Comparisons of Results from Modified Potential Method When Tuning 2 Amplitudes

8.3.4 Discussion of Proposed Damping Method

In this section, we discuss the proposed method to damp out the wave elevation inside the gap. The method is a significant improvement based on the damping method applied in the sloshing problem and the coastal engineering problems. In this method, we introduce damping effect only on the ship hull. The damping effect differs by the location relative to the gap. The assumption is that the damping coefficient is positively correlated with the active level of the fluid domain. If the velocity of the fluid field is large, then the damping effect is also significant.

The method does not require the user to choose a damping domain or change the dispersion relationship. The information from the results without damping is helpful to choose the parameters of the method. We use the resonant frequencies to decide the centers of the Gaussian kernel functions. The amplitudes of the Gaussian kernel functions are initially found by tuning against the

experimental data. Afterward, we find the amplitudes are approximately linear in wave frequency. Therefore, the function $A(\omega)$ assumes a linear function in ω. Alternatively, if we find the amplitude for the minimum and maximum resonant frequencies by tuning against the experiment, we can find the amplitudes of the Gaussian kernel function at other resonant frequencies. In this way, the shortcomings of the method is minimized.

This method is our first trial on the damping problem. If obtaining more experimental data of various floaters or different conditions in the future, we will extend the concept of the method and improve this method using advanced techniques.

9. CONCLUSIONS [1]

In this dissertation, we have studied the problem of body-wave interactions using the potential method. The numerical tool, MDLMultiDYN, is developed to predict the forces and motions of multiple bodies with zero and non-zero forward speed in deep water, using a three-dimensional source formula.

We first repeated the steps to simplify the nonlinear problem into first and second order problems and discussed the motivations behind the key steps. We started with the fully nonlinear problem for zero-speed floaters and extended it to the nonzero-speed problem with a vessel translating coordinate. The motivation of reformulating in the moving coordinate is to maintain a similar form of the boundary conditions with the seakeeping problem. By applying Taylor expansion, we converted the wavy boundary of the free surface into a flat boundary. A perturbation technique was then introduced to decompose the problem into a first order part and a second order part. In the above steps, we assumed that the wave slope and the motion of the floater are both small. By repeating the steps, the background of the problem was presented, which formed a theoretical basis for the discussions in the remaining part of the thesis. It will also help the readers to understand the motivations behind the mathematical derivations.

In the discussion of the first order problem, the formula for multiple floaters with zero speed was derived. We compared the results from MDLMultiDYN against WAMIT and achieved highly consistent results. This proved the correctness of our formula and program. By applying the principle of superposition, we extended the formula to the nonzero speed problem. The speed must be small and multiple floaters are assumed to have the same forward speed to ensure the same encounter frequency. The results for a single floater with nonzero speed are benchmarked against those from MDLHydroD, which was benchmarked against the experiments and multiple computation tools on the single body case. The consistency of the results was achieved to prove

[1] Part of the chapter is reprinted with permission from "A method to remove irregular frequencies and log singularity evaluation in wave-body interaction problems" by Yujie Liu, Jeffrey Falzarano, 2017. *Journal of Ocean Engineering and Marine Energy*, Vol 3, Issue 2, pages 161-189. Copyright 2017 by Springer International Publishing Switzerland.

the effectiveness of the current method. The results for multiple floaters with a small forward speed were also presented to indicate the differences between various forward speeds. The shift of resonant frequencies and the changes of the force and motion RAOs were observed.

Additionally, in the discussion of the nonzero speed cases, we derived and presented the general formula for the added mass and damping[122]. Moreover, we also investigated the formula to transform the integral with a derivative of the potential into that without the derivative. We found the limitations in the derivation and proved that the formula may not be obtained[104]. However, the theorem is beyond the main focus of the paper. Thus, we only presented why it has some issues but have not implemented the correct form to obtain results. This formula will affect the expressions of added mass, damping and other parts about the prediction of the forces on the ship and the ship motions.

An irregular frequency removal module was developed to eliminate the seemingly resonant behavior due to the singularity of the matrix structure at some frequencies. By applying this module, we are able to identify the physical resonance. We proved the uniqueness using Sommerfeld radiation condition, harmonized the theorems about the topic and implemented the extended boundary method[105]. The key step to apply the method is to evaluate the log singularity. We proposed 4 different methods to handle different possible situations[106]. Method 2 was adopted most of the time because of the high accuracy and efficiency. Method 3 and 4 were the alternative approaches to deal with less common cases. The proposed methods were compared against Newman's method on a special case and the difference was o(10^{-7}). The methods were also benchmarked against the converged results using the Gaussian quadrature method. The accuracy was o(10^{-6}). The comparisons ensure the accuracy of our method. After incorporating the irregular frequency removal module into the main program, we conducted the comparisons against WAMIT on some cases which are known to have the irregular frequency effects. An excellent agreement was achieved[108]. The irregular frequency removal module of our in-house program, MDLMultiDYN, is also more efficient than that of WAMIT version 6. For the box barge having 500 panels without the lid and 700 panels with the lid, we conducted the simulation for 50 frequencies. The irregular frequency

removal module in MDLMultiDYN increased the simulation time by about 13s while the increased time in WAMIT is about 24s. The comparison shows that our method is accurate and also very time efficient, which is often a desired feature for practical applications.

The module to calculate 2nd order forces in the previous in-house program MDLHydroD was for the single body problem. The results were validated against the experimental data and a number of numerical methods by other well established researchers in Guha[123]. The sensitivity of different numerical schemes and the effect of hull emergence angle were discussed. To solve for the multi-body problem, the formula need to be re-derived to consider the generality of an arbitrary number of floaters. In this dissertation, the general formula for the multi-body problem was derived and the underlying concepts were also explained. We compared the results against WAMIT and a good agreement was obtained. Additionally, we improved the accuracy of the calculation of the wave elevation around the waterline. We found the wave elevation can be calculated accurately without very fine panels near the free surface. We also demonstrated that the waterline panels needed to be extremely small in the vertical direction (e.g. 0.1) if the user is using WAMIT and conducting the convergence test. Additionally, through the convergent tests, we showed that the difference using various sizes waterline panels is significant in the range of relative higher frequencies[109]. Attention needs to be paid to the sizes of the panels when studying the forces or moments in the higher frequencies.

In the side-by-side offloading problem, we applied the CFD approach to investigate the physical phenomenon occurring inside the gap. We set up the CFD model in STAR-CCM+ 12.06.010 and validated the results against the experimental data provided by Dr Zhao, University of Western Australia. Wave breaking phenomenon or vortex shedding was not observed for this specific case. Therefore, we concluded that it is the viscosity of the fluid that affects the wave elevation inside the gap, which explains the difference in the results of the potential method and the experimental data. To consider the energy loss on the ship hull rather than in the gap, we proposed a wall damping method. It is a significant improvement upon XB Chen[93]. In our method, a lid is no longer needed. However, we found that the damping coefficient needed to be frequency dependent.

Gaussian kernel functions are applied to describe the relationship. Finally, consistent results with the experimental data are obtained for the wave gauge in the middle of the gap. It demonstrates the effectiveness of this method. This method more directly models the energy loss on the ship hull and has more physical meaning as compared against the damping lid method, which assumes the energy loss happens on the free surface inside the gap.

Additionally, the proposed damping wall method is the first step to develop the categories of methods without lid. The motivation is to use small amount of measured data and a simplified model to generate engineering acceptable results. Additional improvements can be made upon this method and given more data, a more general and powerful model can be developed in the future.

REFERENCES

[1] "The Energy Collective," *http://www.theenergycollective.com/biggav/33634/49376*.

[2] "Rigzone.com," *https://www.rigzone.com/training/insight.asp?insight_id=321&c_id=*.

[3] "Armed with Science," *http://science.dodlive.mil/2011/08/24/military-sealift-command-keeps-the-navy-moving/*, 2011.

[4] J. L. Hess and A. Smith, "Calculation of Non-lifting Potential Flow About Arbitraty Three-dimensional Bodies," tech. rep., Douglas Aircraft Division, Arlington, VA, 1962.

[5] J. L. Hess and D. C. Wilcox, "Progress in the Solution of the Problem of a Three-Dimensional Body Oscillating in the Presence of a Free Surface," tech. rep., McDonnell Douglas Corp, Douglas Aircraft Div, Long Beach, CA, 1969.

[6] D. Nakos and P. Sclavounos, "Ship Motions by a Three-Dimensional Rankine Panel Method," in *18th Symposium of Naval Hydrodynamics*, (Ann Arbor, Michigan), 1991.

[7] D. Nakos, D. Kring, and P. Sclavounos, "Rankine Panel Methods for Transient Free-Surface Flows," in *6th Intl Conf on Numerical Ship Hydrodynamics*, (Iowa, USA), pp. 613–632, 1994.

[8] D. C. Kring, *Time Domain Ship Motions by a Three-Dimensional Rankine Panel Method*. PhD thesis, Massachusetts Institute of Technology, 1994.

[9] F. Noblesse, "The Green function in the theory of radiation and diffraction of regular water waves by a body," *Journal of Engineering Mathematics*, vol. 16, pp. 137–169, may 1982.

[10] J. Telste and F. Noblesse, "Numerical Evaluation of the Green Function of Water-Wave Radiation and Diffraction," *Journal of Ship Research*, vol. 30, no. 2, pp. 69–84, 1986.

[11] J. N. Newman, "Algorithms for the free-surface Green function," *Journal of Engineering Mathematics*, vol. 19, no. 1, pp. 57–67, 1985.

[12] J. Newman, "The Evaluation of Free-Surface Green Functions," in *Fourth international conference on numerical ship hydrodynamics*, 1985.

[13] J. Newman, "The approximation of free surface green function," in *Wave Asymptotics* (P. Martin and G. Wickham, eds.), pp. 107–135, Cambridge University Press, 1992.

[14] C. H. Kim, "The hydrodynamic interaction between two cylindrical bodies floating in beam seas," tech. rep., Stevens Institute of Technology, Hoboken, NJ USA, 1972.

[15] M. Ohkusu, "Ship Motions in Vicinity of a Structure," in *BOSS '76 Behaviour of off-shore structures : proceedings of the first International Conference*, 1976.

[16] R. W. Yeung, "On the interactions of slender ships in shallow water," *Journal of Fluid Mechanics*, vol. 85, no. 01, p. 143, 1978.

[17] G. V. Oortmerssen, "Hydrodynamic interaction between two structures floating in waves," in *Second International Conference on Behavior of Offshore Structures*, (London, England), pp. 339–356, 1979.

[18] A. Løken, "Hydrodynamic interaction between several floating bodies of arbitrary form in waves," *HYDRODYNAMICS IN OCEAN ENGINEERING,(198,*, pp. 745–759, 1981.

[19] N. Kodan, "The Motions of Adjacent Floating Structures in Oblique Waves," *Journal of Energy Resources Technology*, vol. 106, no. June 1984, pp. 199–205, 1984.

[20] M. C. Fang and C. H. Kim, "Hydrodynamically Coupled Motions of Two Ships Advancing in Oblique Waves," *Journal of Ship Research*, vol. 30, no. 3, pp. 159–171, 1986.

[21] H. Kagemoto and D. Yue, "Interactions among multiple three-dimensional bodies in water waves: an exact algebraic method," *Journal of Fluid Mechanics*, vol. 166, pp. 189–209, 1986.

[22] S. Mavrakos and P. Koumoutsakos, "Hydrodynamic interaction among vertical axisymmetric bodies restrained in waves," *Applied Ocean Research*, vol. 9, no. 3, pp. 128–140, 1987.

[23] F. T. Korsmeyer, C.-H. Lee, and J. N. Newman, "Computation of Ship Interaction Forces in Restricted Waters," *Journal of Ship Research*, vol. 37, no. 4, pp. 298–306, 1993.

[24] P. Teigen, "Numerical Aspects of Multiple Body Hydrodynamics," in *Proceedings of the Tenth (2000) International Offshore and Polar Engineering Conference*, vol. 1, (Seattle, USA), pp. 165–173, 2000.

[25] B. Buchner, a. van Dijk, and J. de Wilde, "Numerical Multiple-Body Simulations of Side-by-Side Mooring to an FPSO," in *Proceedings of the Eleventh International Offshore and Polar Engineering Conference*, pp. 343–353, 2001.

[26] R. Huijsmans, J. Pinkster, and J. de Wilde, "Diffraction and Radiation of Waves Around Side-by-Side Moored Vessels," in *ISOPE 2001*, vol. 1, pp. 406–412, 2001.

[27] Y. R. Choi and S. Y. Hong, "An analysis of hydrodynamic interaction of floating multi-body using higher-order boundary element method," *Proceedings of the Twelfth International Offshore and Polar Engineering Conference*, vol. 3, pp. 303–308, 2002.

[28] M. Kashiwagi, K. Endo, and H. Yamaguchi, "Wave drift forces and moments on two ships arranged side by side in waves," *Ocean Engineering*, vol. 32, pp. 529–555, apr 2005.

[29] T. Kristiansen and O. M. Faltinsen, "Application of a vortex tracking method to the piston-like behaviour in a semi-entrained vertical gap," *Applied Ocean Research*, vol. 30, no. 1, pp. 1–16, 2008.

[30] G. Chen and M. Fang, "Hydrodynamic interactions between two ships advancing in waves," *Ocean Engineering*, vol. 28, pp. 1053–1078, 2001.

[31] J. M. a. Fonfach, S. Sutulo, and C. Guedes Soares, "Numerical study of ship-to-ship interaction forces on the basis of various flow models," *Second International Conference on Ship Manoeuvring in Shallow and Confined Water: Ship to Ship Interaction*, pp. 137–146, 2011.

[32] X. Xiang and O. M. Faltinsen, "Time domain simulation of two interacting ships advancing parallel in waves," in *Proceedings of the ASME 30th International Conference on Ocean, Offshore and Arctic Engineering - OMAE 2011*, no. 2007, pp. 1–13, 2011.

[33] Y.-b. Kim, *Dynamic Analysis of Multiple-body Floating Platforms Coupled with Mooring Lines and Risers*. PhD thesis, Texas A&M Univeristy, 2003.

[34] B. J. Koo and M. H. Kim, "Hydrodynamic interactions and relative motions of two floating platforms with mooring lines in side-by-side offloading operation," *Applied Ocean Research*, vol. 27, no. 6, pp. 292–310, 2005.

[35] C. Xie, *Statistical estimation of two-body hydrodynamic properties using system identification*. PhD thesis, Texas A&M University, 2009.

[36] F. John, "On the motion of floating bodies II," *Communications on Pure and Applied Mathematics*, vol. 3, pp. 45–101, 1950.

[37] W. Frank, "Oscillation of Cylinders in or Bellow the free surface of deep fluids," tech. rep., Naval Ship Research and Development Center, Bethesda, MD, 1967.

[38] F. Ursell, "Short Surface Waves due to an Oscillating Immersed Body," *Proceedings of the Royal Society A: Mathematical, Physical and Engineering Sciences*, vol. 220, pp. 90–103, oct 1953.

[39] H. A. Schenck, "Improved Integral Formulation for Acoustic Radiation Problems," *The Journal of the Acoustical Society of America*, vol. 44, no. 1, pp. 41–58, 1968.

[40] A. J. Burton and G. F. Miller, "The Application of Integral Equation Methods to the Numerical Solution of Some Exterior Boundary-Value Problems," *Proceedings of the Royal Society A: Mathematical, Physical and Engineering Sciences*, vol. 323, pp. 201–210, 1971.

[41] D. Jones, "Integral Equations for the Exterior Acoustic Problem," *Q J Mechanics Appl Math*, vol. 27(1), pp. 129–142, 1974.

[42] T. F. Ogilvie and Y. S. Shin, "Integral Equation Solutions for Time Dependent Free Surface Problems," *Journal of the Society of Naval Architects of Japan*, no. 143, pp. 41–51, 1978.

[43] P. Sayer, "An integral-equation method for determining the fluid motion due to a cylinder heaving on water of finite depth," *Proceedings of the Royal Society of London*, vol. Series A, no. 372, pp. 93–110, 1980.

[44] F. Ursell, "Irregular frequencies and the motion of floating bodies," *Journal of Fluid Mechanics*, vol. 105, pp. 143–156, apr 1981.

[45] X.-J. Wu and W. Price, "A multiple Green's function expression for the hydrodynamic analysis of multi-hull structures," *Applied Ocean Research*, vol. 9, no. 2, pp. 58–66, 1987.

[46] S. M. Lau and G. E. Hearn, "Suppression of irregular frequency effects in fluidâĂŞstructure interaction problems using a combined boundary integral equation method," *International journal for numerical methods in fluids*, vol. 9, no. 7, pp. 763–782, 1989.

[47] C.-H. Lee and P. D. Sclavounos, "Removing the irregular frequencies from integral equations in wave-body interactions," *Journal of Fluid Mechanics*, vol. 207, p. 393, 1989.

[48] C.-H. Lee, *Numerical Methods for Boundary Integral Equations in Wave Body Interactions*. PhD thesis, Massachusetts Institure of Technology, 1988.

[49] R. Kress, "Minimizing the Condition Number of Boundary Integral Operators in Acoustic and Electromagnetic Scattering," *Quarterly Journal of Mechanics & Applied Mathematics*, vol. 38, no. 2, pp. 323–341, 1985.

[50] X. Zhu, *Irregular frequency removal from the boundary integral equation for the wave-body problem*. PhD thesis, Massachusetts Institute of Technology, 1994.

[51] P. Martin, "On the null-field equations for water-wave radiation problems," *J. Fluid Mech*, vol. 113, pp. 315–332, 1981.

[52] S. Liapis, "A method for suppressing the irregular frequencies from integral equations in water wave-structure interaction problems," *Computational Mechanics*, no. 12, pp. 59–68, 1993.

[53] W. Qiu, H. Peng, and C. Hsiung, "Removal of irregular frequency effect in the computation of wave-body interactions using the panel-free method," *Oceanic Engineering International*, vol. 9, no. 1, 2005.

[54] P. Wood, "State of the Art Report Seakeeping," in *16 ATTC*, Instituto de Pesquisas TecnoloÌĄgicas, Marinho do Brasil, 1972.

[55] T. Angell, G. Hisao, and R. Kleinman, "Recent Developments in Floating Body Problems," in *Mathematical Approaches in Hydrodynamics*, ch. 10, pp. 141–152, Philadelphia: SIAM, 1991.

[56] S. Ohmatsu, "On the Irregular Frequencies in the Theory of Oscillating Bodies in a Free Surface," *Papers of Ship Research Institute*, no. 48, 1975.

[57] R. E. Kleinman, "On the mathematical theory of the motion of floating bodies: An update," tech. rep., David W. Taylor Naval Ship Research and Development Center, Bethesda, MD, 1982.

[58] M. Rezayat, D. Shippy, and F. Rizzo, "On time-harmonic elastic-wave analysis by the boundary element method for moderate to high frequencies," *Computer Methods in Applied Mechanics and Engineering*, vol. 55, no. 3, pp. 349–367, 1986.

[59] C. Lee, J. N. Newman, and X. Zhu, "An extended boundary integral equation method for the removal, of irregular frequency effects," *International Journal for Numerical Methods in Fluids*, vol. 23, no. 7, pp. 637–660, 1996.

[60] J. Newman and P. Sclavounos, "The Computation of Wave Loads on Large Offshore Structures," in *Proceeding of International Conference on Behaviour of Offshore Structures (BOSS 88')*, (Trondheim, Norway), pp. 1–18, 1988.

[61] H. Maruo, "The drift of a body floating on waves," *Journal of Ship Research*, vol. 4, pp. 1–5, 1960.

[62] J. Newman, "The Drift Force and Moment on Ships in Waves.pdf," *Journal of Ship Research*, vol. 11, pp. 51–60, 1967.

[63] O. Faltinsen and F. Michelsen, "Motions of large structures in waves at zero Froude number," in *Proc. Intl Symp. on the Dynamics of Marine Vehicles and Structures in Waves*, (London), pp. 91–106, 1974.

[64] J. Pinkster and G. van Oortmerssen, "Computation of the First and Second Order Wave Forces on Oscillating Bodies in Regular Waves," in *Proceedings of the 2nd International Conference on Numerical Ship Hydrodynamics*, pp. 136–159, 1977.

[65] T. F. Ogilvie, "Second-order Hydrodynamic Effects On Ocean Platforms," in *International Workshop on Ship and Platform Motions,*, pp. 205–265, 1983.

[66] H. Maruo, "The excess resistance of a ship in rough seas," *International Shipbuilding Progress*, vol. 4, no. 35, pp. 337–345, 1957.

[67] H. Maruo, "Resistance in Waves," in *Research on Seakeeping Qualities of Ships in Japan*, ch. 5, pp. 67–102, The Society of Naval Architects of Japan, 1963.

[68] W. Joosen, "Added Resistance of Ship in Waves," in *Proceedings of the 6th Symposium on Naval Hydrodynamics*, (Washington D.C), Netherlands Ship Model Basin, 1966.

[69] J. Gerritsma and W. Beukelman, "Analysis of the Resistance Increase in Waves of a Fast Cargo Ship," *International Shipbuilding Progress*, vol. 19, no. 217, pp. 285–293, 1972.

[70] J. Strom-Tejsen, H. Y. Yeh, and D. D. Moran, "Added Resistance in Waves," *Society of Naval Architects and Marine Engineers, Transactions*, vol. 81, pp. 109–143, 1973.

[71] N. Salvesen, "Second-order steady state forces and moments on surface ships in oblique regular waves," in *International Symposium on Dynamics of Marine Vehicles and Structures in Waves*, (University College, London), pp. 225–241, 1974.

[72] N. Salvesen, "Added Resistance of Ships in Waves," *Journal of Hydronautics*, vol. 12, no. 1, pp. 24–34, 1978.

[73] O. M. Faltinsen, K. J. Minsaas, N. Liapis, and S. O. Skjørdal, "Prediction of Resistance and Propulsion of a Ship in a Seaway," *Proceeding of 13th Symposium on Naval Hydrodynamics*, pp. 505–529, 1980.

[74] C. Hsiung and Z. Huang, "Final Report: The Frequency-Domain Prediction of Added Resistance of Ships in Waves Using a Near-Field, 3-Dimensional Flow Method," *DREA Contractor Report CR/95/484*, pp. 1–88, 1995.

[75] M. Kashiwagi, T. Ikeda, and T. Sasakawa, "Effects of forward speed of a ship on added resistance in waves," *International Journal of Offshore and Polar Engineering*, vol. 20, no. 3, pp. 196–203, 2010.

[76] S. Liu, A. Papanikolaou, and G. Zaraphonitis, "Prediction of added resistance of ships in waves," *Ocean Engineering*, vol. 38, pp. 641–650, mar 2011.

[77] M. Kashiwagi, "Hydrodynamic Study on Added Resistance Using Unsteady Wave Analysis," *Journal of ship research*, vol. 57, no. 4, pp. 220–241, 2013.

[78] J. Pinkster, *Low frequency second order wave exciting forces on floating structures*. PhD thesis, Delft University of Technology, 1980.

[79] C. Lee and J. Newman, "First and Second Order Wave Effects on a Submerged Spheroid," *Journal of Ship Research*, vol. 35, no. 3, pp. 183–190, 1991.

[80] C. Lee, "WAMIT Theory Manual," tech. rep., Department of Ocean Engineering, Massachusetts Institute of Technology, Cambridge, Cambridge, MA, 1995.

[81] J. Newman and C. Lee, "Sensitivity of wave loads to the discretisation of bodies," in *Behaviour of offshore structures : proceedings of the sixth international conference*, 1992.

[82] G. Miao, T. Saitoh, and H. Ishida, "Water Wave Interaction of Twin Large Scale Caissons With a Small Gap Between," *Coastal Engineering Journal*, vol. 43, no. 01, pp. 39–58, 2001.

[83] T. Saitoh, G. Miao, and H. Ishida, "Theoretical Analysis on Appearance Condition of Fluid Resonance in a Narrow Gap between," in *Proceedings of the 3rd Asia-Pacific Workshop on Marine Hydrodynamics*, pp. 170–175, Beijing: China Ocean Press, 2006.

[84] O. M. Faltinsen, O. F. Rognebakke, and A. N. Timokha, "Two-dimensional resonant piston-like sloshing in a moonpool," *Journal of Fluid Mechanics*, vol. 575, p. 359, 2007.

[85] O. M. Faltinsen and A. N. Timokha, "On damping of two-dimensional piston-mode sloshing in a rectangular moonpool under forced heave motions," *Journal of Fluid Mechanics*, vol. 772, no. c, p. R1, 2015.

[86] Y. Liu, H. J. Li, and Y. C. Li, "A new analytical solution for wave scattering by a submerged horizontal porous plate with finite thickness," *Ocean Engineering*, vol. 42, pp. 83–92, 2012.

[87] L. Lu, L. Cheng, B. Teng, and M. Zhao, "Numerical investigation of fluid resonance in two narrow gaps of three identical rectangular structures," *Applied Ocean Research*, vol. 32, no. 2, pp. 177–190, 2010.

[88] H. Iwata, T. Saitoh, and G. Miao, "Fluid resonance in narrow gaps of very large floating structure composed of rectangular modules," in *Proceedings of the 4th International Conference on Asian and Pacific Coasts*, pp. 815–826, Beijing: China Ocean Press, 2007.

[89] N. Moradi, T. Zhou, and L. Cheng, "Effect of inlet configuration on wave resonance in the narrow gap of two fixed bodies in close proximity," *Ocean Engineering*, vol. 103, pp. 88–102, 2015.

[90] N. Moradi, T. Zhou, and L. Cheng, "Two-dimensional numerical study on the effect of water depth on resonance behaviour of the fluid trapped between two side-by-side bodies," *Applied Ocean Research*, vol. 58, pp. 218–231, 2016.

[91] B. Buchner, G. D. Boer, and J. D. Wilde, "The interaction effects of mooring in close proximity of other structures," in *The Fourteenth International Offshore and Polar Engineering Conference*, vol. 1, pp. 297–306, 2004.

[92] Chen XB, "Hydrodynamic analysis for offshore LNG terminals," *In: Proc 2nd int workshop on applied offshore hydrodynamics.*, 2005.

[93] X. B. Chen and S. Malenica, "Interaction hydrodynamique d'un ensemble de flotteurs sur la surface libre," in *10èmes JOURNÉES DE L'HYDRODYNAMIQUE*, (Nantes, France), pp. 1–14, 2005.

[94] A. Pauw, Willemjin; Huijsmans, Rene; Voogt, "Advances in the Hydrodynamnics of Side-by-side moored vessels," in *OMAE 2007*, pp. 1–7, 2007.

[95] T. Bunnik, W. Pauw, and A. Voogt, "Hydrodynamic Analysis for Side-by-Side Offloading," in *ISOPE 2009*, vol. 1, pp. 648–653, 2009.

[96] L. Lu, B. Teng, L. Cheng, L. Sun, and X. Chen, "Modelling of multi-bodies in close proximity under water waves-Fluid resonance in narrow gaps," *Science China: Physics, Mechanics and Astronomy*, vol. 54, no. 1, pp. 16–25, 2011.

[97] R. Zhu, G. Miao, and Y. You, "Influence of Gaps Between 3D Multiple Floating Structures on Wave Forces," *Journal of Hydrodynamics*, vol. 17, no. Ser B, pp. 141–147, 2005.

[98] P. Teigen and J. Niedzwecki, "A Computational Study of Wave Effects Related to Side-by-Side LNG Offoading.," in *The Sixteenth International Offshore and . . .* , vol. 4, pp. 238–247, 2006.

[99] R. ZHU, G. MIAO, and H. ZHU, "The radiation problem of multiple structures with small gaps in between," *Journal of Hydrodynamics, Ser. B*, vol. 18, no. 5, pp. 520–526, 2006.

[100] L. Sun, R. Eatock Taylor, and P. Taylor, "First- and second-order analysis of resonant waves between adjacent barges," *Journal of Fluids and Structures*, vol. 26, pp. 954–978, aug 2010.

[101] K. Markeng, "INVESTIGATION OF FREE SURFACE DAMPING MODELS WITH APPLICATIONS," in *Proceedings of the ASME 2017*, pp. 1–10, 2017.

[102] W. Zhao, H. Wolgamot, S. Draper, P. H. Taylor, R. Eatock Taylor, and M. Efthymiou, "Experimental Determination of Resonant Response in the Narrow Gap Between Two Side-

by-Side Fixed Bodies in Deep Water," in *Proceedings of ASME 2016 25th International Conference on Ocean, Offshore and Arctic Engineering*, (Busan, South Korea), pp. 1–7, 2016.

[103] H. Wang, S. Draper, W. Zhao, H. Wolgamot, and L. Cheng, "Development of a CFD Model To Simulate Three-Dimensional Gap Resonance Applicable to FLNG Side-by-side Offloading," in *Proceedings of the ASME 2017 36th International Conference on Ocean, Offshore and Arctic Engineering*, (Trondheim, Norway), pp. 1–11, 2017.

[104] Y. Liu and J. M. Falzarano, "A Note on the Conclusion Based on the Generalized Stokes Theorem," *Journal of Offshore Engineering and Technology*, vol. 1, pp. 1–17, 2017.

[105] Y. Liu and J. M. Falzarano, "Irregular Frequency Removal Methods: Theory and Applications in Hydrodynamics," *Journal of Marine System and Ocean Technology*, vol. 12, no. 2, pp. 49–64, 2016.

[106] Y. Liu and J. M. Falzarano, "A method to remove irregular frequencies and log singularity evaluation in wave-body interaction problems," *Journal of Ocean Engineering and Marine Energy*, vol. 3, no. 2, pp. 161–189, 2017.

[107] Y. Liu and J. M. Falzarano, "Suppression of Irregular Frequency in Multi-body Problem and Free-Surface Singularity Treatment," in *Proceedings of the ASME 2016 35th International Conference on Ocean, Offshore and Arctic Engineering*, (Busan, South Korea), pp. 1–11, 2016.

[108] Y. Liu and J. M. Falzarano, "Suppression of Irregular Frequency in Multi-Body Problem and Free-Surface Singularity Treatment," *Journal of Offshore Mechanics and Arctic Engineering*, vol. 139, no. October, pp. 1–16, 2017.

[109] Y. Liu and J. M. Falzarano, "Improvement on the Accuracy of Mean Drift Force Calculation," in *Proceedings of the ASME 2017 36th International Conference on Ocean, Offshore and Arctic Engineering*, (Trondheim, Norway), pp. 1–13, 2017.

[110] Z. Xie, Y. Liu, and J. Falzarano, "A More Efficient Numerical Evaluation of the Green Function in Finite Water Depth," *Ocean Systems Engineering*, pp. 399–412, 2017.

[111] A. Guha, *Development and application of a potential flow computer program: determining first and second order wave forces at zero and forward speed in deep and intermediate water depth*. PhD thesis, Texas A&M University, 2016.

[112] N. Salvesen, E. Tuck, and O. Faltinsen, "Ship motions and sea loads," *Trans. SNAME*, vol. 78, no. i, pp. 250–287, 1970.

[113] A. Guha and J. Falzarano, "Estimation of Hydrodynamic Forces and Motion of Ships with Steady Forward Speed," *International Shipbuilding Progress*, vol. 1, no. 979, pp. 1–13, 2014.

[114] A. Guha, *Development Of A Computer Program For Three Dimensional Frequency Domain Analysis Of Zero Speed First Order Wave Body Interaction*. PhD thesis, Texas A&M University, 2012.

[115] W. Zhao, H. A. Wolgamot, P. H. Taylor, and R. Eatock Taylor, "Gap resonance and higher harmonics driven by focused transient wave groups," *Journal of Fluid Mechanics*, vol. 812, pp. 905–939, 2017.

[116] C. W. Hirt and B. D. Nichols, "Volume of fluid (VOF) method for the dynamics of free boundaries," *Journal of Computational Physics*, vol. 39, no. 1, pp. 201–225, 1981.

[117] W. F. Noh and P. Woodward, "SLIC (Simple Line Interface Calculation)," pp. 330–340, 1976.

[118] J. Kim, J. O'Sullivan, and A. Read, "Ringing Analysis of a Vertical Cylinder by Euler Overlay Method," *31st International Conference on Ocean, Offshore and Arctic Engineering*, pp. 855–866, 2012.

[119] W. Finnegan and J. Goggins, "Numerical simulation of linear water waves and wavestructure interaction," *Ocean Engineering*, vol. 43, pp. 23–31, 2012.

[120] B. Duz, *Wave Generation, Propagation and Absorption in CFD Simulations of Free Surface Flows*. PhD thesis, TUDelft, 2015.

[121] M. Zalar, L. Diebold, E. Baudin, J. Henry, and X.-b. Chen, "Sloshing Effects Accounting for Dynamic Coupling Between Vessel and Tank Liquid Motion," in *OMAE 2007*, pp. 1–15, 2007.

[122] Y. Liu and J. M. Falzarano, "Frequency Domain Analysis of the Interactions Between Multiple Ships with Nonzero Speed in Waves or Current-Wave Interactions," in *Proceedings of the ASME 2017 36th International Conference on Ocean, Offshore and Arctic Engineering*, (Trondheim, Norway), pp. 1–17, 2017.

[123] A. Guha and J. Falzarano, "The effect of hull emergence angle on the near field formulation of added resistance," *Ocean Engineering*, vol. 105, pp. 10–24, 2015.

[124] N. Gunter, *Potential Theory and Its Applications to Basic Problems of Mathematical Physics*. New York: Ungar, 1st ed., 1967.

[125] O. Tuck, "A Rational Strip Theory of Ship Motions_ Part I.pdf," 1969.

[126] J. N. Newman, "The Theory of Ship Motions," *Advances in Applied Mechanics*, vol. 18, no. C, pp. 221–283, 1979.

[127] E. V. Lewis, *Principles of Naval Architecture: Motions in Waves and Controllability Vol.3*. SNAME, 2nd ed., 1988.

APPENDIX A

RADIATION FORCE IN NONZERO SPEED CASES

In this appendix, we will derive the radiation force for an asymmetric body. This is going to be a supplement of the results in Salvensen[112] for symmetric bodies.

In the derivation, we will follow the similar notations in the main part. It may contain more subscripts or superscripts, which is just to make it clear to the readers to see the changes.

$$\begin{aligned}\overline{F}_{Rj}^{(1)} &= \iint_S n_j' \overline{P}_R^{d(1)} dS = -\rho \iint_S n_j' (\frac{\partial}{\partial \bar{t}} - U\frac{\partial}{\partial \bar{x}})(\sum_{k=1}^{6} \bar{\eta}_k^{A(1)} \overline{\phi}_{rel-k}^{*(1)} e^{i\omega_e \bar{t}}) dS \\ &= \sum_{k=1}^{6} T_{jk} \bar{\eta}_k^{A(1)} e^{i\omega_e \bar{t}} \end{aligned} \tag{A.1}$$

where,

$$T_{jk} = \rho \iint_S n_j' (i\omega_e - U\frac{\partial}{\partial \bar{x}}) \overline{\phi}_{rel-k}^{*(1)} dS \tag{A.2}$$

From Salvesen[112], the key equation to simplify the problem is as below:

$$\iint_S n_j U \frac{\partial}{\partial x} \phi dS = U \iint_S m_j \phi dS - U \int_{C_x} n_j \phi dl \tag{A.3}$$

If we omit the second term in the right hand side and apply it to T_{jk}, we will get:

$$T_{jk} = \rho i\omega_e \iint_S n_j' \overline{\phi}_{rel-k}^{*(1)} dS + U\rho \iint_S m_j \overline{\phi}_{rel-k}^{*(1)} dS \tag{A.4}$$

where, $n_j = (n_1', n_2', n_3', n_4', n_5', n_6')$, $m_j = (0, 0, 0, 0, n_3', -n_2')$.

A typical assumption about $\overline{F}_{Rj}^{(1)}$ is that it will be proportional to the velocity and acceleration

of the floater. A_{jk} is defined as the added mass and B_{jk} the damping.

$$\begin{aligned}\overline{F}_{Rj}^{(1)} &= \sum_{k=1}^{6}(-A_{jk}\ddot{\bar{\eta}}_k^{(1)} - B_{jk}\dot{\bar{\eta}}_k^{(1)}) \\ &= \sum_{k=1}^{6}(\omega_e^2 A_{jk}\bar{\eta}_k^{(1)} - i\omega_e B_{jk}\bar{\eta}_k^{(1)})\end{aligned} \tag{A.5}$$

This function will lead to:

$$T_{jk} = \omega_e^2 A_{jk} - i\omega_e B_{jk} \tag{A.6}$$

Next, we will study the expressions of T_{jk} based on the value of j, k. There are 4 cases.

1. $j = 1 \sim 4, k = 1 \sim 4$:

$$T_{jk} = T_{jk}^0$$

2. $j = 1 \sim 4, k = 5 \sim 6$:

$$\begin{aligned}T_{j5} &= T_{j5}^0 + \frac{U}{i\omega_e}T_{j3}^0 \\ T_{j6} &= T_{j6}^0 - \frac{U}{i\omega_e}T_{j2}^0\end{aligned}$$

3. $j = 5 \sim 6, k = 1 \sim 4$:

$$\begin{aligned}T_{5k} &= T_{5k}^0 - \frac{U}{i\omega_e}T_{3k}^0 \\ T_{6k} &= T_{6k}^0 + \frac{U}{i\omega_e}T_{2k}^0\end{aligned}$$

4. $j = 5 \sim 6, k = 5 \sim 6$:

$$
\begin{aligned}
T_{55} &= T_{55}^0 + \frac{U^2}{\omega_e^2} T_{33}^0 \\
T_{56} &= T_{56}^0 - \frac{U}{i\omega_e} T_{52}^0 - \frac{U}{i\omega_e} T_{36}^0 - \frac{U^2}{\omega_e^2} T_{32}^0 \\
T_{66} &= T_{66}^0 + \frac{U^2}{\omega_e^2} T_{22}^0 \\
T_{65} &= T_{65}^0 + \frac{U}{i\omega_e} T_{63}^0 + \frac{U}{i\omega_e} T_{25}^0 - \frac{U^2}{\omega_e^2} T_{23}^0
\end{aligned}
$$

Based on the above equations and equation (A.6), we can know the added mass A_{jk} and damping B_{jk} will satisfy the following equations:

1. $j = 1 \sim 4, k = 1 \sim 4$:

$$
\begin{aligned}
A_{jk} &= A_{jk}^0 \\
B_{jk} &= B_{jk}^0
\end{aligned}
$$

2. $j = 1 \sim 4, k = 5 \sim 6$:

$$
\begin{aligned}
A_{j5} &= A_{j5}^0 - \frac{U}{\omega_e^2} B_{j3}^0 \\
B_{j5} &= B_{j5}^0 + U A_{j3}^0 \\
A_{j6} &= A_{j6}^0 + \frac{U}{\omega_e^2} B_{j2}^0 \\
B_{j6} &= B_{j6}^0 - U A_{j2}^0
\end{aligned}
$$

3. $j = 5 \sim 6, k = 1 \sim 4$:

$$
\begin{aligned}
A_{5k} &= A^0_{5k} + \frac{U}{\omega_e^2} B^0_{3k} \\
B_{5k} &= B^0_{5k} - U A^0_{3k} \\
A_{6k} &= A^0_{6k} - \frac{U}{\omega_e^2} B^0_{2k} \\
B_{6k} &= B^0_{6k} + U A^0_{2k}
\end{aligned}
$$

4. $j = 5 \sim 6, k = 5 \sim 6$:

$$
\begin{aligned}
A_{55} &= A^0_{55} + \frac{U^2}{\omega_e^2} A^0_{33} \\
B_{55} &= B^0_{55} + \frac{U^2}{\omega_e^2} B^0_{33} \\
A_{56} &= A^0_{56} + \frac{U}{\omega_e^2} B^0_{52} + \frac{U}{\omega_e^2} B^0_{36} - \frac{U^2}{\omega_e^2} A^0_{32} \\
B_{56} &= B^0_{56} - U A^0_{52} - U A^0_{36} - \frac{U^2}{\omega_e^2} B^0_{32} \\
A_{66} &= A^0_{66} + \frac{U^2}{\omega_e^2} A^0_{22} \\
B_{66} &= B^0_{66} + \frac{U^2}{\omega_e^2} B^0_{22} \\
A_{65} &= A^0_{65} - \frac{U}{\omega_e^2} B^0_{63} - \frac{U}{\omega_e^2} B^0_{25} - \frac{U^2}{\omega_e^2} A^0_{23} \\
B_{65} &= B^0_{65} + U A^0_{63} + U A^0_{25} - \frac{U^2}{\omega_e^2} B^0_{23}
\end{aligned}
$$

We have discussed the added mass and damping for the single-body case. In the multi-body case, the equations will be similar except that the subscripts may vary. For example, when $j =$

$1 \sim 4, k = 11, 12$, we will have the following equations:

$$A_{j,11} = A^0_{j,11} - \frac{U}{\omega_e^2} B^0_{j9}$$

$$B_{j,11} = B^0_{j,11} + U A^0_{j9}$$

$$A_{j,12} = A^0_{j,12} + \frac{U}{\omega_e^2} B^0_{j8}$$

$$B_{j,12} = B^0_{j,12} - U A^0_{j8}$$

APPENDIX B

RELATIVE WAVE ELEVATION

In this appendix, we will discuss the contribution of the relative wave elevation in the 2nd-order forces and moments. This topic has been discussed by several researchers[65][78]. When reading those papers, we find that there are some parts not understandable in the assumptions of the problem. Herein, we want to clarify the concept and the assumptions for the convenience of the future readers.

The equations we are going to discuss are as below:

$$\vec{F}_{rel} = -\iint_{\Delta S} P\,\vec{n}\,dS$$
$$\vec{M}_{rel} = -\iint_{\Delta S} P(\vec{X}\times\vec{n})dS$$

where, the subscript rel denotes that this is only the contribution from the relative wave elevation.

Below are the figures showing that the floater in equilibrium state and motion. The dot-dashed line indicates the waterline when the floater is in equilibrium. The red area indicates ΔS, the area to be integrated. Y', X' denote the position of the point in the vessel coordinate when in equilibrium. η_3, η_4, η_5 are the RAO of the heave, roll and pitch motion.

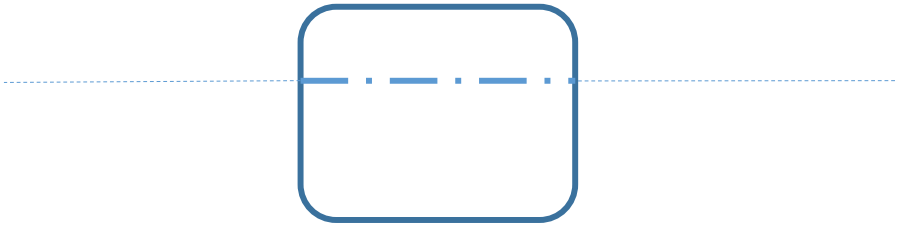

Figure B.1: Floater in Equilibrium State

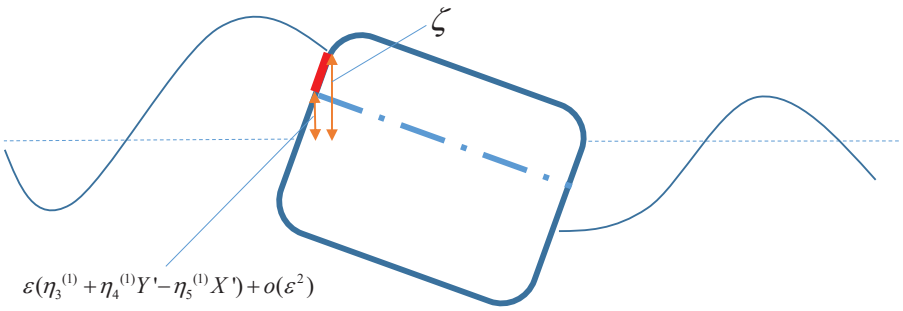

Figure B.2: Floater in Motion

The integral we are going to find is shown in Figure B.2. If considering z direction only, we will integrate from the translated waterline to the absolute wave elevation ζ. However, we want to find the translated waterline based on Taylor expansions. For an arbitrary point P at (x_p, y_p, z_p) on the floater surface when in equilibrium. (x_p, y_p, z_p) is in global coordinate. When the floater is in 6 DOF motion, the position of the point P will be changed in the global coordinate. We use (x'_p, y'_p, z'_p) to denote the translated point P. Then we will get:

$$z'_p = z_p + \eta_3^{(1)} + \eta_4^{(1)} y_p - \eta_5^{(1)} x_p + o(\epsilon^2)$$

The integrating variable is z'_p, however, we want to use z_p instead. Also we assume that the coordinate waterline $z_{wl} = 0$ in the equilibrium state. Then the integral can be written as:

$$\iint_{\Delta S} dS = \int dl \int_{z'_{wl}}^{\zeta} dz'_p = \int dl \int_{z_{wl}}^{\zeta - (\eta_3^{(1)} + \eta_4^{(1)} y_p - \eta_5^{(1)} x_p)} dz_p$$

In the above section, we have finished discussing the concept of the relative wave elevation. In the following part, we will discuss about the integral of the forces and moments.

The integral of the forces can be written as:

$$\begin{aligned}\vec{F}_{rel} &= -\iint_{\Delta S} P\,\vec{n}\,dS \\ &= -\int_{C_{wl}} dl \int_0^{\zeta-(\vec{X}-\vec{X}_0-\vec{X}')_z} P\,\vec{n}\frac{dz}{\sqrt{1-n_3'^2}} \\ &= -\int_{C_{wl}} dl \int_0^{\zeta-(\vec{X}-\vec{X}_0-\vec{X}')_z} (P^{(0)}\vec{n}^{(0)} + \epsilon P^{(1)}\vec{n}^{(0)} + \epsilon P^{(0)}\vec{n}^{(1)})\frac{dz}{\sqrt{1-n_3'^2}}\end{aligned} \tag{B.1}$$

where,

$$\begin{aligned} P^{(0)}\big|_S &= -\rho g\bar{z}\big|_{S_m} \\ P^{(1)}\big|_S &= \big[-\rho(\frac{\partial}{\partial\bar{t}} - U\frac{\partial}{\partial\bar{x}})\overline{\Phi}^{(1)}_{rel} - \rho g\vec{k}\cdot(\vec{\eta}^{(1)} + \vec{\alpha}^{(1)}\times\vec{X}')\big]\big|_{S_m} \\ \vec{n'}^{(0)} &= \vec{n'} \\ \vec{n'}^{(1)} &= \vec{\alpha}^{(1)}\times\vec{n'} \\ (\vec{X}-\vec{X}_0-\vec{X}')_z &= \epsilon(\eta_3^{(1)} + \eta_4^{(1)}Y' - \eta_5^{(1)}X') + o(\epsilon^2)\end{aligned}$$

Before proceeding to the next step, we need to introduce more assumptions. The solution domain for the PDE set is up to $z = 0$. Thus, $\overline{\Phi}^{(1)}_{rel}$ is indeed undefined above $z = 0$. Here, we will assume the 1st-order dynamic pressure is constant inside ΔS. Then only the static component is linearly varying. Also note that $(\frac{\partial}{\partial\bar{t}} - U\frac{\partial}{\partial\bar{x}})\overline{\Phi}^{(1)}_{rel} = -g\zeta^{(1)}$. Based on these assumptions, we will find the final expression of $\vec{F}_{rel}$.

$$\begin{aligned}\vec{F}_{rel} = -\int_{C_{wl}} dl \int_0^{\zeta-(\vec{X}-\vec{X}_0-\vec{X}')_z} \big\{ &-\rho g z\vec{n'} + \\ &\epsilon\rho g[\zeta^{(1)} - (\eta_3^{(1)} + \eta_4^{(1)}Y' - \eta_5^{(1)}X')]\vec{n'} - \epsilon\rho g z(\vec{\alpha}\times\vec{n'})\big\}\frac{dz}{\sqrt{1-n_3'^2}}\end{aligned} \tag{B.2}$$

where, $\zeta - (\vec{X} - \vec{X}_0 - \vec{X}')_z$ has components of $o(\epsilon)$, $o(\epsilon^2)$ etc. Herein, if we define the relative

wave elevation $\zeta_r = \zeta - (\vec{X} - \vec{X}_0 - \vec{X}')_z$ and keep $\vec{F}_{rel}$ to the $o(\epsilon^2)$, we will eventually get:

$$\vec{F}_{rel} = -\int_{C_{wl}} dl\ \frac{1}{2}\epsilon^2 \rho g \vec{n'} \frac{\zeta_r^{(1)^2}}{\sqrt{1 - n_3'^2}} + o(\epsilon^3)$$

Similarly, we can get the expression of moment as below:

$$\begin{aligned} \vec{M}_{rel} &= -\iint_{\Delta S} P[(\vec{X} - \vec{X}_0) \times \vec{n'}] dS \\ &= -\int_{C_{wl}} dl \frac{1}{2}\epsilon^2 \rho g \zeta_r^{(1)^2} (\vec{X}' \times \vec{n'}) \frac{1}{\sqrt{1 - n_3'^2}} + o(\epsilon^3) \end{aligned}$$

The application point of the force resulting from the relative wave elevation is at the waterline because the 1st-order wave profile on the floater surface will be sinusoidal in time and space.

APPENDIX C

GAUSSIAN QUADRATURE METHOD

The quadrature method is used to approximate an integral especially when we cannot find the analytical form of the integral. The equation is usually as below:

$$\int_a^b f(x)dx = \sum_{i=1}^{n} w_i f(x_i)$$

where, x_i are the quadrature nodes, w_i are the quadrature weights.

For a n-term formula, we need to choose not only n nodes x_i but also n weights w_i. That gives us $2n$ degrees of freedom. Therefore, if $f(x)$ is a polynomial, we will be able to integrate a polynomial with degree up to $(2n-1)$.

The procedure to apply Gaussian quadrature method is:

1. Choose n+1 orthogonal polynomials

$$\int_0^1 P_i(x)P_j(x)dx = 0 \; for \; j \neq i$$

2. Find the n roots, i.e. x_i, of the nth-order polynomial

3. Solve for the weights w_i

In our program, we are using Gaussian quadrature methods to integrate the Green function across a quadrilateral or a triangular panel in global coordinate. The panel may be indicated as in Figure C.1.

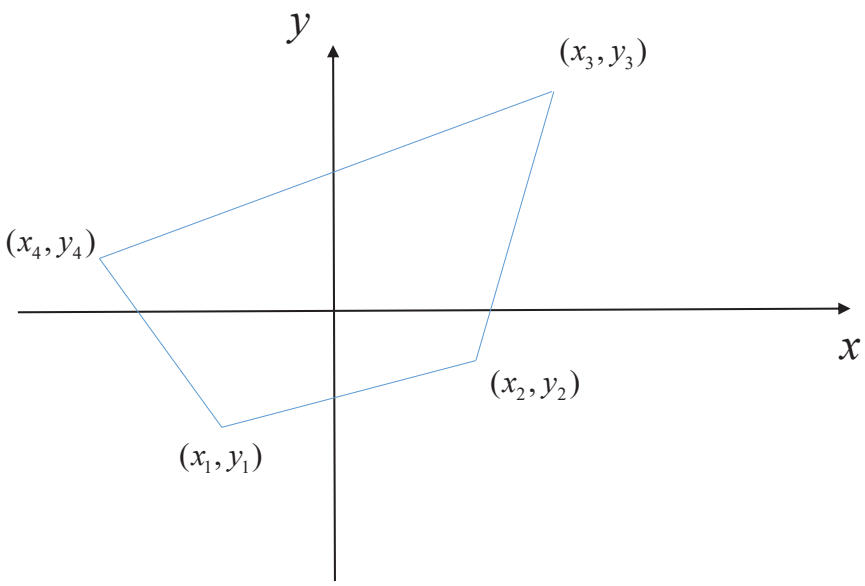

Figure C.1: Arbitrary Quadrilateral Panel

Based on the properties of the Green function, we will choose Legendre polynomial to integrate. The Legendre polynomial is defined in $[-1, 1]$ as shown in Figure C.2.

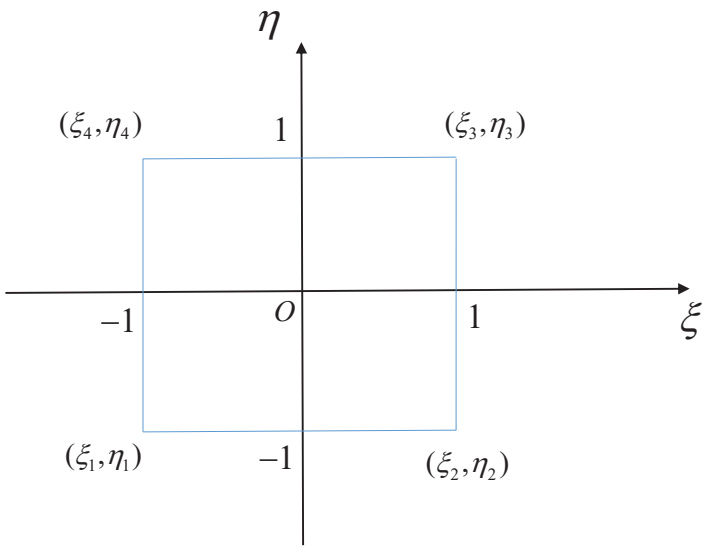

Figure C.2: Square Panel

Once we know the number of nodes we are going to use, we will be able to find the nodes x_i and the weights w_i based on the properties of Legendre polynomial. Next, we will need to find the function value at these nodes. To achieve this, we will introduce the nodal shape functions, which will convert the quadrilateral panel into a square panel. If the some point (ξ, η) is known in the $\xi O \eta$ coordinate, the corresponding (x, y) value in panel coordinate will be:

$$x = X(\xi, \eta) = \sum_{i=1}^{4} x_i N_i(\xi, \eta)$$
$$y = Y(\xi, \eta) = \sum_{i=1}^{4} y_i N_i(\xi, \eta)$$

where, the nodal shape functions $N_i(\xi, \eta)$ are defined as:

$$N_1(\xi, \eta) = \frac{1}{4}(1 - \xi)(1 - \eta)$$
$$N_2(\xi, \eta) = \frac{1}{4}(1 + \xi)(1 - \eta)$$
$$N_3(\xi, \eta) = \frac{1}{4}(1 + \xi)(1 + \eta)$$
$$N_4(\xi, \eta) = \frac{1}{4}(1 - \xi)(1 + \eta)$$

After this transformation, we need to find the corresponding points defined in global coordinate. If we combine the mapping $\xi \to x$ and $x \to x_g$ together, we can write:

$$x_g = X_g(\xi, \eta)$$
$$y_g = Y_g(\xi, \eta)$$
$$z_g = Z_g(\xi, \eta)$$

The 2D integral can be written as:

$$\iint G(x, y) dx dy = \iint G(X_g(\xi, \eta), Y_g(\xi, \eta), Z_g(\xi, \eta)) |J(\xi, \eta)| d\xi d\eta \tag{C.1}$$

where,

$$J(\xi,\eta) = \left|\frac{\partial(x,y)}{\partial(\xi,\eta)}\right| = \begin{vmatrix} \frac{\partial x}{\partial \xi} & \frac{\partial y}{\partial \xi} \\ \frac{\partial x}{\partial \eta} & \frac{\partial y}{\partial \eta} \end{vmatrix} \tag{C.2}$$

If write the integral in discretized form with N nodes, we will get:

$$\iint G(x,y)dxdy \approx \sum_{i=1}^{N}\sum_{j=1}^{N} w_i w_j G(X_g(\xi_i,\eta_j), Y_g(\xi_i,\eta_j), Z_g(\xi_i,\eta_j))|J(\xi_i,\eta_j)| \tag{C.3}$$

This is the Gaussian quadrature formula we use in the program to improve the accuracy of the integral across a certain panel.

APPENDIX D

CAUCHY PRINCIPAL INTEGRAL IN JUMP CONDITIONS [1]

Kleinman[57] adopted the jump condition derived in Günter[124]. Günter applied the integral on a closed surface to prove the jump condition. The conclusion is also valid for an open surface. As a supplement, we will prove the conclusion for the integral on an open surface, which can be adopted for the integral on piecewise smooth surface. Please note that the integral equations are constructed on smooth surfaces or at least piecewise smooth surfaces.

The integral equations we are interested in are listed as below:

$$\lim_{\boldsymbol{x}\to S_b^{\pm}} \frac{\partial}{\partial n_{\boldsymbol{x}}} \int_{S_b} u(\boldsymbol{\xi}) G(\boldsymbol{x};\boldsymbol{\xi}) dS_{\boldsymbol{\xi}} = \mp 2\pi u(\boldsymbol{x}) + \int_{S_b} u(\boldsymbol{\xi}) \frac{\partial G(\boldsymbol{x};\boldsymbol{\xi})}{\partial n_{\boldsymbol{x}}} dS_{\boldsymbol{\xi}} \tag{D.1}$$

$$\lim_{\boldsymbol{x}\to S_b^{\pm}} \int_{S_b} u(\boldsymbol{\xi}) \frac{\partial G(\boldsymbol{x};\boldsymbol{\xi})}{\partial n_{\boldsymbol{\xi}}} dS_{\boldsymbol{\xi}} = \pm 2\pi u(\boldsymbol{x}) + \int_{S_b} u(\boldsymbol{\xi}) \frac{\partial G(\boldsymbol{x};\boldsymbol{\xi})}{\partial n_{\boldsymbol{\xi}}} dS_{\boldsymbol{\xi}} \tag{D.2}$$

Both of the equations are in Cartesian coordinate and the integrand contains a singularity when field point $\boldsymbol{x} \to \boldsymbol{\xi}$. We will evaluate the value by the Cauchy Principal Value integral. Since the integrand only depends on the relative distance between the source point and the field point, we can evaluate the integral in the panel local coordinate. The origin located at panel center, z-axis is aligned long the panel normal vector and the field point located at a distance away from the center on z-axis.

[1] Part of the section is reprinted with permission from "Irregular Frequency Removal Methods: Theory and Applications in Hydrodynamics" by Yujie Liu, Jeffrey Falzarano, 2017. *Journal of Marine System and Ocean Technology*, Vol 12, Issue 2, pages 49-64. Copyright 2017 by Sociedade Brasileira de Engenharia Naval.

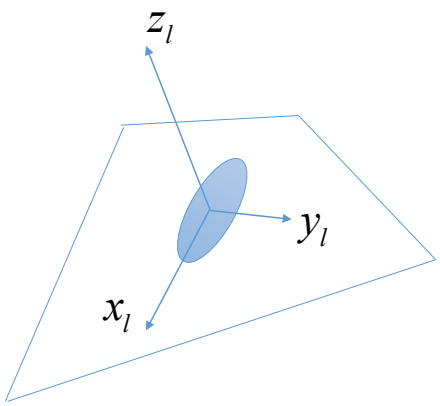

Figure D.1: Panel Local Coordinate

D.1 Jump Condition I

The singular integral can be written as:

$$\lim_{\boldsymbol{x}\to S_b^{\pm}} \frac{\partial}{\partial n_{\boldsymbol{x}}} \int_{S_b} \frac{u(\boldsymbol{\xi})}{\sqrt{(x_l-\xi_l)^2+(y_l-\eta_l)^2+(z_l-\zeta_l)^2}} dS_{\boldsymbol{\xi}}$$

First, we will study the case when $\boldsymbol{x} \to S_b^+$, more specifically, $z_l \to \zeta_l^+$ and assume the field point locates still infinitesimally close to the disk with radius $\epsilon \to 0$, in other words, $|z-\zeta|/\epsilon \to 0$. If writing the integral in cylindrical coordinate, we will get:

$$\lim_{\boldsymbol{z_l}\to\zeta_l^+} \frac{\partial}{\partial z} \int_0^{2\pi} \int_0^{\epsilon} \frac{u(\boldsymbol{\xi})}{\sqrt{r^2+(z-\zeta)^2}} r dr d\theta$$

Assume $r = |z-\zeta|\tan\alpha$, $dr = |z-\zeta|\sec^2\alpha d\alpha$, naturally $\cos\alpha = \frac{|z-\zeta|}{\sqrt{r^2+(z-\zeta)^2}}$.

$$
\begin{aligned}
&\lim_{z_l\to\zeta_l^+}\frac{\partial}{\partial z}\int_0^{2\pi}\int_0^{\epsilon}\frac{u(\boldsymbol{\xi})}{\sqrt{r^2+(z-\zeta)^2}}rdrd\theta \\
&= \lim_{z_l\to\zeta_l^+}\int_0^{2\pi}\int_0^{\alpha(\epsilon)}\frac{u(\boldsymbol{\xi})}{|z-\zeta|}|\cos\alpha|\cdot|z-\zeta|\cdot\tan\alpha\cdot|z-\zeta|\cdot\frac{1}{\cos^2\alpha}d\alpha d\theta \\
&= \lim_{z_l\to\zeta_l^+}\frac{|\cos\alpha|}{\cos\alpha}u(\boldsymbol{x})\frac{\partial}{\partial z}\int_0^{2\pi}\int_0^{\alpha(\epsilon)}|z-\zeta|\cdot d(\frac{1}{\cos\alpha})d\theta \\
&= \lim_{z_l\to\zeta_l^+}\frac{|\cos\alpha|}{\cos\alpha}u(\boldsymbol{x})\frac{\partial}{\partial z}2\pi[\sqrt{\epsilon^2+(z-\zeta)^2}-|z-\zeta|] \\
&= 2\pi u(\boldsymbol{x})\lim_{z_l\to\zeta_l^+}\frac{|\cos\alpha|}{\cos\alpha}\big[-\frac{(z-\zeta)}{\sqrt{\epsilon^2+(z-\zeta)^2}}-\frac{z-\zeta}{|z-\zeta|}\big]
\end{aligned}
\tag{D.3}
$$

When $z_l \to \zeta_l^+$, we will have:

$$
\lim_{z_l\to\zeta_l^+}-\frac{(z-\zeta)}{\sqrt{\epsilon^2+(z-\zeta)^2}} = 0
$$

$$
\lim_{z_l\to\zeta_l^+}-\frac{z-\zeta}{|z-\zeta|} = -1
$$

Then,

$$
\lim_{z_l\to\zeta_l^+}\frac{\partial}{\partial z}\int_0^{2\pi}\int_0^{\epsilon}\frac{u(\boldsymbol{\xi})}{\sqrt{r^2+(z-\zeta)^2}}rdrd\theta = -2\pi u(\boldsymbol{x}) \tag{D.4}
$$

Thus, the integral will become:

$$
\begin{aligned}
\lim_{\boldsymbol{x}\to S_b^+}\frac{\partial}{\partial n_{\boldsymbol{x}}}\int_{S_b}\frac{u(\boldsymbol{\xi})}{\sqrt{(x_l-\xi_l)^2+(y_l-\eta_l)^2+(z_l-\zeta_l)^2}}dS_{\boldsymbol{\xi}} &= -2\pi u(\boldsymbol{x}) \\
+ PV\int_{S_b}\frac{\partial}{\partial n_{\boldsymbol{x}}}\frac{u(\boldsymbol{\xi})}{\sqrt{(x_l-\xi_l)^2+(y_l-\eta_l)^2+(z_l-\zeta_l)^2}}dS_{\boldsymbol{\xi}} &
\end{aligned}
\tag{D.5}
$$

Similarly, if $\boldsymbol{x} \to S_b^-$, we will have $z_l \to \zeta_l^-$. The limit will become:

$$\lim_{z_l \to \zeta_l^-} -\frac{(z-\zeta)}{\sqrt{\epsilon^2+(z-\zeta)^2}} = 0$$
$$\lim_{z_l \to \zeta_l^-} -\frac{z-\zeta}{|z-\zeta|} = 1 \tag{D.6}$$

Therefore, the integral will be:

$$\lim_{\boldsymbol{x} \to S_b^-} \frac{\partial}{\partial n_{\boldsymbol{x}}} \int_{S_b} \frac{u(\boldsymbol{\xi})}{\sqrt{(x_l-\xi_l)^2+(y_l-\eta_l)^2+(z_l-\zeta_l)^2}} dS_{\boldsymbol{\xi}} = 2\pi u(\boldsymbol{x})$$
$$+ PV \int_{S_b} \frac{\partial}{\partial n_{\boldsymbol{x}}} \frac{u(\boldsymbol{\xi})}{\sqrt{(x_l-\xi_l)^2+(y_l-\eta_l)^2+(z_l-\zeta_l)^2}} dS_{\boldsymbol{\xi}} \tag{D.7}$$

Up to this step, we have finished the proof of the first jump condition (D.1) when field pt is approaching the body surface from both sides.

When field pt is approaching the lid surface, the similar procedure will be repeated to the image source.

$$\lim_{\boldsymbol{x} \to S_b^{\pm}} \frac{\partial}{\partial n_{\boldsymbol{x}}} \int_{S_b} \frac{u(\boldsymbol{\xi})}{\sqrt{(x_l-\xi_l)^2+(y_l-\eta_l)^2+(z_l+\zeta_l)^2}} dS_{\boldsymbol{\xi}}$$

$$\lim_{\boldsymbol{z_l} \to \zeta_l^+} \frac{\partial}{\partial z} \int_0^{2\pi} \int_0^{\epsilon} \frac{u(\boldsymbol{\xi})}{\sqrt{r^2+(z+\zeta)^2}} r dr d\theta = 2\pi u(\boldsymbol{x}) \lim_{z_l \to \zeta_l^+} \frac{|\cos\alpha|}{\cos\alpha} \Big[-\frac{(z+\zeta)}{\sqrt{\epsilon^2+(z+\zeta)^2}} - \frac{z+\zeta}{|z+\zeta|} \Big]$$

Please note that at the lid surface, $\zeta = 0$.

$$\lim_{z_l \to \zeta_l^-} -\frac{(z+\zeta)}{\sqrt{\epsilon^2+(z+\zeta)^2}} = 0$$
$$\lim_{z_l \to \zeta_l^-} -\frac{z+\zeta}{|z+\zeta|} = -1 \tag{D.8}$$

Then,

$$\lim_{\boldsymbol{z_l}\to\zeta_l^+}\frac{\partial}{\partial z}\int_0^{2\pi}\int_0^{\epsilon}\frac{u(\boldsymbol{\xi})}{\sqrt{r^2+(z+\zeta)^2}}rdrd\theta=-2\pi u(\boldsymbol{x})$$

When taking the sum of the contributions from source and image source, we will end up in the same expression in Kleinman[57].

$$\lim_{\boldsymbol{x}\to S_i^{\pm}}\frac{\partial}{\partial n_{\boldsymbol{x}}}\int_{S_i}u(\boldsymbol{\xi})G(\boldsymbol{x};\boldsymbol{\xi})dS_{\boldsymbol{\xi}}=\mp 4\pi u(\boldsymbol{x})+\int_{S_i}u(\boldsymbol{\xi})\frac{\partial G(\boldsymbol{x};\boldsymbol{\xi})}{\partial n_{\boldsymbol{x}}}dS_{\boldsymbol{\xi}}$$

Since the point is undefined when $z>0$, thus the jump condition for the lid will be:

$$\lim_{\boldsymbol{x}\to S_i^{-}}\frac{\partial}{\partial n_{\boldsymbol{x}}}\int_{S_i}u(\boldsymbol{\xi})G(\boldsymbol{x};\boldsymbol{\xi})dS_{\boldsymbol{\xi}}=4\pi u(\boldsymbol{x})+\int_{S_i}u(\boldsymbol{\xi})\frac{\partial G(\boldsymbol{x};\boldsymbol{\xi})}{\partial n_{\boldsymbol{x}}}dS_{\boldsymbol{\xi}}$$

D.2 Jump Condition II

If using the same coordinate setting,

$$\lim_{\boldsymbol{x}\to S_b^{\pm}}\int_{S_b}u(\boldsymbol{\xi})\frac{\partial}{\partial n_{\boldsymbol{\xi}}}\frac{1}{\sqrt{(x_l-\xi_l)^2+(y_l-\eta_l)^2+(z_l-\zeta_l)^2}}dS_{\boldsymbol{\xi}}$$

First investigate the case when $\boldsymbol{x}\to S_b^+$, more specifically, $z_l\to\zeta_l^+$ and assume the field point locates still infinitesimally close to the disk with radius $\epsilon\to 0$. If writing the integral in cylindrical

coordinate and assuming $r = |z-\zeta|\tan\alpha$, $dr = |z-\zeta|\sec^2\alpha d\alpha$, we will get:

$$\begin{aligned}
\lim_{z_l\to\zeta_l^+}\int_0^{2\pi}\int_0^{\epsilon}\frac{\partial}{\partial\zeta}\frac{1}{\sqrt{r^2+(z-\zeta)^2}}u(\boldsymbol{\xi})rdrd\theta &= \lim_{z\to\zeta^+}\int_0^{2\pi}\int_0^{\epsilon}\frac{z-\zeta}{[\sqrt{r^2+(z-\zeta)^2}]^3}u(\boldsymbol{\xi})rdrd\theta \\
&= \lim_{z\to\zeta^+}\int_0^{2\pi}\int_0^{\alpha(\epsilon)}\frac{z-\zeta}{[\sqrt{(z-\zeta)^2(\tan^2\alpha+1)}]^3}u(\boldsymbol{\xi})|z-\zeta|\cdot\tan\alpha\cdot|z-\zeta|\cdot\sec^2\alpha d\alpha d\theta \\
&= \lim_{z\to\zeta^+}u(\boldsymbol{x})\int_0^{2\pi}\int_0^{\alpha(\epsilon)}\frac{z-\zeta}{|z-\zeta|}\frac{|\cos\alpha|^3}{\cos^3\alpha}\sin\alpha d\alpha d\theta \\
&= \lim_{z\to\zeta^+}u(\boldsymbol{x})\frac{z-\zeta}{|z-\zeta|}\frac{|\cos\alpha|^3}{\cos^3\alpha}2\pi[-\frac{|z-\zeta|}{\sqrt{\epsilon^2+(z-\zeta)^2}}+1] \qquad \text{(D.9)}
\end{aligned}$$

In this case, $\alpha\to 0$, $\cos\alpha > 0$; from $z\to\zeta^+$ we will have:

$$\begin{aligned}
\lim_{z_l\to\zeta_l^+} -\frac{(z-\zeta)}{\sqrt{\epsilon^2+(z-\zeta)^2}} &= 0 \\
\lim_{z_l\to\zeta_l^+} +\frac{z-\zeta}{|z-\zeta|} &= 1
\end{aligned}$$

Then:

$$\lim_{z_l\to\zeta_l^+}\int_0^{2\pi}\int_0^{\epsilon}\frac{\partial}{\partial\zeta}\frac{1}{\sqrt{r^2+(z-\zeta)^2}}u(\boldsymbol{\xi})rdrd\theta = 2\pi u(\boldsymbol{x}) \qquad \text{(D.10)}$$

$$\begin{aligned}
\lim_{\boldsymbol{x}\to S_b^+}\int_{S_b}u(\boldsymbol{\xi})\frac{\partial}{\partial n_{\boldsymbol{\xi}}}\frac{1}{\sqrt{(x_l-\xi_l)^2+(y_l-\eta_l)^2+(z_l-\zeta_l)^2}}dS_{\boldsymbol{\xi}} &= 2\pi u(\boldsymbol{x}) \\
+PV\int_{S_b}u(\boldsymbol{\xi})\frac{\partial}{\partial n_{\boldsymbol{\xi}}}\frac{1}{\sqrt{(x_l-\xi_l)^2+(y_l-\eta_l)^2+(z_l-\zeta_l)^2}}dS_{\boldsymbol{\xi}}&
\end{aligned}$$

Similarly, we can get:

$$\begin{aligned}
\lim_{\boldsymbol{x}\to S_b^-}\int_{S_b}u(\boldsymbol{\xi})\frac{\partial}{\partial n_{\boldsymbol{\xi}}}\frac{1}{\sqrt{(x_l-\xi_l)^2+(y_l-\eta_l)^2+(z_l-\zeta_l)^2}}dS_{\boldsymbol{\xi}} &= -2\pi u(\boldsymbol{x}) \\
+PV\int_{S_b}u(\boldsymbol{\xi})\frac{\partial}{\partial n_{\boldsymbol{\xi}}}\frac{1}{\sqrt{(x_l-\xi_l)^2+(y_l-\eta_l)^2+(z_l-\zeta_l)^2}}dS_{\boldsymbol{\xi}}&
\end{aligned}$$

Thus, we have proved the second equation in the jump condition:

$$\lim_{\boldsymbol{x}\to S_b^{\pm}} \int_{S_b} u(\boldsymbol{\xi}) \frac{\partial G(\boldsymbol{x};\boldsymbol{\xi})}{\partial n_{\boldsymbol{\xi}}} dS_{\boldsymbol{\xi}} = \pm 2\pi u(\boldsymbol{x}) + \int_{S_b} u(\boldsymbol{\xi}) \frac{\partial G(\boldsymbol{x};\boldsymbol{\xi})}{\partial n_{\boldsymbol{\xi}}} dS_{\boldsymbol{\xi}} \tag{D.11}$$

When the field point is approaching the lid surface S_i, the contribution from the source can be explained by the above equation. Herein, we will investigate the effect from the image source.

First, we assume the field point is approaching the lid surface from above and what will the integral equation behave. Please note that for the image source on the lid surface, we will have $\zeta = 0$. To make the derivation valid for a general case, we keep the notation ζ in the derivation.

$$\lim_{\boldsymbol{x}\to S_b^{\pm}} \int_{S_b} \frac{\partial}{\partial n_{\boldsymbol{\xi}}} \frac{1}{\sqrt{(x_l-\xi_l)^2+(y_l-\eta_l)^2+(z_l+\zeta_l)^2}} u(\boldsymbol{\xi}) dS_{\boldsymbol{\xi}}$$

Then, from similar approach, we will have:

$$\begin{aligned}
&\lim_{\boldsymbol{z_l}\to\zeta_l^+} \int_0^{2\pi}\int_0^{\epsilon} \frac{\partial}{\partial\zeta} \frac{1}{\sqrt{r^2+(z+\zeta)^2}} u(\boldsymbol{\xi}) r dr d\theta \\
&= 2\pi u(\boldsymbol{x}) \lim_{z_l\to\zeta_l^+} \frac{|\cos\alpha|^3}{\cos^3\alpha} \cdot \Big[+ \frac{(z+\zeta)}{\sqrt{\epsilon^2+(z+\zeta)^2}} - \frac{z+\zeta}{|z+\zeta|} \Big]
\end{aligned}$$

From $z \to \zeta^+$ and $\zeta = 0$, we can get:

$$\begin{aligned}
\cos\alpha &> 0 \\
\lim_{z_l\to\zeta_l^+} \frac{(z+\zeta)}{\sqrt{\epsilon^2+(z+\zeta)^2}} &= 0 \\
\lim_{z_l\to\zeta_l^+} \frac{z+\zeta}{|z+\zeta|} &= 1
\end{aligned}$$

Thus,

$$\lim_{\boldsymbol{z_l}\to\zeta_l^+} \int_0^{2\pi}\int_0^{\epsilon} \frac{\partial}{\partial\zeta} \frac{1}{\sqrt{r^2+(z+\zeta)^2}} u(\boldsymbol{\xi}) r dr d\theta = -2\pi u(\boldsymbol{x}) \tag{D.12}$$

Considering the effect from source and its image source, the integral regarding Green function can be written as:

$$\lim_{\boldsymbol{x}\to S_i^-}\int_{S_i} u(\boldsymbol{\xi})\frac{\partial G(\boldsymbol{x};\boldsymbol{\xi})}{\partial n_{\boldsymbol{\xi}}}dS_{\boldsymbol{\xi}} = \int_{S_i} u(\boldsymbol{\xi})\frac{\partial G(\boldsymbol{x};\boldsymbol{\xi})}{\partial n_{\boldsymbol{\xi}}}dS_{\boldsymbol{\xi}} \tag{D.13}$$

Following the same approach, we can get the expression when field point is approaching the lid surface from below and end up with:

$$\lim_{\boldsymbol{x}\to S_i^+}\int_{S_i} u(\boldsymbol{\xi})\frac{\partial G(\boldsymbol{x};\boldsymbol{\xi})}{\partial n_{\boldsymbol{\xi}}}dS_{\boldsymbol{\xi}} = \int_{S_i} u(\boldsymbol{\xi})\frac{\partial G(\boldsymbol{x};\boldsymbol{\xi})}{\partial n_{\boldsymbol{\xi}}}dS_{\boldsymbol{\xi}} \tag{D.14}$$

It shows that if we adopt $\frac{\partial}{\partial n_{\boldsymbol{\xi}}} = \vec{n}_{\boldsymbol{\xi}}\cdot\nabla_{\boldsymbol{\xi}} = \vec{n}_{\boldsymbol{\xi}}\cdot(\frac{\partial}{\partial\xi},\frac{\partial}{\partial\eta},\frac{\partial}{\partial\zeta})$, we will not get the jump condition as that in Kleinman[57].

If we choose $\frac{\partial}{\partial n_{\boldsymbol{\xi}}} = \vec{n}_{\boldsymbol{\xi}}\cdot\nabla_{\boldsymbol{x}} = \vec{n}_{\boldsymbol{\xi}}\cdot(\frac{\partial}{\partial x},\frac{\partial}{\partial y},\frac{\partial}{\partial z})$, the integral equation will be:

$$\begin{aligned}
&\lim_{z\to\zeta^+}\int_{B(x,\epsilon)}\frac{\partial}{\partial z}\cdot\frac{1}{\sqrt{(x-\xi)^2+(y-\eta)^2+(z-\zeta)^2}}u(\boldsymbol{\xi})dS_{\boldsymbol{\xi}}\\
&=\lim_{z\to\zeta^+}\int_0^{2\pi}\int_0^{\epsilon}\frac{\partial}{\partial z}\frac{1}{\sqrt{r^2+(z-\zeta)^2}}u(\boldsymbol{\xi})rdrd\theta\\
&=\lim_{z\to\zeta^+}\int_0^{2\pi}\int_0^{\epsilon}\frac{\zeta-z}{[\sqrt{r^2+(z-\zeta)^2}]^3}u(\boldsymbol{\xi})rdrd\theta
\end{aligned}$$

If set $r = |z-\zeta|\tan\alpha$, then $dr = |z-\zeta|\sec^2\alpha d\alpha$, $\cos\alpha = \frac{|z-\zeta|}{\sqrt{(z-\zeta)^2+\epsilon^2}}$.

$$\begin{aligned}
above = \lim_{z\to\zeta^+}\int_0^{2\pi}\int_0^{\alpha(\epsilon)}\frac{\zeta-z}{[\sqrt{(z-\zeta)^2(\tan^2\alpha+1)}]^3}u(\boldsymbol{\xi})\cdot|z-\zeta|\cdot\tan\alpha\cdot|z-\zeta|\cdot\sec^2\alpha d\alpha d\theta\\
=\lim_{z\to\zeta^+}\frac{|\cos\alpha|^3}{\cos^3\alpha}\frac{-(z-\zeta)}{|z-\zeta|}\int_0^{2\pi}d\theta\int_0^{\alpha(\epsilon)}\sin\alpha d\alpha
\end{aligned} \tag{D.15}$$

where,

$$\int_0^{2\pi} d\theta \int_0^{\alpha(\epsilon)} \sin\alpha d\alpha = 2\pi[-\cos\alpha(\epsilon)+1] = 2\pi[-\frac{|z-\zeta|}{\sqrt{(z-\zeta)^2+\epsilon^2}}+1] \tag{D.16}$$

Substitute into the original integral,

$$\begin{aligned}
&\lim_{z\to\zeta^+} \frac{|\cos\alpha|^3}{\cos^3\alpha}\frac{-(z-\zeta)}{|z-\zeta|}\int_0^{2\pi} d\theta \int_0^{\alpha(\epsilon)} \sin\alpha d\alpha \\
&= \lim_{z\to\zeta^+} 2\pi u(\boldsymbol{x})\frac{|\cos\alpha|^3}{\cos^3\alpha}\frac{-(z-\zeta)}{|z-\zeta|}[-\frac{|z-\zeta|}{\sqrt{(z-\zeta)^2+\epsilon^2}}+1] \\
&= \lim_{z\to\zeta^+} 2\pi u(\boldsymbol{x})\frac{|\cos\alpha|^3}{\cos^3\alpha}\big[\frac{(z-\zeta)}{\sqrt{(z-\zeta)^2+\epsilon^2}}-\frac{z-\zeta}{|z-\zeta|}\big]
\end{aligned} \tag{D.17}$$

The evaluation point approaches the surface from above. Based on the assumptions, we have $\alpha \to 0$, thus $\cos\alpha > 0$. $z \to \zeta^+ \Rightarrow |z-\zeta| = (z-\zeta)$. Also, ϵ needs to be one order larger than $|z-\zeta|$. Thus,

$$\lim_{z\to\zeta^+} \frac{(z-\zeta)}{\sqrt{(z-\zeta)^2+\epsilon^2}} = 0 \tag{D.18}$$

$$\lim_{z\to\zeta^+} \frac{|\cos\alpha|^3}{\cos^3\alpha}\frac{-(z-\zeta)}{|z-\zeta|}\int_0^{2\pi} d\theta \int_0^{\alpha(\epsilon)} \sin\alpha d\alpha = -2\pi u(\boldsymbol{x}) \tag{D.19}$$

Back to the original integral:

$$\lim_{\boldsymbol{x}\to S_b^{\pm}} \int_{S_b} u(\boldsymbol{\xi})\frac{\partial G(\boldsymbol{x};\boldsymbol{\xi})}{\partial n_{\boldsymbol{\xi}}} dS_{\boldsymbol{\xi}} = \mp 2\pi u(\boldsymbol{x}) + \int_{S_b} u(\boldsymbol{\xi})\frac{\partial G(\boldsymbol{x};\boldsymbol{\xi})}{\partial n_{\boldsymbol{\xi}}} dS_{\boldsymbol{\xi}} \tag{D.20}$$

Herein, we have observed the singular terms' contribution. However, the sign of the singular term is not consistent with the jump condition in Kleinman[57].

APPENDIX E

A NOTE ON THE CONCLUSION BASED ON THE GENERALIZED STOKES THEOREM [1]

In this section, we discuss about the variant Stokes theorem in Ogilvie[125]. The formula was adopted in Salvesen[112] to derive an important equation, which converted the integral contains the derivatives of the potential into that containing no derivatives. The significance of the equation is to make the hydrodynamic problem of ships much easier to solve. The original integral involving the derivatives will become part of the expressions for added mass and damping, which makes it possible to define the nonzero-speed added mass and damping matrix based on the information of the zero-speed cases. That conclusion has laid the foundation for the later research on ship hydrodynamics and was cited in many literatures, for example Newman[126], Lewis[127].

We first discuss the application of the variant Stokes theorem in calculating the radiation forces and review the key equations. Afterward, the focus is switched to the discussion on the formula derived in Ogilvie[125] and Salvesen[112]. Some inaccurate or inconsistent parts are found. Finally, we conclude that the mathematical basis for the variant Stokes theorem is not rigid enough and that formula is an approximation method to study the hydrodynamics of ships with nonzero forward speed.

E.1 Formula of the Forces and Motion RAOs

For the purpose of convenience, we collect the relevant formula from the main part of the thesis herein.

[1] Part of the section is reprinted with permission from " A Note on the Conclusion Based on the Generalized Stokes Theorem " by Yujie Liu, Jeffrey Falzarano, 2017. *Journal of Offshore Engineering and Technology* , pp. 1-17 Copyright 2017 by International Association of Ocean Engineers.

E.1.1 Zero Speed

When solving the hydrodynamic problem with zero speed, the wave excitation forces are defined as:

$$F_{Di}^{(1)} = \iint_S i\rho\omega\ (\phi_I^{(1)} + \phi_D^{(1)}) e^{i\omega t}\ n_i'\ dS$$

$$F_{Ri}^{(1)} = \iint_S i\rho\omega (\sum_{j=1}^{6} \eta_j^{A(1)} \phi_j^{*(1)}) e^{i\omega t}\ n_i'\ dS \qquad i = 1 \sim 6$$

where, $\vec{n'} = (n_1', n_2', n_3')$ and $\vec{r} \times \vec{n} = (n_4', n_5', n_6') = (y\ n_3' - z\ n_2', z\ n_1' - x\ n_3', x\ n_2' - y\ n_1')$.

The equations to solve for the motion RAOs are:

$$\sum_{j=1}^{6} [-\omega^2 (M_{ij} + M_{ij}^a) + i\omega B_{ij} + C_{ij}] \eta_j^{A(1)} = \iint_S i\rho\omega (\phi_I^{(1)} + \phi_D^{(1)})\ n_i\ dS$$

E.1.2 Nonzero Speed

For the cases with a nonzero speed, the formula of the forces and the RAO will be mostly similar except the force caused by the radiation potential. The radiation forces can be defined as below:

$$\begin{aligned} \overline{F}_{Rj}^{(1)} &= -\iint_S n_j' \overline{P}_R^{d(1)} dS = \rho \iint_S n_j' (\frac{\partial}{\partial \bar{t}} - U \frac{\partial}{\partial \bar{x}}) (\sum_{k=1}^{6} \bar{\eta}_k^{A(1)} \overline{\phi}_{rel-k}^{*(1)} e^{i\omega_e \bar{t}}) dS \\ &= \sum_{k=1}^{6} T_{jk} \bar{\eta}_k^{A(1)} e^{i\omega_e \bar{t}} \end{aligned} \tag{E.1}$$

where, $T_{jk} = \rho \iint_S n_j' (i\omega_e - U \frac{\partial}{\partial \bar{x}}) \overline{\phi}_{rel-k}^{*(1)} dS$.

The equation is the key equation we are discussing in this paper. The significance of this equation is that it converts the integral involving the derivative of the potential into an integral only about the potential value. This simplification is based on the generalized Stokes theorem. Then the

expression of T_{jk} can be converted into:

$$T_{jk} = \rho i\omega_e \iint_S n'_j \overline{\phi}^{*(1)}_{rel-k} dS - U\rho \iint_S m_j \overline{\phi}^{*(1)}_{rel-k} dS \tag{E.2}$$

where, $n_j = (n'_1, n'_2, n'_3, n'_4, n'_5, n'_6)$, $m_j = (0, 0, 0, 0, n'_3, -n'_2)$.

If the integral involves no derivatives of the potential, the added mass and damping can be explicitly formulated in terms of the potential value. As a result, the motion RAO can be resolved.

E.2 Conclusion Based on the Generalized Stokes Theorem

The key equation to transform T_{jk} is discussed in Salvesen[112]. The equation is acquired by substituting $\vec{q} = \phi U\vec{i}, (j = 1 - 3)$ and $\vec{q} = \phi U\vec{i} \times \vec{r}, (j = 4 - 6)$ in the variant of the generalized Stokes theorem discussed by Ogilvie[125]. The generalized Stokes theorem cited by Salvesen[112] is listed as below:

$$\int_C d\vec{s} \times \vec{q} = \iint_S (\vec{n} \times \vec{\nabla}) \times \vec{q}\, dS$$

The key equation to finish the transformation discussed by Salvesen[112] is as below:

$$\iint_S n_j U \frac{\partial}{\partial x} \phi dS = U \iint_S m_j \phi dS - U \int_{C_x} n_j \phi dl \tag{E.3}$$

where, $n_j = (n'_1, n'_2, n'_3, n'_4, n'_5, n'_6)$, $m_j = (0, 0, 0, 0, n'_3, -n'_2)$.

E.3 Discussion on the Variant of Stokes Theorem

In this section, we will follow the approaches in Ogilvie[125] and Salvesen[112] and discuss the derivations in detail. Some inaccurate parts will be addressed. The discussion on the cases when $j = 1, 2, 3$ and $j = 4, 5, 6$ will be conducted separately.

E.3.1 Variant Formula (j = 1 - 3)

To discuss the cases when , we will first repeat the approach in Ogilvie[125] and check the equations. Then we will move on to the discussion about the methods in Salvesen[112].

E.3.1.1 Ogilvie's Approach

We will first define the notations used in the derivation:

1. $\vec{V}$ is the fluid velocity across the fluid domain. Based on the assumptions of the potential theory method, it satisfies the following equations:
   - $\vec{\nabla} \cdot \vec{V} = 0$ in the fluid domain
   - $\vec{\nabla} \times \vec{V} = 0$ in the fluid domain
   - $\vec{n} \cdot \vec{V} = 0$ on the body surface
2. $\vec{n} = (n_1, n_2, n_3)$, $\vec{r} \times \vec{n} = (n_4, n_5, n_6)$, $\vec{r} = (x, y, z)$
3. $\vec{m} = -(\vec{n} \cdot \vec{\nabla})\vec{V} = (m_1, m_2, m_3)$, $\vec{r} \times \vec{m} + \vec{V} \times \vec{n} = -(\vec{n} \cdot \vec{\nabla})(\vec{r} \times \vec{V}) = (m_4, m_5, m_6)$.

The formula we are going to prove is as below:

$$\iint_{S_b} \left[m_i \phi + n_i (\vec{V} \cdot \vec{\nabla} \phi) \right] dS = \int_{C_{wl}} dl \cdot n_i \cdot \phi (\vec{k} \cdot \vec{V}) \tag{E.4}$$

For the case when $i = 1, 2, 3$, alternatively, the vector format of the above equation can be:

$$\iint_{S_b} \left[\phi \vec{m} + \vec{n} (\vec{V} \cdot \vec{\nabla} \phi) \right] dS = \int_{C_{wl}} dl \cdot \vec{n} \cdot \phi (\vec{k} \cdot \vec{V}) \tag{E.5}$$

The details of the proof will be discussed in Appendix F. The general idea of the proof is: we starts from the generalized Stokes theorem, applies the equations which satisfies to simplify the original expression into the objective formula.

E.3.1.2 Salvesen's Approach

In Salvesen[112], the term $\vec{q} = \phi U \vec{i}$ is chosen to substitute into the variant of Stokes theorem. It ends up in the following equations:

$$\iint_{S_b} \left[\phi\vec{m} + \vec{n}(U\frac{\partial}{\partial x}\phi)\right] dS = 0 \tag{E.6}$$

In such a way, the integral containing the derivative is correlated with the integral involving only the potential ϕ. The conclusion is obtained by substituting the potential ϕ directly into the variant Stokes theorem discussed in Ogilvie[125].

However, in the derivation of the variant of Stokes theorem, $\vec{V}$ should satisfy: $\vec{\nabla} \cdot \vec{V} = 0$ in the fluid domain, $\vec{\nabla} \times \vec{V} = 0$ in the fluid domain, $\vec{n} \cdot \vec{V} = 0$ on the body surface. In the derivation of Salvesen[112], we are indeed using $\vec{V} = U\vec{i}$. Apparently, the requirements on $\vec{V}$ are not satisfied. This leads to the inaccuracy of the conclusion.

E.3.2 Variant Formula (j = 4 - 6)

We will follow the similar approach to discuss the formula for the cases when $i = 4, 5, 6$. The formula we are going to prove is:

$$\iint_{S_b} \left[\phi(\vec{r} \times \vec{m} + \vec{V} \times \vec{n}) + (\vec{r} \times \vec{n})(\vec{V} \cdot \vec{\nabla}\phi)\right] dS = \int_{C_{wl}} dl(\vec{r} \times \vec{n})\phi(\vec{k} \cdot \vec{V}) \tag{E.7}$$

E.3.2.1 Ogilvie's Approach

In deriving the formula, one important vector identity was used in Ogilvie[125] as below:

$$[(\vec{n} \times \vec{\nabla}) \times (\phi\vec{V})] \times \vec{r} = \phi[\vec{r} \times \vec{m} + \vec{V} \times \vec{n}] + (\vec{r} \times \vec{n})(\vec{V} \cdot \vec{\nabla})\phi$$

However, based on the derivation for the cases when $i = 1, 2, 3$. We have:

$$(\vec{n} \times \vec{\nabla}) \times (\phi\vec{V}) = \phi(\vec{n} \cdot \vec{\nabla})\vec{V} - \vec{n}(\vec{V} \cdot \vec{\nabla}\phi) \tag{E.8}$$

When we substitute the above equation into the LHS of the vector identity, we find the RHS cannot be obtained. We will end up in the following equation:

$$\begin{aligned}[(\vec{n}\times\vec{\nabla})\times(\phi\vec{V})]\times\vec{r} &= -[\phi\,\vec{m}+\vec{n}(\vec{\nabla}\phi\cdot\vec{V}]\times\vec{r}\\ &= -\phi\vec{m}\times\vec{r}-(\vec{n}\times\vec{r})(\vec{V}\cdot\vec{\nabla}\phi)\\ &= \phi(\vec{r}\times\vec{m})+(\vec{r}\times\vec{n})(\vec{V}\cdot\vec{\nabla})\phi\end{aligned}$$

We will easily find the difference with the vector identity. The observation has also put the validity of the objective function in doubt. Thus, we choose to use an example to examine the objective function. The details can be found in Appendix G. It turned out that the following equation, serving as the basis of the variant formula for $i = 4, 5, 6$, is not valid.

$$\iint_{S_b} dS\big[(\vec{n}\times\vec{\nabla})\times(\phi\vec{V})\big]\times\vec{r} = \int_{C_{wl}}\big[\vec{dl}\times(\phi\vec{V})\big]\times\vec{r} \tag{E.9}$$

E.3.2.2 Salvesen's Approach

In Salvesen[112], the term $\vec{q} = \phi U\vec{i}\times\vec{r}$ was used to substitute into the variant formula based on Stokes theorem. Indeed, the following equation is chosen for the cases when $i = 4, 5, 6$, which is not consistent with the formula in Ogilvie[125].

$$\iint_{S_b} dS(\vec{n}\times\vec{\nabla})\times(\phi\vec{V}\times\vec{r}) = \int_{C_{wl}}\vec{dl}\times(\phi\vec{V}\times\vec{r}) \tag{E.10}$$

E.4 Conclusion

In this section, we discussed about the variant Stokes theorem. The formula has converted the integral containing the derivative of the potential into that without the derivative, which has greatly simplified the hydrodynamic problem. The formula is widely applied in the research about the

hydrodynamic problem of the ship with nonzero speed. It is used in the strip theory method and panel method. Herein, we chose the panel method to illustrate the importance of the formula. The results are presented and discussed.

Additionally, we have discussed some inaccurate parts in the derivations in Ogilvie[125] and Salvesen[112]. To conclude, the variant Stokes theorem is an approximation method used in the engineering problems. The mathematical basis is not rigid enough and may put a limitation on possible applications in some problems.

APPENDIX F

DISCUSSION FOR THE VARIANT STOKES THEOREM (I = 1, 2, 3) [1]

F.1 Objective Equation

As mentioned in E, the objective equation is as below:

$$\iint_{S_b} \left[\phi\vec{m} + \vec{n}(\vec{V}\cdot\vec{\nabla}\phi)\right] dS = \int_{C_{wl}} dl\cdot\vec{n}\cdot\phi(\vec{k}\cdot\vec{V}) \tag{F.1}$$

We will start from the generalized Stokes Theorem by substituting $\vec{q} = \phi\vec{V}$. Thus, we will get:

$$\iint_{S_b} (\vec{n}\times\vec{\nabla})\times(\phi\vec{V}) = \int_{C_{wl}} \vec{dl}\times(\phi\vec{V}) \tag{F.2}$$

F.2 Discussion on the LHS

We simplify the left hand side (LHS) by using the vector identities:

$$(\vec{n}\times\vec{\nabla})\times(\phi\vec{V}) = \phi\left[(\vec{n}\times\vec{\nabla})\times\vec{V}\right] + \left[(\vec{n}\times\vec{\nabla})\phi\right]\times\vec{V} \tag{F.3}$$

Where,

$$\left[(\vec{n}\times\vec{\nabla})\phi\right]\times\vec{V} = (\vec{n}\times\vec{\nabla}\phi)\times\vec{V} = (\vec{n}\cdot\vec{V})\vec{\nabla}\phi - (\vec{\nabla}\phi\cdot\vec{V})\vec{n} \tag{F.4}$$

$$(\vec{n}\times\vec{\nabla})\times\vec{V} = \vec{n}\times(\vec{\nabla}\times\vec{V}) + (\vec{n}\cdot\vec{\nabla})\vec{V} - \vec{n}(\vec{\nabla}\cdot\vec{V}) \tag{F.5}$$

The second formula can be proved by expanding the expression in the tensor notations. We use

[1] Part of the section is reprinted with permission from " A Note on the Conclusion Based on the Generalized Stokes Theorem " by Yujie Liu, Jeffrey Falzarano, 2017. *Journal of Offshore Engineering and Technology* , pp. 1-17 Copyright 2017 by International Association of Ocean Engineers.

the conditions for $\vec{V}$: $\vec{\nabla} \cdot \vec{V} = 0$ in the fluid domain, $\vec{\nabla} \times \vec{V} = 0$ in the fluid domain, $\vec{n} \cdot \vec{V} = 0$ on the body surface. Then we get:

$$(\vec{n} \times \vec{\nabla}) \times (\phi \vec{V}) = \phi(\vec{n} \cdot \vec{\nabla})\vec{V} - \vec{n}(\vec{V} \cdot \vec{\nabla}\phi) \tag{F.6}$$

Notice the definition of $\vec{m} = -(\vec{n} \cdot \vec{\nabla})\vec{V}$, we will finally get:

$$\iint_{S_b} (\vec{n} \times \vec{\nabla}) \times (\phi \vec{V}) dS = -\iint_{S_b} [\phi \, \vec{m} + \vec{n}(\vec{\nabla}\phi \cdot \vec{V})] dS \tag{F.7}$$

F.3 Discussion of the RHS

In the right hand side (RHS) of the formula, the vector in the line integral can be defined as:

$$\vec{dl} = -dl(\vec{k} \times \vec{n}) \tag{F.8}$$

Also, we have:

$$(\vec{k} \times \vec{n}) \times (\phi \vec{V}) = \big[\vec{k} \cdot (\phi \vec{V})\big]\vec{n} - \big[\vec{n} \cdot (\phi \vec{V})\big]\vec{k} = \vec{n}\phi\big[\vec{k} \cdot \vec{V}\big] \tag{F.9}$$

Thus, the RHS becomes:

$$\int_{C_{wl}} \vec{dl} \times (\phi \vec{V}) = -\int_{C_{wl}} dl(\vec{k} \times \vec{n}) \times (\phi \vec{V}) = -\int_{C_{wl}} dl \, \vec{n} \, \phi\big[\vec{k} \cdot \vec{V}\big] \tag{F.10}$$

Thus, the objective equation is proven. Please note that there is a sign difference when comparing this equation against that in Salvesen[112].

APPENDIX G

DISCUSSION FOR THE VARIANT STOKES THEOREM (I = 4, 5, 6) [1]

G.1 Verification of the Generalized Stokes Theorem

We will check this formula:

$$\iint_{S_0} (\vec{n} \times \vec{\nabla}) \times \vec{q}\, dS = \int_{C_0} \vec{dl} \times \vec{q} \tag{G.1}$$

If we assume $\vec{q} = x\vec{i} + y\vec{j}$, $\vec{n} = (0, 0, 1)$, the contour C_0 is made up of the following black lines.

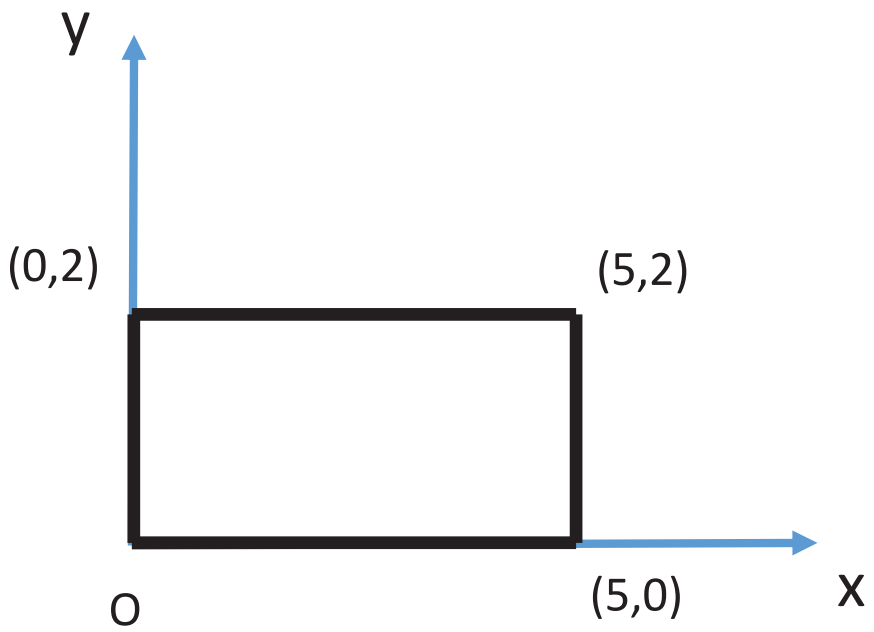

Figure G.1: Integral Path

[1] Part of the section is reprinted with permission from " A Note on the Conclusion Based on the Generalized Stokes Theorem " by Yujie Liu, Jeffrey Falzarano, 2017. *Journal of Offshore Engineering and Technology*, pp. 1-17 Copyright 2017 by International Association of Ocean Engineers.

In the LHS of the formula, we will get:

$$\vec{n} \times \vec{\nabla} = \partial_x \vec{j} - \partial_y \vec{i}$$
$$(\vec{n} \times \vec{\nabla}) \times \vec{q} = -2\vec{k}$$
$$\iint_{S_0} -2\vec{k} dS = -20\vec{k}$$

In the RHS of the formula, we will get:

$$\vec{dl} \times \vec{q} = (y\, dx - x\, dy)\vec{k}$$
$$\int_{C_1} = 0 \qquad y = 0,\ x \in [0, 5]$$
$$\int_{C_2} -5dy\vec{k} = -10\vec{k} \qquad x = 5,\ y \in [0, 2]$$
$$\int_{C_3} 2dx\vec{k} = -10\vec{k} \qquad y = 2,\ x \in [5, 0]$$
$$\int_{C_4} = 0 \qquad x = 0,\ y \in [2, 0]$$

Sum up all the terms, we will get $-20\vec{k}$, which equals to the LHS.

G.2 Check the Formula for $i = 4 \sim 6$

We will check this formula:

$$\iint_{S_0} [(\vec{n} \times \vec{\nabla}) \times \vec{q}] \times \vec{r}\, dS = \int_{C_0} (\vec{dl} \times \vec{q}) \times \vec{r} \tag{G.2}$$

If we assume $\vec{q} = x\vec{i} + y\vec{j}$, $\vec{n} = (0, 0, 1)$, the contour C_0 is made up of the following black lines.

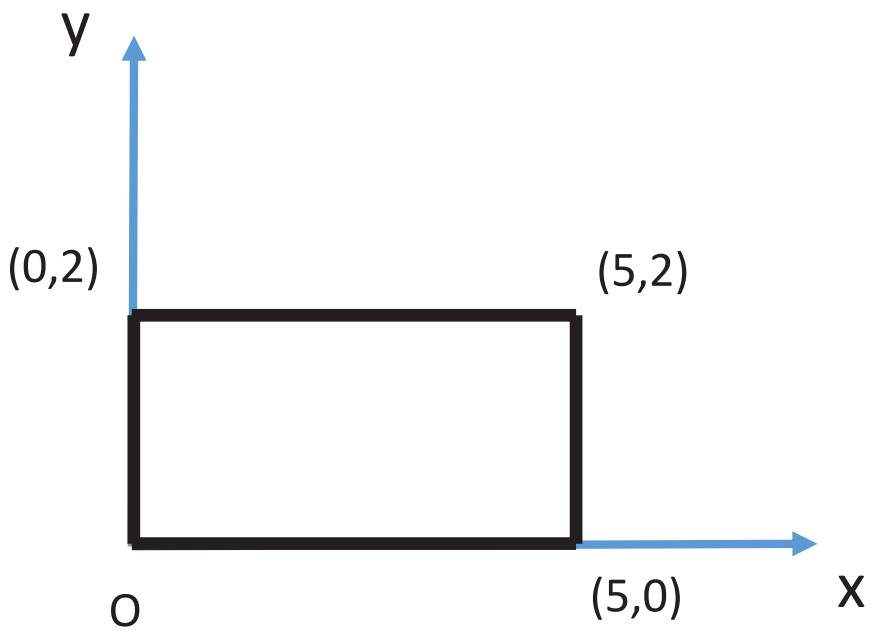

Figure G.2: Integral Path

In the LHS of the formula, we will have:

$$(\vec{n} \times \vec{\nabla}) \times \vec{q} = -2\vec{k}$$

$$[(\vec{n} \times \vec{\nabla}) \times \vec{q}] \times \vec{r} = (-2\vec{k}) \times \vec{r} = -2x\vec{i} + 2y\vec{j}$$

$$\iint_{S_0} dS[(\vec{n} \times \vec{\nabla}) \times \vec{q}] \times \vec{r} = \int_0^5 dx \int_0^2 dy(-2x\vec{i} + 2y\vec{j}) = -50\vec{j} + 20\vec{i}$$

In the RHS of the formula, we have:

$$
\begin{aligned}
&(\vec{dl} \times \vec{q}) \times \vec{r} = (xy\ dx - x^2\ dy)\vec{j} - (y^2\ dx - xy\ dy)\vec{i} \\
&\int_{C_1} = 0 \qquad y = 0, x \in [0, 5] \\
&\int_{C_2} (-25dy)\vec{j} + 5ydy\vec{i} = -50\vec{j} + 10\vec{i} \qquad x = 5, y \in [0, 2] \\
&\int_{C_3} (2x\ dx)\vec{j} - 4dx\vec{i} = -25\vec{j} + 20\vec{i} \qquad y = 2, x \in [5, 0] \\
&\int_{C_4} = 0 \qquad x = 0, y \in [2, 0]
\end{aligned}
$$

Sum up the four terms, we can get $-75\vec{j} + 30\vec{i}$. LHS is not equal to RHS. Thus the formula is questionable.